Optimisation of the interfaces of solid-state batteries

Cameron Bathgate

A thesis submitted for the degree of PhD
at the
University of St Andrews

2024

Identifier to use to cite or link to this thesis:

DOI: https://doi.org/10.17630/sta/815

Candidate's declaration

I, Cameron Bathgate, do hereby certify that this thesis, submitted for the degree of PhD, which is approximately 45,000 words in length, has been written by me, and that it is the record of work carried out by me, or principally by myself in collaboration with others as acknowledged, and that it has not been submitted in any previous application for any degree. I confirm that any appendices included in my thesis contain only material permitted by the 'Assessment of Postgraduate Research Students' policy.

I was admitted as a research student at the University of St Andrews in September 2018.

I received funding from an organisation or institution and have acknowledged the funder(s) in the full text of my thesis.

Date 31st January 2023 Signature of candidate

Supervisor's declaration

I hereby certify that the candidate has fulfilled the conditions of the Resolution and Regulations appropriate for the degree of PhD in the University of St Andrews and that the candidate is qualified to submit this thesis in application for that degree. I confirm that any appendices included in the thesis contain only material permitted by the 'Assessment of Postgraduate Research Students' policy.

Date 31st January 2023 Signature of supervisor

Permission for publication

In submitting this thesis to the University of St Andrews we understand that we are giving permission for it to be made available for use in accordance with the regulations of the University Library for the time being in force, subject to any copyright vested in the work not being affected thereby. We also understand, unless exempt by an award of an embargo as requested below, that the title and the abstract will be published, and that a copy of the work may be made and supplied to any bona fide library or research worker, that this thesis will be electronically accessible for personal or research use and that the library has the right to migrate this thesis into new electronic forms as required to ensure continued access to the thesis.

I, Cameron Bathgate, have obtained, or am in the process of obtaining, third-party copyright permissions that are required or have requested the appropriate embargo below.

The following is an agreed request by candidate and supervisor regarding the publication of this thesis:

Printed copy

No embargo on print copy.

Electronic copy

No embargo on electronic copy.

Date 31st January 2023 Signature of candidate

Date 31st January 2023 Signature of supervisor

Underpinning Research Data or Digital Outputs

Candidate's declaration

I, Cameron Bathgate, understand that by declaring that I have original research data or digital outputs, I should make every effort in meeting the University's and research funders' requirements on the deposit and sharing of research data or research digital outputs.

Date 31st January 2023 Signature of candidate

Permission for publication of underpinning research data or digital outputs

We understand that for any original research data or digital outputs which are deposited, we are giving permission for them to be made available for use in accordance with the requirements of the University and research funders, for the time being in force.

We also understand that the title and the description will be published, and that the underpinning research data or digital outputs will be electronically accessible for use in accordance with the license specified at the point of deposit, unless exempt by award of an embargo as requested below.

The following is an agreed request by candidate and supervisor regarding the publication of underpinning research data or digital outputs:

Embargo on all of electronic files for a period of 5 years on the following ground(s):

- Publication would be commercially damaging to the researcher, or to the supervisor, or the University (e.g. Intellectual Property Rights)

Supporting statement for embargo request

Some industrial partners wish to keep some of this information as a patent.

Title and Description

- I require an embargo on the description only.

Date 31st January 2023 Signature of candidate

Date 31st January 2023 Signature of supervisor

Abstract

The development of solid-state batteries aims to implement lithium metal in a battery to utilise the total capacity and voltage it applies. A full solid-state battery would also prevent a fire hazard by removing the volatile organics. Solid oxide electrolytes of $Li_{3x}La_{2/3-3x}TiO_3$ (LLTO) and $Li_7La_3Zr_2O_{12}$ (LLZO) are promising electrolyte materials that can be used in these applications. However, one of the main limitations is the high interfacial tension at the interface between lithium metal and the solid electrolyte.

In this work, LLTO electrolytes were synthesised using an aqueous system providing a double perovskite structure with a pseudo-cubic structure after sintering the material at 1350°C for 6 hours provided a unit cell parameter of a = 3.86 Å. It was also possible to dope the b-site with aluminium to allow for a cubic phase formation at a lower temperature, 1100°C, at a shorter time of ten minutes.

This thesis describes the use of LLTO and LLZO electrolytes wetting experiments investigating the intrinsic wetting of solid lithium. The results demonstrated that lithium is intrinsically poor at wetting solid electrolyte surfaces with contact angles greater than 90°. The adhesion of lithium to these electrolytes is also low, which explains why pressure is typically implemented to cause lithium to stick to the surface. Using wetting state calculations, most of the interactions between lithium and the solid oxide electrolytes are described as Cassie-Baxter wetting states. By the same calculations, some interactions present capillary filling, providing evidence that electrolyte modification may permit lithium infiltration. This can be done by coating protective sacrificial electrolytes (LLTO) on top of others (LLZO). Another conclusion from the wetting experiments was that altering the surface tension of lithium is one of the easiest and most beneficial ways to allow for the impregnation of the lithium into the pores, improving the contact angle at the micro-scale.

The coating of an LLZO pellet with a sol-precursor of LLTO was successful. It provided some improvement ($1x10^{-3}$ Scm^{-1}) to the ionic conduction when placed in a symmetrical cell with lithium, and the contact angle of lithium to this coated LLZO improved in the microscale. Bulk lithium adhesion and impregnation will require further improvement by either improved coverage of LLTO on the surface of LLZO or by using higher vacuum pumps at a temperature of around 180°C.

The LLTO coating also protects the LLZO surface from absorbing CO_2 to form impurities of $La_2Zr_2O_7$. LLTO stability with the desired cathode material $LiFePO_4$ (LFP) is noted and may lead to an implementation of LFP, LLTO and LLZO in a full cell, which would be an exciting step as a proof of concept.

Acknowledgements

I want to thank many people whose help, support and expertise allowed me to complete this study and grow in confidence as a researcher and a person. Firstly, I would like to express my appreciation and thanks to my supervisor, Professor John T. S. Irvine. Without his encouragement, guidance, knowledge and support over the pandemic and these four years, I am not sure I would have completed this work. Secondly, I would like to thank Candice Mitchell and Gillian McCowan for their encouragement and support in making the most of the opportunities presented to me.

I would also like to thank Dr Mihkel Vestli for his support and expertise in material synthesis and for providing the garnet materials for the wetting experiments. Also, for helping me understand how to follow a research plan. In addition, I would like to thank Dr Ioanna (Marianna) Pateli for the emotional support, and Raman guidance will also run the equipment for precise results. Thanks also to Dr. David Miller for assisting me with pellet polishing techniques, running the FIB-SEM, and teaching me how to use SEM. To Dr Cristian Savaniu and Dr Aida Cuesta for their expertise and guidance in sol-gel synthesis. To Dr Paul Connor and Dr Gavin Irvine for their help setting up and implementing the wetting rigg for performing wetting experiments. And to my friend and work colleague Chao Dun Tan, whose expertise and running of AFM allowed for the addition of exciting data.

Thanks to the Faraday Institution and the PhD cohort that helped me emotionally and enhanced my battery knowledge to be used in an industrial setting. It was a fantastic opportunity and training session, and I feel incredibly fortunate to have these opportunities. Thank you to Frann Long, who has supported and organised all the PhD events that kept us engaged and learning the up-to-date battery science with an insight into different commercial applications.

Thank you to the JTSI group and technicians who helped me in the lab and made the past four years enjoyable with fun and laughter.

Thank you to my friends outside of chemistry who have kept me grounded and supported me throughout my academic career.

To my mother, father and the rest of my family who have looked after me, supported me and loved me despite my struggles. They are a big reason I can give things outside of my comfort zone a shot and are a big inspiration in my life.

Above all, I give this work to the **LORD Almighty** in view of His grace toward me.

Contents

Chapter 1 Introduction

1.1 Summary of this thesis

With the ever-increasing demand to electrify the world to reduce the total emissions of CO_2[1] , electric vehicles (EVs) will need to increase their presence in the transport sector[2]. Current Li-ion battery technology has enormous safety issues and will require higher energy[3] and power density if EVs want to travel further distances and charge faster[4].

Solid-state batteries are a future technology that replaces flammable organic liquid electrolytes with non-flammable solid electrolytes[5–10]. Making everything in the battery solid also allows metallic lithium to be used as a part of the battery, which should satisfy the energy and power density requirements needed for pushing EVs to travel around 300 miles.

In this work, I have studied lithium metal's synthesis and interface interaction against promising solid oxide electrolytes. Of the solid electrolytes that can be used, oxide ceramics are a promising material. Most of the work focuses on the high ionically conductive and atmosphere-stable perovskite material $Li_{3x}La_{2/3-3x}TiO_3$ (LLTO) and the promising garnet $Li_7La_3Zr_2O_{12}$ (LLZO), which is known to be stable against lithium metal.

The first results chapter (chapter 3) demonstrates that it is possible to synthesise a cubic structure of $Li_{0.5}La_{0.5}TiO_3$ (LLTO) using an aqueous sol-gel reaction.

In chapter 4 wetting calculations are performed on lithium metal with pellets of the synthesised LLTO material and LLZO material. Dr. Mihkel Vestli supplied the LLZO material as he worked on developing a tape-cast method for another research project. This chapter highlights the biggest problem of most solid oxide electrolytes. Lithium is intrinsically non-spontaneous in forming good contact with solid electrolytes compared to organic liquid electrolytes. This conclusion is reached using wetting experiments that investigate the contact angle of molten metals on the surfaces of solid oxide electrolytes. A more optimistic conclusion from these experiments is that alloying lithium should theoretically improve the contact with the payoff of losing some capacity.

In the final chapter, a thin coating of this $Li_{0.5}La_{0.5}TiO_3$ material was applied to the more promising solid oxide electrolyte, $Li_7La_3Zr_2O_{12}$. Initial experiments demonstrate good contact between the two electrolytes and can be used to improve the contact of lithium metal to $Li_7La_3Zr_2O_{12}$. Also noteworthy is that $Li_{0.5}La_{0.5}TiO_3$ will act as a protective coat to $Li_7La_3Zr_2O_{12}$ to minimise the volume of CO_2 that can be adsorbed to the surface.

In the same chapter, we also found that the protective coating of $Li_{0.5}La_{0.5}TiO_3$ can be used to allow for the promising cathode material $LiFePO_4$ to be used with $Li_7La_3Zr_2O_{12}$. Without it, there are stability issues and would help the solid-state battery market move away from $LiCoO_2$, which is expensive and violates human rights in extracting Co[11].

1.2 Sustainability and environmental concerns

With population growth and development, the need for electricity will keep increasing. A section of this increasing energy demand includes generating the energy required to charge EVs (Figure 1-1). EVs are necessary to reduce the overall CO_2 emissions, with the total emissions in the region of 31 Gt[1] in 2021. Passenger vehicles make up 53% of transport emissions in 2021[2], and oil is the second largest contributor to CO_2 (Figure 1-2). To achieve the demand for an increase in electric vehicles, the current battery technology will need to advance from their current energy capacity[3] of approximately 240 Wh kg^{-1} and power output[4] of 5 kW l^{-1}. A low cost of below \$100 kW h^{-1} is still the goal for global companies, but the current geopolitical market, with the increasing price of lithium[12], has influenced the time we have to reach the goal. A kwh^{-1} measures the energy to keep a one kW application running for one hour.

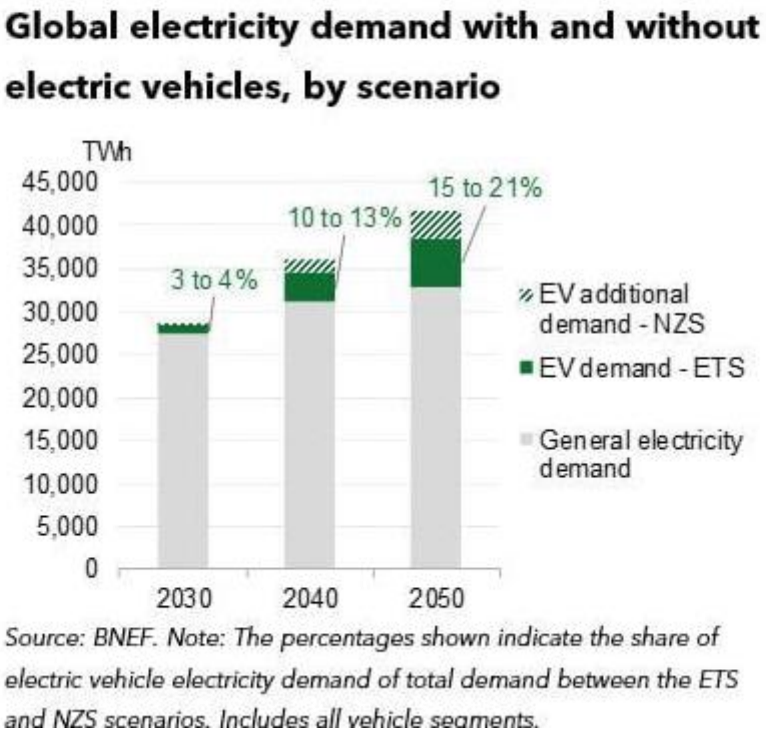

Global electricity demand with and without electric vehicles, by scenario

Source: BNEF. Note: The percentages shown indicate the share of electric vehicle electricity demand of total demand between the ETS and NZS scenarios. Includes all vehicle segments.

Figure 1-1: The electric demand over the next three decades focuses on the demand that EVs will generate because of an economic scenario (ETS) and a net zero scenario (NZS).

Although not in the scope of this thesis, there will need to be future consideration for the primary anode material as lithium demand increases exponentially, thus limiting availability significantly. There is, therefore, a requirement for improved recycling capacities of current Li-ion technology or a shift to different metals and materials (Figure 1-3).

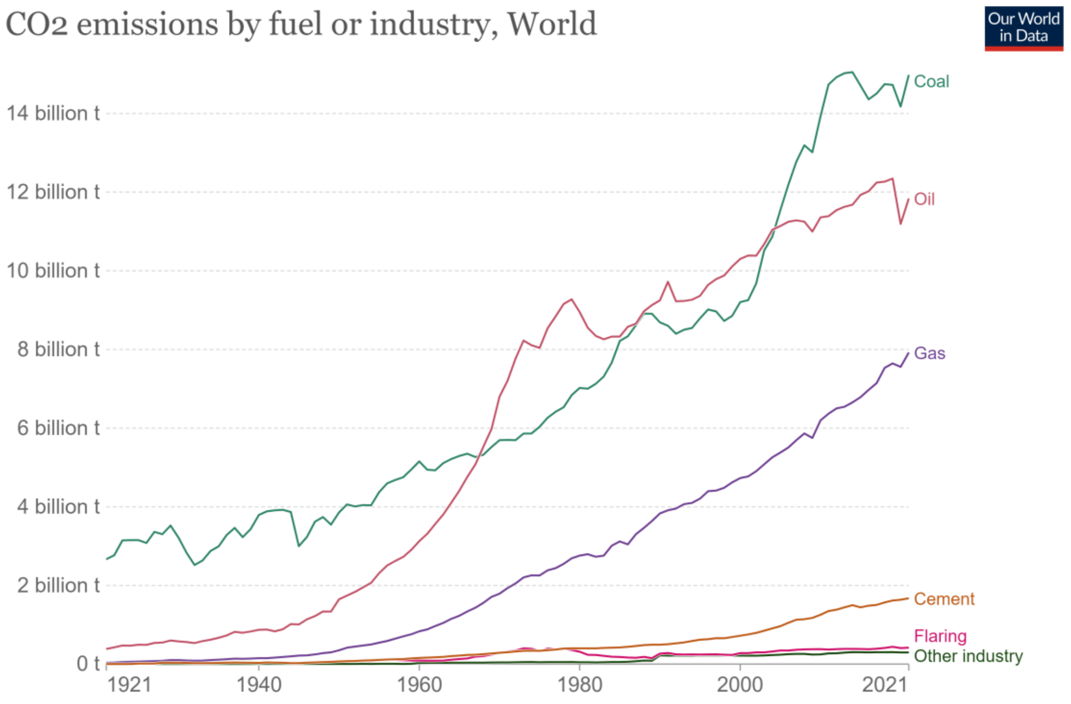

Source: Our World in Data based on the Global Carbon Project (2022) OurWorldInData.org/co2-and-other-greenhouse-gas-emissions • CC BY

Figure 1-2: CO_2 gas emissions by fuel or by industry over one hundred years

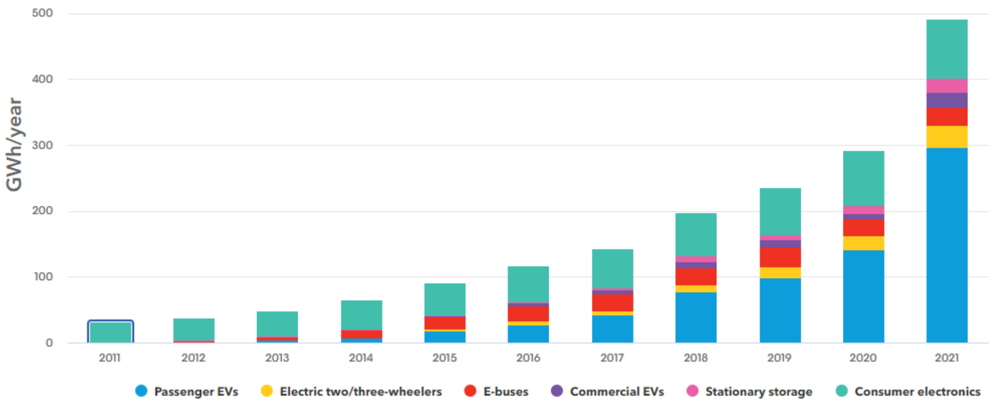

Source: BNEF.

Figure 1-3: The annual lithium-ion battery demand by application

1.3 A brief history and explanation of the battery

Despite some theorising that the Babylonians invented the oldest batteries back in 205 B.C., the first working battery is accredited to Alessandro Volta, who in 1800 in Italy invented the 'Voltaic pile' in an exploration of how current works[13,14]. It comprised a cloth soaked in brine sandwiched with zinc and copper metal. He demonstrated that continuous electric current could flow by some force gradient, which would go on to be named after him, voltage.

To explain the potential voltage gradient, electrodes need to be discussed first. The two conducting metals in Volta's pile are called electrodes, and although an electrode does not need to be solid, it does have to be a conducting phase for both ions and electrons. The electrode must form an interface between a conducting phase for ions, called an electrolyte or brine in Volta's case, and allow a potential voltage gradient to form with a second electrode. These electrodes can be inert and catalytic, such as in fuel cells or batteries active in electrochemistry[15]. In the 1830s, Michael Faraday worked extensively on these electron transfer reactions for the electrodes and noted that to understand any electrochemical system, one of these electrodes needs to be an anode. Another must be a cathode; more fundamental steps occur at the interface between an electrode and an electrolyte.

An anode half-reaction generates an electron for an external circuit by electron transfer as it oxidises the electrolyte species after it has been adsorbed to the surface of the electrode (Equation 1.1). A desorption reaction follows, allowing the oxidised ion to flow into the bulk of the electrolyte[16].

$$Zn_{(s)} - 2e^{-} \rightarrow Zn^{2+}_{(aq)}\ otherwise\ written\ as\ Zn_{(s)} \rightarrow Zn^{2+}_{(aq)} + 2e^{-}$$

Equation 1.1

This electron follows an external circuit, producing the current we use, and meets an oxidised ion as it passes through the electrolyte and is adsorbed onto the cathode electrode. There a reduction transfer occurs, reducing the electroactive species.

$$Cu^{2+}_{(aq)} + 2e^{-} \rightarrow Cu_{(s)}$$

Equation 1.2

It is important to note that Equation 1.1 and Equation 1.2 are the half-reactions used in the volta experiment and are an example of a galvanic cell in which the anodic and cathodic half-reactions drive spontaneous electric work through an external circuit. Also, there is a requirement for ionic and electronic neutrality throughout the cell, so two electrons are transferred for one mole of ionic species. Moreover, in both electrodes, cleaving and the formation of new bonds of the ionic species at the electrode surfaces lead to only partial or no desorption of the species. Resulting in a build-up of material on the surface of the electrodes, leading to a phase formation or intercalation in the case of current EV electrodes. This occurs when ions insert between planes of atoms in the structure without altering the phase or unit cell parameters of the electrode[17].

This spontaneous electrical work results from the half-cell REDOX (reduction and oxidation combined) reactions. Therefore, an overall energy change occurs with electrons moving from the anode electrode to the cathode electrode. Measuring the total number of electrons flowing through the external circuit is analogous to measuring the chemical change at each electrode surface. Finding the total charge, Q, as an integration of the current (I) regarding the measurement time leads to applying Faradays' law (Equation 1.3)[15].

$$Q = \int Idt = mnF$$

Equation 1.3

Faraday's law uses *m* as the number of moles of reactant or product formed, *n* as the number of electrons required for this conversion and *F* as the Faraday constant (96485 $\mathrm{Cmol^{-1}}$), providing information on the charge of the cell powering applications. The time frame used in battery technology is Amp hours ($\mathrm{Ah^{-1}}$) as 1 $\mathrm{Ah^{-1}}$ = 3600 C. Assuming that all of the charges are used in electron transfer reactions, which is not usually the case, a current efficiency (φ) needs to be defined (Equation 1.4).

$$\varphi = \frac{charge\ consumed\ in\ electron\ transfer}{Total\ charge}$$

Equation 1.4

This energy change of the electrochemical species occurring at the anode and the cathode involves the chemical potential, which is the sum of their electrostatic interactions within their shells and subshells and, in the case of electrons, involves the movement of charge from fermi levels in the conduction bands[18]. This movement of energy can be associated with Gibbs free energy of change as it occurs spontaneously, and there is a free movement of electrons and ions[19]. This Gibbs free energy of change (ΔG) shows that an electromotive force, otherwise known as the equilibrium cell potential (E°_{cell}) occurs creating the voltage difference between the anode and the cathode (Equation 1.5).

$$\Delta G = -nFE^{\circ}_{cell}$$

Equation 1.5

Understanding the potential of electrodes and the overall cell is essential in battery technology. However, the very nature of potential is that there must be this energy difference. Therefore, a working electrode and a reference material must be present. This information is typically gathered by a three-electrode system using a working electrode, the material of interest, a large counter electrode to help the kinetics of the working electrode, and a reference electrode to keep those electrodes' voltages relative. So, the resting potential of an electrode needs to be set in a cell with no charge extracting, meaning there is no change to the concentration of the surface of the electrode, but there is still a dynamic equilibrium in which both the oxidation reaction and reduction reaction are occurring. Consider a simple working electrode with an electron transfer reaction (Equation 1.6), with *O* being the oxidised species and *R* being the reduced species. The Nernst equation (Equation 1.7) calculates the electrode potential with the concentration (*c*) of the species. If the system is in equilibrium, the Nernst equation can be simplified further (Equation 1.8)[16].

$$O + ne^{-} \rightarrow R$$

Equation 1.6

$$E_e = E^{\circ}_e - \frac{2.3RT}{nF}\log\frac{c_O}{c_R}$$

Equation 1.7

$$E_e = \frac{627.9R}{nF}\log K$$

Equation 1.8

The initial potential E_e is the equilibrium potential for electrochemical couple O/R species used in the cell and as E°_e is the formal potential for the electrochemical couple at standard conditions, then allowing the working electrode to rest in standard conditions allows the removal of this factor, as seen in Equation 1.8. *R* is the gas constant, *T* is the temperature of 298 K at standard conditions, *n* is the number of electrons used, and *F* is the Faraday constant[16]. At standard conditions, the equilibrium constant (*K*) can be simplified further if metals are used as their activities equate to 1. If a working electrode is against the standard hydrogen electrode (SHE) or other laboratory-based references, then the cell potential of that working electrode is known.

The cell potential at equilibrium E°_{cell} on either, a discharge or a charge will include the individual electrode potentials so that the charge flow will flow spontaneously through the external circuit from the lowest potential electrode to the highest potential electrode of a battery. Which ultimately means that E°_{cell} and thus, the cell voltage is the difference between the cathode (E_c) and anode (E_a) potential of that reaction (discharge or charge).

$$E^{\circ}_{cell} = E_c - E_a$$

Equation 1.9

The theoretical maximum voltage of a cell is the difference between the chemical potentials of the cathode by the anode divided by the charge. Each electrode potential originates from the energy of the redox reactions of that electrode. Each electrode potential should be contained within the potential 'window' of the electrolyte to prevent damage to the electrolyte and lead to cell failure. That is the energy gap between the HOMO/Conduction band and the LUMO/valence band of the electrolyte. The anode potential needs to be below the conduction band, or it reduces the electrolyte (unless SEI forms). Cathode energy must be above the valence band or its oxides (unless SEI forms). The anions in the oxide host and the cathode may overlap, which may prevent the necessary redox reaction from occurring. Polyanions reduce the anion-p band but cause a drop in the overall capacity. The electrolyte window is around 5 V for a cell[6].

There are multiple characteristics of a suitable electrolyte for battery technology. Firstly, the potential window (E_g) should be large enough to contain the electrode potentials so there is no decomposition on the charge and discharge. Secondly, the electrode and electrolyte interface must remain even after the electrodes' changing volumes after ion movement[20,21]. The ionic conductivity must be above 10^{-4} S cm^{-1} and the electronic conductivity below 10^{-10} S cm^{-1} over the operating temperature range of the battery while maintaining a transference number of around one[20,21]. Chemical stability is needed over ambient temperatures and temperatures under a higher power load while also maintaining electrode stability, such as forming a pacifying solid electrolyte interface (SEI) [20,21]. Finally, the electrolyte materials must ideally be safe while maintaining low toxicity and cost[20,21].

1.4 Li-ion battery technology

The Li-ion battery (LIB) was developed by John Goodenough, Michael Stanley Whittingham and Akira Yoshino [13,14,22–25]with Sony making the first LIB commercial release for a video recorder in 1991 [13,14,24]. Michael Stanley Whittingham started using the intercalation of lithium-aluminium as the positive electrode and titanium disulfide as the negative electrode in the 1970s as the first secondary lithium-ion battery. Due to safety issues of these electrodes, work was done to find more suitable materials. In 1980, John Goodenough switched out the positive electrode to lithium cobalt oxide, and in 1985, Akira Yoshino used a graphite-based negative electrode[13,14]. These two electrodes and organic liquid electrolytes that can contain compounds such as LiPF6 in ethylene carbonate (EC) are still used today. The volume of electrodes, active particle size and morphology have been improved to their limiting value with continued reliance on Li ions due to their fast ion mobility at room temperature[26].

The capacity of Li-ion improves due to increasing the area or arranging the cells in parallel. The electrolyte performs ionic conduction, forcing external electrical conduction. Ionic mobility is the charge per weight (Ah kg^{-1}) and volume (Ah L^{-1}). This process is reversible, unlike electrode volume change, electrode decomposition and any electrode-electrolyte reactions. Another irreversible capacity drop comes from forming the SEI (solid-electrolyte interphase) after the first discharge.

1.5 Why solid-state lithium batteries?

The biggest concern with Li-ion batteries currently is a safety issue. Using organic electrolytes to allow Li-ion transport for the electrochemical reactions allows for very high ionic conductivity but is highly flammable and toxic[26,27]. Especially when there is a short circuit issue after multiple cycles of charging and discharging, the lithium will build up at target areas at the electrode surface to form nonhomogeneous dendrites[26,28]. Short-circuiting can lead to the ignition of the organic electrolyte leading to thermal runaway, which is very fast in Li-ion. Hydrogen fluoride gas is also emitted during the combustion, and the issue becomes more pronounced as the battery gets bigger to provide even more energy density for larger vehicles[25,29]. As the dendrite formation is self-propagating reaction[23,30,31].

In solid-state lithium batteries, toxic and flammable organic solutions that could be leaked cause an explosion are not present[5–8]. Having all solid electrolytes means that the thermal conductivity of the battery is higher than current LIB[32,33] due to the ability of free electrons and elastic vibrations to transfer the heat energy through a material[32,34]. Therefore, when higher C-rates are applied to these batteries, there is faster heat release, and no heat spots occur, meaning there are no thermal runaways[33].

Another advantage solid-state lithium batteries have is the higher energy densities theoretically achievable by using metallic lithium as the negative electrode (anode). Liquid electrolytes in current LIBS need a lithium ion at the negative electrode rather than metallic lithium due to the explosion issues mentioned earlier. Metallic lithium, the lightest alkaline metal, has a high theoretical capacity of 3860 mA h g^{-1} [26]. It is possible to use a smaller weight and volume of lithium to achieve gravimetric and volumetric energy densities of 400 Wh Kg^{-1} [33,35–37] and 900 Wh l^{-1} [33,35–37], respectively. It also opens up the voltage window of cells[33] as metallic lithium has a low reduction potential, against the standard hydrogen electrode, of -3.04 V[6,8,10,11]. This high energy density will help meet the energy demand required for the complete electrification of the transport centre.

A disadvantage is that lithium dendrites still occur[33,39,40], the Li dendrite growth can be suppressed by applying a low pressure below two mPa [26,41–44]. This results from the electrolyte having a higher mechanical strength[33,45,46] and a shear modulus larger than lithium[45–47]. Preventing the lithium dendrite formation issue should also help increase the stability cycle lifetime of the battery[33].

1.6 Solid electrolytes

The first recorded work of a solid electrolyte was silver sulfide by Michael Faraday back in 1833[48,49], facilitating his work on ion conduction laws as previously noted [22]. Nernst followed by using solid electrolytes in a patent in 1901[50]. Work on silver halides allowed Tubandt and Lorenz to observe lattice changes that allow anions to become mobile with increasing temperature leading to ionic conduction rather than just electronic[51]. Setting the foundation for a new science called defect chemistry, investigating how stoichiometric doping[22] and intrinsic point defects allow ion conduction[49].

With that, another type of defect occurs in the materials interstitial site of materials[44] which leads to the discovery of the NASICON structure $NaA_2(PO_4)_3$ series where A is a cation with an oxidation state of +4, namely Ge, Ti or Zr in 1968 by L. Hagman *et al.*[31,52]. A sodium conducting electrolyte with sodium at the interstitial cation sites can hop through bottlenecks between AO_6 octahedra and PO_4 tetrahedra in a 3D network[8,31].

A point defect material that created additional vacancies that were a lithium *s*uper*i*onic *con*ductor, more commonly known as LISICON, was $Li_{14}ZnGe_4O_{16}$ was described by Bruce and West in 1983[31,53,54]. With very good lithium conduction reporting 0.125 Scm^{-1} at 300°C but only around $1x10^{-7}$ Scm^{-1} at room temperature[54]. A sulphides glass $Li_{10}GeP_2S_{12}$ (thio-LISICON by literature)[9,31,55,56] was introduced by R. Kanno *et al.* in 2000[56] reporting electrical conductions in the 1.03 $x10^{-2}$ S cm^{-1} [9,55] at room temperature, good thermal activity[27] and electrochemical stability to 5V[9]. They are like the oxygen ion conduction LISICON material but with S^{2-}, which has weaker interactions with Li^+ than O_2 and allows faster ion mobility with these sulphide glasses.

In 1985 J. Sudworth and A. Tilley took the material called beta alumina (β-Al_2O_3) reported by Rankin and Merwin in 1916 and were able to make a sodium sulphur battery[57]. This sodium-conducting solid electrolyte is actually of the composition $(Na_2O)_{1+x}11Al_2O_3$, but the name for this material stuck[57]. This oxide is composed of closed-packed layers of Al_2O_3 octahedra and tetrahedra existing as a hexagonal[58,59] and rhombohedral crystal systems[59,60] and loosely packed layers that contain the mobile sodium layers called conduction planes [57–60]. The sodium moves via the Frenkel defect mechanism[58,59], in which interstitial oxygen is stabilised by adding an aluminium ion, generating an oxygen vacancy in the phases—allowing two extra sodium ions into that plane[59]. The rhombohedral phase is more significant, allowing for higher sodium conduction around $1x10^{-1}$ Scm^{-1} at 300 K[59,61], and it is possible to do a cation exchange with the sodium to allow for different ionic conduction such as lithium and silver[58]. It obtained activation energy for silver and sodium conductions of 0.18 eV and 0.17 eV, respectively[58].

Another possible solid electrolyte is a solid polymer electrolyte, a solid solution of the polymer poly(ethylene oxide) in an alkali metal salt[62]. The advantage to using a polymer electrolyte is utilising the easy polymer processing with the electrochemistry of liquids[62,63] to create mechanical stable and flexible leak-free batteries. They also do not show as high ionic conduction, presenting values around 1x10^{-5} Scm^{-1} at room temperature and low transference numbers resulting in bad kinetics[8,62,64].

There are also promising solid electrolytes that conduct sulphur ions that possess high ionic conductivity[65]. The problem is that it is reactive to conventional electrode materials, cannot be constructed in polar solvents and have high liability at high voltages. Some scientists have constructed a Li_3PS_4 (LPS) membrane in THF, allowing for a broader range of polymeric binders, such as Polyvinyl Chloride (PVC) and nitrile butadiene (NBR)[65]. However, the PVC seems to decompose at raised temperatures. Furthermore, the highest ionic conduction occurs with just LPS[65]. It is a 'single step', so anodic or cathodic material is mixed with P_2S_5 and Li_2S and the binder in THF at room temperature. It is then cast using a doctor blade and heat treated under a vacuum creating a bendable film. The EDS shows that the LPS had a capacity of 153 mA h g-1 at 0.05 C because of the increased interface resistance. Although sulphur is not with the active material, the grains are sporadic, leading to poor electrical connection and low ionic conductivity—ball-milled precursors for enhanced performance. NCM622/graphite demonstrated a capacity of 110 mA h g^{-1} at 15 C, 100°C with 86% retention after 250 cycles. However, it is not clear which binders were used. Lithium ion can also be conducted by oxide ceramics which will be discussed in the following section.

1.7 Lithium-ion solid-state electrolytes

Multiple types of lithium-ion solid-state electrolytes conduct lithium differently. It could occur as a point defect as seen in a point defect such as in LISICON showing Arrhenius behaviour[49,66]. Unfortunately, *LISCON* reacts with lithium metal and CO_2, decreasing its ionic conductivity and not making it a suitable electrolyte[31]. Recently the stability of thiol-LISICON against metal lithium has come into question as decomposition voltages have been observed below 5V forming insulating materials at the interface[9]. Processing and cycling these batteries in ambient pressure is still an issue due to the material moisture sensitivity and still requires to be improved[9].

A lithium conducting family member of the NASICON family found in $Li_{0.3}Al_{0.3}Ti_{1.7}(PO_4)_3$ (LATP) in 1989 was found to have bulk conduction in 1x10^{-3} Scm^{-1} at room temperature[31,67,68]. The substitution of Ti^{4+} for Al^{3+} will lead to stability by increasing the M-O bonds and decreasing the Li-O bonds. However, there are stability issues as Ti^{4+} ion will reduce contact with lithium metal and increase the electronic conduction of the electrolyte[31,69,70].

The existing micro batteries are full solid state[71] containing the amorphous $Li_{2.88}PO_{3.73}N_{0.14}$ (LIPON)[72]. It is formed using radio frequency magnetron sputtering of Li_3PO_4 in N_2 atmosphere, allowing for controlled sizes of the Li-conducting phosphate chains[9,73]. It is stable against lithium metal[9], but the main issue is that the ionic conduction is not high enough for EV applications[9,47,73] resting at $2x10^{-6}$ Scm^{-1}, which is not nearly high enough for the power application of EVs[9]. It is also sensitive to oxygen and moisture[69], which can make the scale-up of this material challenging.

$Li_{3x}La_{2/3-3/x}TiO_3$ is a perovskite (Figure 1-4) with the advantages of $Li_{0.3}La_{0.63}TiO_3$ ionic conductive hopping mechanism 10^{-3} Scm^{-1} at room temperature[74], the amorphous is stable with lithium metal[75,76] and has a voltage window[77] of 1.8 V to 3.8V Li/Li^+.

The parent material of $La_{2/3}TiO_3$ is promising by having the doping of lithium onto the A sites, there is a shift in the vacancy along the *c* axis, allowing for improved ionic conductivity at the higher temperatures as the cation vacancies on the A-sites (extrinsic behavior) will exceed the generation of intrinsic vacancies that result naturally in all material by the increase of temperature[78]. For $Li_{3x}La_{2/3-3/x}TiO_3$, there is the Li_2O volatilisation issue at higher temperatures[78.] Perovskite LLTO, with lithium migration occurring via a vacancy hopping mechanism through a square planar bottleneck created by four oxygen ions, provides the highest ionic conductivity[70] $5.25x\ 10^{-5}$ S cm^{-1}. Drawbacks involve Li intercalation when in contact with Li, and because of the reduction of Ti^{4+} to Ti^{3+}at 1.5 V[24] electronic conduction increases. In addition, there is lithium loss at higher sintering temperatures. A summary of the lithium-ion conducting solid electrolytes is recorded in Table 1.1.

Table 1.1: Summary of the lithium-ion conducting electrolytes containing their short hand name, composition and ionic conduction of lithium at room temperature.

Electrolyte short name	**Composition**	**Ionic conduction at room temperature**	**References**
LISICON	$Li_{14}ZnGe_4O_{16}$	$1x10^{-7}$ Scm^{-1}	[54]
thio-LISICON	$Li_{10}GeP_2S_{12}$	$1.03\ x10^{-2}$ S cm^{-1}	[9,55]
LATP	$Li_{0.3}Al_{0.3}Ti_{1.7}(PO_4)_3$	$1x10^{-3}$ Scm^{-1}	[31,67,68]
LIPON	$Li_{2.88}PO_{3.73}N_{0.14}$	$2x10^{-6}$ Scm^{-1}	[9,47,73]
LLTO	$Li_{3x}La_{2/3-3/x}TiO_3$	10^{-3} Scm^{-1}	[70,74]
LLZO	$Li_7La_3Zr_2O_{12}$	$0.1\ x\ 10^{-3}$ Scm^{-1}	[92,93]

The desired phase to be synthesised is the primitive cubic phase (*Pm*-3*m*). with Ti^{4+} in the corner (B sites) and in the A-site alternating Li^+ and La^{3+} rich layers[24,79,80]. In which the a-site holds vacancies creating La-poor layers along the *c*-axis, allowing Li leaping mechanism to occur either in 2D or 3D depending on the concentration of the La present in each of the layers[81,82]. There are diffusion barriers that arise as there is some mixing of the channel layers of Li as they permeate through into the La layers. Li-ion transport works as Li replaces La in the A site creating Li vacancies. It was found that x = 0.067, 40% Li vacancies show the best Li conduction[83]. Indicating that site proclamation and the square planar bottleneck are the primary factors affecting Li^+ ionic conduction[24].

The main diffusion barrier comes through the square planar bottleneck, created by four oxygen ions, preventing Li from continuous travel. Inserting a larger atom in the A site could reduce the time waiting for the bottleneck channel to return to the correct size. La is the largest, rare-earth metal (ionic radius is 1.06 Å). Therefore, looking for larger dopants such as Ba^{2+} (ionic radius =1.35 Å) to combat the loss of Li conduction in high-temperature sintering by the diffusion barriers at the grain boundaries improving the proclamation threshold [24]. It is important to note that the dopant would need a similar oxidation state to reduce the amount of charge balancing required in the material. Ba^{2+} would need additional support due to its different oxidation state[24].

It is also possible to have a hexagonal phase when the TiO_6 octahedra tilt become tilted[24,79,83]. Moreover, at temperatures below 1350°C, the tetragonal $Li_{0.3}La_{0.56}TiO_3$ (*P4/mmm*) and orthorhombic phases can exist[79]. The tetragonal phase of $Li_{0.3}La_{0.56}TiO_3$ can also form as a result of uneven distribution of La^{3+} and Li^+ vacancies in the a-site, creating a larger super unit cell[84] that's actual formula should be considered $Li_{3x}La_{1.33-x}Ti_2O_6$[85]

Synthesis of $Li_{3x}La_{2/3-x/3}TiO_3$ via Pechini synthesise method with calcining occurring at 900°C for 3 hr in air[86]. W. Kon *et al.* [86] synthesised a pellet to higher temperatures to achieve the cubic phase of *Pm*-3*m*[87] known to form around 1350°C after 6 hours in air[79]. They observed that at around 1200°C it is possible for the tetragonal structure of $Li_{0.3}La_{0.65}TiO_3$ (*P4/mmm*)[87] with La-rich and La-poor layers to form, creating irregular domain boundaries due to the mismatch of the different lattices[86]. At the grain boundaries in the EIS, high grain boundary resistance is observed as La^{3+}-rich domains block the Li^+ migration in the La^{3+}-poor domains[86]. There is also the risk of different phases forming at the grain boundary due to strain increased by the mismatch domains[86]. W. Kon *et al.* [86] suggested implementing a 30%

mol excess of Li^+ to keep activation energy low and improve ionic conduction. At 1400°C they reported an activation energy of 0.391 eV for the total ionic conduction; at 1200°C the activation energy was 0.453 eV[86].

The garnet material of $Li_7La_3Zr_2O_{12}$ (LLZO) (Figure 1-4) was known for 15 years (1988-2003) before focused research was performed[9,70,88]. Garnet structures are typically $A_3B_2C_3O_{12}$ with CO_4 tetrahedra and BO_6 Octahedra edge sharing[89]. The Li content can be increased to 7 if the B site uses Zr, Hf and Sn. The cubic phase of LLZO[90,91] is very conductive, around 0.1 – 1 mS sm^{-1}, at room temperature [92,93] and has a wide electrochemical window of up to 6 V[41,94]. There has even been substitution work done by Ferraresi *et al.*[95] replacing some Zr with Ta to reduce the cost and sintering time and improve the stability of Lithium transport within the electrolyte[9]. It is a very promising solid-state electrolyte for its chemical stability when in contact with metallic lithium[38,92].

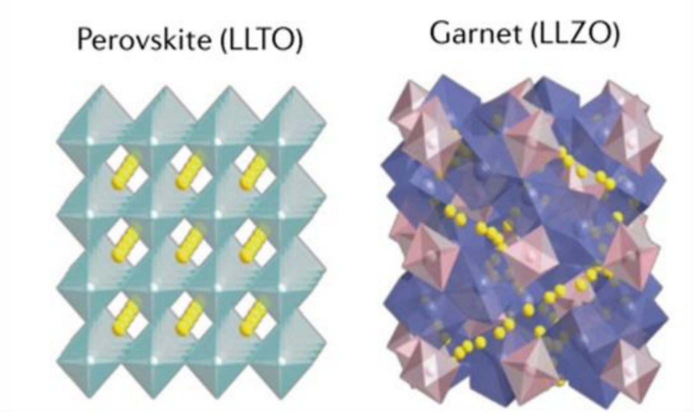

Unit cells from Figure 1,b Y. Zhu, et al, Nature review materials, 2020

Figure 1-4: Unit cells of the perovskite solid oxide electrolyte LLTO and the garnet solid oxide electrolyte LLZO. Image published in figure 1, b of the Nature review materials paper titled' Lithium-film ceramics for solid-state with ionic devices' written by Y. Zhu et al in 2020.

Stabilising the cubic phase of LLZO can also be done by doping Al^{3+} into the Zr^{4+} site and helps to reduce the sintering temperature time from 1200°C for 30 hours to 6 hours[96,97]. There are limits to the solubility of Al^{3+} in LLZO[97,98]. The substitution removes lithium to balance out the charges, reducing the unit cell parameters because Al^{3+} is smaller than Li^+. Although smaller particles can increase the surface area, it also reduces the green body density, making it more difficult for fuller densification[98,99]. Additional Al will also lead to unwanted Al-rich impurities such as $LaAlO_3$, which generates the unwanted phases of $La_2Zr_2O_7$[97,98]. L. Cheng *et al.*[98] demonstrated the solid-state synthesis of a single-grain LLZO substituted with Al^{3+} with a density of 94% after being sintered at 1100°C for 12 hours using fresh sacrificial LLZO powder. This material gave an $x10^{-4}$ Scm^{-1} bulk ionic conduction at 25°C with minimum grain boundary resistance because the more prominent grain reduced the number of grain boundaries[98]. Providing the Al content remains low, approximately 0.24 molar concentration, the optimal conductivity can be reached, and the cubic phase is sintered at lower temperatures[96,97].

1.8 Electrodes

As negative electrode lithium with the high capacity and voltage window remains the most ideal, as noted with LLTO, most solid electrolytes are unstable with metallic lithium. However, one of the main issues that still arise is the formation of lithium dendrites[39,40]. Moreover, although unaltered lithium is still the negative electrode of choice in this work, other researchers have altered the nature of lithium to present good results[38,100,101].

Through the electrochemical deposition of lithium on the surface of different electrolyte materials, glassy lithium anodes are a possibility[102]. X.Wang *et al.* demonstrated that with an increasing current density, from 0.1 to 2.5 mA cm^{-2} to a disorder-order lithium transition in which large microdomains of lithium clump from amorphous to a crystalline phase if the number of atoms is greater than 700. This mismatch of phases creates these defects by the different orientations of large grains, especially when using large current densities. These defects lead to surface roughness. Glassy lithium also avoids epitaxial growth in multiple dimensions. Although the electrochemical reversibility (CE), structural performance (i.e., the lack of defect formation (dislocations, voids, grain boundaries) and ideal deposit density should match the thermotical density of lithium (0.534 g cm^{-3}).

A possible electrode reported is the spinel $Li_4Ti_5O_{12}$ observes Li insertion on 16c octahedra sites on a charge[103]. This electrode has unique properties with its ability to prevent unit cell axis growth upon intercalation with lithium[104] to form the phase $Li_7Ti_5O_{12}$, but it has been noted that at low temperatures, there is a limiting lithium-ion transfer reaction[105]. As on the discharge, the intermediate $Li_{4+x}Ti_5O_{12}$ interfacial state is formed with the Li occupying adjacent face-sharing 8a and 16c polyhedra[106]. This is a poor Li conducting phase resulting in sluggish Li transport properties[106]. This distorted face-sharing interface highlights that interfaces need low energy barriers for the migration of Lithium[106].

Excellent Li mobility results in low interface resistance as the internal resistance depends on the mobility of Lithium in the electrode. Lower interface resistance creates faster charger rates allowing cycling stability allowing for larger electrode loads that can be used which help reduce the irreversible degradation[106].

Nano-sizing the electrode particles will improve the diffusion pathways while reducing the practical electrode densities[107]. Increasing the electrode-electrolyte contact area can increase the decomposition reactions and shorten the battery cycle life. Can use metastable intermediates in solid-state materials to create faster mobility properties.

$LiCoO_2$ (LCO), most commonly used for the cathode material, exists in spinel at low temperatures and layered hexagonal at higher temperatures[108]. Discovered by Goodenough and is the parent material[5,25]. This hexagonal 2D arrangement orientation is important to the diffusion ability of Li through the electrode[108]. The insertion potential of the Li-ions is 3.9 V and has a theoretical capacity of 137 mA h g^{-1} and 700 mA h cm^{-3} at 97 $Å^3$ $Li_3Co_3O_6$ unit cell[108].

In order to reduce the amount of Co lately different materials have been substituted for the cobalt such as Mn, Al and Ni creating high Ni content cathodes families such as $LiNi_{0.8}Co_{0.15}Al_{0.05}O_2$ (NCA) and $LiNi_xMn_yCo_{(1-x-y)}O_2$ (NMC)[109,110]. High Ni content (x=0.8) can be stabilised by the redox couples of the Mn and Al dopants allowing for higher gravimetric capacity than LCO[109–111]. Although they suffer from structure instability as a result of the dopants[109] leading to voltage decay and poor cycle life[109,110].

One of the most promising cathode materials is the olivine structure of $LiFePO_4$[112]. Li_xFePO_4 adopts an olivine structure, has a rechargeable voltage at 3.4 V, and can achieve Li cycling between $0.1<x<1$ providing a capacity of 152.9 mA h g^{-1} while there is 610 mA h cm^{-2} from the larger $Li_4Fe_4P_4O_{16}$ (291 $Å^3$) unit cell[108]. Chemically it is helpful as the polyanion drops, by inductive effects, the fermi energy of Fe^{3+}/Fe^{2+}, reducing the coulombic interactions of the Fe with the PO_4 tetrahedra, helping with the 20% energy reduction[108,112]. $Li_{1-y}FePO_4$ allows 25 cycle stability, 3.4 V plateau with a capacity of 130 $mAhg^{-1}$ at y=0.8 at 2.1 mA g^{-1} current rate[112]. Li_xFePO_4 is desirable for its reduced cost, reduced human rights violations, and safety[2,5,113].

1.9 Interfaces

The most significant limiting factor for implementing either LLTO or LLZO as solid oxide electrolytes in a solid-state battery is the high typical interface resistance of grain boundaries and the interaction between the electrodes and the electrolyte[93,114,115].

One of the primary culprits is still dendrite and void formation at the interface of the lithium metal with solid electrolytes. P. Bruce and team show that even with the pressure increasing to 3 MPa formation of lithium dendrites[45,116] on the charging still occurs. Presenting this idea that voids form as the lithium cannot be replenished fast enough at the interface due to lithium creep and diffusion slower than the lithium migration into the solid electrolyte upon discharging[116,117]. Void formation leads to a decrease in the contact angle and contact area of lithium to the interface and results inhomogeneous spread of lithium transfer across the interface. The remaining interfaces between lithium metal and the solid electrolytes then experience localised current densities and overpotentials. These localised areas observe the formation of lithium dendrites upon multiple stripping and plating of lithium[45,116–118]. Wu *et al.*[43] also stress the importance of a homogenous, even ionic transfer of lithium across the interface as Li nucleation in areas leads to cracking and weakening of the contact between electrolyte and Lithium metal[45,118]. Therefore, losing contact of lithium to the electrolyte at the interface leads to an increase in the charge transfer resistance leading to high interfacial resistances.

Current research, therefore, is searching for methods to reduce this interface resistance with the four main strategies: 1) composition tuning of electrolytes[92,95,98,119] 2) addition of barrier layers[26,114,120,121], 3) alloying lithium metal[100,120,122,123] and 4) using polymers[124–126].

The composition tuning of electrolytes includes methods such as substitution, or doping, to form stable and higher ion conducting phases[92] demonstrated in work done by Ferraresi[95]. Synthesised amorphous Li-Nb-O transition phases prevent mutual diffusion of $LiCoO_3$ with LLZO, forming non-conducting Li phases[95]. This transition phase will decrease the non-conducting phase from 100 nm to 40 nm and prevent cavities from forming at the interface. The Li-Nb-O transition phase is Li-conductive allowing for Li transport across the interface. Laser deposition deposits a 10 nm layer of Nb on LLZO; this thickness provided the optimum reduction in area-specific resistance of the interface (150 Ωcm^2). This Li-Nb-O phase provided enough coverage without blocking the Li-ion transport. The transition Li-Nb-O phase demonstrates improved cycling stability and specific and practical discharge capacity.

Another material doped in LLTO and LLZO solid electrolytes is Al_2O_3[38,92,93,114]; this hopes to produce a stable interface over multiple cycles but allows Li^+ to diffuse the interface[38]. An example of this work was observed by R. Sudo *et al.* [92] by substituting a weight percentage of 0.5% of Al_2O_3 in LLZO, the grain boundaries ionic conduction increased from $x10^{-4}$ Scm^{-1}, in the undoped LLZO, to $x10^{-3}$ in the dopped material[92]. Increasing the weight of Al_2O_3 content resulted in harm to both the bulk and grain boundary conduction, presumably due to the increased distance the Li^+ ion had to travel across the interface[8]. Once an Al-doped the LLZO, the material can undergo rapid hot pressing to reduce the interfacial resistance down to 2 Ω cm^2, improving the wetting of lithium to the electrolyte in the process[93]. Although the rapid hot pressing technique at 1000°C at 40 MPa is not easy to scale up[97].

Ga has been known to work well as a dopant as in one doped cubic LLZO example, an interfacial resistance against metallic lithium was demonstrated to be below[43] 100 Ω cm^{-2} in an argon atmosphere. With J. Wu *et al.* [43] demonstrate that the contact of lithium to the electrolyte, in other words, the wetting, without any surface modification, exhibits a contact angle of around 55°. The contact angle was determined to be a good contact of the Li metal leading to a homogenous current distribution and a 49 Ω cm^{-2} interfacial resistance. The NMR observed no Li dendrite growth after 200 cycles or 70 hours, and a maximum capacity of 900 mA h g^{-1} was reached. The potential gap of 2.3 V to 4.7 V was achieved after cycling over 410 cycles and increasing coulombic efficiency up to 99%. Despite the capacity reaching only 110 mA h g^{-1}.

Introducing protective barriers is another method to minimise the high interface resistance. One example is using an Al_2O_3 barrier[114] formed via atomic layer deposition (ALD) on $Li_7La_{2.75}Ca_{0.25}Zr_{1.75}Nb_{0.25}O_{12}$, allowing for a tight fitting of the garnet-like electrolyte with the Li electrode[114]. This layer improved the surface and contact area between the electrolyte and lithium metal[38,43,93,114,120], increased ionic conductivity, and decreased activation energy at 22°C[43,114]. There is also a significant drop in the interface resistance[43,114] down to 1 Ω cm^{-2}. The low interfacial resistance, they claim, is achieved by the ALD layer creating a Li-Al-O phase in between the Li and garnet, allowing for improved Li mobility and Li diffusion. Because of improved wetting, Li's binding energies with the $Li_{1-x}Al_2O_{3-x/2}$ are high, allowing for stronger chemical bonding. The pure Al_2O_3 layer is not conducting, but this method did not form any

Li-resisting phases, and the tight-fitting prevented Li dendrite formation. In a large cell, this reduced polarizability and the ability to undergo 90 hours of cycling at 0.2 mA cm^{-2} for 30 min in each cycling/discharging direction and maintain a stable voltage of 22 mV[114].

Altering the surface tension of lithium by adding different metals such as Sn[100,127], In[128], or Ga[129,130] is another crucial strategy to improve the contact of lithium with the solid electrolyte. The addition of 50 wt.% of Sn[100] improved the viscosity of the alloys, making them easier to stick, improved the wetting of lithium metal to the solid electrolyte and reduced the interface resistance to 7 Ω cm^2. Another example is if one GaLi-Li alloy achieves a contact angle of 0° in the wetting of the alloy to the electrolyte and achieves 1500 cycles at a current density[129] of 5 mA cm^{-2}.

On the positive electrode side, there is an instability issue with most lithium cathode materials with the most promising LLZO electrolyte[131]. With $LiCO_2$, cathode decomposition occurs above 700°C, making any heat treatment of LLZO forming unwanted $LaCO_3$ rhombohedral crystal systems[131,132]. Furthermore, on the cycling of $LiCO_2$ with LLZO, it is possible to see delamination at the interface leading to a drop in electrochemical performance and an increase in the interface resistance[133]. With $LiFePO_4$, decomposition occurs at 300°C when forming an interface with LLZO due to poor thermal stability leaving phases of $LaPO_4$, Li_3PO_4, $La_2Zr_2O_7$ and Fe_2O_3 [131,134]. The decomposition to $Li_3Fe_2(PO_4)_3$ leads to voltage drops from 3.2 V to 2.5 V [134].

1.10 Fabrication of batteries

For solid-state batteries, many fabrication processes are still being trialled but strongly follow the conventional LIB fabrication process so that the same equipment can be used. When processing and fabricating battery technology in a typical LIB battery, the liquid organic electrolyte would have an interface with all other cell components: including the positive and negative electrodes' active material, their current collectors, separator and any other inert materials in the electrode[135]. In a full solid battery, there would be no need for a separator as the electrolyte acts as the natural blocker. They would form an interface with all other components except the current collectors, which the electrodes would cover. Cell design looks at how these interface phenomena affect electrochemistry, and the only concern is a solid-state battery of the electrochemical activity of the electrodes to the interface.

As mentioned earlier, one promising solution to the lithium volume change and void formation problem would be to implement a scaffold design for the electrolyte as employed by K. Kravchyk *et al.* [136] and others[7,102,134,137]. In which there are two porous LLZO components co-sintered to a more densely synthesised middle layer[134]. At the University of St Andrews, Dr Mihkel Vestli has replicated this design for battery applications (Figure 1-5). The desired outcome is that lithium infiltration into the pores should be possible to minimise the pressure applied to the cell and improve the contact area of lithium to the electrolyte, improving transfer kinetics[131]. It is also possible via the tape-casting method to make the electrolyte in the micro aiding the electrochemical performance of the battery.

Once the cell design and the mass of the active materials and components needed for the electrode are calculated, the electrode coating stage follows. The precursors of the active components will be mixed thoroughly in either water or N-Methyl-2-pyrrolidone (NMP) with binders and carbon additives to boost the conductivity. This mixing process can last hours, after which the slurry's solid content, viscosity and particle size will be checked. Quality testing of the slurry will help determine if the materials have been mixed homogeneously. Then the electrode slurry will be coated onto its appropriate current collector. For cathode material in LIB, the electrodes are coated onto aluminium; for anode material, the slurries are coated onto the copper foil. Doctor blade, reversed rolling, or a slot die is used to determine the initial thickness of the coating to ensure that all the material will fit into the battery casings[135,138]. Then the coating is heated at a controlled rate to remove the solvent without creating cracks to the coat.

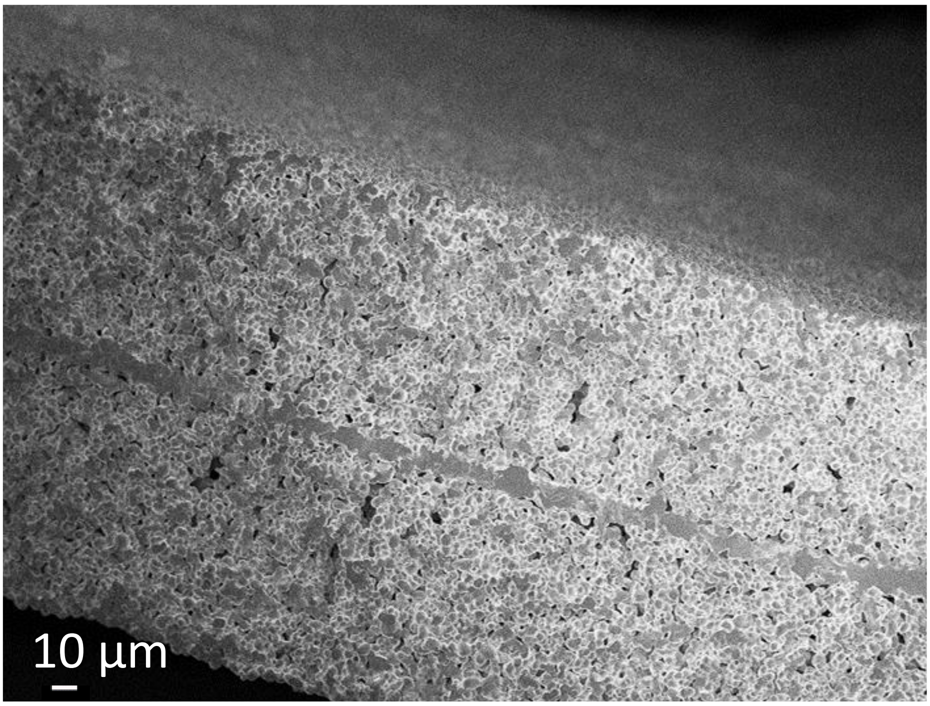

Figure 1-5: Secondary microscope image of scaffold design of $Li_{6.3}La_3Zr_{1.5}Ta_{0.5}O_{12}$ courtesy of Dr M. Vestli

Once dried, the coated electrodes are calendared in rolling machines to increase the electrodes' density[135]. The thickness of the is tailored to the battery's application. High-energy batteries will have thicker electrodes with more active material to allow for more intercalation or ion storage on the charge and discharge[47]. While high-power batteries will have thinner electrodes but more of them this is to minimise the path ions need to travel between the charge and the discharge[47].

Depending on whether the battery needs a pouch, cylindrical or prismatic cell, the electrodes are assembled in their appropriate method in a low moisture environment, typically a dry room. Each of these cells will have multiple cathode and anode electrodes stacked against each other with a separator in between that can be soaked with the electrolyte via vacuum injection.

All the battery cells assembled will be discharged, so the first charging activates the electrodes and is called the formation cycle[135]. The first charge will be at a lower current to allow the formation of the protective SEI before applying the desired current[135]. The voltage achieved at this first charge will be held for some time, called the aging process[135]. Further electrochemical tests can be done to check the stability of the cells after multiple cycles.

In solid state fabrication, one of the main differences compared to conventional LIB is that the solid electrolyte will have its own slurry mixing, tape casting and calendar process. Rather than just being a liquid that can be injected into a cell stacked together. Meaning that for the case of oxides there are now high temperature sintering steps required that make it a challenge to scale-up[139]. Not only that but the brittleness of inorganic solid electrolytes provides challenges when mechanical strain is applied so processes need to minimise this as much as possible[139–141]. The positive electrode material can be mixed and casted in a similar manner to LIB but may need to be mixed and casted in an unreactive environment[139]. Li-metal electrodes will need to be constructed in a dry atmosphere and although will also have a calendaring step there are a few different ways the initial lithium metal layer can form. It can be extruded onto a current collector, but the calendaring step can be a challenge[139,141]. It can be melted on using a dip coating or infiltration technique into the porous electrolyte side if the cathode material has been applied first[139,142]. Finally, a lithium source can be deposited on the surface either by vapour deposition or electrochemical plating[139,143].

Chapter 2 Experimental techniques and theory

2.1 List of chemical reagents

Sol-gel

$LiNO_3$, 99 % (Alfa Asear)

$La(NO_3)_3 .6H_2O$, 99% (Alfa Asear)

Titanium bis(ammonium lacto)dihyrdoxide 55 % (Alfa Asear)

Citric acid, 99.5%, (Arcos Organics)

Ammonia solution, 95% water (Alfa Asear)

$Al(NO_3)_3.9H_2O$, 99.9% (Alfa Asear)

Solid-state

Li_2CO_3, 99% (Sigma-Aldrich)

La_2O_3, 99% (Sigma-Aldrich)

TiO_2, 99% (Sigma Aldrich)

Lithium metal source

Rods, 12.7 mm, (Sigma-Aldrich)

2.2 Sol-gel

A sol is a solid phase dispersed in a liquid medium, and a gel is a liquid dispersed in a solid medium. In the sol-gel reaction mechanism, the particle size can be smaller and controlled in finer detail due to the hydrolysis and condensation reactions occurring in the sol compared to a solid-state reaction.

Sol-gel synthesis brings about the growth of grains via wet chemistry methods more than the typical firing methods in solid-state synthesis. This method allows for sintering at temperatures around 400°C to 900°C, which in turn allows for phase purity and material synthesis at lower temperatures than solid-state counter parts[144].

Sol-gel

This synthesis method uses hydrolysis and condensation reactions of aqueous or organic precursors to synthesise smaller particles with different morphologies. All variations of the sol-gel method will evaporate the solvent of the precursors to leave behind a solution containing the metal cations in olation or oxolation bonds; this is called the sol. Applying heat to the solution will allow for continued evaporation of the solution through this cation-oxygen network to leave behind a gel. Depending on the pH conditions, the aging process affects the bonding nature of the gel. Calcination of this gel will remove any hydroxide bonds remaining on the surface of the particles. During this calcination, the gel network could collapse to form a dense xerogel, or the network can retain its porosity synthesising a xerogel. The charge, thus the electronegativity, of the metal cation and the pH of the precursors will affect the rates of hydrolysis and condensation, which influence the density of the finished powder due to the precursor relying on hydrolysis and condensation reactions to create the metallic bonds generating the crystal structures[144].

Controlling the pH is important for sol-gel synthesise to control ions that predominates the sol[144]. For sol forming, condensation and hydrolysis reactions must be quick and not limited[144]. The optimal pH, therefore, depends on the precursor's temperature and concentration. Hydrolysis reaction is followed by condensation reaction with slow gelation occurring in acidic pHs and faster gelation in basic pHs[145]. For the fastest rates of condensation and hydrolysis acidic pHs are the best, but when a higher condensation rate is need than a hydrolysis rate then a basic pHs are preferred[144]. Around 7 the hydrolysis rate of reaction will be at its minimum while the rate of condensation is still increasing in rate[144]. By adding in more ammonium hydroxide solution the pH of the sol and can be changed to see if varying the pH creates different structures[144]. A pH of approximately five was chosen to allow cubic and tetragonal unit cells to form[144].

Within the variations of sol-gel synthesis, the Pechini method entraps metal cations using a mixture of ethylene glycol and citric acid[144,146]. The citrate route is an alteration by not including any ethylene glycol. Citric acid aids sol-gel synthesis as it has three carboxylic ligands per acid molecule to act as chelating agents that improve the olation and oxolation bond formation—allowing for an extended metal-polymer network. [147] The acid is an oxidant that propagates the combustion reaction with the mass depending on the fuel-to-oxidiser ratio (φ). The ratio is equal to the sum of the oxidising valences divide[147] by the sum of the reducing valences (Equation 2.1)[147]. The valences themselves are equivalent valences and are the sum of the moles of each component (n_i^{ox} and n_i^{red})by the oxidation state of each component (x_i^{ox} and x_i^{red}). It is then possible to assess the requirement to be fuel deficient, stoichiometric or fuel rich to allow for oxygen excess and strong combustion[147].

$$\varphi = \frac{\sum x_i^{ox} \times n_i^{ox}}{(-1)\sum x_i^{red} \times n_i^{red}}$$

Equation 2.1

The citrate route for forming the perovskite material $Li_{3x}La_{2/3-x}TiO_3$ uses nitrate precursors. Not only do nitrate precursors act as chelating agents, but they are oxidants that propagate the combustion reactions in gel and powder formation[144].

The Pechini process uses citric acid to help as a chelating agent and a self-propagating combustion agent in the burn-off stage of the sol-gel process. However, unlike the citrate route, ethylene glycol is not added to allow for esterification reactions to occur and build new chains within the sol. Instead, it aids the aqueous solutions of nitrates used to burn off efficiently as well as aiding in the hydrolysis and condensation reactions via its three carboxylic acids. The advantage of the citrate route is that less organic material is required, and there will be less shrinkage of the gel itself.

2.3 Solid-sate reaction

Solid-state reactions are a scalable and quick process that can use carbonates and other precursor oxides to lower the activation energy of primary recrystallisation and grain growth, typically two solid materials, to make a finished crystalline product. Grain growth is when the average grain size of strain-free material increases in heat treatment without adjusting the grain-size distribution. The Initial heating of the precursor material, typically annealing, (heating in air) is required for all of the wanted stoichiometric amounts to allow for the decomposition of unwanted elements and phase transformation[99]. The mixed and milled materials reduce the particle size of the solid components to allow for equal grain size to improve the kinetics of matter transport when the grains combine and reduce the grain-size distribution and aid the energy difference between the fresh grains and the larger grain product[99].

Care is required for the initial stoichiometry as this will influence the final crystal structure (phase) as particular initial precursor material will require higher mass to have a suitable timeframe to allow for diffusion of ions to the reaction interface. These reactions require higher temperatures, typically above 1300°C, and require a long time for the necessary coarsing and densification between the grains. Coarsening increases the size of the grains, and densification decreases the surface area of the grains, which, when combined, gives the process called sintering[144].

Higher temperatures increase the nucleation exponentially and decrease the time required for grains to grow. Temperatures also allow processes as ionic diffusion to occur creating new compounds[99]. The grains of this new compound can increase in size by mass transport mechanisms such as the evaporation condensation mechanism, which depends on a concentration gradient down the curved surface. Volume and surface diffusion are also critical mechanisms typically hindered by the bulk material and the atomic mobilities of the material used.

2.4 Powder X-ray diffraction (PXRD)

Powder X-ray diffraction (PXRD) is a powerful technique that utilises the periodicity of crystalline structures to uncover the crystal system of a material by the symmetry of the material. Different orientations of material produce different symmetry elements. It is not sufficient to use an optical image to determine if the material is one of the nine crystal structures: cubic, hexagonal, trigonal, tetragonal, orthorhombic, monoclinic, and triclinic. Thus X-rays, which have a wavelength of 1 $Å$, is roughly the same size as the distance between planes of atoms in a crystal structure. These planes of structures are described using Miller indices that treat the periodicity of a crystal as an infinite number of parallel planes in a specific direction. Miller indices are the reciprocals of the location at which one plane of molecules intercepts the a(x), b(y) or c(z) axis and are a means of describing the different planes inside a crystal structure[148].

As there are planes of atoms within a crystal structure, the diffraction of X-rays around a grating creates maxima and minima via constructive and destructive interference, and observing this interference leads to the introduction of Bragg's law. Knowing that the incident X-ray is perpendicular to specific directions, the planes will exist in parallel with a distance between these planes termed *d*-spacings (d). Incident X-rays will reflect off the planes of atoms at that specific direction with constructive interference occurring with other X-rays reflecting lower planes in the material provided that the *d*-spacing is like the wavelength of the incident X-rays (Figure 2-1). The X-rays diffract from the electron clouds around each of the atoms present in the planes. X-rays in lower levels will travel an extra distance in which that distance is equivalent to a whole integer of the wavelength of the X-ray. Then by implementing simple geometry, when the angle at the top plane and the extra wavelength distance is the same as the reflection of the incident X-ray on the top level. This angle and geometry use leads to the construction of Bragg's law (Equation 2.2).

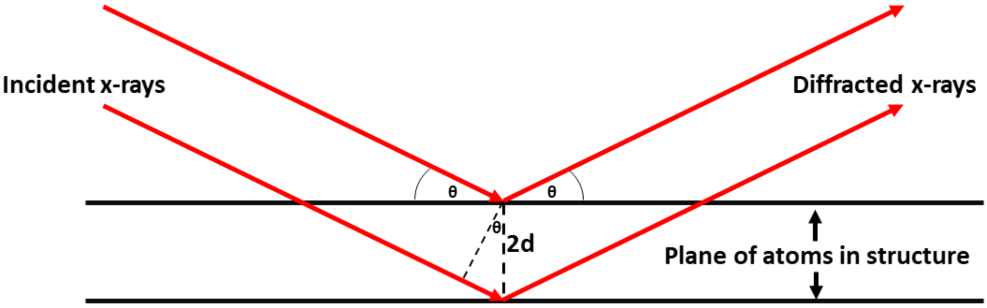

Figure 2-1: A graphical representation of Bragg's law with incident X-rays diffracting due to the distance between planes of atoms in the structure.

$$2d\sin\theta = n\lambda$$

Equation 2.2

The θ value is the angle of reflection from the plane of atoms, but it is recorded in the diffractometer as 2θ as it follows the X-ray through the incident and reflected pathways. The incident X-rays wavelength λ used in all the experiments in this work is Cu Kα at 1.54 Å. The *d*-spacing (d) and the n indicate the order of reflection occurring, but typically, this is observed by the Miller indices as there are no distinctions between different orders concerning the Miller indices by X-ray diffraction standards. Therefore, for convenience, n is adsorbed by the Miller indices and is dropped for calculations of the *d*-spacing.

Bragg's law would ideally work with single crystals, but synthesising a pure-phase single crystal can be challenging. Therefore, PXRD will take a polycrystalline sample, and when the incident X-rays hit the sample, some of the crystal's orientations will be in the correct orientation with their Miller indices to satisfy Bragg's law allowing for 2θ reflection[148]. Thus, creating a cone for each set of indices for possible reflections with 2θ. A detector can observe these cones and record the 2θ position as a line in the spectra. Therefore, the Miller indices give information about the distance between the planes of atoms for that orientation. Rotating the sample allows for the incident X-ray to hit the sample for different 2θ values, and for this set of experiments, the range was between 10° and 90°.

As 2θ can identify the d spacings in a material sample, it is possible from the Miller indices to determine the unit cell parameters of the materials used. Further analysis of the intensity of the peaks diffracted by the Miller planes provides information on the coordinates and occupancy of atoms in the Miller planes[148]. However, this is not important for the thesis experiments. The structure factor of the material is required to be known as the intensity of the radiation of the reflected plane (hkl) is proportional to the absolute value of a coefficient F(hkl) known as the structure factor.

The structure factors (F(hkl)) originate from a Fourier expansion relationship that describes the periodic nature of the scattering of X-rays by the electron density (ρ) of an atom. A Fourier series is used when the electron density can be represented mathematically periodically as $\rho(xyz)$ to describe the number of electrons per unit volume near the unit cell point with the coordinates x, y, and z. A Fourier system allows for cosine and sine graphs to represent a function, and by using Euler's relationship, it is possible to express the electron density as presented in Equation 2.3[148].

$$\rho(xyz) = \sum_{\mathrm{h}} \sum_{k} \sum_{l} F(hkl) e^{(-2\pi i(hx+ky+lz)}$$

Equation 2.3

Three summations are present because of the three-dimensional nature of the electron density, and the structure factors are the coefficient that needs to be solved. By multiplying both sides by the $e^{(-2\pi i(hx+ky+lz)}$ factor, integrating for x,y and z and also if h=h', k=k' and l=l', although ignoring the unit cell volume leads to Equation 2.4.

$$\iiint_{0}^{1} \rho(xyz) e^{(-2\pi i(hx+ky+lz)} \, dxdydz = F(hkl)$$

Equation 2.4

Therefore, knowing all the values of $\rho(xyz)$ for every coordinate or, in other words, knowing the crystal structure, then $F(hkl)$ could be calculated for all values of h, k and l. If $F(hkl)$ is known, then the electron density can be calculated. Although this is a challenge to use Equation 2.4 to find the values of $F(hkl)$ using just the intensities as different factors such as temperature variation make this task difficult.

Systematic absences are one way to help indicate different types of symmetry and, therefore, a structure that is present or not present. Face-centered symmetry has all the Miller indices, either odd or even, and body-centered symmetry Miller indices all add up to be even. This help determines the unit cells' symmetry and can help identify the type of bravas lattice present from each crystal system.

The equations linking the Miller indices to the cubic (Equation 1.1) and tetragonal crystal systems (Equation 1.2) must be known to calculate some unit cell parameters. (*a* for cubic and *a* and *c* for tetragonal). From there, a number termed multiplicity is calculated by dividing the suspected unit cell parameters by the *d*-spacings (*d*) of 2-theta values. This multiplicity will be linked to the squared of the Miller planes (h, k, and l).

$$\frac{1}{d^2} = \frac{h^2 + k^2 + l^2}{a^2}$$

Equation 2.5

$$\frac{1}{d^2} = \frac{h^2 + k^2}{a^2} + \frac{l^2}{c^2}$$

Equation 2.6

The PXRD was collected on a PANalytical Empyrean using a primary beam monochromator using CuKa1 X-rays. The 2Theta range was 10° to 90° over an hour with data collected at room temperature. Indexing and peak positioning was performed using and the reference materials of precursors and phases were collated from the Inorganic crystal structure database (ICSD).

2.5 Scanning Electron Microscope (SEM)

Scanning electron microscope (SEM) is analogous to an optical microscope to provide high-resolution images within the range of 10 μm to 0.1 μm[89,149]. This technique is beneficial in materials chemistry for observing grain sizes, morphology, surface defects and density shifts on the surface of materials. It works on a reflection principle using electrons as the "light" and lenses to help establish a depth of field to create topographical images that appear in 3D but only reflect in 2D.

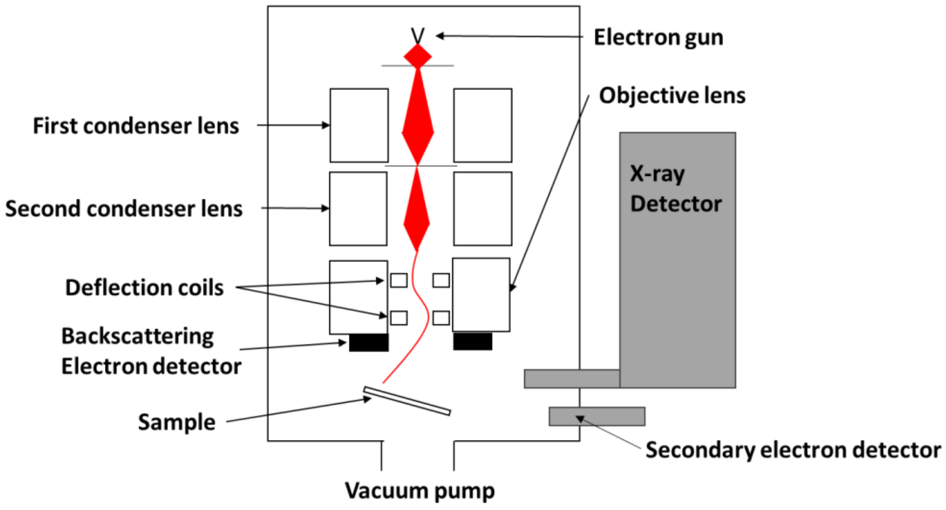

Figure 2-2: Schematic of a Scanning electron microscope.

A schematic of the SEM (Figure 2-2) demonstrates the electron source starts from the electron gun which is applying a voltage to a tungsten filament. The potential can be adjusted to increase the image's brightness by realising a higher concentration of electrons. Then the beam of electrons passes two condenser lenses condensing the electron beam to a thin spot before reaching the sample and interacting with the sample resulting in an interaction volume at which the electrons can scatter or be adsorbed. This allows for two types of electron detection, namely secondary electron emission and backscattering.

Secondary electrons (SE) are the generation of electrons as the incident electron beam will have a higher photon energy value than the bands' energy gaps. It is exciting for the surface atoms to ionise the electron that generates a secondary electron. The detector then collects secondary electrons and can be formed by atoms one μm from the surface, providing that the electrons avoid secondary collisions. Secondary electrons generate an almost 3D image of the surface that provides topographical, morphology and defect-spotting information. It has a good depth of field and thus almost provides a 3D image (a) in Figure 2-3).

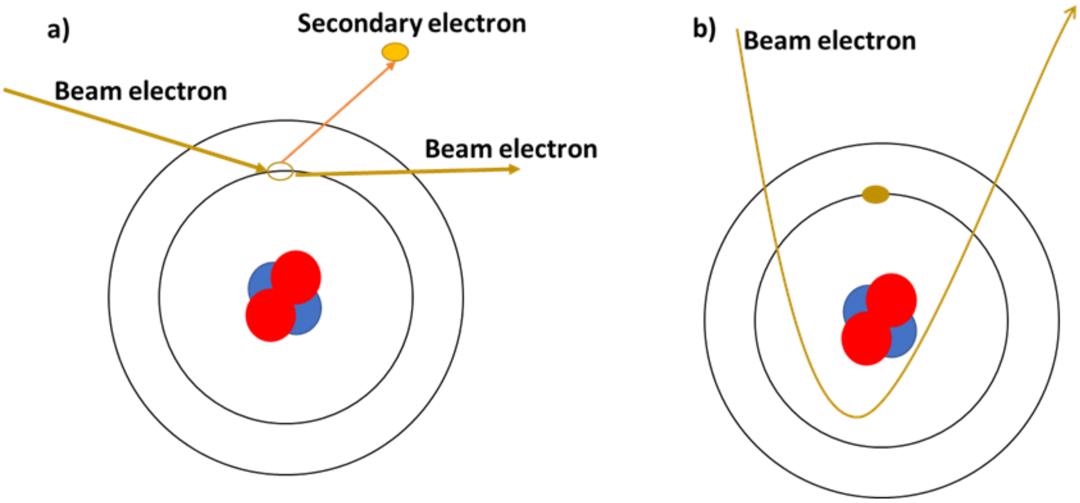

Figure 2-3: Schematic describing the process of a) secondary electron generation and b) backscattering electrons.

Backscattering electron (BSE) is when the incident beam trajectory wraps around the atoms by the slightly positive dipole of the atomic nucleus allowing for a magnetic pull and redirecting the incident beams to a different detector. Heavier atoms result in more backscattering electrons reaching the detector; hence, the heavier atoms appear lighter in the image. Furthermore, there is a higher chance for elastic collision in this material[150].

A JEOl JSM-IT200 with a tungsten filament SEM was used in this work. It allowed spatial resolution down to 3 to 5 nm and a dual screen for both SE and BSE imaging. Most images were captured using a voltage of 15 kV for the electron gun and a working distance of 12 for the lens.

2.6 Energy dispersive X-ray Spectrometry (EDX)

EDX is complementary to SEM as a compositional tool at a point or line or by generating an area map showing the distribution of the elements throughout the map[146,149]. The energy dispersion comes from photons on additional electron movement through the electron shells of atoms occurring when high-energy electrons hit atoms of the material's surface, generating a secondary electron that passes to the detector. Then higher energy electrons can move to these fixed energy shells, and on the transfer, a photon of the energy difference between the high energy levels escapes. The Silicon detector (typically) in this energy dispersive takes note of the energy of the photon, which is specific to an energy step of a material[1.] The energy of these photons can then be mapped or associated with a point allowing for accurate elemental fingerprinting of the materials used.

Provided that the elements are heavy enough, their X-ray generation will be detected as lighter elements such as lithium cannot be picked up by this technique. Compositional data can be gathered over small areas of samples and compositional maps for those areas can be generated. As in later experiments, point analysis is a helpful tool for checking the composition of different phases. A JEOL DrySD attached to the IT-200 was used for the experiments.

2.7 Electrochemical impedance spectroscopy (EIS)

A material will always have a resistivity (ρ) if an electrical circuit is applied, creating a mean-free path because of any material having an area (A) and a length (l) (Equation 2.7). It will also contain a resistance (R) governed by Ohm's law when an applied direct voltage to the material allows a charge (current) to move through the material[34].

$$\rho = \frac{RA}{L}$$

Equation 2.7

The ionic conductivity (σ) is known to be the inverse of resistivity, as it reflects a charge carrier’s (ion in this case) ability to move through the material, and so calculating the ionic conductivity if the area and length of the free mean path are known, comes down to finding the resistance of the material (Equation 2.8)[34].

$$\sigma = \frac{1}{\rho} = \frac{L}{RA}$$

Equation 2.8

However, the resistance via a direct voltage will not allow distinctions of the resistance. Thus, no information about the individual chemical resistances such as the electrodes bulk resistance, the electrodes grain boundary resistance, the electrolytes charge transfer resistance (occurring at the electrode/electrolyte interface), or the electrolyte bulk (diffusion) could be obtained. However, electrochemical impedance spectroscopy (EIS) technique can allow for the resistances and capacities of these processes to be separated and measured independently of each other[151].

EIS is a non-invasive technique that works on the assumption that a cell will behave like an electrical circuit. An A.C. potential is applied to the cell and the current feedback is measured. Small changes to the amplitude are applied to allow for pseudo-linear alterations to the current response from the cell. The electrical perturbation input is a sinusoidal signal and having a pseudo-linear behavior means that there can be a phase difference and a decrease in the amplitude as the cell responds due to cell phenomena, such as moving across the grain boundary or a charge transfer reaction. The frequency of the initial perturbation varies as these different chemical, and physical cell phenomena vary with the frequency, with each frequency corresponding to an experimental time scale[17]. The impedance is defined as seen in Equation 2.9 and is analogous to the general resistance of ohms law with the potential of the perturbation divided by the cell response current (I).

$$Z = \frac{V}{I}$$

Equation 2.9

The A.C. potential applied to the cell can have the form listed in Equation 2.10. In Which V_t is the potential at the time, V_0 is the amplitude of the signal, and ω is the radial frequency. The radial frequency can be expressed in Hz (*f*) (Equation 2.111).

$$V_t = V_0 \sin(\omega t)$$

Equation 2.12

$$\omega = 2\pi f$$

Equation 2.13

The current response (I_t) is represented in Equation 2.14 with the phase change of cells phenomena being noted as φ. Implementing and into and using Eulers relationship (Equation 2.15) it is possible to present the impedance as a complex number(Equation 2.16)[152]. Therefore, by plotting the real part as the x-axis and the imaginary part as the y-axis you create a Nyquist plot (Figure 2-4)[152,153].

$$I_t = I_0 \sin(\omega t + \varphi)$$

Equation 2.14

$$e^{ix} = \cos x + isinx$$

Equation 2.15

$$Z_\omega = \frac{V_0 \sin(\omega t)}{I_0 \sin(\omega t + \varphi)} = Z_0 e^{i\varphi} = Z_0(\cos\varphi + i\sin\varphi)$$

Equation 2.16

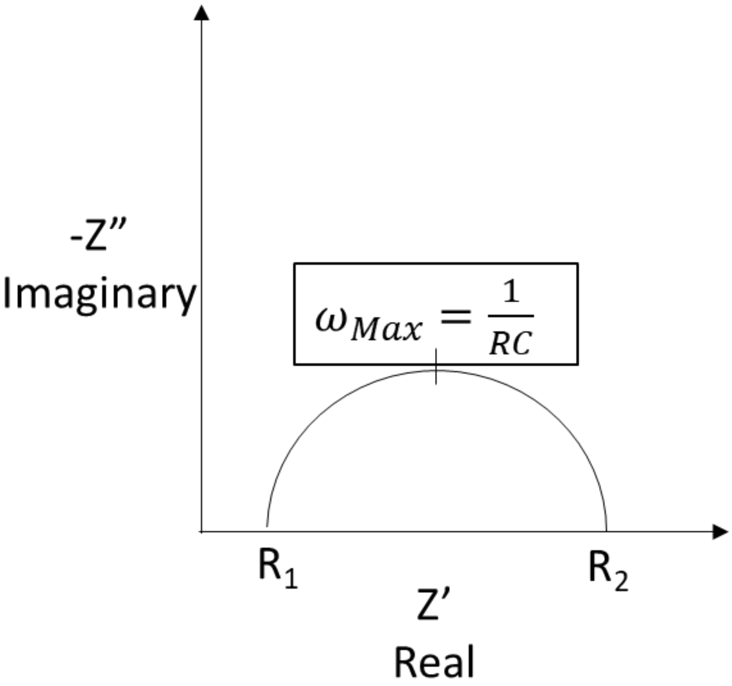

Figure 2-4: The Nyquist plot of the electrical response in an EIS shows which components of the impedance (Z) are real or imaginary. The arc response begins (R1) and ends (R_2) at different resistance values. The maximum frequency of the arc (ω_{Max}) provides access to the resistance and the characteristic capacitance of the reaction or ceramic microstructure that's response constructed the arc.

As the electrochemical cell tested will have different microstructures and phenomena, some, like an interface between an electrode and an electrolyte, will contain some capacitance and resistance components meaning that an arc of that phenomena will form. Resistance alters the amplitude of the current response while capacitance alters the phase by +45°. The arc intercept at the x-axis is when the impedance will be purely resistive, so the difference between the two intercepts (R_2-R_1 in Figure 2-2) will provide the resistance of that phenomenon. Looking at the maximum frequency, which is located at the top of a phenomena arc (ω_{Max}), the resistance (*R)* and the capacitance (*C*) are separable by the relation shown in Equation 2.17. The RC is described as the characteristic time constant of the system.

$$\omega_{Max} = 1/RC$$

Equation 2.17

As these components are separable, the capacitance can be calculated for this phenomenon, which is a characteristic capacitances[151] for each cell phenomenon. For example, bulk material produces a response at 10^{-12} F cm^{-1}. Grain boundaries produces a response around 10^{-11} to 10^{-8} F cm^{-1}, surface layer responses at 10^{-9} F cm^{-1} and electrode-to-sample interfaces at 10^{-7} to 10^{-5} F cm^{-1} around x10^{-9} F cm^{-1} [151]. Therefore, when the characteristic capacitance of an arc is known, the resistance for that phenomenon can be recorded. Taking that resistance, knowing the area of the mean free path of the charge and the length of the movement of the charge, the ionic conduction of the electrochemical cell can be calculated (Equation 2.8).

In addition the activation energy (E_a) of that phenomena can be measured from the impedance response using a temperature range, as the activation energy has a dependence on the Arrhenius law(Equation 2.18)[2] We then add natural logs to the Arrhenius equation to remove the exponential component and also allow for a straight-line curve to be plotted (Equation 2.19)[154].

$$\sigma T = \sigma_0 e^{(-\frac{E_a}{kT})}$$

Equation 2.18

$$\ln \sigma T = \ln(\sigma_0) - \frac{E_a}{1000K}\left(\frac{1000}{T}\right)$$

Equation 2.19

The temperature (T) is recorded in Kelvin and requires to be divided by 1000 to create a linear response allowing the gradient of the line to contain the Boltzmann constant ($8.617x10^{-5}$ eVK^{-1}) and the activation energy.

The semi-circles from a Nyquist plot Figure 2-4 form because of a cell phenomenon that contains both a capacitor and a resistor. A capacitor exists with no real component, so is parallel to the y-axis, while the resistor has no imaginary part and therefore is parallel to the x-axis. Therefore, by treating the cell phenomena as combinations of capacitors and resistors in series and in parallel they form semi-circles on the Nyquist plot. The characteristic time constants of these cell phenomena may be close in frequency such as charge transfer and grain boundary that create perturbations at similar capacitance value creating semi-circles that might join into a bigger semi-circle making it difficult to distinguish the separate arcs. Equivalence circuits have been used to aid this separation, but it is more appropriate to use other techniques to distinguish the possible phenomena occurring in the electrochemical cell.

In this thesis the was used with a frequency range of 5 Hz to 13 MHz on a 4192 LF impedance analyser for the lower temperature ranges bellow 100°C. For the higher temperature ranges a SI 1260 impedance gain-phase analyser was used with each temperature dwelling for thirty minutes before the frequency range was subjected 13 MHz to 5 Hz with a current amplitude of 0.1 V with 10 points per decade.

A solid electrolyte had gold paste circles of 6 mm diameter painted either end to act as blocking electrodes and form a symmetrical cell. The gold was then heated to 700°C slowly at 2°C per min and held there for five hours. For the SI 1260 the symmetrical cell is held together using platinum contact points before being placed into a tube furnace to be heated to temperatures above 100°C.

For the 4192 LF analyser silver wires are needed to be attached to gold blocking electrode already present using more paste as the glue to hold the wires in place. The gold is then dried again to stick the wires to the gold paste as a current collector. The pellet can then be placed in a small tube heater to reach different temperatures under 100°C.

2.8 Atomic force microscopy (AFM)

Atomic force microscopy (AFM) is a powerful tool for uncovering the topography and interacting forces of the surface of a nano-material[155]. It involves a microcantilever probe that can vibrate or be dragged across a surface[156]. In the experiments, a silicon cantilever is used, and as the tip comes close to the sample, there is an attractive force experienced by the cantilever as the response by the potential difference between the conductive atom size tip of the cantilever and intrinsic charge on the surface as well as van der Waals interactions. However, as the tip approaches the surface, repulsive forces such as columbic force[157], van der Waals interaction or physical deformation of the cantilever occur due to the interaction of applying the tip to the surface and then pulling back. This allows for measurement of the cantilever deflection, which is proportional to the interacting force between the tip and the sample[155]. The maximum force applied to remove the cantilever tip from the surface is the adhesion of the sample (Figure 2-5).

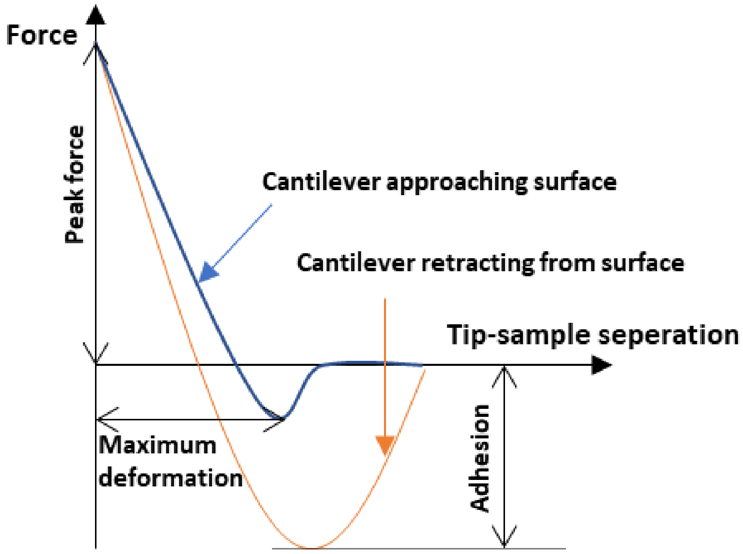

Figure 2-5: Force that the cantilever experiences while the tip is proximate to the sample. Adhesion information on the surface is acquired by force required to be applied to the cantilever to remove it from the surface.

Atomic force microscopy (AFM)

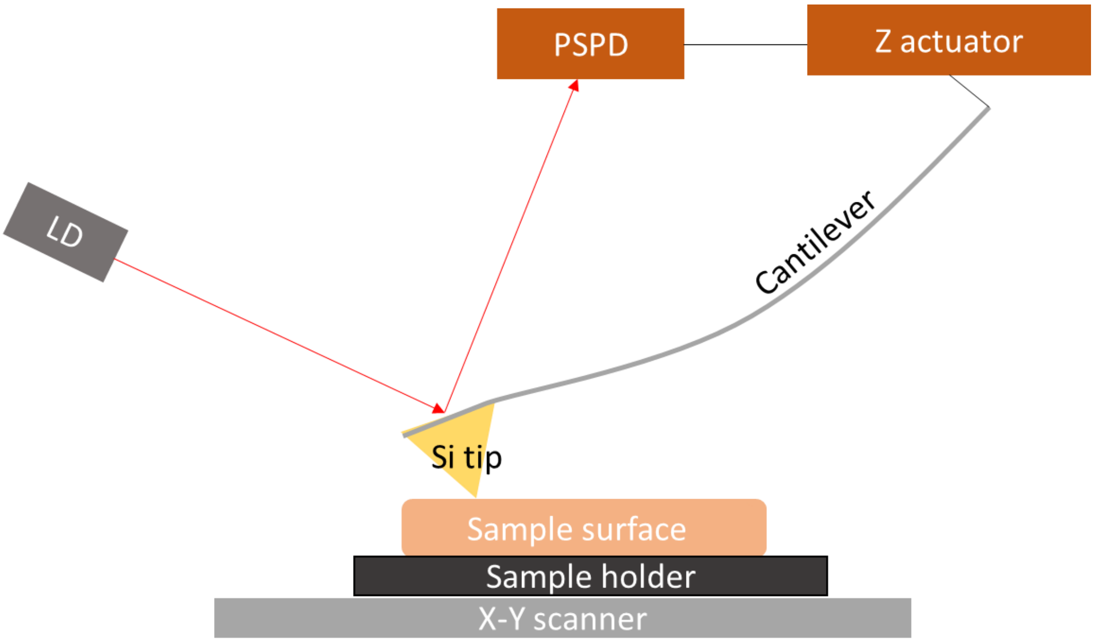

Figure 2-6: Principle of AFM to keeping a steady Z value or height. Light from the laser diode (LD) bounces off the reflective end of the cantilever and moves from the aligned centre of the position-sensitive photodiode (PSPD). This alteration is corrected by an electrical pulse by the z actuator to fix or measure the change in height.

Considering a force applied to the cantilever, it could be measured using Hook's law if the AFM is static, but as the cantilever can vibrate, this may result in a change of the vibrating amplitude, phase and resonance frequency and is termed dynamic AFM[156]. Height topography is recorded by keeping the cantilever at a fixed force and the tip moving across the surface using an X-Y scanner. With a laser emitting diode (LD) fixed to the cantilever's reflective back, it can reflect any change to the height of the cantilever. The reflected light is focused on the center of a position-sensitive photo-diode (PSPD). Any deviations from the center are tracked in the x and y direction. As the cantilever has a fixed force, any changes in the PSPD are sent to the Z actuator to fix the position and height and, in turn, records the height required to maintain the height needed for the fixed force (Figure 2-6). The surface sample must be smooth as too rough a surface will multiply pores, and significant alterations in height will lead to cantilever deformation.

In this work, adhesion maps were acquired using Peakforce Tapping (PFT), which uses a sinusoidal wave as the driving force to oscillate the cantilever—preventing any sharp changes to the cantilever, which exerts a force on the cantilever larger than the setpoint due to the drastic movements creating a force signal that masks the adhesion values. PFT utilises a synchronisation algorithm in which the synchronisation is set to half the period, allowing for the actual vertical maximum force to be extracted and a minimum force to be measured in pN. The algorithm also removes any parasitic motion of the cantilever caused by the vibration ringing due to dampening or surface topography as a form of background subtraction. It also allows the separation of tip-sample interaction and non-interaction energies, which are averaged to create the baseline, allowing for high-speed scanning as the baseline helps determine fluctuations of the cantilever that are not a response of the surface interactions. This results in some detailed maps of adhesion to be constructed across a surface.

2.9 Thermal gravimetric analysis (TGA)

Thermal gravimetric analysis (TGA) is a thermobalance measure of the change in the weight of a material over a temperature or time range[146,158,159]. A blank of the crucible is first measured to get accurate mass variations of the sample. The blank then undergoes the desired heating profile to be analysed to construct a background to help clarify the decomposition steps. One important consideration is whether the material undergoing thermal decomposition is stable in the crucible. Aluminium crucibles were used throughout this work as they only reacted with solid oxide electrolyte material at a very high-temperature range. The variation in the mass in a temperature range can be associated with different material decompositions and gives an estimate of the different mass reactions occurring during a heating stage of an experiment[146,159]. These mass differences are typically fundamental properties of the sample although this is only useful when the slope is a single-step decomposition.

Differential thermal analysis (DTA) can be measured alongside a TGA and is used to measure the difference in temperature between the sample and an inert reference material[11]. DTA can identify either endothermic or exothermic reactions such as water evaporation; with an exothermic reaction, there will be an increase in the change of temperature of the sample compared to the reference material[11] appearing as an increase in the DTA. It is important to be careful with buoyancy errors when there is a decrease in the atmosphere's density at the balance leading to small gradual increases in mass[20,89] or any fluctuations in the heating rates, as DTA will treat them as thermal events[11].

In this thesis a STA 449 Jupiter TGA was used following the synthesis processes of the LLTO coating seen later. This allowed for the gases to switch from air to argon creating a similar atmosphere.

2.10 Particle analyser

These experiments used a Malvern instrument Mastersizer 2000 laser diffractometer d with a Hydro 2000MU pump accessory. A red HeNe laser at 0.632 µm provides the measurements and a blue LED laser at 0.466 µm with forward and backscattering detection is used to enhance sizing calculations[160]. Using sonication, the particles pass through the focussed laser beam scattering the light at angles inversely proportional to their size and allowing amble sample dispersion[161]. The scattered light results from electromagnetic theory; the oscillating electrons at the same frequency of the incident beam will then radiate electromagnetic radiation at the same frequency of the oscillating electron. Thus, following Raleigh's theory, assuming this electron oscillations in the particle is the same phase and frequency of the incident monochromatic wave-light[162]. A particle oscillation of an electron will lead to a dipole moment resulting in scattered light, meaning a series of photosensitive detectors such as backscattering, forward angle, and large angle detectors will detect any deviation. One assumption made is that the particle is spherical, and that the radius of the particle (a) is significantly smaller than the wavelength of the incident beam (λ_0). This is represented the Rayleigh expression (Equation 2.20 and Figure 2-7)[163].

$$I = \frac{16\pi^4 a^6 n_{med}^4 I_0}{r^2 \lambda_0^4} \left| \frac{m^2 - 1}{m^2 + 2} \right| \sin^2(\theta)$$

Equation 2.20

For this expression, I is the intensity of light scatted at 90-θ° from the incident red laser beam as it travels through the sonicating water, the refractive index of the medium surrounding the particle (n_{med}), to follow unscattered light as it hits the focal plane detector at the end. The angle θ° is the angle between polarised light and the scattered light beam that has travelled r to reach a detector, which is a large angle (LA) detector. The m is the relative refractive index of the bulk particle material.

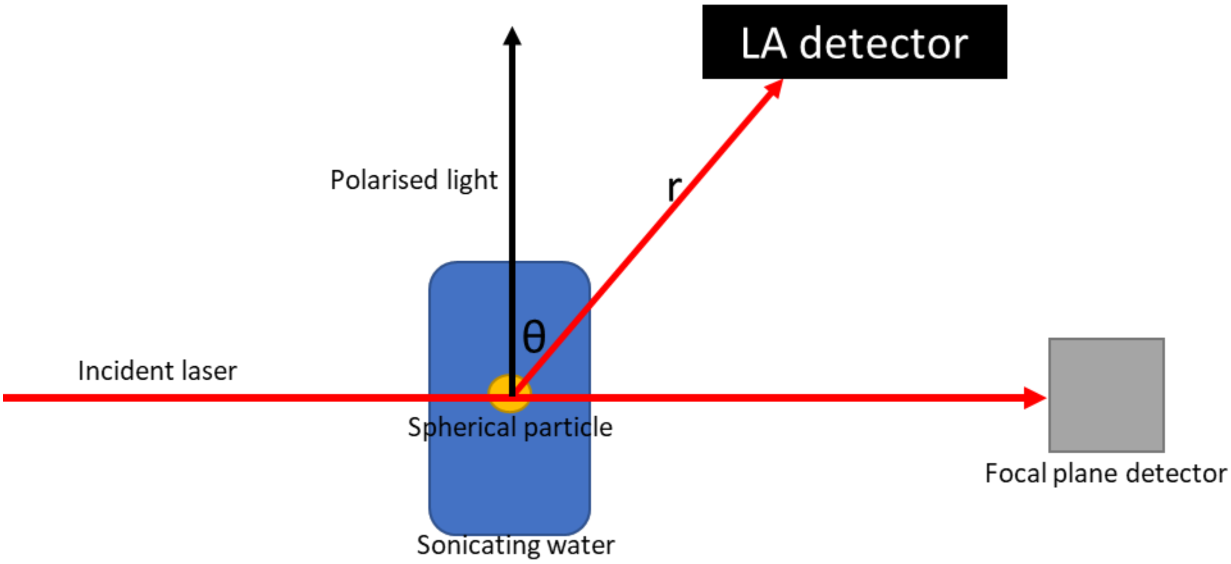

Figure 2-7: Simple schematic of how a particle analyser measured the size of a particle using scattered light at an angle of θ to polarised light, travelling a certain distance (r) to reach a large angle (LA) detector.

2.11 Raman analysis

Raman spectroscopy is a non-destructive vibrational technique that takes advantage of the interaction of incident light to provide insight into the chemical bonds, structure, and crystallinity and detect contaminants on the surface of a material[89]. A monochromatic light with a specific initial frequency (v) irradiates the molecule, polarising the cloud of electrons around the nuclei of atoms forming a short-lived state known as a virtual energy state[164]. Two types of scattered light occur; Rayleigh scattering (v), when the scattered light has the same energy and wavelength as the incident light (elastic scattering), and Raman scattering (±vi-v), which is less intense than Rayleigh scattering with either a reduction or an increase in energy[89,124]. The laser's photons can be a similar energy as the gap of the electron at its energy level to be excited up to the virtual energy state. The electron will then relax down to either a higher vibrational level (stokes) or a lower vibrational level (anti-stokes) (Figure 2-8).

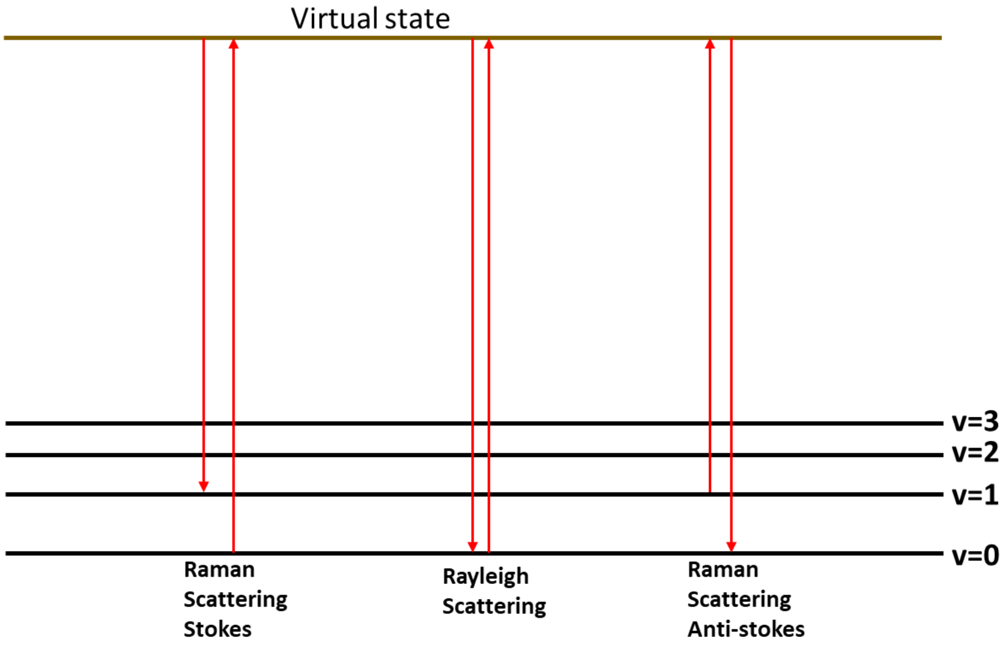

Figure 2-8: Red laser photons causing Rayleigh scattering and shifting the vibrational level of the material by Raman scattering via stokes and anti-stokes energy scattering.

Raman spectrum measures the shift from the incident laser photons to this scattered light of ±Δv (v is the notation for an energy state), and typically the stokes energy is preferred due to a higher probability of a single shift from a lower level to a higher level. A polariser allows only the scattered light to hit the detector and does not allow the incident photons (Rayleigh scattering) to be analysed. Any symmetry of the bonds used that allows for a change in the polarizability of electron clouds will be intense via the Raman spectrum, so it is possible to distinguish the types of symmetry present in a surface.

Inorganic solids have characteristic vibrational spectra, and Raman is especially helpful in fingerprinting crystalline solids since the band position gives information about the chemical composition of the sample under analysis. Other information, such as the crystallinity, defects, and deformation, can be extracted by the intensity of the peak or using the full width half maximum intensity or the shift of bands (Figure 2-9). Furthermore, the strength of the bond will influence a material's ability to oscillate and alter the polarizability of the electron clouds.

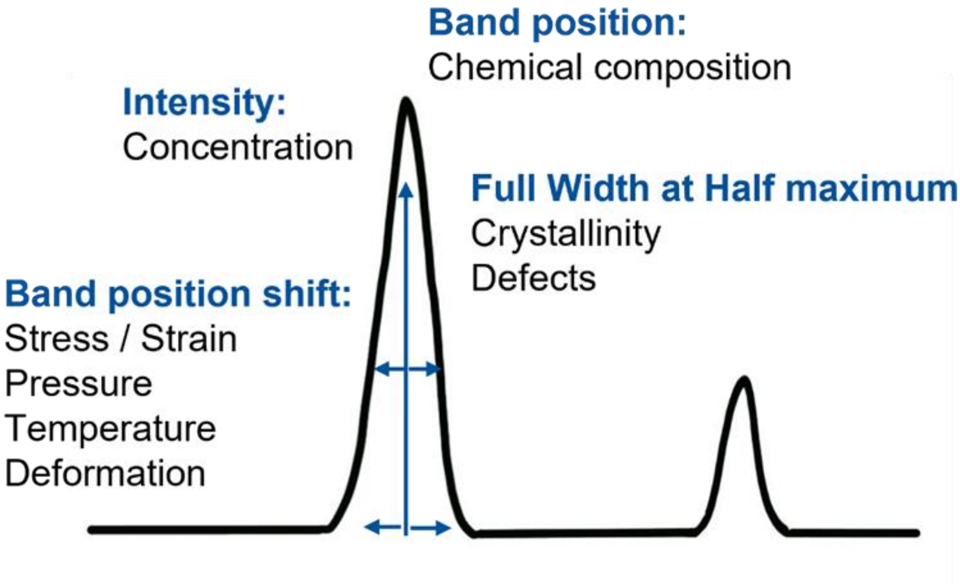

Figure 2-9:Information that Raman spectra can extract on the nature of a material surface.

Raman spectra were collected with a 532 nm wavelength laser using the Raman system (Reishaw inVia Qontor Confocal microscope) and 1800 lines per mm holographic grating. An optical microscope with Leica 50 x objective lens focuses on the samples. Spectra were collected at 10-20 random spots on the surface with various µm intervals, and the average of these points in the plots used in this thesis to assume that the plots are more similar to bulk material[164]. The estimated laser power on the sample was 2.5 mW, the laser exposure time on the samples was 10 seconds, and 2 to 5 accumulations were obtained for each sample depending on the noise of the spectra. Accumulations enhance the ratios of the peaks generated by the vibrations of different bond lengths and strengths compared to noise by measuring the sample again. Furthermore, a baseline was taken for each spectrum to improve clarity and reduce any error in the peaks.

2.12 Dry room

The dry room used for wetting experiments was achieved using Munter IceDry dehumidifer[165]. In which the air in the dry room passes through a desiccant rotor and then returns to the dry room as dry air. The desiccator rotor rotates slowly so incoming air will always be able to hit the composite material of the rotors that retains water vapour[166]. The moist and warm air leaves as warm reactivation air dry's the rotor[166]. This in turn increases the humidity down to approximately 0.01% which lowers the dewpoint; the temperature which air will become completely saturated by water vapour[167]. Keeping the room cool at approximately 18°C and lowers the dewpoint down to -25°C. This humidity allows for handling metallic lithium preventing immediate oxidation and enabling handling on the bench for 48 hours before Li_2O forms.

A Carbolite Gero tube furnace within the dry room allows for the sintering and wetting of materials in a drier atmosphere (Figure 2-10). The alumina tube has two engineered stainless-steel holders at either end, with lens windows in the middle. These permit the Canon EOS 600DDSLR camera to take pictures of the contact angles of the melts during wetting experiments.

To set up wetting experiments, the sample to be wetted is placed upon either an alumina or a MgO plate and placed in the middle of the tube. To provide some light to the melt and substrate small LIHAO balloon LED lights is placed in the tube close to the stainless-steel ends. Everything in the tube is then sealed off and then purged to -20 mBars. Zero Grade Argon (BOC set to 20 PSI) is allowed to flow into the system at 20 ml min^{-1}. After filling for 10 minutes, the gas is allowed to exit the alumina tube. The gas passes through two parafilm bubblers before being directed outside. A desk light can provide backlighting to allow for some more illuminated images. On occasion copper cuttings were used to remove excess oxygen flowing through the system before reaching the sample as cooper will naturally capture oxygen and being in a furnace will likely improve the oxygen affinity kinetics.

Figure 2-10: Carbolite Gero tube furnace in a dry room with a stainless-steel end with the lens allows for wetting reactions of metals to be seen at different temperatures.

2.13 Wetting calculations

Wetting is a technique to indicate the spreading of a liquid phase on a solid phase. In this work the liquids used are melts which mean that wetting characterisation methods such as the Owens, Wendt, Radel and Kaelble (WORK) model are difficult to use as they require dispersion, polar, hydrogen, induction and acid-base tensions, easily attributed to other liquids, in their equations[168,169].

The fundamental wetting equation is the Young-Dupre (Equation 2.21). The energy tension at the interface of a melt and a solid ($\boldsymbol{\gamma_{sl}}$) is influenced at this three-phase boundary, by the surface energy of the solid being wetted (γ_{sv}) and the surface tension of the melt (γ_{lv}). Surface energy thermodynamically is the work required to generate an area of new surface[99] while surface tension is a liquids ability to attract the particles in the surface layer by the bulk of the liquid resulting in the minimum surface area. For optimising the interface, an indication of the energy value at which lithium will spread over a surface indicates the modifications required to reduce the interfacial resistance.

$$\boldsymbol{\gamma_{sl}} = \gamma_{sv} - \gamma_{lv} Cos(\theta)$$

Equation 2.21

A melt will spread over the surface, creating a thin film that will lower the whole system's energy while competing with vapour tension at the three-phase boundary. Surface tensions is expressed in joules per metre squared and is essentially the force that the atoms of the melt will exert at the surface of the melt. The spreading parameter is simply the surface energy per unit surface of the dry solid surface (Equation 2.22).

$$S = \gamma_{sv} - (\gamma_{sl} + \gamma_{lv})$$

Equation 2.22

If S>0, the liquid prefers a thin film arrangement with maximum interaction with the surface. If S<0, then there is the formation of a droplet. Then the contact angle (θ)of the liquid on the surface indicates the degree of wetting. Values above 90° indicate non-wetting, and contact angles below 90° indicate poor wetting (Figure 2-11).

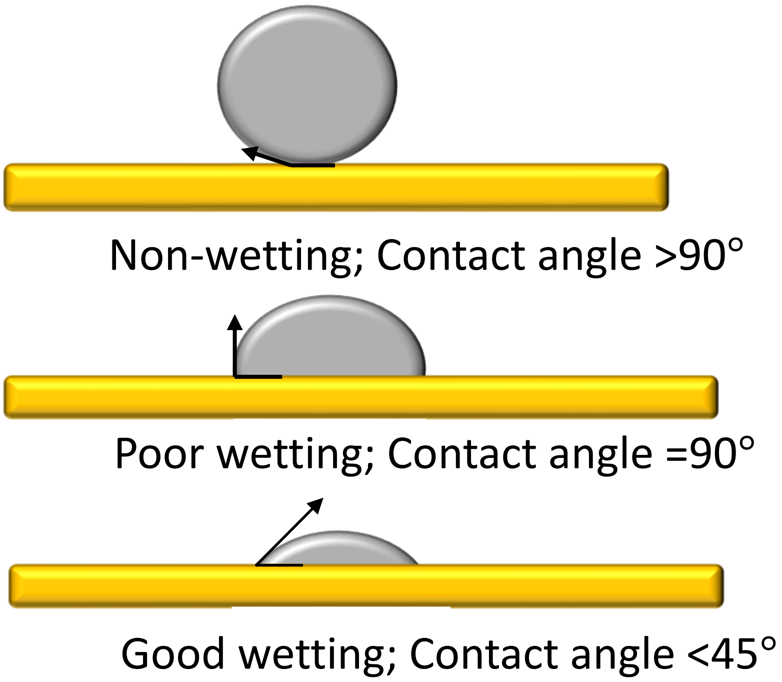

Figure 2-11: Schematic showing the contact angles for non-wetting conditions, poor wetting conditions and good wetting interactions between lithium melt and the surface of an electrolyte.

J. Wang *et al.* suggested that the driving force for the wettability of liquid lithium is the Gibbs free energy of the reaction between lithium melt and the surface[170]. Emphasising the importance of any energy shift that occurs due to physical or chemical alteration of the surface of the solid electrolyte; such as an addition of a secondary phase—concluding that the more negative the Gibbs free energy of the interface and the lower the interface tension, the lower the contact angle and therefore better wettability[171]. They also highlight that the construction of any Li_2O film can cause a cage to form around the lithium melt providing a spreading resistance and creating a wetting equilibrium with an incomplete spread of lithium across the surface[170]. They summarise this reaction using an equation (Equation 2.23) that takes into account the surface tension of the melt (γ_{lv}), any physical or chemical alteration to the interface energy of the solid and the melt ($\Delta\gamma_{sl}$), the free Gibbs energy of the reaction (ΔG) the contact angle in the absence of a reaction ($\cos\theta^0$) and the contact angle after the reaction($\cos\theta^1$).

$$\cos\theta^1 = \cos\theta^0 - \frac{\Delta\gamma_{sl}}{\gamma_{lv}} - \frac{\Delta G}{\gamma_{lv}}$$

Equation 2.23

An important manipulation that can be performed to allow for the reaction Gibbs energy to become the y-component of a scatter plot. It is done by rearranging Equation 2.23, measuring the initial contact angle metal before the melting point ($\cos\theta^0$) and perform additional wetting experiments to get this variation in the interface energy as a result of the molten metal ($\Delta\gamma_{sl}$) and using the fact that the surface tension can be calculated using known thermodynamic values and the temperature (γ_{lv}) as shown later in this chapter (Equation 2.24).

$$\Delta G = \gamma_{lv}(\cos\theta^1 - \cos\theta^0) + \gamma_{sl}$$

Equation 2.24

One issue we face is identifying the surface energy of the pellet materials. In this thesis, the surface tension of melts, at their melting temperatures, are taken from the articles, Surface energies of metals in both liquid and solid states[172] and a unified model for the cohesive enthalpy, critical temperature, surface tension and volume thermal expansion coefficient of liquid metals of bcc, fcc and hcp crystals[173]. These papers present the surface tension's thermodynamic components and allow the melt's temperature variations to be considered (Equation 2.25).

$$\gamma_{lV} = H_s + (T - T_m)\left(\frac{d\gamma}{dT}\right)$$

Equation 2.25

H_s is the excess Gibbs surface energy[172], the energy required to increase the area of a liquid in an air atmosphere. Thermodynamically it is linked to the coordination number and thus the enthalpy of cohesion against the atoms of the metal's bulk and a metal surface when it is melting[173]. T_m is the melting temperature of the material used. $\frac{d\gamma}{dT}$ is the surface excess entropy, a negative value that indicates the change in the energy of the surface tension with variation to temperature change.

For calculating the surface energy of the wetted solid, an equation is used that is derived from a set of simultaneous equations observed by G. Triantafyllou *et al.* [174]. Triantayllou and their team used the elemental melts of Sn, Ni, Fe and Cu on eleven different oxide surfaces (such as Al_2O_3 and TiO_2) to create a general equation for elemental melts on an oxide surface (Equation 2.26).

Wetting calculations

$$\boldsymbol{\gamma_{sv}}\ (Jm^{-2}) = (A + \boldsymbol{\gamma_{lv}})\cos\theta + B$$

$$A\ = 0.970 \times 10^{-3}\ T - 5.491\ (Jm^{-2})$$

$$B = \ 1.825\ \times 10^{-3} T - 3.106\ (Jm^{-2})$$

Equation 2.26

The elemental melt needs to have a non-wetting interaction with the solid surface. Therefore, values must be determined as any wetting contact angles will affect the cosine value. It provides a way of assessing the material's surface energy, and results will demonstrate if it is a reliable way to measure the surface energy of surfaces.

Using the Young-Dupre equation[99], it is then possible to compare calculated surface interface tension to establish the ideal lower surface tension. This is ideal for a lithium metal solid electrolyte interaction as this indicates energetic favourability to bond at the surface physically and chemically. The physical bonds occur as Van der Waal's interaction while the chemical bonds occur new ionic bonding depending on the crystal's orientation and the solid electrolyte's structure.

Following the work of Triantafyllou [174], the experiments of this thesis will investigate the change in the contact angle of lithium melt and gallium melt over temperature changes. The contact angles over a temperature range generate a trendline of the temperature variation with respect to the contact angle. The contact angle equation, acquired from these trendlines, is then inserted into varying equations that calculate the surface tension, surface free energy and the surface energy of a material.

Another important energy property to investigate is the work of adhesion. This is the energy required to separate a liquid and the solid, that form an interface, into their two separate phases. The Young-Dupre equation usually dictates this, needing only the contact angle and the surface tension of the liquid being removed (Equation 2.27).

$$W_{ab} = \gamma_{lv}(1 + \cos(\theta))$$

Equation 2.27

Moreover, when combined with Young's equation, the work of adhesion can be calculated from the contact angle, called the Young-Dupre equation. The main issue here is the assumptions made on the form of the liquid part once removed from the surface. Energetically, it assumes the liquid returns to the original shape and morphology before creating the interface, leading to situations where the work of adhesion tends to infinity on lower contact angles when in contact with water.

Thus an altered Young-Dupre equation was presented by Scrader[175] (Equation 2.28), in which the liquid (melt in this case) will not return to a droplet shape after being removed from the surface.

$$\boldsymbol{\Delta F_N} = \pi r^2 \gamma_L [\left(\frac{\boldsymbol{2a}}{\boldsymbol{sin\theta}}\right)^{\frac{2}{3}} - \mathrm{a}]$$

$$a\ = (2/(1 + \cos\theta)) - \cos\theta$$

Equation 2.28

Subsequently, calculations of the surface tension of the melt followed equation 3 using corresponding values in Table 2.1 for the melt used in the wetting experiment.

Table 2.1: The thermodynamic properties of a melt of lithium, gallium, silver, and gold when calculating the surface tension at a specific temperature. They include the melting temperature, the positive excess surface enthalpy, and the opposing surface excess entropy.

Melt	**Excess Gibbs surface enthalpy (H_s, mJ m^{-2})**	**Surface excess entropy ($\frac{d\gamma}{dT}$, mJ m^{-2})**	**Melting temperature (°C)**
Lithium	491	-0.16	180
Gallium	740	-0.09	30
Silver	1088	-0.19	962
Gold	1340	-0.19	1064
Sodium	216	-0.09	98

The trendlines of the contact angles and radius melting interactions with the solid surfaces allow for a range of solid surface and interfacial energies and for work of adhesion to be calculated over the same temperature range.

When a molten metal is wetting across a surface with pores underneath it there are a few wetting states that are possible: Wenzel, Cassie-Baxter, a hybrid impregnation Cassie-Baxter state or a capillary filling (Figure 2-12). The Wenzel (b) in Figure 2-12 is when complete wetting occurs in the pores of a material by the melt or liquid directly above them[176,177]. Moreover, the roughness of the surface will improve the solids' surface contact tangle with the melt. For a Wenzel state the observed contact angle (θw^*) will be larger than the expected contact angle if the material is preferring to prioritise limited surface area contact with the liquid (liquid phobic). If the material lowers its overall energy by increasing the contact area of the liquid then the observed contact angle will be smaller than expected contact angle[178].

The Cassie-Baxter state wetting state (c) Figure 2-12), the observed contact angle (θ_{CB}^*) will always be larger than the expected contact angle as gas trapped in the pores will prevent any liquid infiltration into the pores via capillary pressure[176–179]. For the Cassie-Baxter impregnating state, or capillary filling, (d) Figure 2-12) is a combination of both the Wenzel and the Cassie-Baxter state. The observed contact angle will still be a bit larger than expected but the difference between these contact angles will not be as big as the Wenzel or Cassie-Baxter state. The imbibition processes, a diffusion displacement reaction in which a wetting fluid displaces a non-wetting fluid, of the Wenzel state occur. There will also be spreading out in the pores ahead of the droplet itself meaning that there is less liquid on the surface and so that liquid will have a higher observed contact angle as there is less volume present[176].

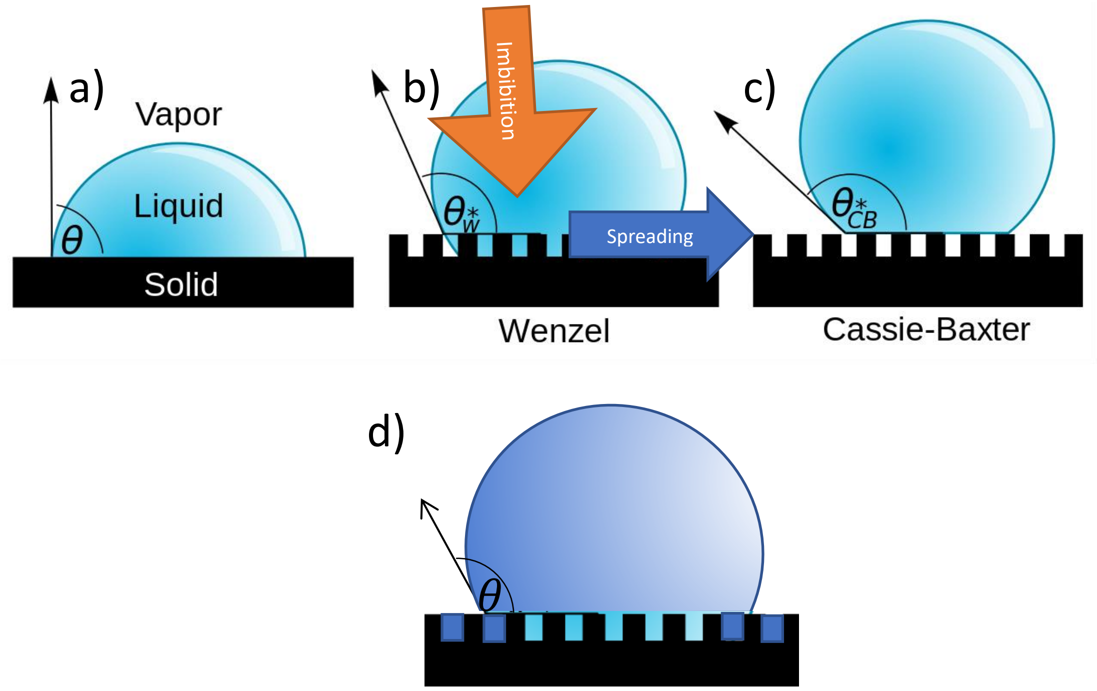

Cassie-Baxter impregnating state (capillary filling)

Figure 2-12: A regular liquid wetting the surface of solid a) in comparison to the altered contact angle of the imbibition process and spreading resulting in the Wenzel state b). The Cassie-Baxter states change the contact angle due to gas underneath preventing any wetting infiltration c) and a mixture of both the Cassie-Baxter and Wenzel states that allows filling of the capillaries of the solid d). a), b), and c) were taken from Vladsingers work[180] *with the addition of the processes arrows and the fourth state being a capillary filling state.*

O. Pierre-Louis[177] used a wetting parameter (χ) to describe which wetting state occurs kinetically using Monte-Carlo simulations due to the bond energies. The nature of the equation is analogous to Young's equation without the contact angles (Equation 2.29). An assumption in the calculations is that the temperature must satisfy the requirement, $K_BT \ll J$ when J is the typical bond energy. Using the contact angle trendlines would be appropriate because the temperature can be assigned absolute zero, which is significantly lower than the average bond energy [177]. Furthermore, as the contact angle trendlines can calculate the supposed surface energy, interface energy and liquid tension at absolute zero, the wetting state at absolute zero can be determined using the equation.

$$\chi = \frac{1}{2}(1 + \frac{\gamma_{sv} - \gamma_{sl}}{\gamma_{lv}})$$

Equation 2.29

Their observations in the kinetic simulation dictates[177] that Cassi-Baxter wetting states occurred when χ was very small between values of 0 and 0.34. Then Wenzel states are between 0.34 and 0.48, and the capillary filling states occur from 0.48 to 1.

The contact angles were measured by capturing images using a Canon EOS 600DDSLR camera set to capture ten pictures every 5 minutes. Thus, the temperature can be altered to observe contact angle shifts for different temperature increments.

Image J software measures the contact angle of the melt between the flat solid surface and the melt's edge. At least seven contact angles were measured for each temperature point and the mean calculated (Figure 2-13).

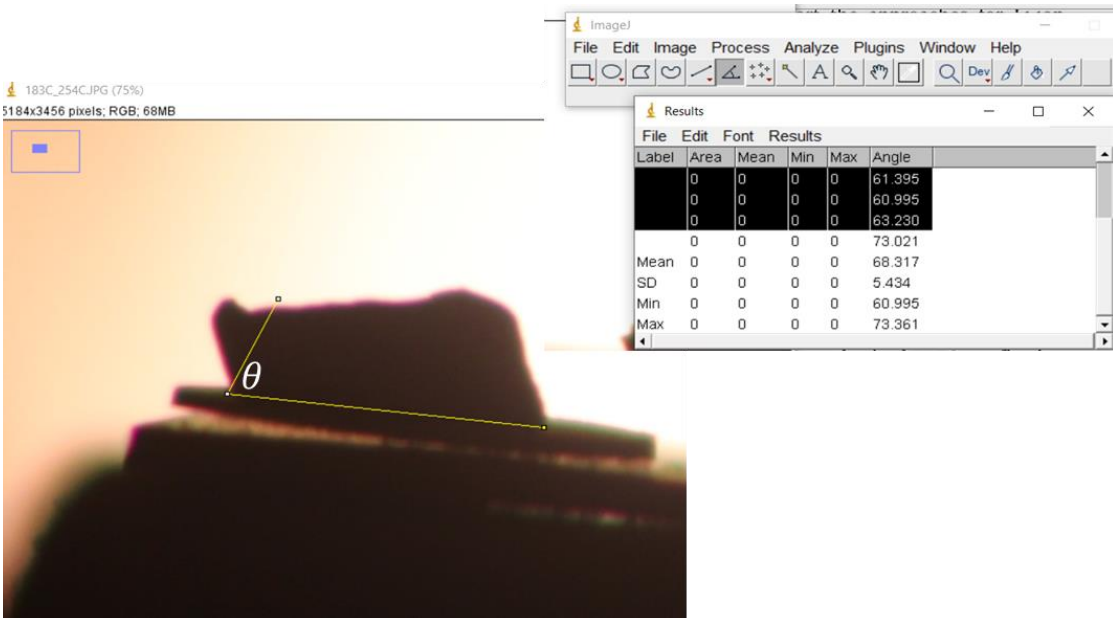

Label	Area	Mean	Min	Max	Angle
	0	0	0	0	61.395
	0	0	0	0	60.995
	0	0	0	0	63.230
	0	0	0	0	73.021
Mean	0	0	0	0	68.317
SD	0	0	0	0	5.434
Min	0	0	0	0	60.995
Max	0	0	0	0	73.361

Figure 2-13: Image J software measuring the contact angles of lithium melt on the surface of a solid electrolyte pellet with the recorded contact angles, mean, standard deviation (SD) min and max values on the right window.

The contact angles (θ) over the temperature range are then applied over a temperature range, allowing a trendline to form the contact angles wetting a solid over a particular temperature range. The minimum and maximum of each specific contact angles measured at that temperature will translate over to be the low and high error, respectively, when that contact angle is plotted on the contact angle against temperature plot.

The radius of the melted spread over the solid surface was measured using ImageJ, and a pixel-to-image ratio was established by measuring the pellet beforehand to assess the spread of a melt over a temperature range. This also had a minimum and maximum and was also charted against temperature to create a trendline.

For the wetting calculations involving LLZO tape-casted samples were synthesised and prepared by Dr Mihkel Vestli. Tape-casted mechanism is in the process of being used in a patent so can not disclose the procedure.

Chapter 3 Investigation of the solid electrolyte series $Li_{3x}La_{2/3-3x}TiO_3$

3.1 Introduction

One of the promising solid oxide electrolytes[68,84,126,181] as noted in the introduction is $Li_{0.5}La_{0.5}TiO_3$ (LLTO) which has good ionic conduction at an order of 10^{-3} Scm^{-1} at room temperature[74]. However, Li loss is a significant issue amongst the solid oxide electrolyte materials due to the higher temperature range of their sintering (900° – 1300°C)[87,182].

The wet chemistry sol-gel technique called the citrate-nitrate route is an exciting possibility as the synthesis can be carried out in aqueous systems rather than relying on organic materials. Still, it wants a more industry-focused synthesis pathway. Sol-gel systems to create LLTO exist, but they are primarily based on organic systems. Organic precursor systems lead to mass shrinking problems and can be challenging to upscale due to the cost of the precursors. With alkoxides solvents using 2-methloxyethanol[181] costing around £44 from fishers and an acetate alkoxide route[181] have a total cost of around £ 90 per litre from the organic solvents alone. Although aqueous systems have been synthesised before by I. Zveria's team in 2016[183], they used an expensive titanium source of ammonium titanyl oxalate monohydrate costing $ 449.50 for 100 g at Fisher Scientific.

A sol-gel approach. Its stability with lithium metal is also an issue, and the synthesis at lower temperatures, which retains the higher lithium concentration within that unwanted side products are formed as Li_2TiO_3 and $La_4Ti_9O_{24}$ are intermediate phases on the way to the cubic phase of Pm-3m.

The synthesis route implemented in these experiments will implement Dihydroxybis(ammonium lactate)titanium (IV), 54 wt.% in water costing $ 50 for 250 g at Fisher Scientific (CAS 65104-06-5). To create good lithium conducting $Li_{3x}La_{2/3-3x}TiO_3$ material that can be implemented in solid-state applications.

The aim of this chapter was to prove that it is possible to synthesis LLTO and Al-doped LLTO using a set of cheaper nitrate precursors in water. It was also necessary to show that the ionic conduction of these synthesised LLTO is comparable to other LLTO materials in literature.

3.2 Experimental methods and conditions

3.2.1 Solid-state synthesis

The precursor materials of La_2O_3 TiO_2 and Li_2CO_3 were hand milled and heated to 650°C for 2 hours to allow for decomposition. Then after hand-milling the powders, a pellet of a mass of 0.5 g was pressed from a 13 mm diameter die. The pellet was then sintered at 900°C for six hours at 5°C min^{-1}.

3.2.2 Sol-gel precursors

The lithium source comes from Nitrates help the chelating process but also act as an oxidant in the self-propagation combustion around 200°C.Lanthanum is provided using lanthanum nitrate hexahydrate hydrophilic material and so held in a desiccator but added to water. Dihydroxybis(ammonium lactate)titanium (IV) is miscible in water and thus can condense and hydrolyse.

Citric acid help as a chelating agent as a self-propagating combustion agent in the burn-off stage of the sol-gel process. Following the fuel oxidiser ratio (Equation 2.1) the oxidiser values are $LiNO_3$ = -5 (Equation 3.1) and $La(NO_3)_3.9H_2O$ =-15 (Equation 3.2). Moreover, for citric acid, the reducing agent and the fuel, the value is 18 (Equation 3.3) and combined, the ratio is 1.11 (Equation 3.4), which means that the experiments follow a 2:1 ratio of citric acid to the nitrate precursor solutions.

$$LiNO_3 = 1 + (-2) \times 3 = \ -5$$

Equation 3.1

$$La(NO_3)_3.\,9H_2O = 3 + (-2) \times 3 \times 3 + 9 \times (2 \times 1 - 2) = \ -15$$

Equation 3.2

$$C_6H_8O_7 = 4 \times 6 + 1 \times 8 + (-2) \times 7 = 18$$

Equation 3.3

$$\varphi = \frac{-5 + -15}{-18} = \frac{10}{9} \approx 1.11$$

Equation 3.4

3.2.3 Procedure and conditions.

The nitrate precursor solutions of lithium and lanthanum are weighed in occurrence with the stoichiometric amounts and dissolved in water to 0.4 M solutions. Likewise, citric acid is measured and weighed out, a 2:1 ratio with the lithium, lanthanum, and titanium precursors solutions. The precursor solutions are stirred for at least half an hour. The Dihydroxybis(ammonium lactate)titanium (IV) is added directly to the citric acid and allowed to disperse within the chelating agent. Then the lanthanum nitrate precursor solution is added to the citric acid and Dihydroxybis(ammonium lactate)titanium (IV) solution. Finally, the lithium nitrate precursor is added.

The sol is then heated to 150°C to begin precipitating; then ammonia solution is added to alter the pH of the sol. Adding no ammonia solution does not remove the precipitate. Controlling the amount to ammonia solution added to the sol and monitoring the pH using Fisherbrand pH paper testing strips (Scientific number 10642751)allowed the pH of the sol to be altered to 4, 5, 6, 8 and 10. The sol then undergoes evaporation overnight to leave a yellow-brown gel. The gel is then heated to around 300°C to burn off nitrates overnight.

The gel is then annealed to 750°C for 4 hours, leaving a fluffy white powder. The powders are then pressed into a 13 mm die of around 0.26 g and pressed at 5 T or 3 T for one minute. The pellet is sintered in air at temperatures ranging from 1100^{o}C, 1200°C and 1350°C for hourly rates. A summary of the whole procedure is provided in Figure 3-1.

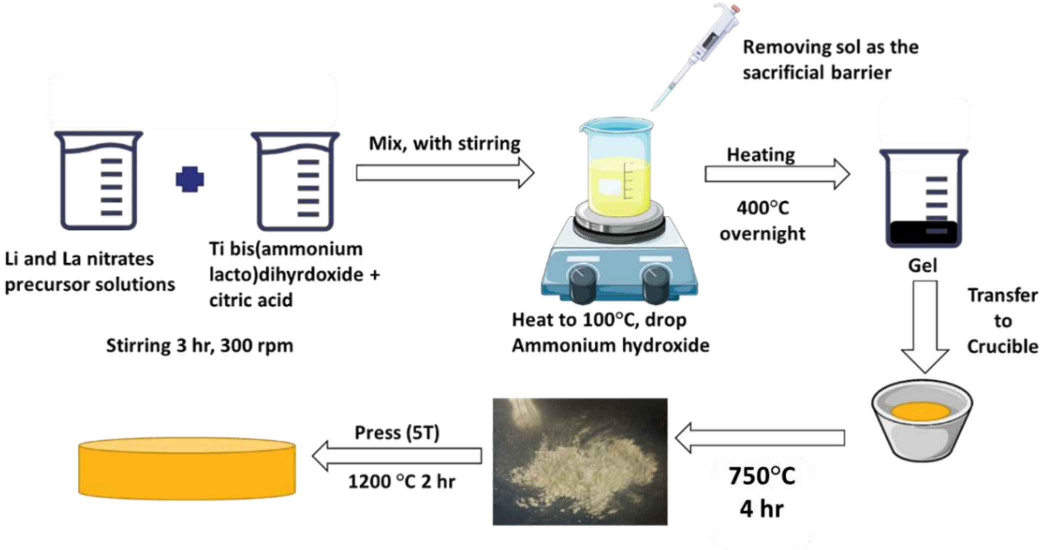

Figure 3-1: The sol-gel synthesis procedure of synthesis of $Li_{3x}La_{2/3}TiO_3$ solid electrolyte material as a pellet.

For hitting the desired cubic phase of $Li_{0.5}La_{0.5}TiO_3$ the masses used for each precursor are listed in Table 3.1 and the volume of water used for the lithium and lanthanum precursors is 15 cm^3.

Table 3.1: The masses of reagents need for the sol-gel synthesis of $Li_{0.5}La_{0.5}TiO_3$.

Reagents	Mass (g)
$LiNO_3$	0.044
$LA(NO_3)_3.6H_2O$	2.294
Dihydroxybis (ammonium lactate) titanium (IV)	5.717
Citric acid	4.071

The pellets then undergo PXRD with a range of 10° to 90° 2theta values for one hour. Undergo SEM analysis and will then be used in wetting experiments with molten lithium.

3.2.4 Synthesis of Aluminium doping LLTO.

The reaction profile of the Al-doped LLTO was based off the stoichiometry for $Li_{0.45}La_{0.55}Ti_{0.9}Al_{0.1}O_3$. The precursors used are the same listed as in (Table 3.2) but there is a reduction in the Dihydroxybis(ammonium lactate)titanium (IV) used and $Al(NO_3)_3.9H_2O$ is used for the Al source.

The reaction profile was followed in a similar fashion outlined by Figure 3-1 with Ammonium hydroxide solution added for the sol to reach a pH of 6. The sintering temperature of the pellet was also different as this was done at 1100°C for 10 minutes in air. The XRD parameters was subjected to a Cu X-ray in the range 10° to 90° 2theta values for one hour but the pellet was placed with a Teflon holder to minimise the stainless-steel peak signals and to move the top of the pellet to be at the same height of the top of the PXRD holder.

3.3 Results and discussion

3.3.1 Reference materials

From previous reports there has been great dispute at what the unit cell parameter of the cubic phase of $Li_{0.5}La_{0.5}TiO_3$ either a = 3.904 Å [184], 3.8704 Å[185] or 3.8703 Å[186], all of the space group *P m -3 m*. Although there are cases when there is a tetragonal that follows the pattern of $\sqrt{2}a$ x $\sqrt{2}a$ x $2a$ when a is the unit cell parameters of the cubic material and this has been found to have the space group of *P4/mmm* (123)[79,187,188]. Resulting in a large peak around 15° 2Theta. For this work the reference peaks for the cubic phase for $Li_{0.5}La_{0.5}TiO_3$ will be based of the unit cell parameter of a = 3.8704 Å[185] (Table 3.3 ,Figure 3-2). And the tetragonal phase for the double unit cell $Li_{0.29}La_{0.57}TiO_3$ unit cell parameters will be a = 3.862 Å and c = 7.775 Å (Table 3.4,Figure 3-2).

Table 3.3: Peaks from the reference material of the cubic phase $Li_{0.5}La_{0.5}TiO_3$ with a unit cell parameter of a= 3.8704 Å[185]

2ϑ (°)	***d*-spacings (Å)**	***Miller indices***
32.703	2.738	110
40.285	2.239	111
46.949	1.935	200
52.797	1.734	210
58.39	1.580	112
68.573	1.368	202
73.299	1.291	221

Table 3.4: Peaks from the reference tetragonal system of a double unit cell for the tetragonal $Li_{0.29}La_{0.57}TiO_3$. With the unit cell parameters of a= 3.862 Å and c = 7.775 Å[188]

2ϑ (°)	**d-spacings (Å)**	**Miller indices**
11.368	7.775	001
22.877	3.862	100
25.733	3.462	011
32.686	2.740	102
34.777	2.580	111
40.336	2.236	112
41.951	2.154	013

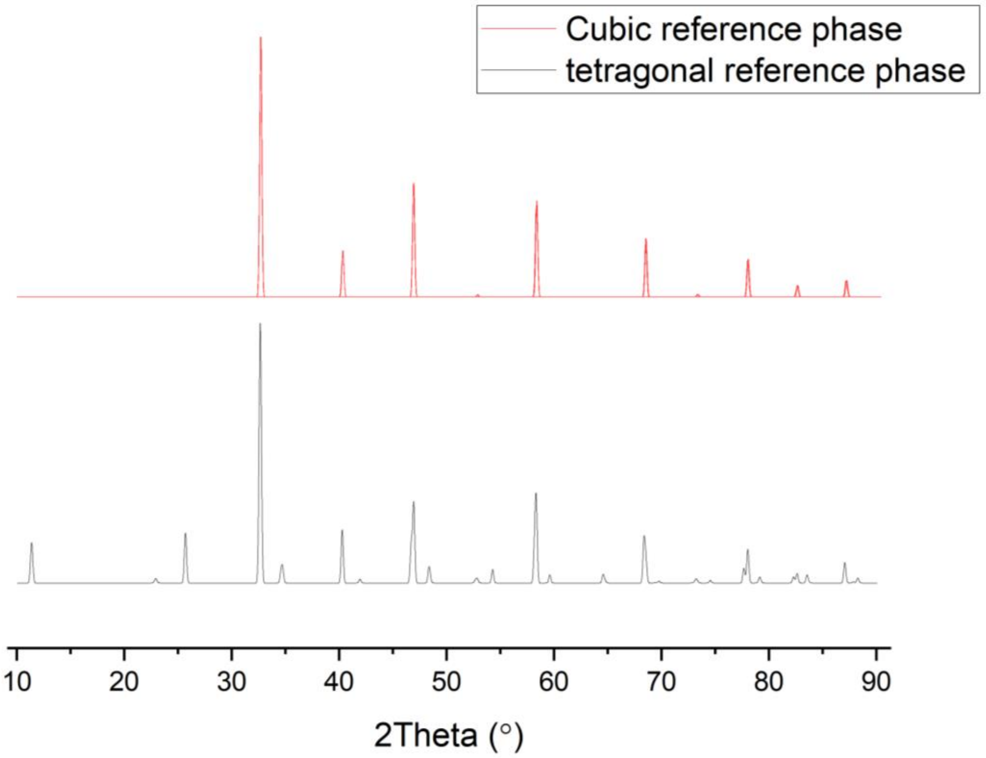

Figure 3-2: XRD pattern of the reference cubic phase of $Li_{0.5}La_{0.5}TiO_3$ and tetragonal phase of $Li_{0.3}La_{0.57}TiO_3$

3.3.2 Solid state synthesis

Analysing the solid-state synthesis reaction at 900°C for 6 hours, the final pellet of $Li_{0.5}La_{0.5}TiO_3$ is impure (Figure 3-3). Leftover TiO_2 and La_2O_3 precursors present as a result of low temperature used in the sintering step and not held at the temperature for long enough[89,99]. Usually, to allow mass transport reactions and grain growth, the sintering temperature can be left for as long as a week[89]. There are also mixed phases with some of the tetragonal reference phase, as noted in the introduction, and some of the double structure forming. More fine-tuning would be required to make the material pure, which has been achieved by others[78,189]. A. West also observed unreacted La_2O_3 even with sintering the same precursors for 24 hours. They determined that the observed tetragonal phase is of the double cell with a larger unit cell axis of 7.864 Å and observed phases of La_2TiO_5. It is very likely that the solid-state synthesis material here also obtains this unwanted phase and is most likely a $La_2Ti_2O_7$, a monoclinic structure[190] confirmed to exist in $La_{2/3}TiO_3$[191]. A sol-gel process will be used to generate pure material to avoid these mixed phases and unwanted side phases forming. Therefore, after analysing this material the sol-gel method will be the sol process to create the cubic phase.

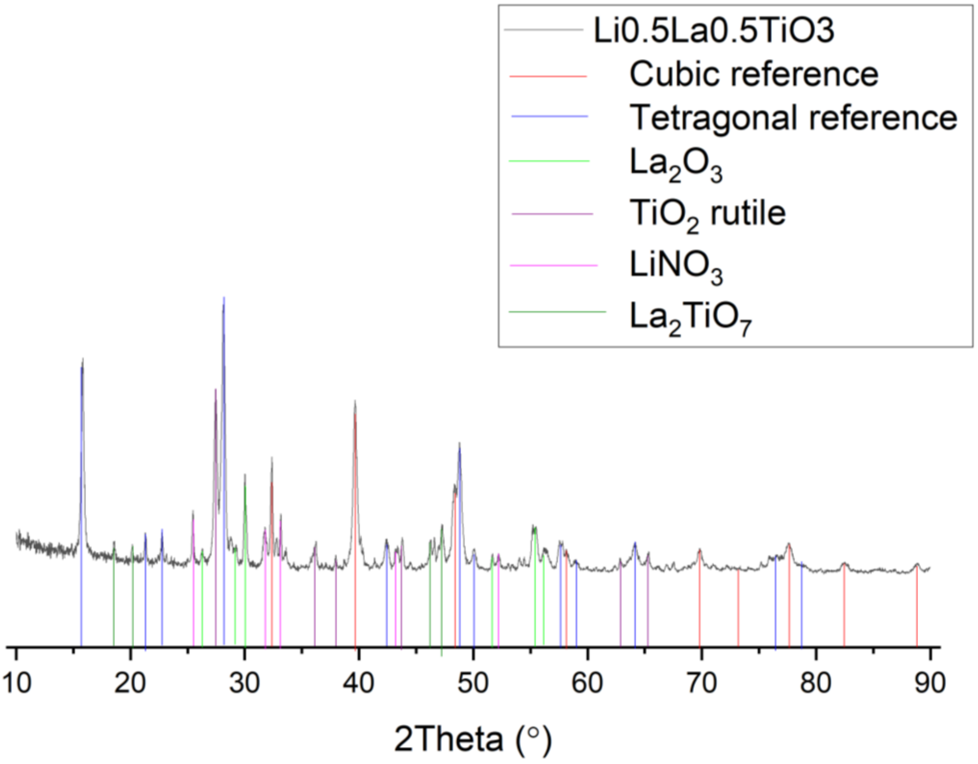

Figure 3-3: XRD pattern of the solid state synthesised $Li_{0.5}La_{0.5}TiO_3$ material

3.3.3 Temperature and pH effect on phase purity of $Li_{3x}La_{2/3-3/x}TiO_3$

Using the sol-gel method, the pH of the sol could be altered by adding the ammonia solution to create LLTO powder. Therefore, the following pHs of the sols were synthesised: 4, 5,6, 8 and 10.

For the pH 10, LLTO material initial referencing for the cubic system with a unit cell parameter of the space group (*P m -3 m*) was *a* = 3.89104 (4) Å (Figure 3-4). Multiple peaks were unrefined but looking at the reference cubic nature (Table 3.3), it was found that the peak at 22.83° is the 100 plane as it contained a *d* spacing equivalent to the unit cell parameter (Figure 3-4). There are two peaks unrefined at 39.8° and 40.12°, but with the multiplicity using the refined unit cell, their multiplicities are the same plane of 111. This splitting could be a result of the fact that a pellet of the material was used in the XRD rather than powder. As the X-rays will have multiple directions for their reflections and diffractions in the pellet because of this, then there can be a splitting occurring. With the cubic values using a = 3.89104 Å of the peaks, a square root error of 1.73×10^{-5} was obtained. This fit might be ideal, especially considering the unindexed peaks. The 100 peaks at 22.877° appear in the reference tetragonal material (Table 3.4), hinting at this supercell characteristic of LLTO[79,187] instead of outright identifying the tetragonal phase as there is no strong peak around 18°.

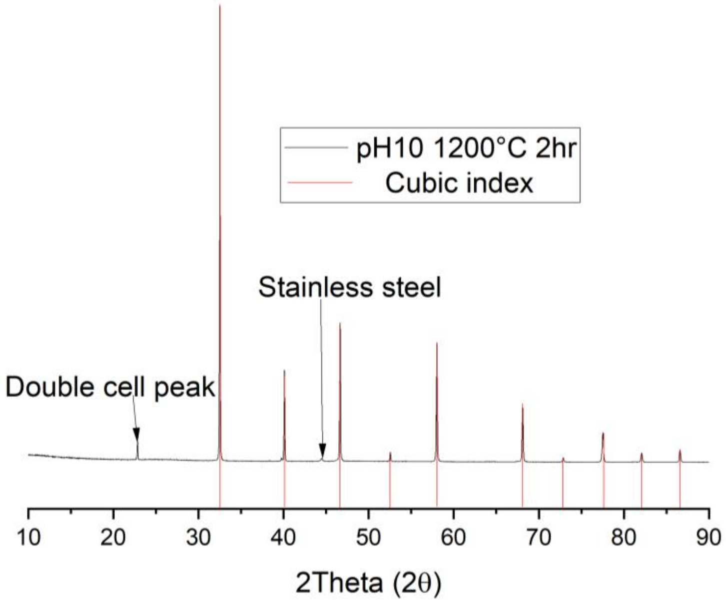

Figure 3-4: XRD pattern of $Li_{0.5}La_{0.5}TiO_3$ synthesised using a sol solution of pH 10 sintered at 1200°C for 2 hours.

For pH 4 (Figure 3-5), there is a possible tetragonal system occurring in which the unit cell parameters are *a* = 3.8662 (16) , *c* =7.7753 (6) *P4/mmm* (123)[188] although there is no strong (001) peak at 11 2theta[188]. Furthermore, a possible cubic system like the ones experienced at pH 10 [184] but there appears to be a splitting effect occurring. Assuming it was the cubic phase, the usual unit cell parameters were inserted into the peaks expected that were off from expected values by at least 0.2 delta[192] from the Wegner algorithm.

Initial spectra calculations using a wide 2theta window and the unit cell parameter of *a* = 3.7 Å and *c* = 7.1 Å. The indexed spectra provide the first peak at 24.946° with an observed *d*-spacing of 3.5665 Å (002). Then using multiplicity with indexing and refinement the unit cell parameters were found to be of *a*= 7.504 (16) Å and *c*= 14.708 (6) Å. These unit cell parameters allow 19 of the 36 peaks to be indexed. Within the 36 peaks, there will be some cubic peaks, and because a pellet was used instead of powder, many of the peaks split further. Another indicator of the tetragonal phase is a minor splitting of the 47° (200) peak due to the different sizes of the *a* and *c* axis [98].

Although there was an assumption that a Li_2TiO_4 was forming as presented by the diffraction patterns, there is a possibility that there are some other lithium titanium impurities[193] of $(Li_4Ti_5O_{12})_{0.33}$ as they have similar diffraction patterns as the tetragonal and the cubic phases. They are most likely the unidentified peaks in Figure 3-5. Despite the splitting, it is possible to use the Miller indices again to determine a cubic phase with a unit cell parameter of *a* = 3.9211 (14) Å. Although the difference between the observed and the calculated can be high, the positions are close to the reference material peaks (Table 3.3). However, regardless of the unit cell axis, it is safe to assume that the purity of this material is poor, and further clarification of the unit cell will be a challenge.

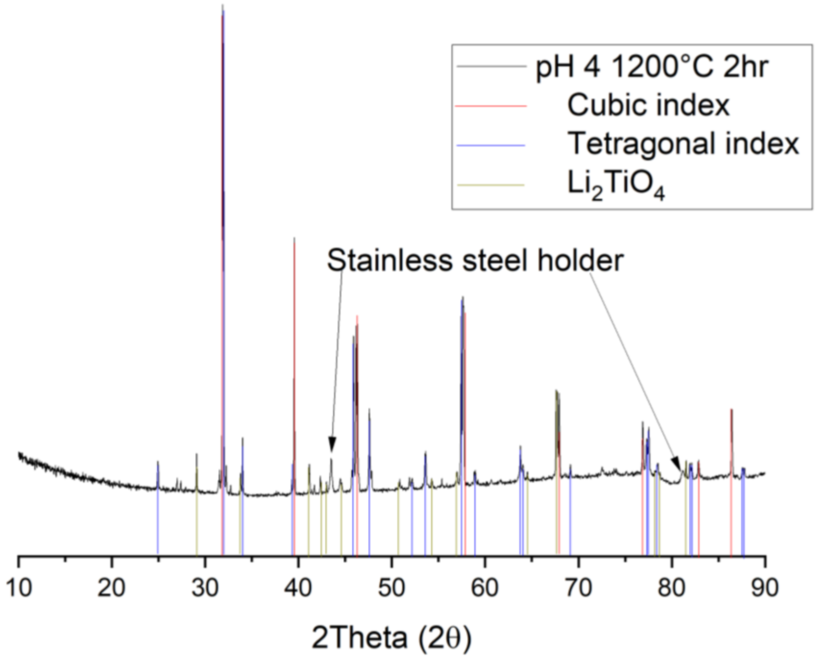

Figure 3-5: XRD spectrum of a LLTO sample sintered at 1200°C for 2 hours with a pH of 4.

The synthesised LLTO material at 1200°C for 2 hrs with a pH 8 was refined by the cubic patterns providing a unit cell parameter with *a* = 3.8662 (3) with all nice indexing except two peaks marked by an asterisk the XRD pattern (Figure 3-6).

The asterisk peak, around 45° that is not part of the stainless holder, has also been reported by A. Várez *et al.*, who stated it might be a result of a microdomain giving rise to the tetragonal phase seen in other reports[187]. The higher *d*-spacings peaks are typically present if a tetragonal phase is present. Therefore, there is likely another phase or a microdomain present. It has been found that Li_2TiO_3, as a second phase, was found at the grain boundary junctions when the unit cell edges are doubled in size when trying to form $Li_{0.5}La_{0.5}TiO_3$ as a result of La-Ti-O ordering[79,194]. There is a spinel impurity of $Li_{1.33}Ti_{1.67}O_{3.6}$ with a unit cell parameter of *a* = 8.355 (5) Å with a prominent 040 peak at 43.311° and a peak at 82° which is a possible impurity that may have resulted from an imbalance of condensation and hydrolysis rates meaning that the lithium and lanthanum bond together[193].

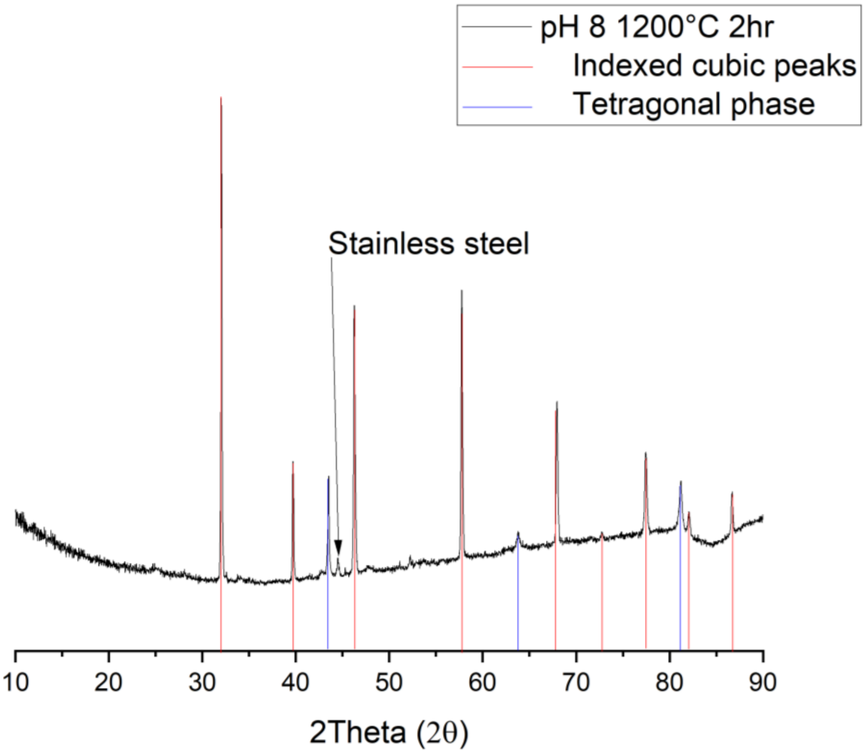

Figure 3-6: XRD pattern of a LLTO powder sintered at 1200°C for 2 hours compared to a cubic phase of the LLTO at a= 3.89 Å.

At pH 5 1200°C 2 hrs, the expected cubic peaks are coming through as seen when compared to the reference material provided by Maria Sotomayor *et al.* using a unit cell axis of *a*=3.86539 Å for the space group of 221[195]. However, we can observe a shift of 0.255 2theta of the sample in the direction of unit cell expansion. This is considered with the index fitting. There are additional peaks that behave similarly to the titanium impurity but may be due to the unit cell of a double length of around 7.86429 Å accounting for (221) *Pm3m* space group.

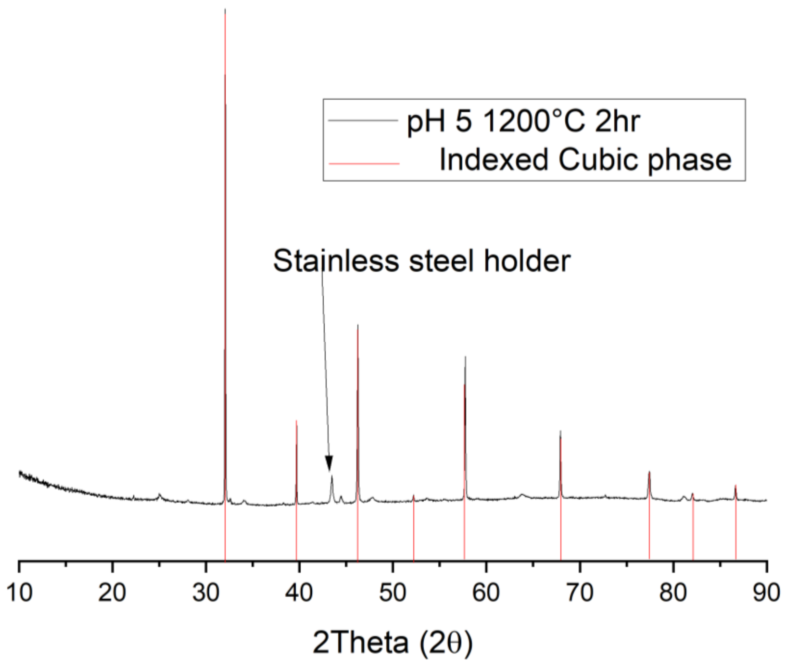

Figure 3-7: XRD of LLTO synthesised with a sol precursor of pH 5 for 1200°C for 2 hours.

This pH there is splitting at the 32 peaks as well. As with the usual cell cubic parameter peaks, there is a more considerable distance between the obs-calc than pH 10 or 8. The pellet splitting can be a result of reduction of the symmetry of the cubic phase from {110} to {011}[196].

In comparison to other phases, the cubic parameters seem to be present at all pH sol conditions, but as shown with the reference cubic phase[185] of a = 3.8704 Å, variation in the peak of 32° or the 110 planes is obvious. Therefore, to compare the unit cell parameters of a for the cubic phases at different pHs pellets synthesised at 1200°C for 2 hours (a in Figure 3-8 and XRD pattern in Figure 3-9). A summary of the values of the a unit cell parameter in Figure 3-8 are summarised in Table 3.5. The unit cell parameters of a were then collated together to show that the extreme pHs, 4 and 10, result in more extensive unit cell parameters while collating around a neutral pH, 6, will allow for fewer minor cubic phases. It is worthwhile that the lowest unit cell parameters were formed at 1350°C at a pH of 6 (b in Figure 3-8), although that may be due to the significant increase in the sintering temperature and time as sintering arguably has a more significant influence on the unit cell parameters than the sol of the precursor. As the pH effects the rate of condensation reactions and hydrolysis reactions, approaching pH 7 leads to a minimum in the hydrolysis rate will condensation rate is increasing. Meaning the chain of oxalates holding the precursors metal ions together is at its smallest distance leading to lower unit cell parameters of the finished products.

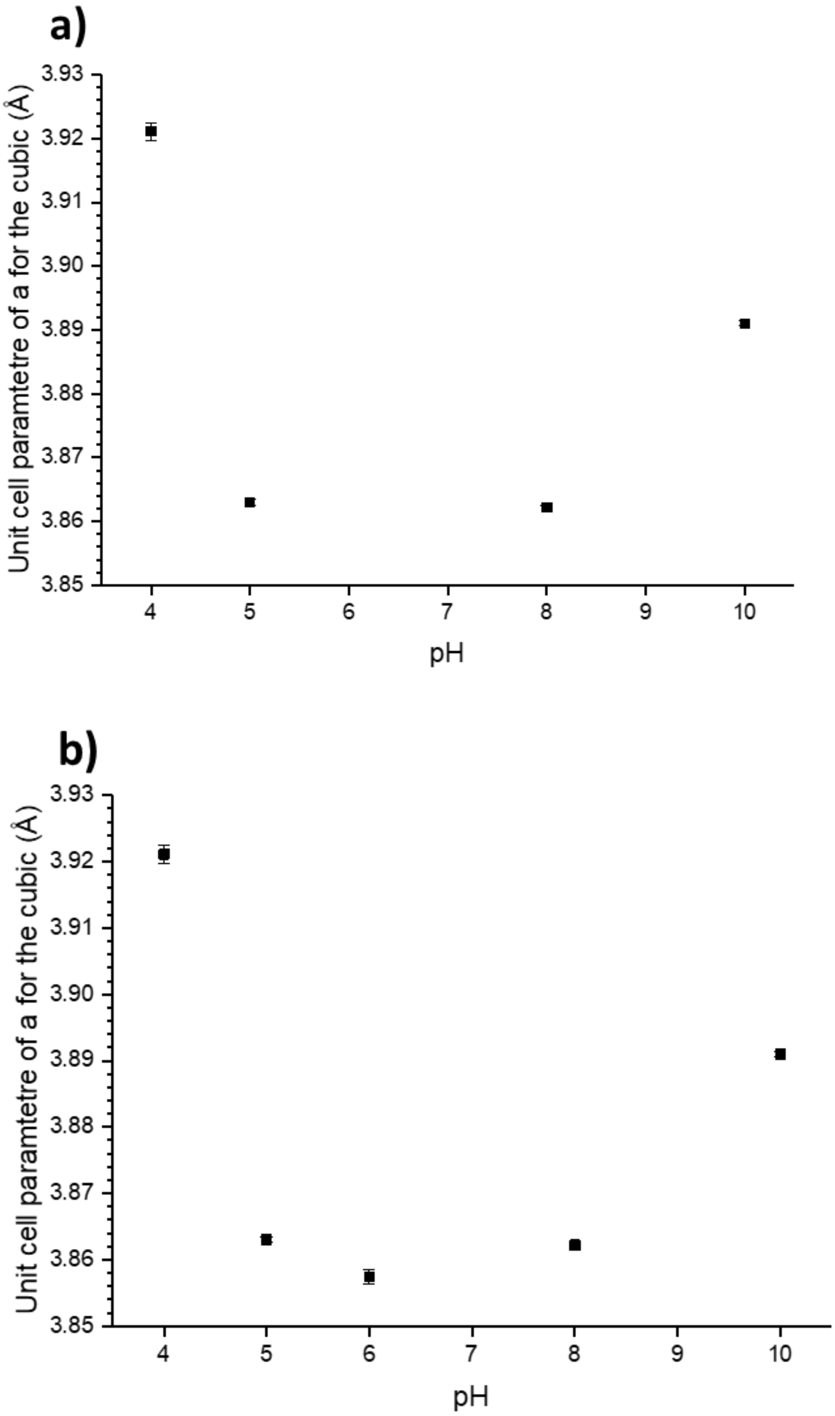

r

Figure 3-8: a) The variation of the unit cell parameter a, for the cubic phases for different pH of the sol to synthesise LLTO as a pellet for 1200°C for 2 hours. With b) the inclusion of the unit cell parameter of the cubic phase of $Li_{0.5}La_{0.5}TiO_3$ being synthesised at 1350°C for 6 hours.

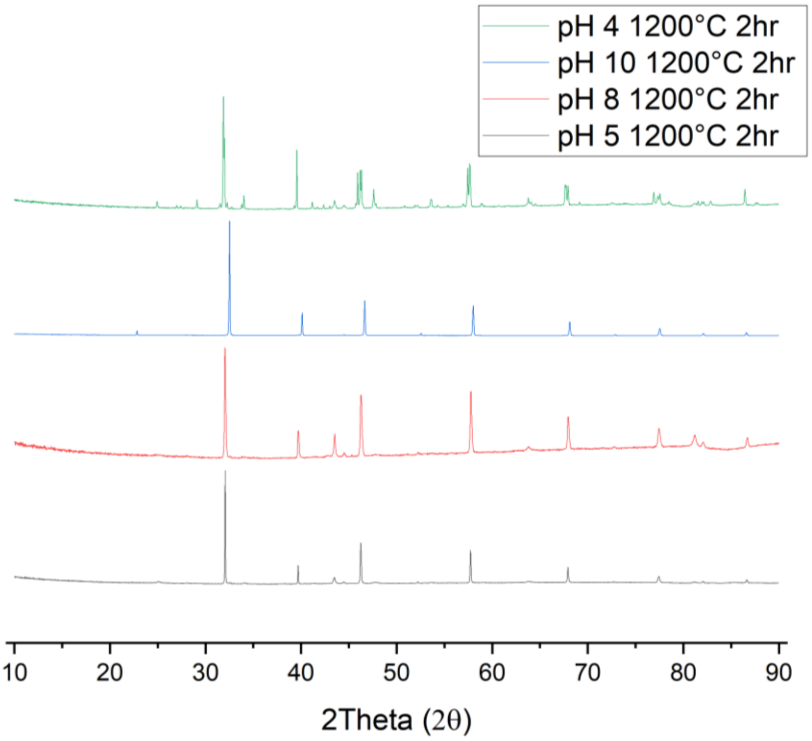

Figure 3-9: XRD pattern of the $Li_{0.5}La_{0.5}TiO_3$ *pellets synthesised using aqueous sol-gel synthesiss with different pHs used for the sols.*

Table 3.5: Summary of the unit cell parameter (a) points for Figure 3-10 b) with the varying pHs of the sol used for their sol-gel synthesis. It also includes the errors of each of the unit cell parameter.

pH of solution	**Unit cell parameter *a* (Å)**	**Error in unit cell parameter**
4	3.921	0.0014
5	3.863	0.0004
6	3.857	0.0011
8	3.862	0.004
10	3.891	0.0004

A temperature shift was introduced for the sintering time as the XRD data suggested that the excess titanium and phases are that some of the bonds have been unable to reach their maximum symmetry. Thus following the advice of S Stramare[79], the sol-gel material was sintered at 1350°C for 6 hours in the air to attempt to achieve a cubic phase (Figure 3-11).

Moreover, this resulted in a good index providing a cubic unit cell of *a*= 3.8574 (3) with all the peaks indexed well.

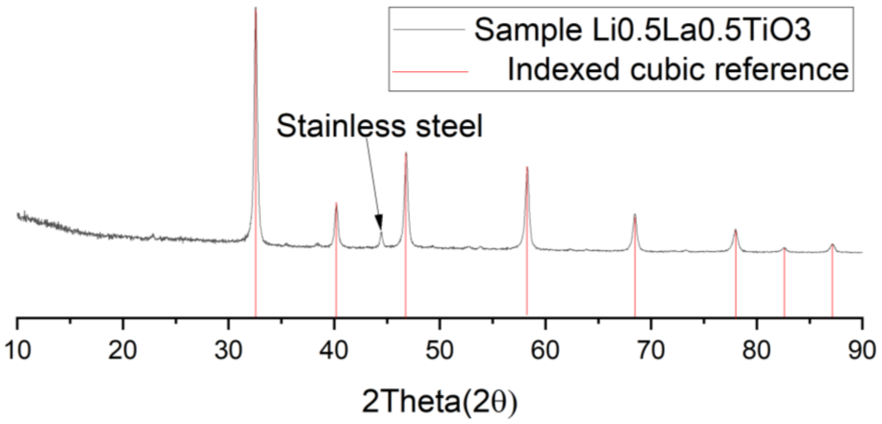

Figure 3-11: LLTO spectra of powder of $Li_{0.5}La_{0.5}TiO_3$ sintered at 1350°C for 6 hr.

SEM images of the $Li_{0.5}La_{0.5}TiO_3$ sintered at 1350°C for 6 hrs showed a dense cross-section compared to the pH 4 LLTO pellet, as the longer sintering time and the higher temperature helped the growth of bigger single grains (Figure 3-12). Observing the surface of the pellet (Figure 3-13), some areas have longer unit cells, which provides evidence for the existence of a cubic phase with an extended super structure[79,80,197,198]. Observations using EDX also present a pure phase containing only lanthanum and titanium (Figure 3-15). Although with this sintering temperature, be careful to provide sacrificial power below the pellet to present any doping off the holder substrate. MgO holders were used, but in some cases, Mg streaks could be observed (Figure 3-14).

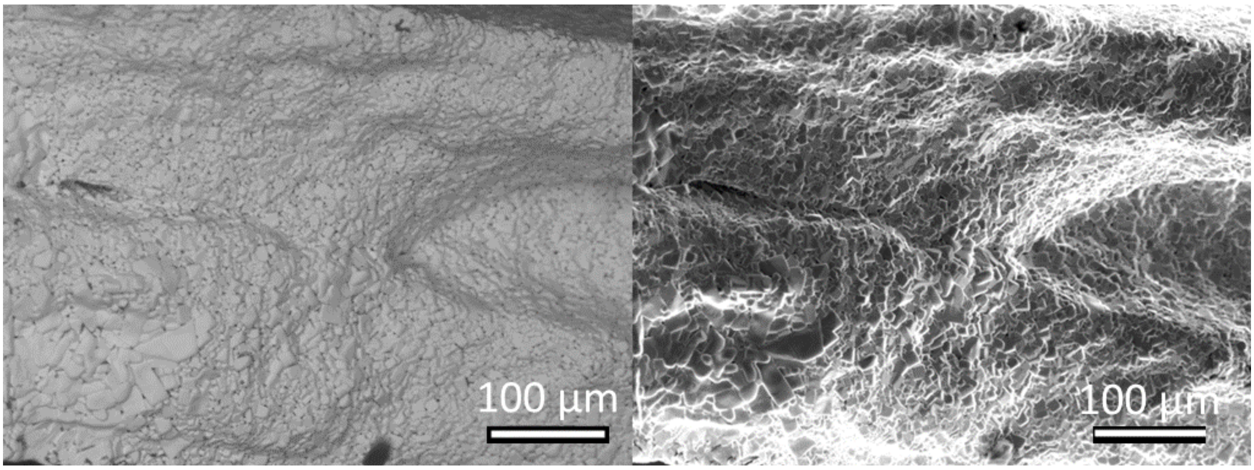

Figure 3-12: Bulk material of $Li_{0.45}La_{0.55}TiO_3$ *originating from a pellet sintered at 1350°C for 6 hours.*

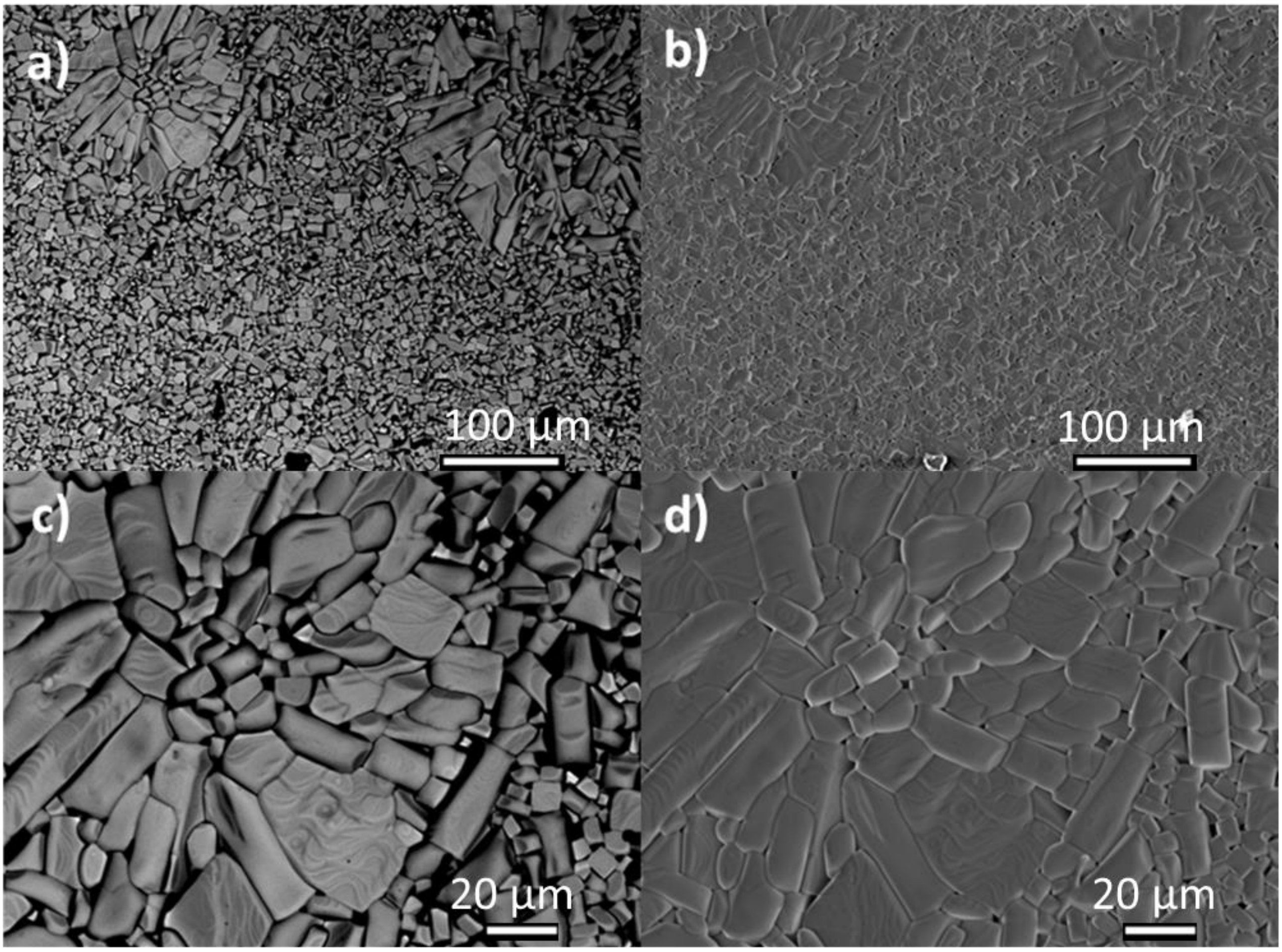

Figure 3-13: Pellet of $Li_{0.45}La_{0.55}TiO_3$ *sintered at 1350°C for 6 hours with backscattering electrons at a magnification of 230 a) and 700 b). The complementary secondary electron image is presented at the exact magnifications at 230 b) and 700 d).*

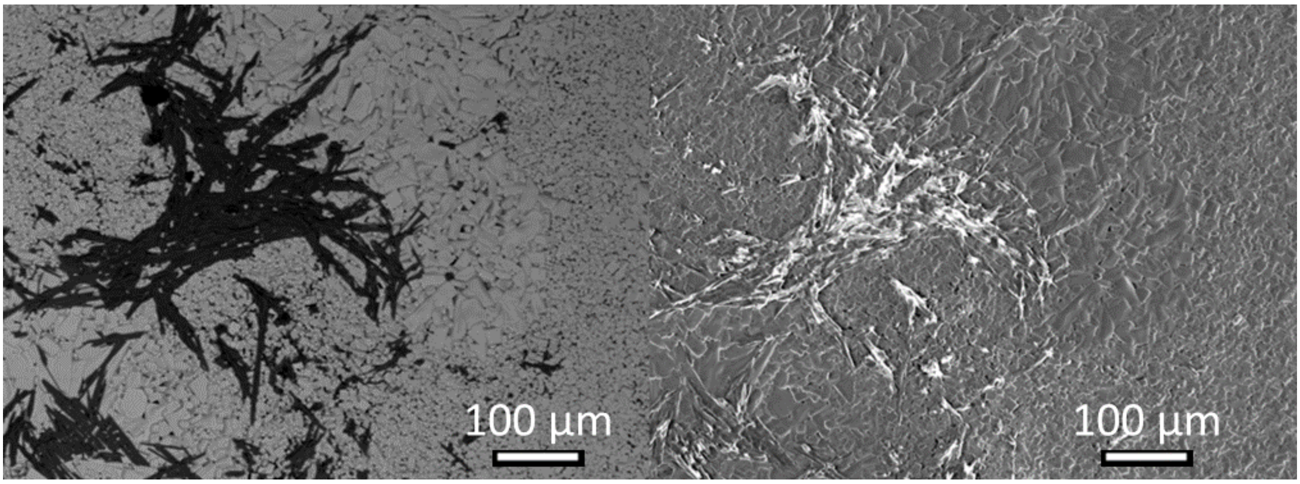

Figure 3-14: Mg streaks in LLTO pellet sintered at 1350C for 6 hours due to the MgO plate holding the pellet.

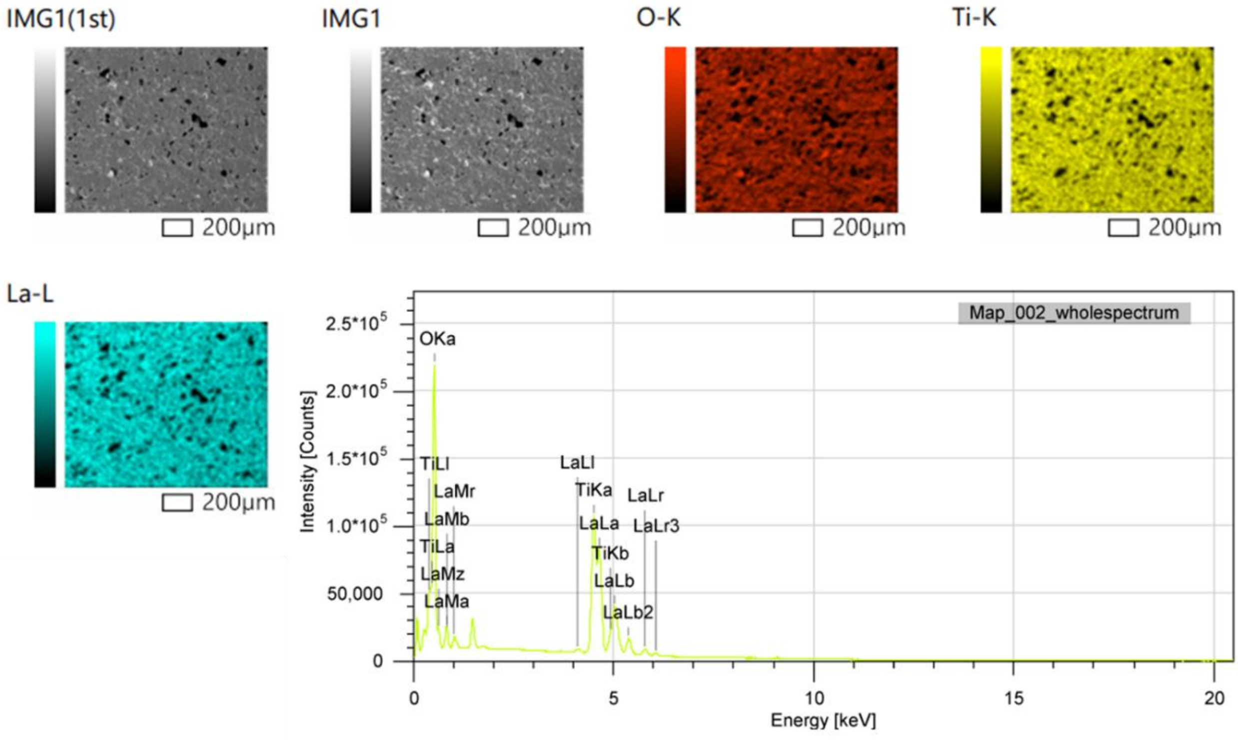

Figure 3-15: EDS spectrum and maps of $Li_{0.45}La_{0.55}TiO_3$ with a sol precursor of pH six and sintered at 1350°C for 6 hrs.

Initially, experiments utilised 10 cm^3 of ammonia solution to get the desired pH of 6, but instead of slowly adding the content in a dropwise manner, the pH increased rapidly to pH 10. To improve the control of the sol's pH a digitial pH meter could be used as the ammonia solution is added. As well as using a measuring a pipette, instead of a dropwise pipette, the volume of ammonium solution needed to create the different pHs of the sol can be recorded . Making it easier to reproduce the desired pH sol and repeat the different phases to improve the accuracy of the unit cell parameters. These changes to the equipment would also make it easier to acquire all the missing pHs and if necceasry any intermediate pH valeus such as 5.5.

In conclusion, for the cubic phase of $Li_{0.5}La_{0.5}TiO_3$ it is possible to form it at 1200°C for 2 hours using a sol with a pH of 5 rather than having to phase synthesised from sintering at 1350°C for 6 hours at the same pH.

3.3.4 Particle size

Investigation of the particle size for targeted $Li_{0.5}La_{0.5}TiO_3$ powder after they were annealed at 750°C for 4 hours was performed to investigate if ball milling was required to create small particles or if hand milling is all that is needed. Using a sonicator and applying the spinner at different percentages, we can see a wide variation in the size of particles from hand milling (Figure 3-16). Initially no ultrasonication was used as shown by the green line in Figure 3-16 will the spinner was set to 50 %. Believing agglomerates to have formed the sonicator was used for the red and blue scans in Figure 3-16. Seeing smaller particle sizes around 0.05 µm to 1 µm suggested that sonication helped break apart any agglomerates tha had formed once in solution. Stirring power affects the agglomerations a little bit as at (1750 rpm) 100%, observing that most of the particle sizes are around 0.25 µm, with most particles being around 20 µm in size and then four µm in size. Observing the milled samples in SEM, an estimation of the particle size created by the initial sol-gel reaction is an average size of 0.25 µm . Contributed to the construction of the interesting crystallographic of $Li_{3x}La_{2/3-3x}TiO_3$ or could result in a mixed phase formation that we see in the pH four material.

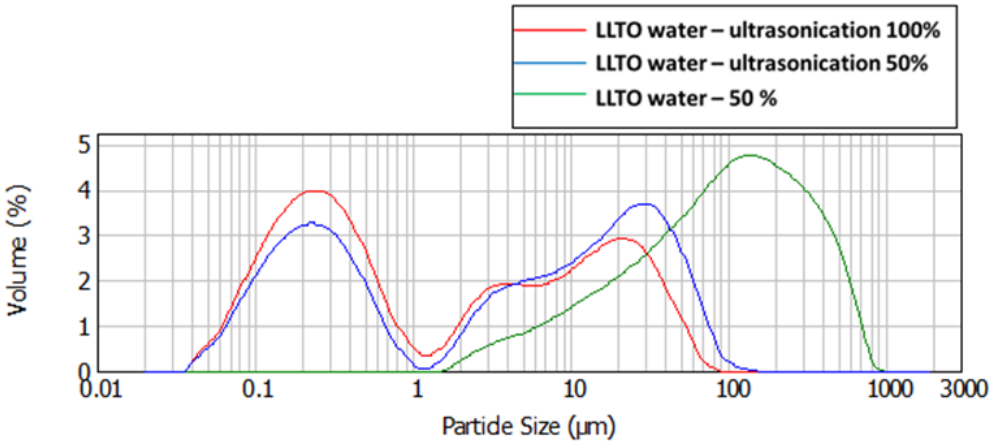

Figure 3-16: Particle size distribution of LLTO powders annealed at 750°C for four hours with a precursor solution of pH 5. The size of the particles recorded in a water solution with sonication used with 100%

Ball milling the $Li_{0.3}La_{0.56}TiO_3$ powder with zirconium balls at 400 rpm shows a shift in most of the particle size being around 40 µm to slightly greater than 1 µm in size (Figure 3-17). This comparison was done with powder annealed after 750°C to confirm whether the hardness of the powder would be an issue for creating small enough particles to small particles to provide dense sintering. Moreover, with the knowledge that smaller particle sizes will improve the grain growth when sintering, it would be better for equal size distribution to make good dense pellets[99], but as was observed in the 1350°C sintered at 6 hours pellet (Figure 3-12 and Figure 3-13) hand milled particle size is sufficient for pellet wetting analysis.

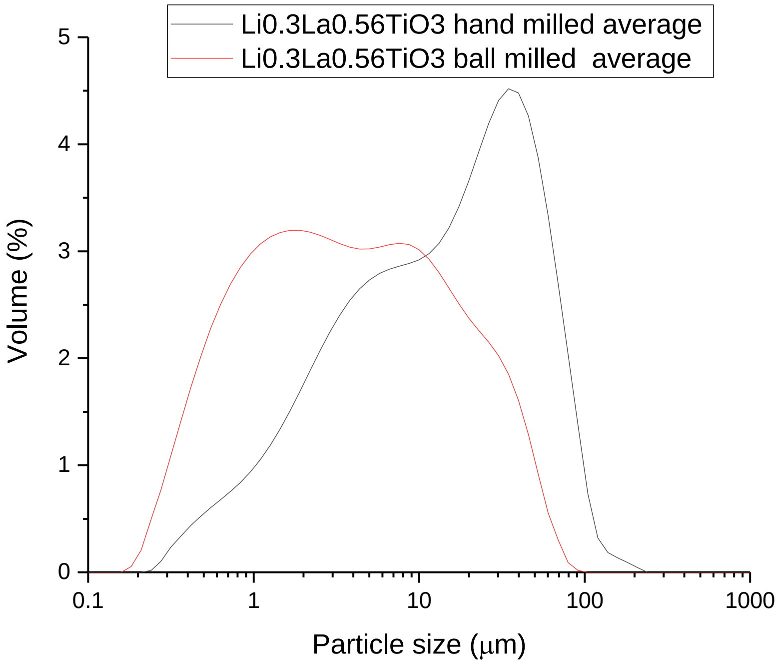

Figure 3-17: Comparing the particle distribution of LLTO powder annealed at 750°C for 4 hours with mortar and pestle grinding (hand milling) and ball milling the sample.

3.3.5 The electrochemical response of LLTO material

Electrochemical impedance spectrum (EIS) was performed on a symmetrical cell using gold as the blocking electrode at either side of the rough LLTO surface, 1200°C for 2 hr at pH 4 (Figure 3-19). It has been reported that in LLTO systems, the larger the lattice parameter, the higher the ionic conductivity and the lower the activation energy[24]. Therefore, although showing mixed phases (both the cubic $Li_{0.5}La_{0.5}TiO_3$ and the tetragonal $Li_{0.3}La_{0.56}TiO_3$), the pH 4 material was used to analyse the electrochemical performance of LLTO. Preferably all the pellets would have been subjected to EIS, but pellet thickness was a limiting factor with the equipment for the SI 1260 set up. With the other pellets being smaller than 2 mm thick.

The experiment was performed by heating and then cooling up to 250°C the pellet measuring the EIS at each 50°C interval. Heating and cooling demonstrated very little change to the large main arc (Table 3.6), with the significant tail-off typical behaviour for a blocking electrode[154,199].

To gather the resistance and the capacitance the auto arc feature from Zview software as shown in the example for when the resistance and the capacitance was gathered for the LLTO pellet as it was heated to 50°C (Figure 3-18). The capacitance of the arc remains around $x10^{-9}$ F cm^{-1} meaning that it is either the characteristic capacitance of a grain boundary[151] or as suggested by the work of work of W. Kwon *et al*[86] the shape of their tetragonal phase LLTO has a similar arc shape to the one presented in Figure 3-19. They determine that the arc is a combination of bulk impedance and grain boundary impedance. So, the first intercept of these arcs can be taken as the bulk value of resistance while fitting arcs can be fitted providing information on the capacitance and resistance of both the bulk and grain boundary resistances[199]. By taking the values of the resistance and capacitance as the pellet is heated up and cooled down the average resistance and the capacitance can be taken as an average between the two. Therefore, the average grain boundary resistances are 525 Ω (50°C), 191 Ω (100°C), 110 Ω (150°C) and 88.5 Ω (200°C). These arc resistances taken on the increasing and decreasing temperature are then used in the Arrhenius equation to determine the activation energy of the total resistance. However, the grain boundary resistance will dominate the ionic conduction although it is still not possible to provide specific activation energies for these cell processes from this Arrhenius plot.

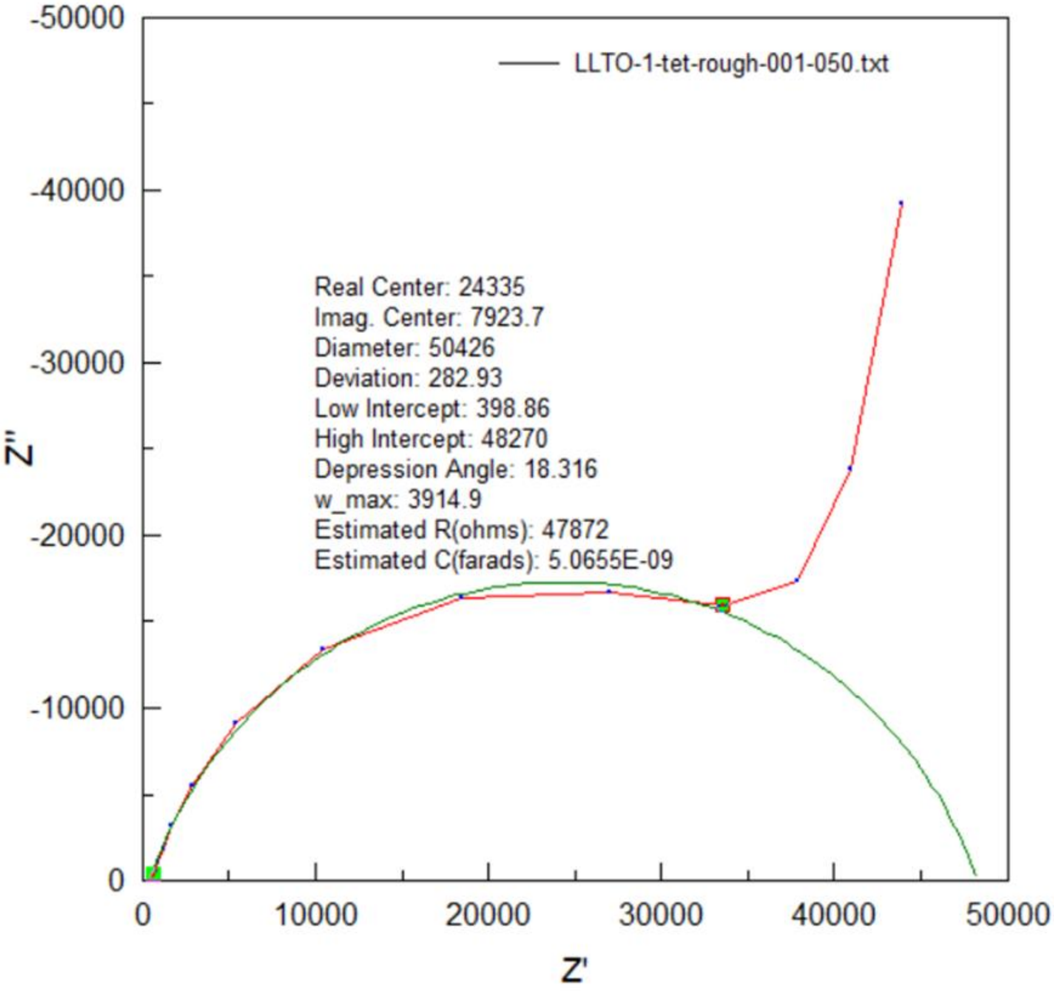

Figure 3-18: EIS fitting using the arc feature of Zview for the LLTO pellet as was heated to 50°C. The arc shows the maximum frequency of the behaviour (w_max), the estimated resistance of the behaviour (R) and the estimated capacitance (C).

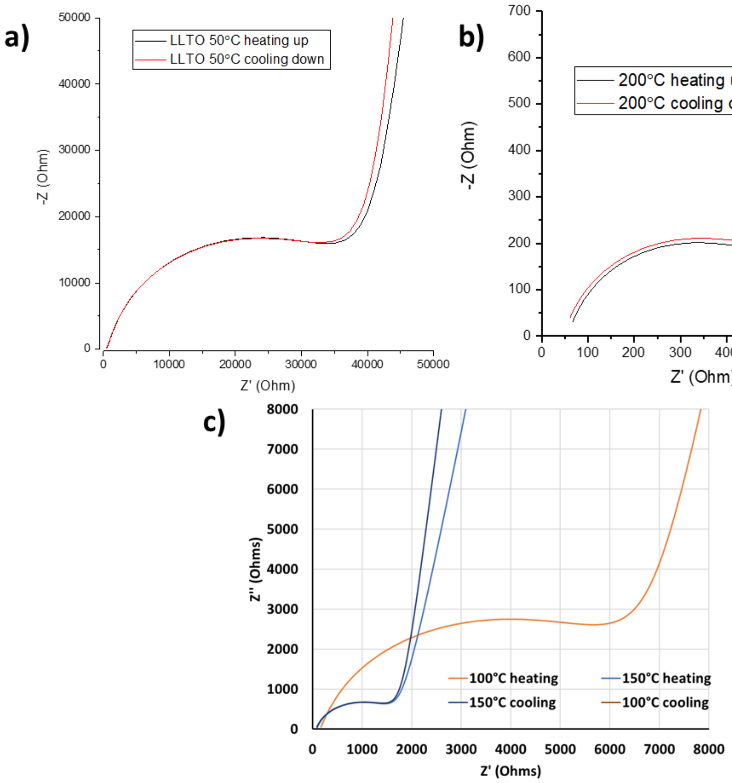

Figure 3-19: Rough surface LLTO gold blocking symmetrical cell EIS at temperatures a) 50°C, b) 200°C and a combination of c) 100°C and 150°C

Table 3.6: The average resistance, max frequency and capacitance extracted from the arcs as the Au/LLTO/Au increased and decreasing in temperature.

Temperature (°C)	**Average resistance (Ω)**	**Average capacitance (F cm^{-1})**	**Average peak frequency (Hz)**
50	47900	5.666x10^{-9}	3882
100	7886	5.060x10^{-9}	25070
150	1967	4.740x10^{-9}	2.083 x10^{-5}
200	640.6	4.778x10^{-9}	3.272 x10^{-5}

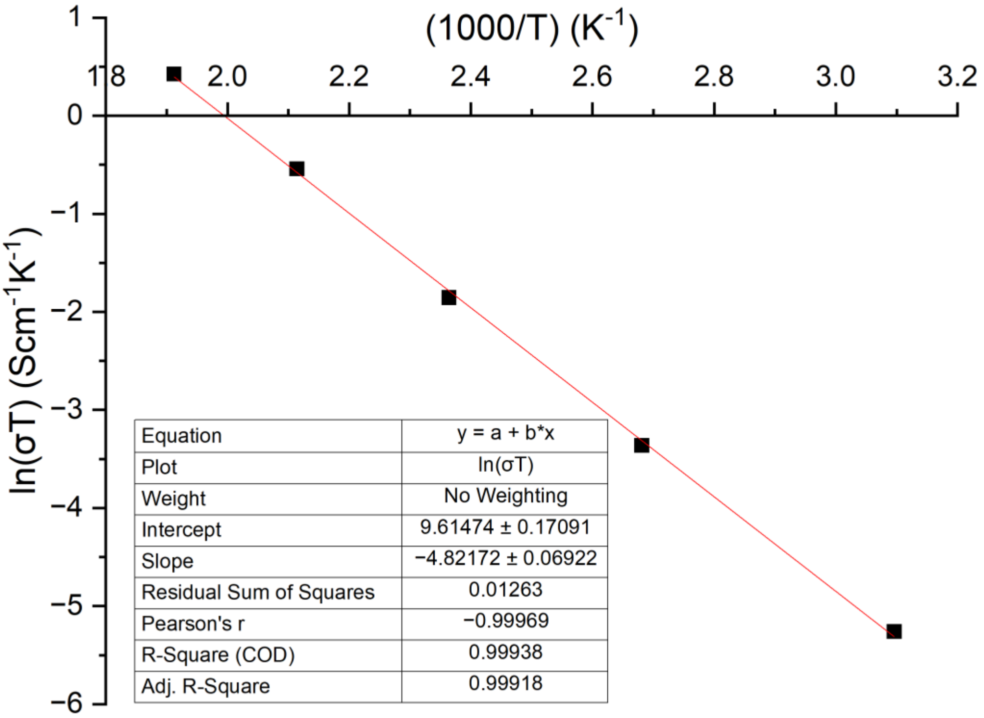

Equation	y = a + b*x
Plot	ln(σT)
Weight	No Weighting
Intercept	9.61474 ± 0.17091
Slope	−4.82172 ± 0.06922
Residual Sum of Squares	0.01263
Pearson's r	−0.99969
R-Square (COD)	0.99938
Adj. R-Square	0.99918

Figure 3-20 Ionic conduction against temperature of 'rough' surface LLTO pellet using the total average resistances from the grain boundary. With the activation energy being the gradient of the line.

Using the total average resistances from the grain boundary arcs as reported in table 3.7 a LLTO ionic conduction against temperature graph can be constructed of the 'rough' surface LLTO pellet (Figure 3-20).The total ionic conduction at 200°C was observed to be $1.3x10^{-3}$ S cm^{-1}, similar to the ionic conduction values of other synthesised LLTO material[74,199–201]. And the total ionic conduction is 1.6 $x10^{-5}$ Scm^{-1} at 50 °C with an activation energy of 0.415 eV (Figure 3-20). The order of magnitude for the ionic conduction is comparable to other LLTO grain boundary ionic conduction values[74] 10^{-4} to 10^{-5} S cm^{-1}.

The gradient then contains the activation energy for the ionic conduction of the total system, but this will need to be divided by the Boltzmann constant (*k*), which is $8.62 \times 10^{-5} eV\ K^{-1}$ when looking at the hopping mechanisms. The activation energy is higher than the expected values of 0.34 eV or even 0.58 eV (Figure 3-20). The issue could arise from excluding the gas constant or a different conduction mechanism. The activation energy is similar to work done by Hiroki Moriwake[202] *et al.* They use HAADF-STEM to present two potential Li-ion movements with one migration pathway occurring in a La layer with no cavities. Without La vacancies, the activation energy of this pathway was around 3.58 eV. Suggesting that the mixed phases lack vaccines to enhance Li migration and, thus, ionic conduction. The electrochemical performance performs comparably to phase pure LLTO materials.

A modelling paper written by Moriwake, H. *et al.* [202] provides an explanation to the activation energies of 0.3 eV for LLTO material, especially in the *P4/mmm* space group[202]. In the paper, STEM evidence demonstrates that 90° microdomains reduce the ionic conduction of the system as they create 'micro-interfaces' of coherent nature. Especially in the (010)/(001) and (100)/(001) directions taken as Pseudo-perovskites. LLTO materials indicate a perovskite double unit cell. The *P4/mmm* space group arrangement of the LLTO material gives rise to two types of lanthanum layers one is a La-rich (La1) and the other a partially La vacant (La2)[202]. The anti-phase rotation of the TiO_6 octahedra allows for higher Li migration[202]. From Moriwake calculations the activation energy of ionic through these Lanthanum vacant layers is to be 0.19 eV lower than the experimental values, helped by anti-phase rotation of the TiO_6 octahedra allowing for higher Li migration[202]. There are 'three Li migration paths: (a) migration through a La1 layer; (b) migration through a La vacancy in a La layer; and (c) migration through a Li vacancy in a La2 (Li) layer'. Migration routes (a) has a higher activation energy of around 3.58 eV as the Lanthanum ions block the Li migration implying that in this material with multiple phases of tetragonal and cubic the higher activation energy can be a result of more lanthanum ions blocking Lithium migration.

Furthermore, fitting to the arcs of Electrochemical systems is comparable to other materials. However, this may be attributed to the mixed phases present—especially the grain boundary arcs with a more significant resistance because different tetragonal and cubic phases exist.

Further work would include performing a cyclic voltammetry analysis and try full cell cycling and discharging to present the voltage window of these materials and their stability over multiple cycles. However, the very brittle nature of the pellets, and when applied to swage lock cells, would break the electrolytes perform the testing could begin. Using button cells would be an option in the future, but as the impurities of these materials were still prevalent thus, parasitic side reactions are likely to occur, and the discharge and charge curves of the batteries are likely not to reflect preferred industrial quality.

3.3.6 Aluminium doping of LLTO to stabilise the cubic phase.

Al doping has been seen to help stabilise the cubic phase of the garnet material. It is also known that Al doping in the B- site replacing Ti has seen better ionic conductivity as an electrolyte[203]. To help the sintering between the cubic phase of LLZO, stabilising the cubic phase of LLTO is needed. Adding dopants to LLTO Al is an easy choice due to the benefits of Al_2O_3 in improving the contact of lithium and as a possible cubic stabilising agent. It has been known that Al within the LLTO system does help to form a cubic phase[195]. It has also been shown that Al doping will maintain a high conductivity at 1010^{-3} Scm^{-1} provided that the Al doping on the B -the site is kept to a minimum with the conduction value of activation energy of 0.28 eV is found with a meagre stoichiometric amount of aluminium[204].

The synthesis method is outlined in section 3.2.4 earlier but involves similar sol reaction with the addition of $Al(NO_3)_3.9H_2O$ as the aluminium source. With the sol pH kept around 6 during the condensation step and then the powder is annealed at 1100°C for 10 min in air.

The $Li_{0.45}La_{0.55}Ti_{0.9}Al_{0.1}O_3$ unit cell parameter was found to be a = 3.8697 Å[185] and also belonging to the 221 space group of *Pm-3mm*. The fitting was good after accounting for Teflon and stainless-steel holder peaks that were present to hold the powder when performing PXRD (Figure 3-21). In the fitting performed the synthesised material was indexed to have a unit cell parameter of a= 3.8770 (5) Å.

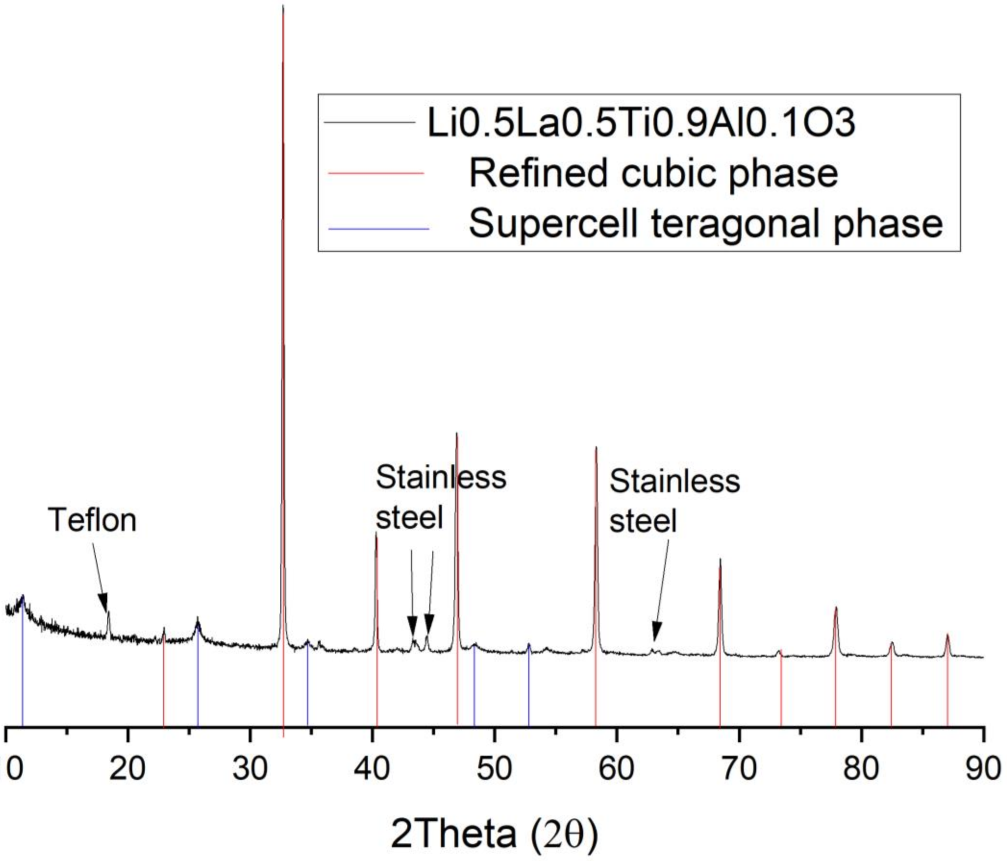

Figure 3-21: XRD pattern of $Li_{0.45}La_{0.55}Ti_{0.9}Al_{0.1}O_3$ *synthesis at 1100°C for 10 mins*

The pattern points to a cubic system, but as noted by D. Lakshmi *et al.*, peaks are forming that look like the tetragonal phases of $Li_{0.3}La_{0.56}TiO_3$ with properties[198] indicating that LLTAO will follow a similar double perovskite effect, labelled here as the super cell tetragonal phase . This pure phase will be used in a chapter 5 to utilise a doped LLTO sol to provide a protective layer for moisture reactive surfaces.

3.4 Conclusion

The synthesis of $Li_{3x}La_{2/3-3x}TiO_3$ powder was possible using a citrate route in water without additional combustion or chelating agents. Throughout the whole range of pH of the sol precursors, it was possible to spot a $Li_{0.5}La_{0.5}TiO_3$ superstructure that reflects a cubic phase. The same synthesis method was also possible to form a cubic doped material of $Li_{0.5}La_{0.5}Ti_{0.9}Al_{0.1}O_3$.

With varying the pH of the sol from 4 to 10, it appeared as though the unit cell parameter of this cubic phase makes a parabola 3.92 (14) Å fluctuating from a high unit cell parameter when there are also tetragonal phases forming in the pH 4 sol, to a lower unit cell parameter of 3.86 (3) Å at a pH of 8.

Despite the benefit of using a ball mill to reduce the magnitude of the particle size by a factor of 10, it was observed in the 1350^{o}C for 6 hr $Li_{0.5}La_{0.5}TiO_3$ material that 98 % dense pellets are formed using hand-milled particle sizes, so the extra step is not necessary.

The material of the mixed phase and performing EIS analysis see the single expected arc with the two processes containing the grain boundary diffusion and the bulk performance. There is a higher activation energy of 0.4 eV and a lower ionic conduction value in the x10^{-4} S cm^{-1} following the expected conduction trends of other reported LLTO materials. A possible explanation for the difference in the activation energy is that the lithium prefers to travel through the La-rich layers of LLTO when there is a mixed phase reducing the mobility of lithium through the electrolyte.

It was also shown that it is possible to synthesise a cubic $Li_{0.45}La_{0.55}Ti_{0.9}Al_{0.1}O_3$ at 1100°C for 10 minutes material a lower temperature than the cubic LLTO material.

The various LLTO pellets synthesised using this sol gel method will then be subjected to lithium wetting experiments. Allowing for information of the intrinsic wetting of lithium on these surfaces to be investigated.

Chapter 4 Surface and interfacial analysis of molten lithium on solid oxide electrolytes

4.1 Introduction

In this chapter the solid oxide-electrolytes of LLTO and LLZO were tested for their suitability of being used in a lithium metal solid-state battery. The experiments performed used different LLTO synthesised by sol-gel method as noted in Chapter 3 and LLZO and doped LLZO pellets and tape casted material provided by Dr Mihkel Vestli in his work with SOLBAT and clarifying his patent synthesis route for the tape casted material. In this chapter the contact angles from melted lithium, gallium, tin, silver, and gold on both LLTO and LLZO electrolytes were observed and placed into the wetting calculations seen in chapter 2.13. These experiments and analysis were performed to suggest the best form of interface alteration requited to optimise the interface of solid -oxide batteries.

Metallic lithium is wetted by organic electrolytes in conventional LIB batteries very well and lithophilic to graphite electrodes[205]. Lithium, however, exhibits poor contact with most solid electrolyte contenders due to the metal's surface tension. It limits the number of possible electron transfers across the negative electrode-electrolyte interface, decreasing the batteries' feasible energy and power density. Void formation occurs at the interface over LIBS lifetime due to the inhomogeneous movement of lithium ions on charge and discharge [45].

It is clear then that to optimise the interface; it is necessary to improve the contact of lithium to the surface of the solid electrolytes. A clear indication of good contact with a surface is to see if the molten of that metal wets the surface of that electrolyte in question well. For good wetting, a contact angle below 45º is observed. Poor wetting presents a contact angle between 45° and 90°; a non-wetting or no contact between the melt and electrolyte will observe contact angles above 90° (Figure 2-11). Therefore, contact angle measurements can be used to understand if the lithium will have good interfacial contact with the electrolyte[170,206].

In the current research, quantitative analysis from melts requires fluid contact angle reading devices (OCA – optical contact angles) to measure the surface energy of the oxide electrolytes at the interface. Surface energy thermodynamically is required to generate an area of a new surface. Like a voltage, it is only valuable for comparative senses as having a quantitative value for surface energy means nothing unless compared to other surfaces. Computational models provide surface energy results of solid surfaces with metals for lithium-ion batteries as an OCA temperature range is too low for the heat required to melt lithium and measures the contact angles generated by the melt[207]. Therefore, the measured surface energy of the electrolytes, when in contact with lithium, are estimations.

Researching the wettability of the solid oxide electrolyte material on the anode interface could lead to an improvement by being able to identify materials and or conditions that may optimise the spread of lithium at the interface. These experiments will also identify any intrinsic attraction of these solid electrolyte materials to the lithium metal.

For example, Yu Cui and his group looked at the effect of temperature, substrate surface and topography on the contact angle of lithium[170]. Their observations were performed in an Argon glovebox and observed the lowest contact angles at 215°C, around 15° for 34 nm coating of silver, 50 nm of aluminium and 48 nm coating of ZnO[170].

They also observed a negative correlation between the contact angle of lithium and the coating thickness of the additive to improve wettability[170]. At 215°C, stainless steel, titanium, molybdenum, nickel, lithium fluoride and carbon foil surfaces exhibited non-wetting behaviour with contact angles above 120°. Although increasing temperature achieved a reduction in the contact angle, this only resulted in poor wetting around 60°-70° at 350°C, and nickel even showed wetting behaviour at this temperature with a contact angle of approximately 30°.

Optimising the contact between Li and the SE will improve interfacial stability[45] and electron transfer, increasing capacity by having a more homogenous spread of the lithium and reducing the interfacial resistance.

The garnet LLZO was also chosen for these wetting experiments due to their widespread interest and promising stability to lithium metal when forming an interface. As noted, the material was provided by Dr Mihkel Vestli as he did work for various companies developing a scalable tape casted version of the LLZO material. This work would see LLZO doped with Nb and Al as a means to stabilise the promising cubic phase of the material.

The chapter aims to investigate the intrinsic wetting properties of lithium metal with LLTO and LLZO solid electrolytes. Using the estimated liquid tension of the melt as outlined in Equation 2.25 and Table 2.1, the observed contact angles of the melt surface energy equation can be calculated using Equation 2.26. Young-Dupre equations, Equation 2.21, with the known surface tension of the molten metal and the surface energy of the solid electrolyte under the molten metal, will provide the surface interface tension. The data collected from these equations can then be used to provide interface energy baselines for optimised interfaces in solid-state batteries and present which SSE (LLTO or LLZO) has the optimal physical contact with metallic lithium. Other molten metals of gallium, gold, silver and tin are also used on LLTO electrolyte pellet surfaces to help overcome impurity issues, which has not been done before in previous lithium wetting experiments[72,205,208]. Also, experiments on the work of adhesion can be calculated by using the shift in the radius of the molten metal, surface tension and the contact angle of the molten metal on the surface of the solid electrolyte in Equation 2.28. Performing these calculations with metals on porous materials will provide insight into the conditions that will aid lithium impregnation into a porous LLZO material[209]. This porous LLZO scaffold electrolyte, which is worked on by colleagues in the University of St Andrews such as Dr. Mihkel Vestli and Dr. Ioanna Pateli as patent process to be used with industries for full solid-state batteries.

4.2 Experimental methods and conditions

4.2.1 Wetting

The Canon EOS 600DDSLR camera was set to capture ten pictures every 5 minutes. Thus, the temperature can be altered to observe contact angle shifts for different temperature increments.

Poor fitting of the alumina tube in the tube furnace and the nature of the cold room caused discrepancies in the temperature that the sample experienced in the tube furnace. The correct temperatures are within a degree or two for the images put through image-J, therefore, the error compared to the contact angle measurements is negligible.

Lithium wetting of different surface was a standard temperature profile outline in Figure 4-1. The DSLR camera was set to three pictures every five minutes. Therefore, up to 170°C any image there was discarded, then heating the samples at 0.2°C per minute with the camera taking three pictures every five minutes to up to 210°C.

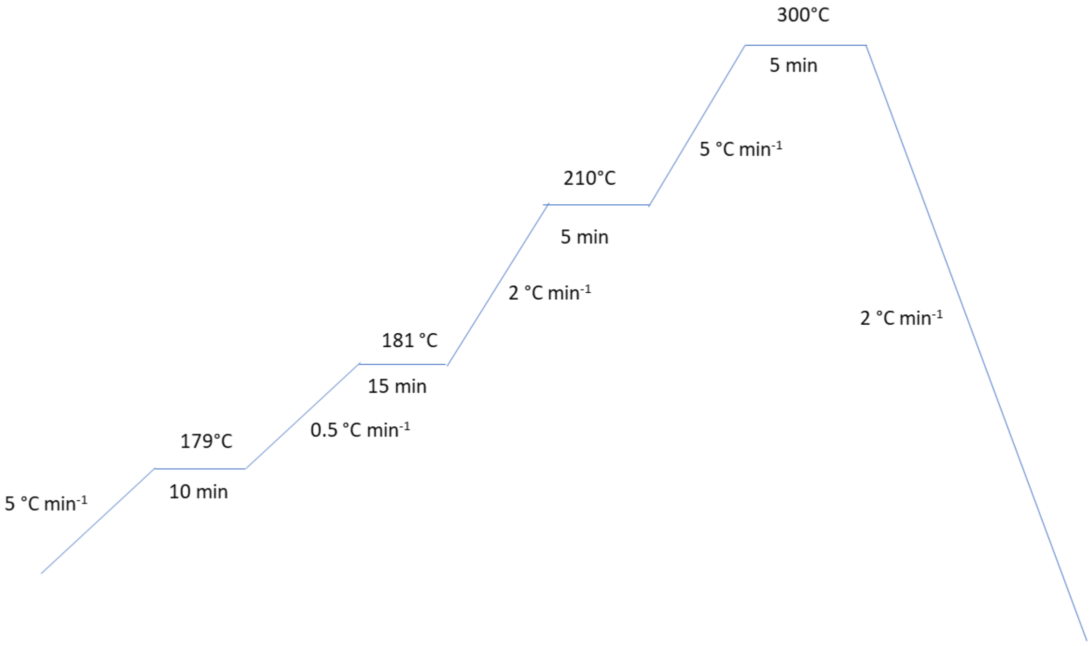

Figure 4-1: Heating rates for the tube furnace as the DSLR takes pictures of lithium melting a solid oxide electrolyte surface.

The surface properties of a solid electrolyte can be calculated by melting different metals on the surface utilising equations listed in chapter 2.13. Gallium was heated gradually from room temperature at 18°C to 50°C at two °C per minute, and around the melting point of 30°C, the heating ramp was 0.2°C per minute. Gallium also allows contact angle measurements outside the tube furnace on the desk at set temperatures using a hot plate or any other heating source.

In a similar manner listed in gold, tungsten, and silver were slowly heated to their melting temperatures while the DSLR camera took pictures every 5 minutes with slower rates of 0.1 °Cmin^{-1} used closer to each metals melting point. This was done to create a graph of surface tensions of the different metals against the surface energy change of LLTO. Providing information of the surface energy change over a temperature range and what surface tension subjected to the LLTO pellet will provide the best contact in the form of the lowest contact angle.

Al doped LLZO garnet material was provide by Dr. Mihkel Vestli after being supplied by Morgan material. And the Ta doped LLZO scaffold tape cast material was synthesised by Dr. Mihkel Vestli alongside his work the Faraday institution SOLBAT project.

Different LLTO and LLZO pellets were ‘polished’ before being placed into the wetting furnace. These pellets were polished by using resin to stick the pellets to a steel disk. It will then be manually moved in a figure of eight pattern over a diamond paste of 10 nm. Finally, it will then be attached to a stainless-steel holder using resin and then manually polished using a Metaserv 2000 grinder and polisher. Initially the pellets will be smoothed down by a P600 abrasive paper without waters (from Meta Prep) and then smoothed down using P1200 abrasive paper. For each level a ‘figure of eight’ motion was used to try and keep the pellet level and was polished for 2 minutes at each sandpaper level.

Plasma polishing treatment for some of the LLTO pellets was done using a Henniker HPT-100. The conditions that the pellets experienced were a 50% power source with argon gas for 5 minutes.

4.3 Results and discussion

4.3.1 Wetting lithium on solid oxide surfaces

Wetting experiments, although simple in methodology, are complicated in theory, with multiple parameters shifting the energy values of the materials significantly. As the temperature increases, the surface tension of lithium will be determined by using the equation mention in chapter 2.13 (Equation 2.25). Then excess enthalpy (H_s) is $0.491\ \mathrm{J\ m^{-2}}$, the melting temperature used (T_m) is (180ºC +273) $453\ K$ and the excess entropy ($\frac{d\gamma}{dT}$) value used is $-1.6 \times 10^{-4} J\ m^{-2}$ required (Equation 4.1).

$$Y_{sl(Li)} = 0.491\ \mathrm{J\ m^{-2}} + (T(K) - 453\ K)(-1.6 \times 10^{-4} J\ m^{-2})$$

Equation 4.1

Using the trendlines from the measured contact angles, the surface tension of lithium (Equation 4.1) and Equation 2.26, Equation 2.28 and Equation 2.21, multiple trendline graphs present the surface energy of the solid electrolyte, the work of adhesion between the lithium melt and the electrolyte, and the interface tension of the electrolyte with lithium. Using the example of lithium melting with a $Li_7La_3Zr_{1.4}Ta_{0.6}O_{12}$ pellet, provided by Morgan materials and processed to Purity by Dr. Mihkel Vestli, of 13mm in diameter and 2 mm in height (Figure 4-2), we can observe that a decreasing contact angle correlates to an increase in the surface energy of the solid electrolyte surface which leads to an increase the interface energy between the lithium and the electrolyte. However, the decrease in the work of adhesion required to remove the lithium from the surface indicates that there is very little adhesion occurring in the wetting of lithium on the solid electrolyte. The work of adhesion can sometimes appear as a curve but like the interface energy profile it is linear in these systems. Experimentally this is demonstrated as lithium falls off the surface of the solid electrolyte. External pressures of just 35 MPa allow for plastic deformation of lithium to help maintain lithium contact at the interface and improve the adhesion of lithium to this interface[210]. Without external physical factors, lithium appears to have no chemical bonding to the solid oxide electrolyte.

Determining the intrinsic wetting of lithium melt via contact angle measurement experiments was subject to error. Due to lighting issues creating silhouettes of the melt, difficulty determining distinctions between the boundaries and human error in the contact angle measuring. The mean of the contact angles was calculated to minimise human error. Backlighting improved the accuracy of measuring the contact angles while adding using the software's contrast .and finding edge options to help determine the interface.

Despite the reduced humidity of the dry room, lithium appeared darker in colour after some wetting experiments suggesting the possibility of lithium nitride forming on the surface. Water-catching material was added at one end of the tube to minimise water inside the melting tube. Adding small copper turnings as oxygen getters removes any residual moisture in the tubes.

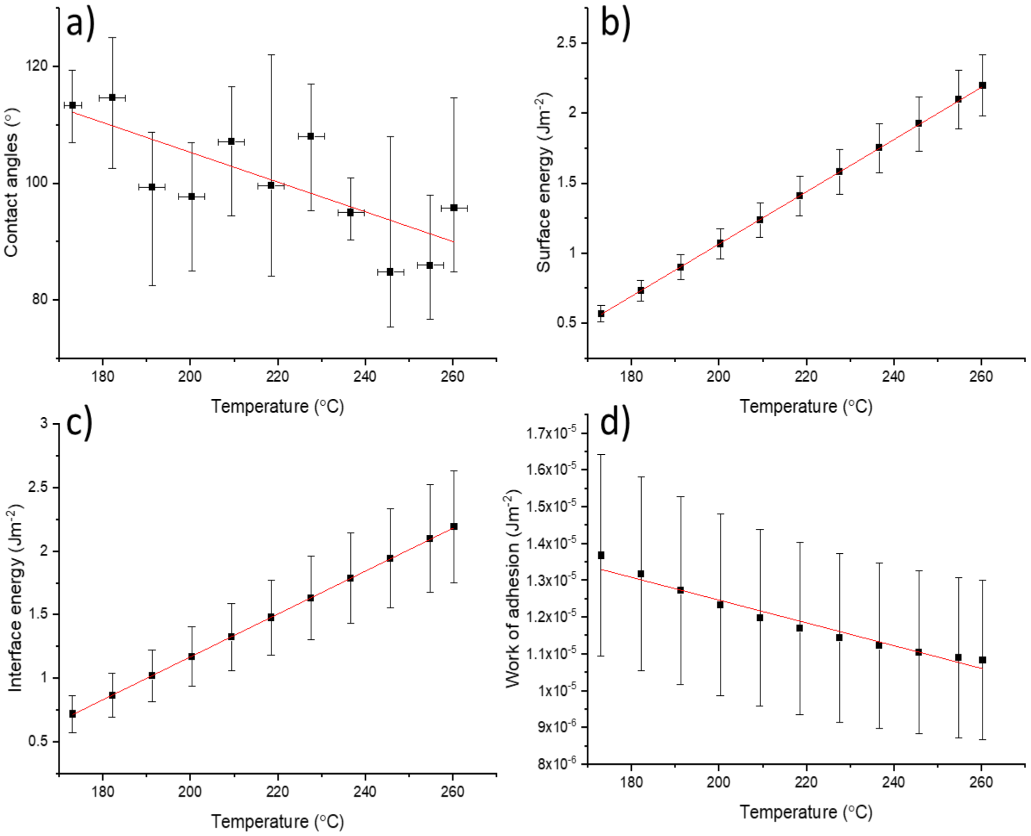

Figure 4-2:Lithium melting on the surface of $Li_7La_3Zr_{1.4}Ta_{0.6}O_{12}$ pellet a) the contact angles of lithium measured over temperature b) the surface energy of $Li_7La_3Zr_{1.4}Ta_{0.6}O_{12}$ against temperature c) the interface energy of lithium with of $Li_7La_3Zr_{1.4}Ta_{0.6}O_{12}$ against temperature and d) the work of adhesion to remove lithium from the surface of $Li_7La_3Zr_{1.4}Ta_{0.6}O_{12}$. With the maximum error bar being the highest contact angle and the minimum error bar being the lowest measured contact angle.

Pellet and tape casted LLZO garnets processed by Dr. Mihkel Vestli, for Morgan materials and different synthesis methods for the perovskite LLTO materials were used with different sintering temperatures to identify any alterations to the contact angles, the surface energy, and the work of adhesion of lithium to the solid electrolyte surface. Table 4.1 presents the trendlines generated by the contact angle measured of lithium melting over the temperature range 180°C to 300°C and the change of the radius of the lithium droplet as the temperature increases over the same temperature range is recorded in Table 4.2. The radius change equation is a linear trendline using the diameter of the lithium at the different temperatures between the range of 180°C to 300°C. The units of this equation are regarding the pixels so the ratio with each equation is dependent on the distance of the pellets from the camera. Knowing the distance of the pellet itself and then measuring the distance by the pixel ratios will then get the melt in mm.

Recorded are the sintering conditions and pH of the sol-gel precursors for some of the LLTO materials. Some pellets have the pressure applied by the uniaxial press to the material to form the pellet. It is recorded in tonnes (T) but, in practice, is tonnes per cm^2. However, all the pellets had their masses weighed at 0.25g and pressed in a 13 mm die.

The standard error of these trendlines is also provided and indicates that this experiment's quantitively values need a validation test with known surface energies to confirm if these energy interface values are misleading. The range of the contact angles at 180°C and 250°C on these trendlines highlight the expected range that LLTO and LLZO will intrinsically provide to lithium melt.

Table 4.1: The changing contact angle trendlines of lithium melt with their respective standard errors for multiple $Li_7La_3Zr_2O_{12}$ *(LLZO) and* $Li_{3x}La_{2/3-3x}TiO_3$ *(LLTO) electrolytes with different conditions. With the contact angle equation formed as a straight trendline through all the observed contact angles over the 180°C to 300°C temperature range.*

Material	**Conditions**	**Contact angle equation**	**The standard error for contact angle**	**Contact angle at 190°C (°)**
LLZO	1100°C 1hr air unpolished	CA = -0.1006*T+94.92	0.0577	76
Al doped LLZO	950°C 1hr air unpolished	CA = -0.0493*T+66.985		58
Al doped LLZO	1200°C 1hr air polished	CA=-0.1772*T+70.864	0.136	37
Al doped LLZO	1200°C 1hr air polished plasma	CA=-0.171*T+114.29	0.123	82
Al doped LLZO	950°C 1hr Argon unpolished	CA = -0.1651*T+75.875	0.0348	45
Al doped LLZO	950°C 1hr Argon Heat treatment unpolished	CA=-0.0139*T+77.758	0.103	75
Ta doped LLZO	tape casting	CA=-0.0811*T+38.113	0.0331	23
LLZO	1100°C 1hr air polished	CA=-0.2125*T+110	0.0623	70
LLZO	1100°C 1hr with heat treatment in air polished	CA=-0.3604*T+174.99	0.0623	107
LLZO	1100°C 1hr air covering polished	CA=-0.003*T+94.203	0.0638	94
Al doped LLZO	Al_2O_3 covering 1047°C 1hr air	CA=0.034*T+74.7514	0.0591	81
LLTO	1100°C 1hr PH10	CA = 0.4984*T-54.763	0.0440	40
LLTO	pH 8 950°C 1hr	CA =-0.1951*T+134.32	0.0839	97
LLTO	pH 5 3T 1200°C 1hr, polished	CA=-0.2127*T+104.27	0.0756	64
LLTO	pH 5 5T 1200°C 1hr, polished	CA=-0.0234*T+71.511	0.221	67
LLTO	pH6 1200°C 1hr	CA=-0.178*T+51.94	0.219	18
$Li_{0.27}La_{0.58}TiO_3$	solid state synthesis 1100°C 1hr	CA=-0.1038*T+145.32	0.108	126
$Li_{0.33}La_{0.56}TiO_3$	pH6 1100°C 1hr	CA=-0.1066*T+89.749	0.048	69
$Li_{0.5}La_{0.5}TiO_3$	pH 5 1200°C 2hr 5T, polished	CA=-0.021*T+68.687	0.280	65
LLTO	pH 5 5T 1200°C 2hr	CA=0.0248*T+46.711	0.214	51
LLTO	pH 5 5T 1200°C 1hr	CA=0.0255*T+79.783	0.077	85
LLTO	pH 5 1200°C 2hr 3T	CA=0.0752*T+29.759	0.0944	44

Table 4.2: The trendlines of the change of the lithium droplet as lithium melts with temperature with the respective standard errors for multiple $Li_7La_3Zr_2O_{12}$ *(LLZO) and* $Li_{3x}La_{2/3-3x}TiO_3$ *(LLTO) electrolytes with different conditions. The radius change equation is a linear trendline using the diameter of the lithium at the different temperatures between the range of 180°C to 300°C.*

Material	**Conditions**	**radius change equation**	**The standard error for radius change**	**Diameter of lithium at 190°C (mm)**
LLZO	1100°C 1hr air unpolished	R = 1E-6*T+0.0018	2.52E-07	1.99
Al-LLZO	950°C 1hr air unpolished	R= 3E-6*T+0.0051		5.67
Al-LLZO	1200°C 1hr air polished	R=1E-6+0.002	3.17E-06	2.00
Al-LLZO	1200°C 1hr air polished plasma	R=7E-7*T+0.002	2.85E-07	2.13
Al-LLZO	950°C 1hr Argon unpolished	R=6E-6*T+0.0009	1.78E-07	2.04
Al-LLZO	950°C 1hr Argon Heat treatment unpolished	R=3E-08*T+2E-5	2.01E-09	0.03
Ta-LLZO	tape casting	R=3E-6*T+0.0025	1.11E-06	3.07
LLZO	1100°C 1hr air polished	R=-3E-7*T+0.002	1.06E-06	1.94
LLZO	1100°C 1hr with heat treatment in air polished	R=7E-6*T+0.0005	1.22E-6	1.83
LLZO	1100°C 1hr air covering polished	R=3E-06*T+0.0041	7.13E-7	4.67
Al-LLZO	Al_2O_3 covering 1047°C 1hr air	R=9E-6*T+0.00067	1.35E-6	2.38
LLTO	1100°C 1hr PH10	R =-4E-06*T+0.0027	2.20E-06	1.94
LLTO	pH 8 950°C 1hr	R=6E-07*T+0.0038	0.04	3.91
LLTO	pH 5 3T 1200°C 1hr, polished	R=4E-6*T+0.0006	2.39E-07	1.36
LLTO	pH 5 5T 1200°C 1hr, polished	R=1E-06*T+0.0011	4.74E-07	1.29
LLTO	pH6 1200°C 1hr	R=7E-6*T+0.0041	1.61E-06	5.43
$Li_{0.27}La_{0.58}TiO_3$	solid state synthesis 1100°C 1hr	R=9E-7*T+0.003	5.25E-7	3.17
$Li_{0.33}La_{0.56}TiO_3$	pH6 1100°C 1hr	R=4E-07*T+0.0008	9.18E-8	0.88
$Li_{0.5}La_{0.5}TiO_3$	pH 5 1200°C 2hr 5T, polished	R=2E-6*T+0.0017	2.91E-06	2.08
LLTO	pH 5 5T 1200°C 2hr	R=5E-07*T+0.0044	1.99E-06	4.50
LLTO	pH 5 5T 1200°C 1hr	R=4E-6*T+0.0022	8.6E-7	2.96
LLTO	pH 5 1200°C 2hr 3T	R=1E-6*T+0.0042	1.25E-06	4.39

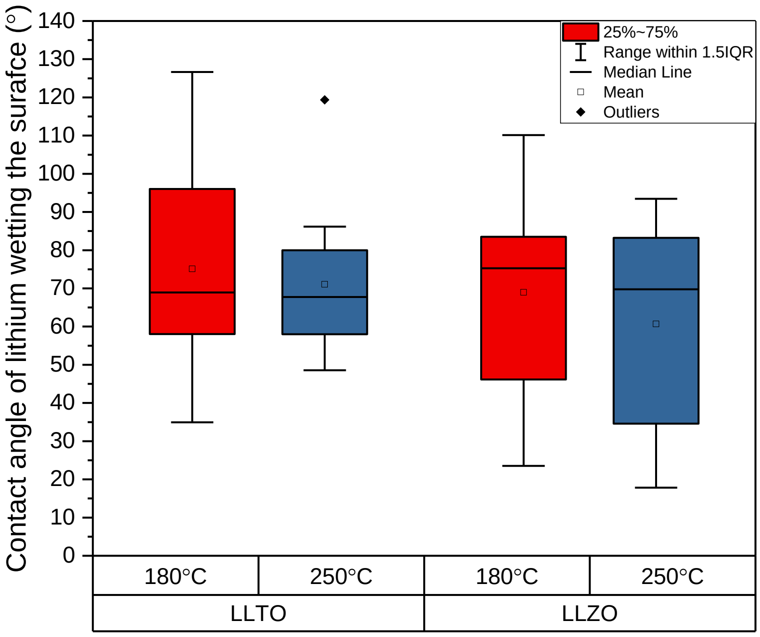

Figure 4-3: Contact angles of lithium melt on the surface of the $Li_{0.5}La_{0.5}TiO_3$ (LLTO) and $Li_7La_3Zr_2O_{12}$ (LLZO) at lithium melting temperature (180°C) and at 250°C derived from the trendline equations.

The lowest contact angle at 180°C for LLTO is 34° by the electrolyte synthesised via sol-gel and sintered at 1100°C for 1hr. The lowest contact angle for LLZO was 23° by tape cast Ta doped LLZO. The median contact angle for LLTO is approximately 67° while LLZO is approximately 74°, although LLZO has a lower mean value at 180°C of approximately 67° compared with LLTO has a mean contact angle closer to 75°. Therefore, at the melting point of lithium, the intrinsic behaviour of LLTO and LLZO with metallic lithium is poor wetting rather than non-wetting, with only a few exceptions in some of the synthesis procedures. Increasing the temperature decreases the median and mean contact angles for both LLTO and LLZO of lithium metal to the solid oxide electrolyte. For LLTO, the lowest contact angle was 34° with median and mean values around 68° and 71°, respectively. The outlier at this temperature belongs to the LLTO material synthesised by solid-state reactions which is not phase pure and contains multiple impurities. Also highlighting that impurities in solid oxide electrolytes will negatively affect the contact angle of lithium with these solid electrolytes. LLZO median has only decreased to 71°, with the mean lowered to 58°. Despite the comprehensive errors, these trendlines show that the promising solid oxide electrolytes are intrinsically poor wetting in their characteristics without doping, alloying or external pressure to help aid creep reactions that improve the adhesion and, therefore, the wettability of lithium.

Through this work, the surface energy of many of these solid electrolyte materials became negative. Furthermore, surface energy, stated earlier, is the reversible work required, in other words, the change in Gibbs free energy of the system at constant pressure and temperature, to generate an area of new surface[99,211]. Negative surface energy would imply that an area would form spontaneously, which is not possible if the surface energy is the only component in the system[211]. It would be expected that increasing the heat in their surroundings would minimise the amount of internal work needed by the material creating the surface area (LLTO in) and lower the surface energy. C. Rulison and others at KRUSS pointed out that in some examples, the change in surface energy is so tiny that the surface energy does not seem to change. For example, they showed that Chrome plated steel surface energy decreases from 42.16 mJ m^{-2} to 42.02 mJ^{-2} from 40°C to 160°C while aluminium foil changes from 45.31 mJ m^{-2} to 38.21 mJ m^{-2} in the same temperature range[212]. Granted, they used polar liquids to help make this clear distinction rather than metals.

However, if there is a multi-component system (such as solid electrolyte and molten lithium, the multi-component system in Figure 4-4) in which the chemical effects of each component will affect the Gibbs energy and, therefore, the surface energy of each other[211]. So, surface energy in multi-component systems will include the reversible work to generate a new surface and the chemical interactions between the newly formed surface and the other components[211,213,214]. The energy of adsorption, for example, is endothermic, which would make the surface energy negative if that absorbance reaction was more significant than the reversible work to generate a surface[211,213].

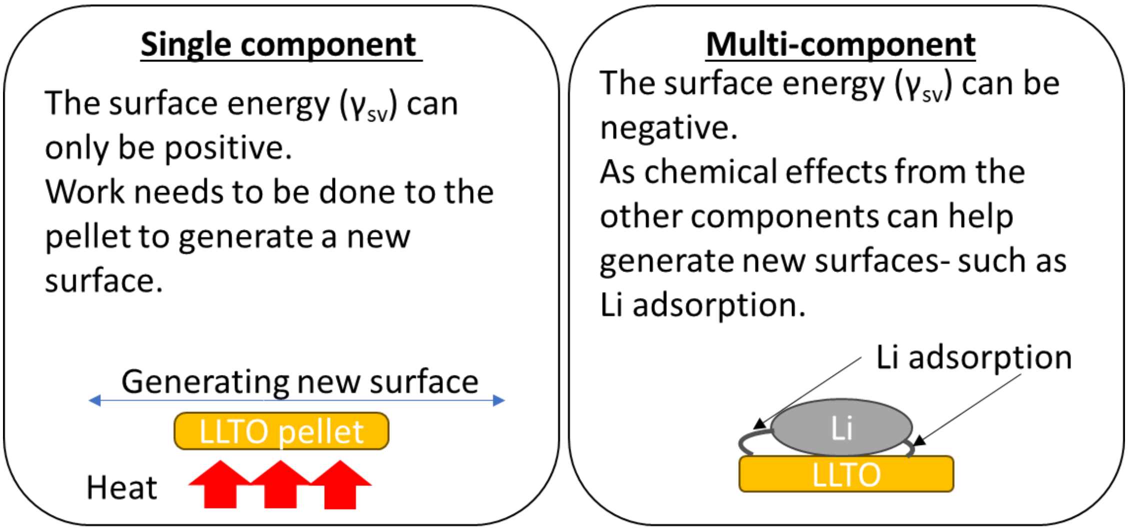

Single component

The surface energy (γ_{sv}) can only be positive.
Work needs to be done to the pellet to generate a new surface.

Multi-component

The surface energy (γ_{sv}) can be negative.
As chemical effects from the other components can help generate new surfaces- such as Li adsorption.

Figure 4-4: The two types of component systems that can occur during these wetting experiments. Single components, that behave like a single pelelt with positive surface energy. And multi-component systems that can have negative surface energy as a result of chemical interactiosn with the liquid metal.

Initially, in this section, the surface energy values were kept positive to treat the surface energy equation like a single-component system to make comparisons between LLTO and LLZO easier. However, lithium's effect on the new surfaces generated for the electrolytes may differ between the material and the sintering conditions. However, keeping it positive here would keep the analysis consistent between the surfaces of the different materials. For interfacial analysis, the multi-component analysis will be considered, allowing the energies to become negative as this will directly depend on the lithium interaction.

These contact angle values can then be substituted into Equation 2.26 to provide an overview of the surface energy value of LLTO and LLZO at 180°C and 250°C (Figure 4-5). The energy range of LLTO is 26 to 396 mJ m$^{-2,}$ and LLZO has an energy range of 16 to 443 mJ m^{-2} in the lithium melting range. The mean values at 180°C are 205 mJ m^{-2} for LLZO and 190 mJ m^{-2} for LLTO. The median values are around 160 mJ m^{-2} for LLZO and 180 mJ m^{-2} for LLTO. Increasing the temperature of lithium melting the surface by 70°C, the surface energy range of LLZO shifts to be between 126 mJ m^{-2} and 450 mJ m^{-2}. There is a corresponding shift in the mean to around 213 mJ m^{-2} and the median to around 162 mJ m^{-2}. With LLTO, a decrease in energy range (30 mJ m^{-2} to 311 mJ m^{-2}) is observed, with the median increasing to 193 mJ m^{-2} and the mean decreasing to 175 mJ m^{-2}.

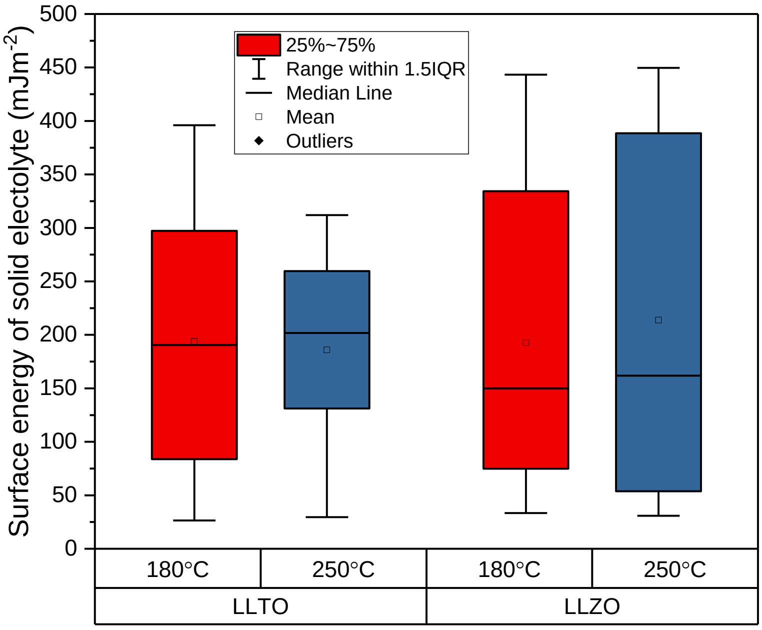

Figure 4-5: Surface energy values of $Li_{3x}La_{2/3-3x}TiO_3$ *(LLTO) and* $Li_7La_3Zr_2O_{12}$ *(LLZO) electrolytes at lithium melting temperature (180°C) and at 250°C derived from the trendline equations.*

Using these surface energy values, the work of adhesion required to remove lithium from the perovskite and the garnets can be calculated. The maximum energy to remove lithium from the surface is just under 0.1 mJ m^{-2} (Figure 4-6). Good work of adhesion, such as Fe bonding to FeO, is known to be around 2.5 Jm^{-2} [215], showing that thermodynamically lithium will not intrinsically adhere well to these surfaces without any surface modifications. The values obtained are far from suitable good wettability conditions; for example, Al wetting SiC has a work of adhesion of 416 mJ m^{-2} [216]. However, if none of the adhesion values are negative, then no active disbonding occurs between lithium and the solid oxide surface[215].

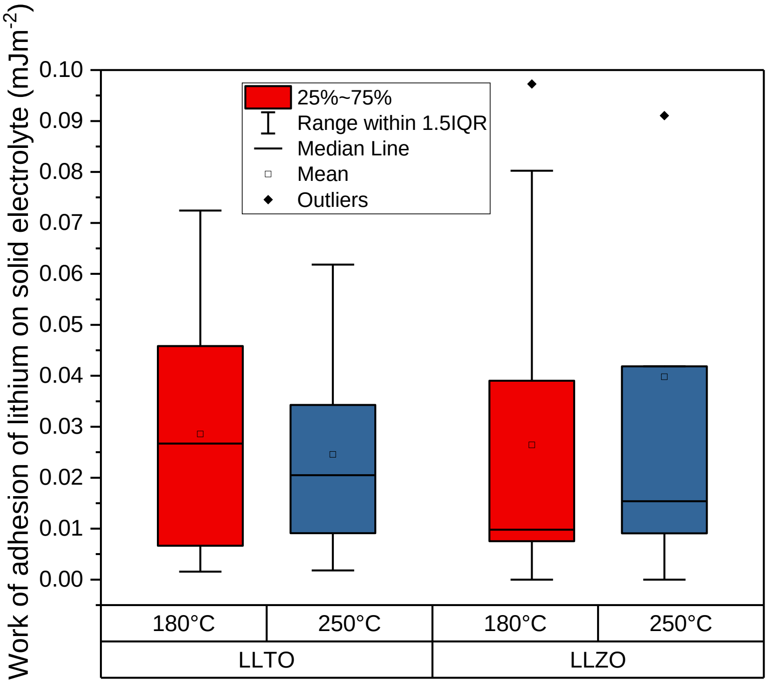

Figure 4-6: Work of adhesion of lithium to be removed from the surface of $Li_{0.5}La_{0.5}TiO_3$ (LLTO) and $Li_7La_3Zr_2O_{12}$ (LLZO) at 180°C and 250°C.

The median and mean values of LLTO are 0.0267mJ m^{-2} and 0.0285 mJ m^{-2}, respectively, at 180°C, decreasing to 0.0205 mJ m^{-2} and 0.0246 mJ m^{-2} at 250°C. The LLZO median and mean values increase from 0.00981 mJ m^{-2} and 0.0295 mJ m^{-2} at 180°C to 0.0154 mJ m^{-2} to 0.0398 mJ m^{-2} at 250°C. The outlier throughout is the tape-casted LLZO sample with a work of adhesion of 0.0973 mJ m^{-2} at 180°C and 0.181 mJ m^{-2} at 250°C. The other outlier at 250°C is 0.0911 mJ m^{-2} attributed to Al-LLZO unpolished with sintering,1 hour, at 950C in the air. The same conditions also provide the upper limit for the lithium melting at 180°C at 0.0802 mJ m^{-2}.

The tape-cast LLZO demonstrated the lowest contact angle at lithium melting, the highest surface energy, and the higher work of adhesion. It provides the most favourable conditions for a solid-state battery application. An explanation for these results could be a result of the higher number of pores on the surface permitting different wetting states to occur in

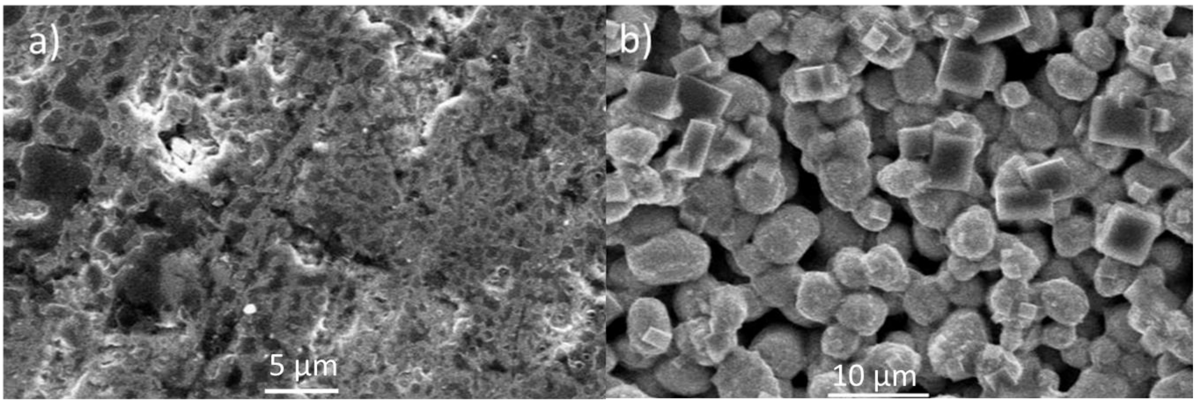

comparison to the other LLTO surfaces (Figure 4-7). It is worth noting here that the tape-cast LLZO high work of adhesion is the minimum amount of energy required to remove the lithium from its surface. Although some lithium-to-electrolyte interfaces will require energy, it is relatively easy for lithium to peel from all the surfaces. Therefore, the wetting of lithium on these interfaces is not the result of permanent physio-chemical interactions such as bonding alterations between the lithium atoms and solid electrolytes surface but rather an electron transfer. Thus additional creep effects, as noted by P. Bruce group [116] with sulphur electrolytes, mean that additional engineering factors must be applied to the interface to allow for proper adhering, improved wettability and thus lower interfacial resistance.

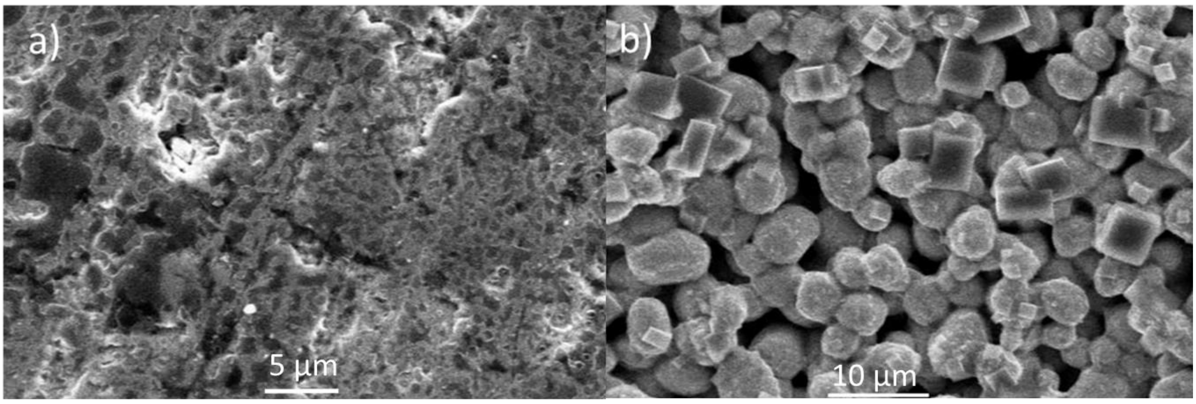

Figure 4-7: SEM images of a) the LLTO sintered at 1200°C for 2 hours at 5T, polished and b) LLZO tape-cast before being wetted by molten lithium.

4.3.2 Indirect measurement of surface energy interactions using other metals.

As mentioned earlier, using the absolute value for surface energy equations is necessary to determine the solid surface of the material as we treat those surfaces as single-component systems. However, there is intrinsically some chemical interaction with the molten metal, such as lithium adsorption, so the system at the interface needs to be treated as a multi-component system. To create a real surface energy equation for LLTO multiple metals will be needed as the generate a full range of surface tensions which will occur over a temperature range as the melting points of the metal's gallium, lithium, silver, and gold are different. It should be stated that the expected trend for surface tensions of the molten metals is to decrease with temperature.

But a baseline with this technique needs to be established so an alumina plate, which has a known surface energy of 169 mJ m^{-2} anodised at 298 K (25°C)[217] can be used. Typical surface energy values are quoted in mJ m^{-2} such as copper being 1360 mJ m^{-2} and polytetrafluoroethylene (PFTE) being 19.1 mJ m^{-2} [217]. A wetting experiment of melting gallium and lithium on an alumina plate will allow us to see how any surface impurities of Li_2O or Li_2CO_3 affect the wetting. Performing this experiment, and then assuming it is a single component system by making the surface energy values generated positive, will help show if the surface energy equations are close to the known surface energy values of Al_2O_3. Placing both surface energy trendlines without altering the sign of the values in mJ m^{-2} in a plot with the known surface energy value of Al_2O_3, we can see that this technique is an excellent approximation to finding the surface energy of wetting a material. The energy difference from the expected 169 mJ m^{-2} is 40 mJ m^{-2} for gallium (24% energy difference from the reported Alumina value) and 27 mJ m^{-2} for lithium (16% energy difference from the reported Alumina values). The apparent differences between gallium and lithium are that the surface energy of Al_2O_3 increases in temperature when in contact with gallium, and it decreases when in contact with lithium.

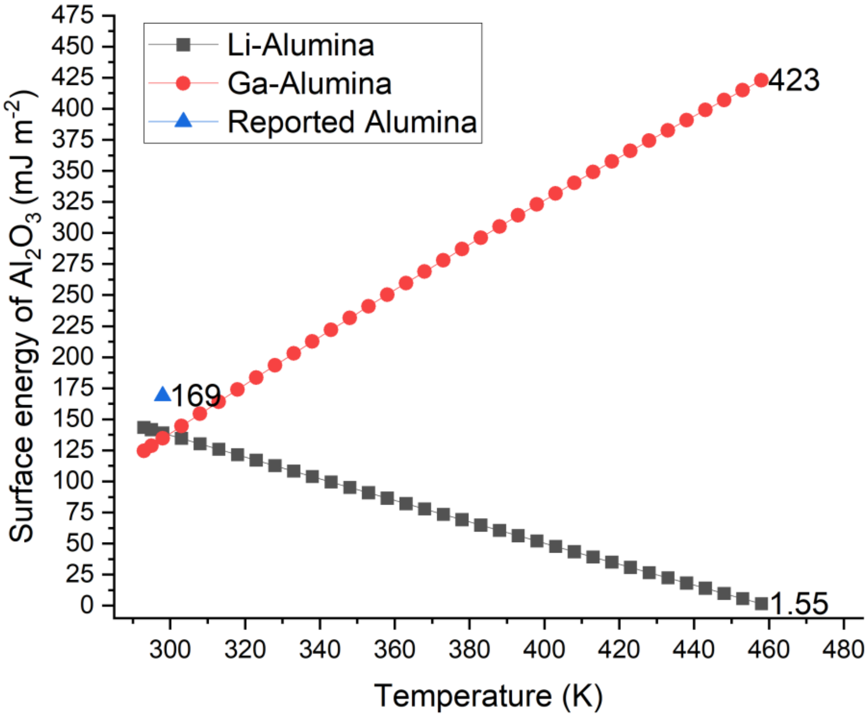

Figure 4-8: Surface energy calculated from the contact angle trendline equations of an Al_2O_3 *plate using lithium and gallium melting over a temperature range with the recorded* Al_2O_3 *value shown as 169 mJ* m^{-2} *at 298K (25°C).*

The gradient of lithium melt follows the expected surface tension trend as proven by the work of Lei Gan[218]. Who collated surface tensions of Al_2O_3 at different temperatures, reported by other researchers, over the last decade[218]. However, when calculating the expected contact angle using the surface energy of alumina using the gallium melt surface tension, there is a difference in the contact angle expected and the calculated contact angle (Table 4.3).

The difference in contact angle is significant and increases with temperature. A graph with altered surface energies can be constructed. In this figure the surface energy for the gallium and lithium melt are shifted to start at the known surface energy of Al_2O_3 (Figure 4-9:) as a way to show how the lithium interaction against Al_2O_3 influences the surface energy differently to what is expected of a single component system as listed out by Lei Gan[218]. But in fact, that there is an alloying effect observed as a colour change of the plate at higher temperature and bonding to the plate, leading to an increase in the surface energy and hinting at the effects of a multi-component system. Furthermore, incorporating the difference of gallium and lithium surface energies from the known Al_2O_3 surface energy (169 mJ m^{-2}) at room temperature allows for new trendlines to be generated with increasing temperature from that point.

Table 4.3: The back-calculation of the contact angle of lithium on an Al_2O_3 plate using the surface energy values of gallium wetting the Al_2O_3 plate with the difference between this calculated value and the observed contact angle.

Temperature (°C)	Surface energy from gallium's trendline (mJ m^{-2})	Contact angle from the back calculation of surface energy (°)	Contact angle from trendline (°)	The difference in contact angle (°)
30	146	73	107	34
50	183	68	105	36
150	364	41	94	53
160	382	37	93	55
170	400	33	92	58
180	418	29	90	62
190	436	23	89	66
200	454	17	88	72

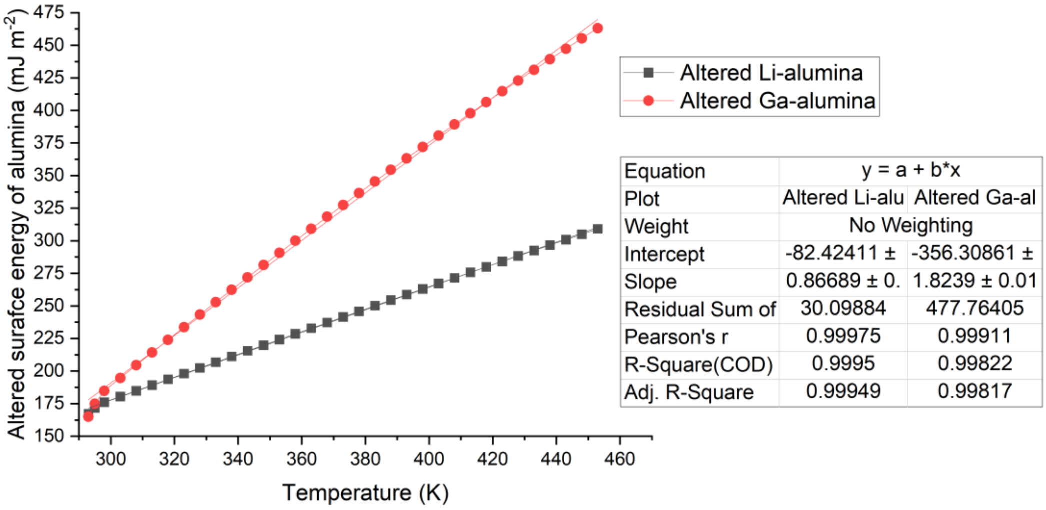

Equation	y = a + b*x	
Plot	Altered Li-alu	Altered Ga-al
Weight	No Weighting	
Intercept	-82.42411 ±	-356.30861 ±
Slope	0.86689 ± 0.	1.8239 ± 0.01
Residual Sum of	30.09884	477.76405
Pearson's r	0.99975	0.99911
R-Square(COD)	0.9995	0.99822
Adj. R-Square	0.99949	0.99817

Figure 4-10: Altered surface energy of Al_2O_3 using the contact angles of lithium and gallium melts and adding the reported alumina values at room temperature.

Because the gradient of the surface energy of the lithium interaction with Al_2O_3 is different by a magnitude of ten compared with the gallium interaction, this gradient deviation explains the difference in the chemical and physical bonding occurring between the lithium and gallium surfaces and Al_2O_3. There is evidence that having an absolute value of the surface energy around the melting might provide a rough estimation of the surface energy of the material then, and it shows that positive surface energy may be close to the actual values; it highlights that with increasing temperature different reactions are occurring with the lithium. Primarily when it is known that lithium alloys with Al_2O_3 well, these deviations from the contact angle and the surface energy gradient may indicate either wetting states occurring, alloying or different levels of adsorption.

This variation in the expected contact angles from Table 4.3 and the reported variation in expected surface area from both the gallium and lithium trendline can give us the Gibbs free energy of the wetting of lithium. Using Equation 2.23 and lithium's negative surface energy values, as the sign of these values is essential to Gibbs free reaction, and the reported values in Table 4.3, a correlation between temperature and the reaction Gibbs energy was plotted. The reaction profile of the reaction Gibbs of lithium wetting because of Al_2O_3 alloying is -463 kJ m^{-2} at 200°C.

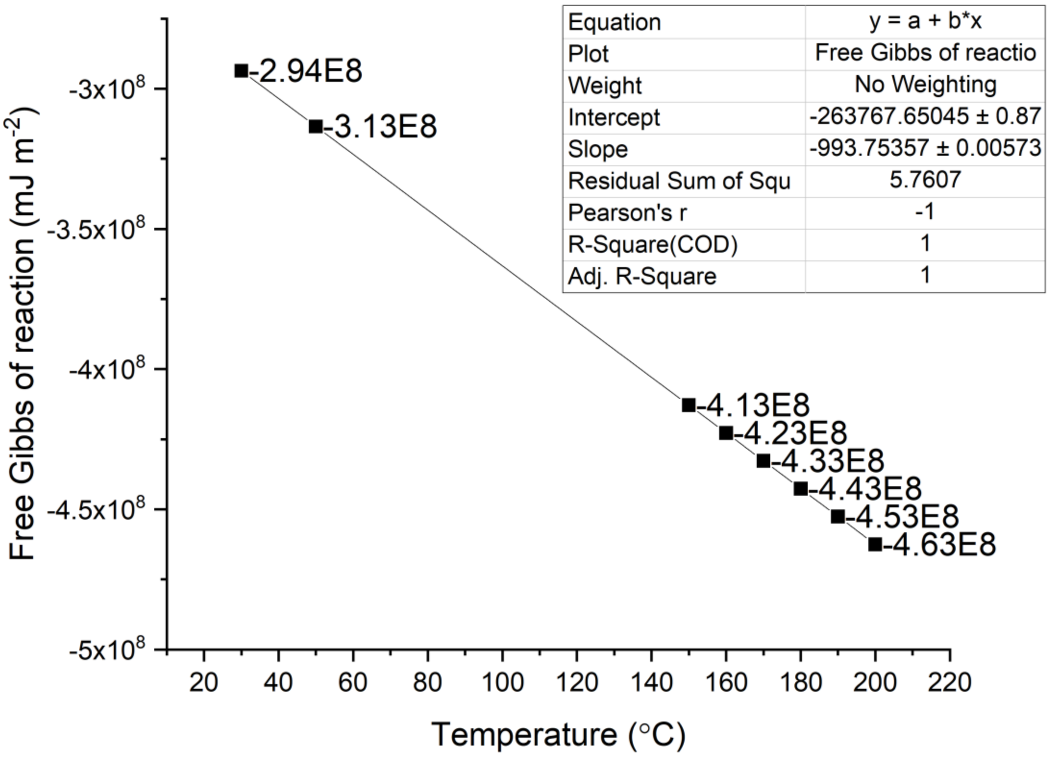

Figure 4-11: The free energy of the reaction of lithium wetting the surface of an Al_2O_3 plate against temperature. Using gallium as the unreacted surface energy and interface energy, the free reaction Gibbs is the reaction wetting of lithium with potential alloying and secondary phases forming.

Additionally, to confirm if presenting the surface energy concerning contact angles against temperature is a viable, appropriate way of accurately calculating the surface energy, the Zisman method[219] can be utilised. This method involves using different surface tensions on the same solid surface and then by calculating the surface energy of the solid surface using the surface energy equation as presented in chapter 2.13 (Equation 2.26) a new trendline can be collected Figure 4-12. This new trendline, can allow for a back calculation to see the surface energy at absolute zero[219]. Therefore, using the surface tensions of gold, silver, gallium and lithium (calculated using Equation 2.25 and values from Table 2.1) on a $Li_{0.3}La_{0.567}TiO_3$ tetragonal surface pellet, the surface energy can be calculated in Jm^{-2} (Figure 4-12).

The surface energy trendline generated suggests that the surface energy of $Li_{0.3}La_{0.56}TiO_3$ is around 8 Jm^{-2} at 0K, implementing the third law of thermodynamics. This value is roughly off by a factor of 1 Jm^{-2} compared to the highest surface energy observed from contact angle calculations of lithium melting, which is the LLTO synthesised at 1000°C for 1 hr in a sol precursor of pH 10. And in this figure, we can compare it to another $Li_{0.5}La_{0.5}TiO_2$ species which appears as an orange line in Figure 4-12. Here at absolute zero the difference for the surface energy is 1.33 J m^{-2}. The gradient is the same for the observed surface energy of the LLTO material with just lithium on the surface.

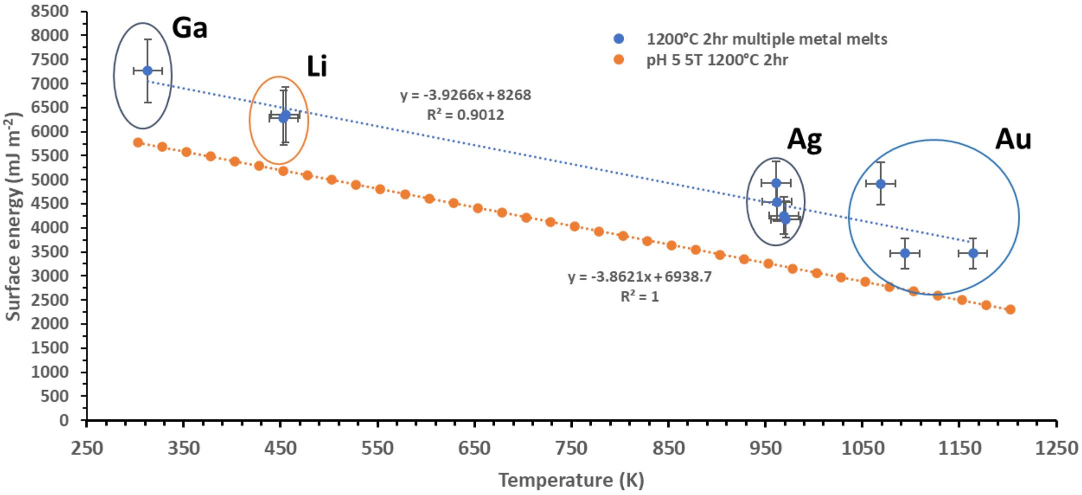

Figure 4-12:The Zisman method using the surface tensions and contact angles observed of melting gallium, lithium, silver and gold on $Li_{0.3}La_{0.56}TiO_3$ pellet synthesised 1200°C 2hr, in air, to back-calculate the surface energy in Jm^{-2}.

4.3.3 Surface and interface energies using the negative multi-component values for garnet materials.

Taking the absolute value at the surface energy trendline plots is necessary for calculating the surface energy of a solid surface independent of whatever the melt used. However, to consider the interface reaction of lithium with the solid surfaces, the sign of the resulting surface energy needs to be considered, resulting in negative surface (Figure 4-13) and interface energy values. But, as discussed earlier this is a result of it being a multi-component system with various chemical interactions such as adsorption of lithium resulting in possible negative values for the interface energy.

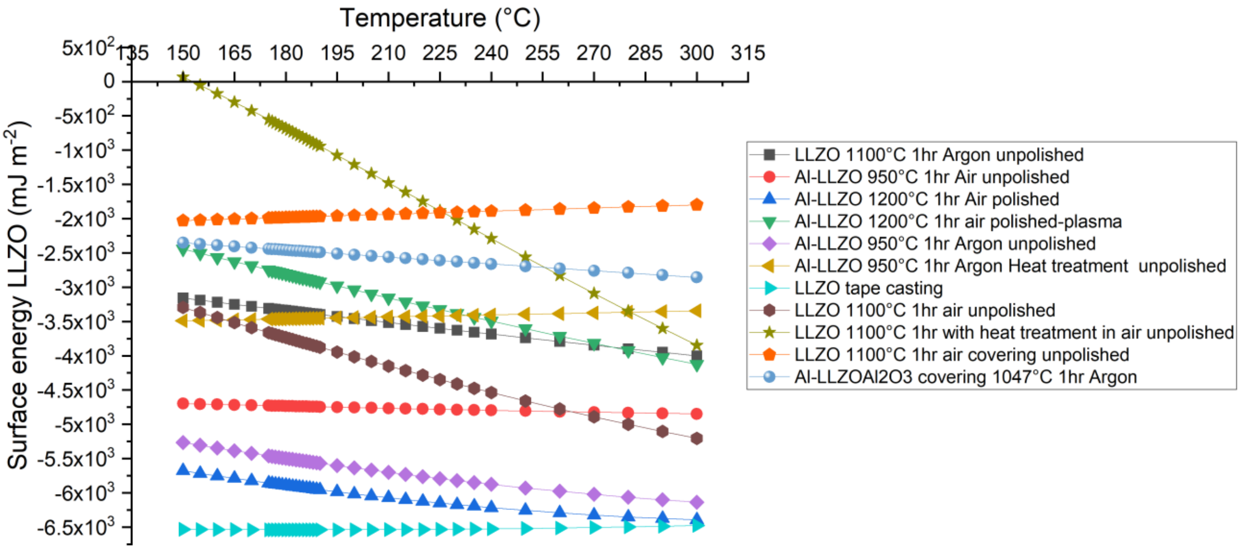

Figure 4-13: The surface energy of $Li_7La_3Zr_2O_{12}$ (LLZO) with their sintering conditions using the trendlines from the observed contact angles over the melting temperature range. The energy of the materials is in mJ m^{-2}.

Thus, many of the observations and discussion made when surface energy is positive, considered back in section 4.3.1 remains the same, but their relative position has changed. For example, the largest surface and only positive surface energy are now the LLZO sintered at 1100°C for 1hr in the air with heat treatment. Furthermore, the lowest energy is now LLZO synthesised via tape casting to make a more porous surface. With most of the sintering conditions resulting in negative values, it hints that lithium provides a non-zero excess component to the change in Gibbs energy in creating a new surface area[211]. Physically this means that lithium interacts with the solid surface implying that the surfaces are not only performing their reversible work to create a new surface area but that the surfaces are either alloying, mass diffusion or an electrochemical reaction.

To help highlight the relative contact angles of the lithium melting with the surface energies, Figure 4-14 shows the highest, median, and lowest surface energy of the LLZO materials with their corresponding contact angles.

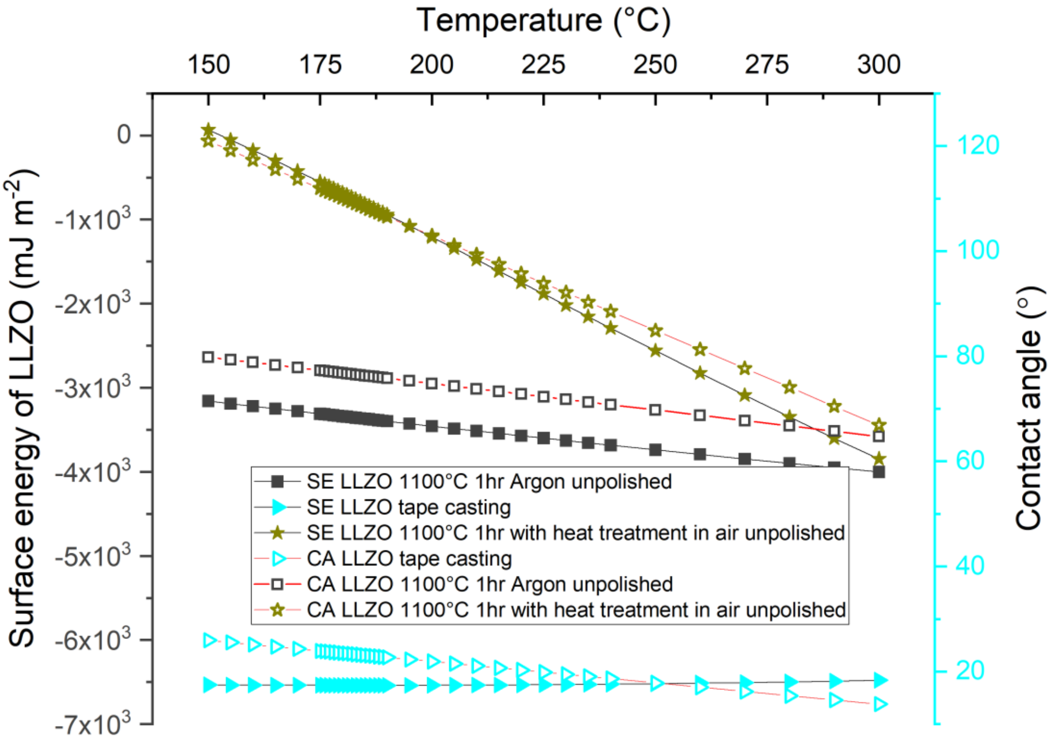

Figure 4-15: The largest, median, and lowest surface energy (SE) of the collected LLZO samples with their respective contact angles (CA) of lithium wetting the surfaces. The highest energy is LLZO 1100°C 1hr with heat treatment in air unpolished, the median is LLZO 1100°C 1hr argon unpolished, and the lowest is LLZO tape casting.

All the lithium melting interactions with LLZO show that the contact angle of the lithium melting will decrease with an increase in temperature. The variation of the contact angle is a result of number of interactions occurring which in turn will affect the surface energy such as different rates of surface impurities forming. The garnet LLZO 1 hr sintered in air at 1100°C will most likely have the highest $LiCO_3$ and LiOH impurities as observed in Raman data seen later when comparing LLZO with LLTO (Figure 5-1) and thus demonstrates a wetting contact angle of around 120°; non-wetting. LLZO sintered in argon for 1100C for 1hr in argon is the same starting composition of the pellet but with no heat treatment and kept with minimum air exposure. With surface contaminants at a minimum, the lithium interaction is unfavourable as the contact angle is 90°, the definition of non-wetting. Thus, as argon sintering is the difference, surface impurities of LLZO material increase the overall surface energy implying that the LLZO surface is doing more work in creating the surface impurities than interacting with the lithium as evidenced by the non-wetting interaction of lithium observed. Nevertheless, even with the surface not performing surface reactions to react with the surface impurities, lithium interaction is poor, implying that there is no favourable Gibbs reaction for the adhesion and melting of lithium melt to the surface and that it is more energetically favourable for the LLZO material to work on generating a new surface.

For the tape cast material, a different situation appears to be occurring. Since the composition is the same, the engineering of the material to be more porous (is an attempt to hold lithium as an electrolyte for solid-state batteries; this may result in a partial wetting infiltration with an increase in surface energy. Typically, surface energy should decrease with temperature as the reversible work required to generate a new surface will decrease with increasing temperature as the movement of the grains increases and the surface reactions kinetics improve, meaning it is easier for the material to generate a surface. The material's porosity increase would mean that more work is required to mass-transport the material to its larger surface area and that it would want to densify the local grains. However, this should not increase surface energy. Thus, a different lithium interaction is occurring. Either lithium is infiltrating into the grain boundaries, implying that the surface reactions now need to work on moving lithium away from the surface, or the surface is actively adsorbing lithium.

The surface energy of the pellet is the most significant influencing factor on the interface energy Figure 4-16 between the garnet material and lithium wetting, reflecting the surface energy in terms of the relative placement of the energy values of the synthesis LLZO material. Tape-cast material presents the lowest interface energy.

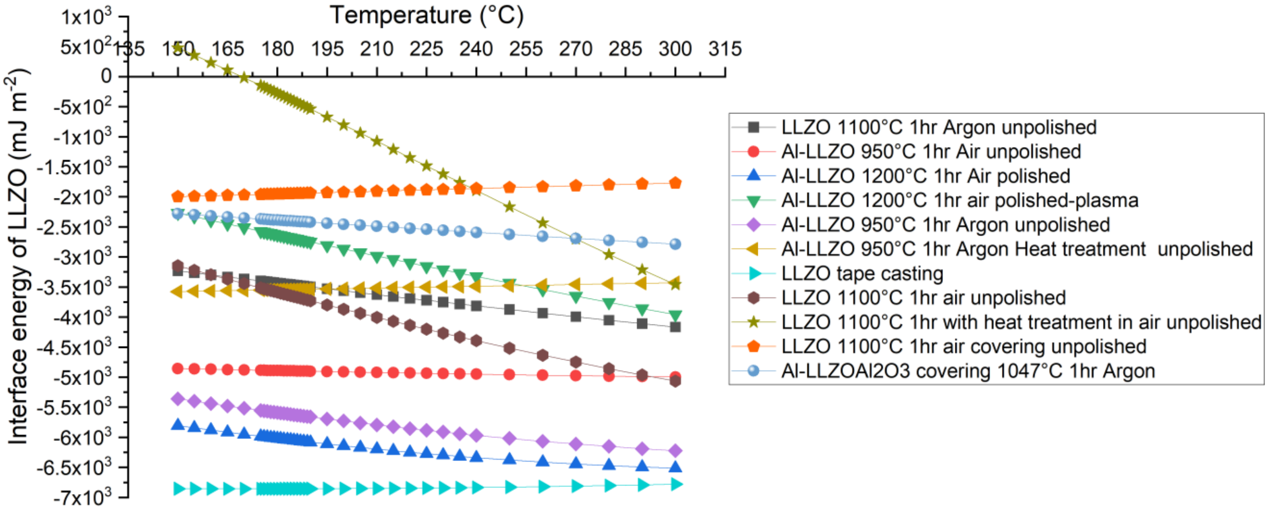

Figure 4-16: The interface energy in mJ m^{-2} of $Li_7La_3Zr_2O_{12}$ (LLZO), with their processing conditions and lithium melt. Absolute values of the surface energy are not considered.

Calculating the spreading parameters using Equation 2.22 for the temperature range without taking the magnitude means that all the spreading parameter values are below zero (Figure 4-17), indicating that lithium melt prefers an energetic state to be in a droplet, thus a non-wetting situation. Therefore, any good wetting interactions are not a result of lithium or the interface tension but different surface modifications.

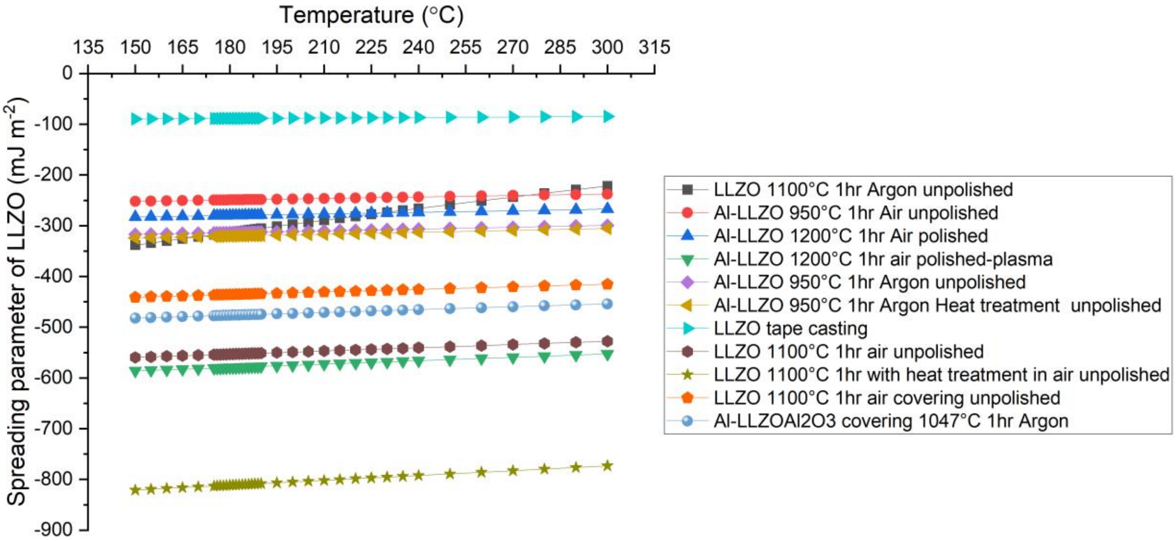

Figure 4-17: Spreading parameters of different synthesis conditions of garnet LLZO material concerning their melting with lithium.

It is also possible to use the variation of the interface energy of multiple LLZO materials and Equation 2.23 to highlight the change of Gibbs energy by using argon, plasma cleaning, heat treatment and covering to aid the interface (Figure 4-16). Each of the pellets contact angle and reaction free Gibbs energy used is summarised in to generate Figure 4-16.

Table 4.4 summarises the samples used to provide the reaction free gibs energy for each of the surface cleaning processes. The samples that provide the initial reaction free Gibbs energy and the samples that provide the reaction free Gibbs energy because of the surface process treatment needed for Equation 2.23 are from Figure 4-16.

Table 4.4: The surface process treatment performed on the LLZO pellets. With the sample used for the initial contact angles listed in the middle column. The sample used for the contact angle changed as a result of the surface process treatment is listed in the right column.

Surface process treatment	**Sample that provides initial reaction free Gibbs energy before surface process.**	**Sample that provides reaction free Gibbs energy because of the surface process.**
Argon sintering	Al-LLZO 950°C 1 hr air unpolished (red circle in Figure 4-16)	Al-LLZO 950°C 1 hr argon unpolished (purple diamonds in Figure 4-16)
Plasma cleaning	Al-LLZO 1200°C 1 hr air polished (blue triangles in Figure 4-16)	Al-LLZO 1200°C air 1 hr polished plasma (green triangles in Figure 4-16)
Air heat treatment	LLZO 1100°C 1 hr air unpolished (brown circle in Figure 4-16)	LLZO 1100°C 1hr with heat treatment in air unpolished (gold star in Figure 4-16)
Argon heat treatment	Al-LLZO 950°C 1 hr unpolished (pink diamond in Figure 4-16)	Al-LLZO 950°C 1 hr argon heat treatment unpolished (yellow triangle in Figure 4-16)
sacrificial covering material	LLZO 1100°C 1 hr air unpolished (brown circle in Figure 4-16)	LLZO 1100°C 1 hr air covering unpolished (orange hexagon in Figure 4-16)

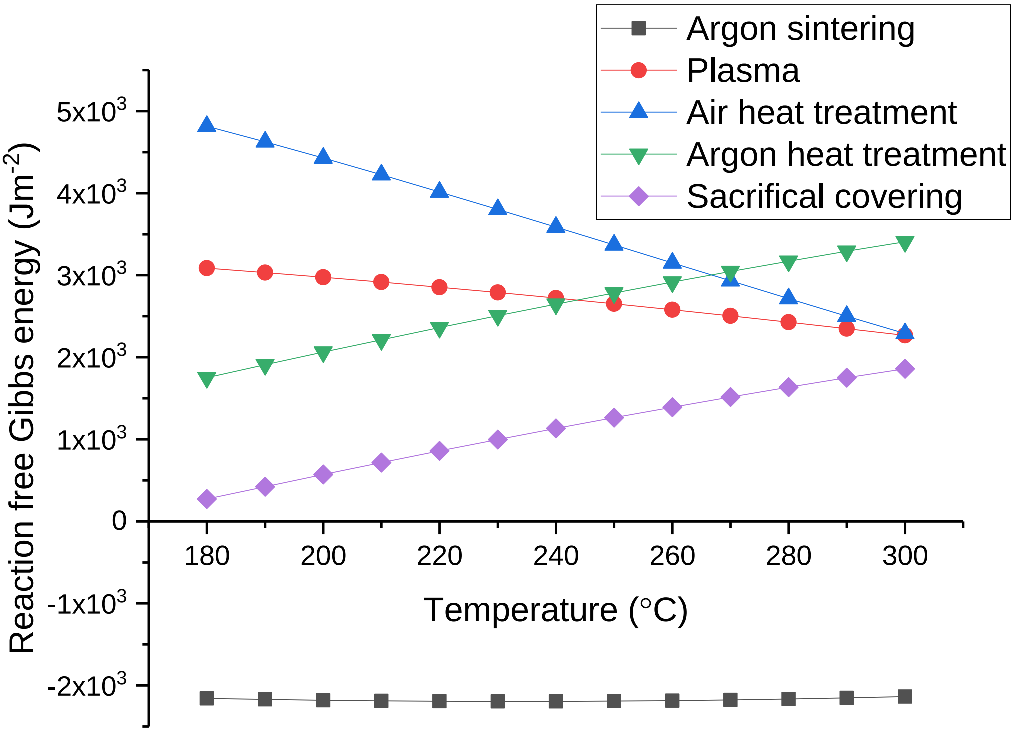

Figure 4-18: The change in reaction-free Gibbs energy of lithium melting wetting the LLZO surface after surface modifications on the surface: Argon sintering, plasma cleaning, heat treatment in air, heat treatment in argon and a sacrificial coating layer.

The change of Gibbs free energy of a reaction in argon sintering suggests that sintering LLZO material in an argon-rich environment will improve the surface's wettability. The increasing values confirm that reduced exposure to H_2O and CO_2 would lead to surface impurities and reduce the surface's wettability with these lithospheric materials. The other surface modification results are surprising and could result in a lack of variation in the interface tension after the surface modification occurred. Although the sacrificial covering and the argon heat treatment slopes suggest that the wettability of lithium can improve at lower temperatures below the melting point of lithium at 156°C and 50°C, respectively. However, this is unlikely to occur as lithium is not melted at these temperatures, so an entropy increase at lower temperatures means that sacrificial covering and argon heat treatment has little effect on the spontaneity of lithium wetting the surface. The temperatures of the lithium melt for plasma and air heat treatment, required to generate a negative Gibbs free energy, are 636°C and 419°C, respectively. Plasma treatment affected the grains by rounding their boundaries and improving pore entrances to the bulk material, as shown in the SEM image (Figure 4-19).

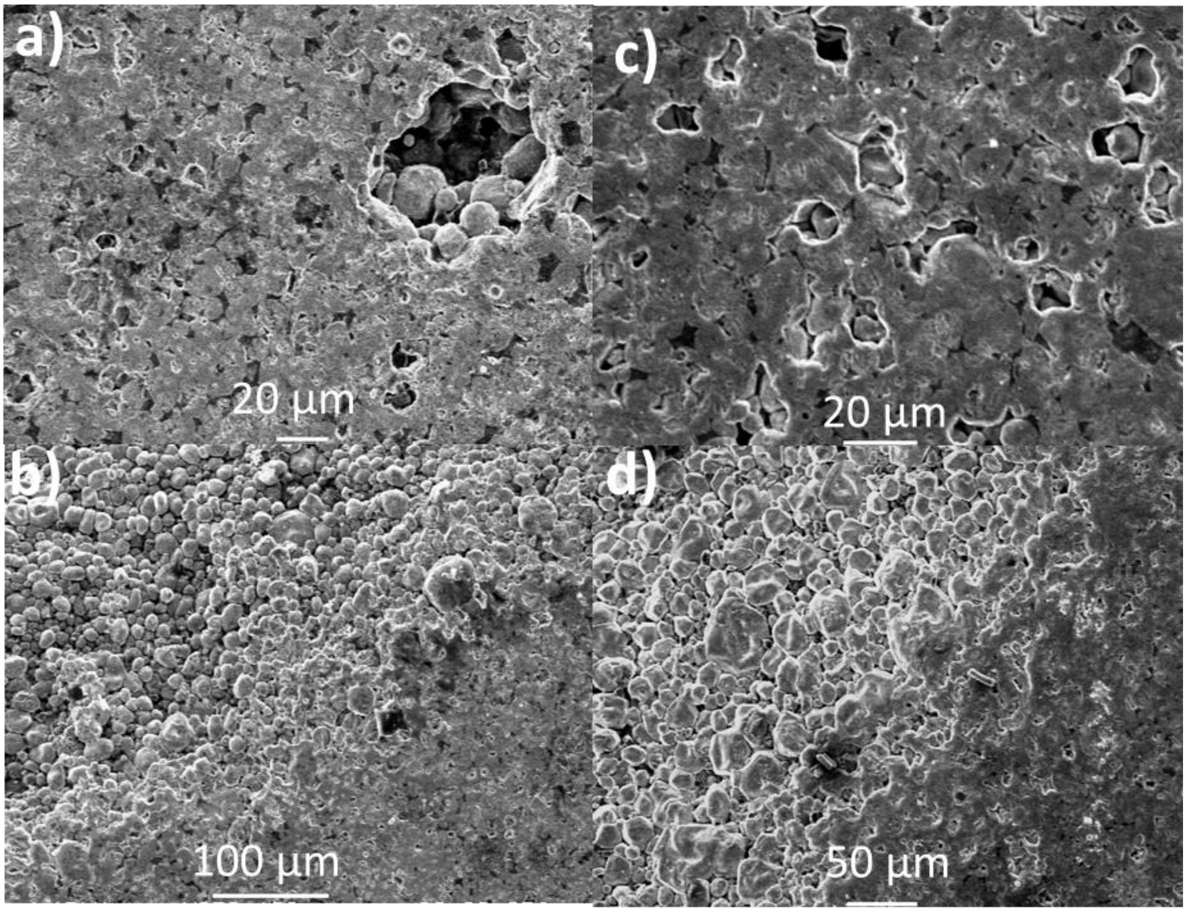

Figure 4-19: SEM of the surface of Al-LLZO pellet sintered at 1200°C for 1 hr in the air after polishing (a and b) and after argon plasma treatment (c and d).

It is also essential to consider the wetting state of lithium as it melts on the surface of these solid oxide electrolyte materials and whether these wetting states cause low energies of adhesion at the interface. There is the possibility of a few additional wetting states Wenzel, Cassie-Baxter, a hybrid impregnation Cassie-Baxter state or a capillary filling (Figure 2-12). They can be calculated using Equation 2.29. For the LLZO materials, out of the 12 synthesis conditions, 6 are Cassie-Baxter states, 1 is a Wenzel state, and five are capillary filling as a Cassie-Baxter impregnating state (Table 4.5).

Table 4.5: The wetting parameters describing the wetting state that the different LLZO materials are experiencing during lithium melting.

Sintering condition	**Wetting parameter**	**Wetting state experienced**
1100°C, 1hr, air, unpolished,	0.232	Cassie-Baxter
1200°C, 1hr, air, polished	0.256	Cassie-Baxter
1200°C, 1hr, air polished plasma	0.027	Cassie-Baxter
950°C, 1hr, argon, unpolished	0.243	Cassie-Baxter
1100°C, 1hr, air	0.011	Cassie-Baxter
Al_2O_3 covering, 1047°C, 1hr	0.269	Cassie-Baxter
1100°C 1hr air covering	0.456	Wenzel
950°C 1hr unpolished	0.583	Capillary filling
950°C, 1hr Argon, Heat treatment, unpolished	0.573	Capillary filling
tape casting	0.748	Capillary filling
1100°C, 1hr, with heat treatment in air	0.529	Capillary filling
950°C, 1hr, air, unpolished	0.573	Capillary filling

The Cassie-Baxter states suggest that higher temperatures have poor wetting infiltration, as observed by the SEM images shown in Figure 4-19: SEM of the surface of Al-LLZO pellet sintered at 1200°C for 1 hr in the air after polishing (a and b) and after argon plasma treatment (c and d). The relative density of the pellets can be very high. Therefore, very few pores are present and not large enough for lithium infiltration into the material. With the Cassie-Baxter wetting state occurring in half of the systems, this suggests the intrinsic thermodynamic state of bulk lithium when wetting this material.

As the interface tension increases in energy with an increase in temperature, it is more likely for the wetting state to be a capillary filling or a Cassie-Baxter impregnating state. All the interface energies that decrease energy with an increase in temperature have a Cassie-Baxter state.

The tape-casting garnet material had an optimal wetting state of a capillary filling and exhibited the lowest contact angle over the temperature range. In practice, when looking at the interface, it is still difficult for the lithium to melt within the pores themselves, which is likely due to a bulk issue of the melt. Difficulty with lithium infiltration shifts energy to the interface tension across the solid surface, resulting in a Wenzel state, limiting the electron transfer reactions occurring and reducing the contact area, allowing for an inhomogeneous spreading of lithium stripping and plating on cycling.

Lithium's high absorbance at the interface energy may be related to the liquid's bulk contribution influencing the liquid's overall liquid tension rather than the chemical and physical contributions of the solid. Surface forces of the LLZO material, such as a small Van der Waal force, favourability to create chemical bonding and alloying effects, shift the molten metal wettability lineally, an effect noted by M. Brada[220].

4.3.4 Surface and interface energies using the negative multi-component values for perovskite materials.

For simplicity and clarity, the LLTO pellets that were synthesised using a sol outside of the pH range of 5 to 8 were removed to create Figure 4-20, which investigated the surface energy generated from their respective contact angles as lithium melted on their surface and spread. The surface energy now drops into the negative energy region, except for the solid-state synthesis material, and with surface energy values being negative, this suggests that, at that temperature, there is no reversible work on creating a new surface area. Suggesting that the solid-state synthesis material was incomplete in its synthesis to make a pure phase. In the positive region lithium interface reaction, any shift in the contact angle was lithium contributing to the phase formation and generating of new surface energy and then shifted to lithium adsorption on the surface.

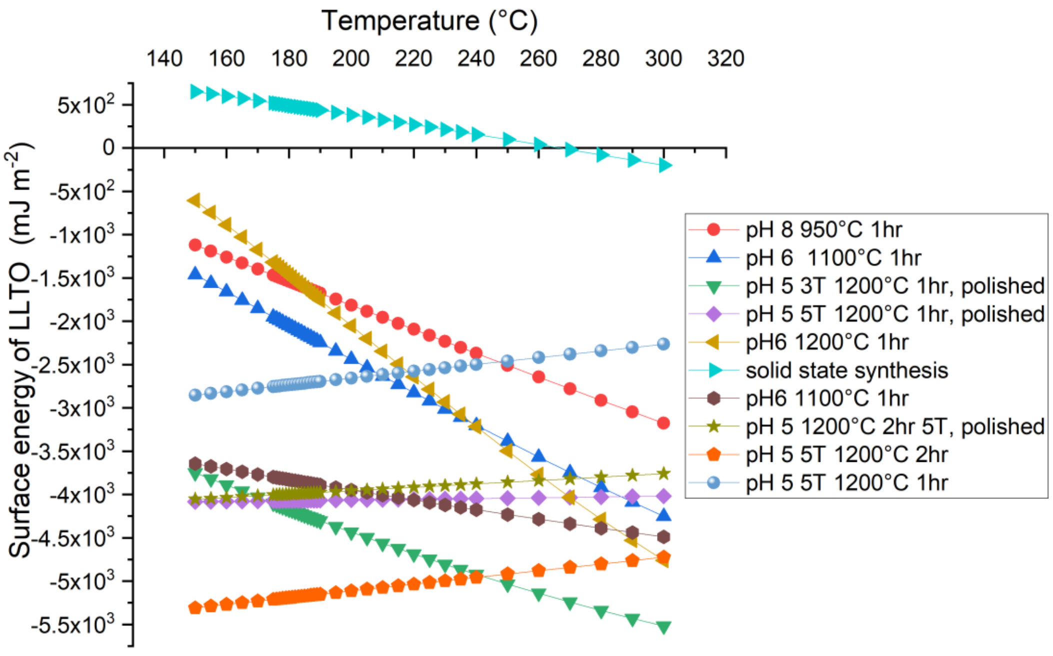

Figure 4-20: The surface energy of $Li_{0.5}La_{0.5}TiO_3$ materials in mJ m^{-2} using the contact angles as lithium melted on their surfaces.

For the perovskite materials, more conditions have a positive gradient with the increase in temperature. All the increased surface areas appeared to press with 5 Tonnes of pressure to create the pellets, synthesised using a precursor solution of pH 5 and sintered at 1200°C for at least one hour. There are two surface energy clusters at lithium melting point, one at around -1.25 Jm^{-2} by the pH 8 at 950°C for 1 hour and two precursor pH 6 materials, one sintered at 1100°C for 1 hour and the other at 1200°C for 1 hour. The second cluster of surface energies is around -3.6 mJ m^{-2} and -4.4 mJ $m^{-2,}$ with the highest LLTO materials around this point. This cluster contains much pH 5 precursor solutions materials, synthesised at 1200°C. The expected contact angles, excluding the solid-state synthesis material, demonstrate that the first cluster contact angles are in the non-wetting region above 90° as exhibited by pH 6 1200°C sintered for 1 hr in Figure 4-21. The second cluster includes the median, the pH 5 3 T 1200°C for 1hr polished, and the expected contact region is around 65°, thus exhibiting poor wetting. The lowest surface energy, pH 5 T 1200°C 2 hr (Figure 4-21), also exhibits poor wetting around 50°.

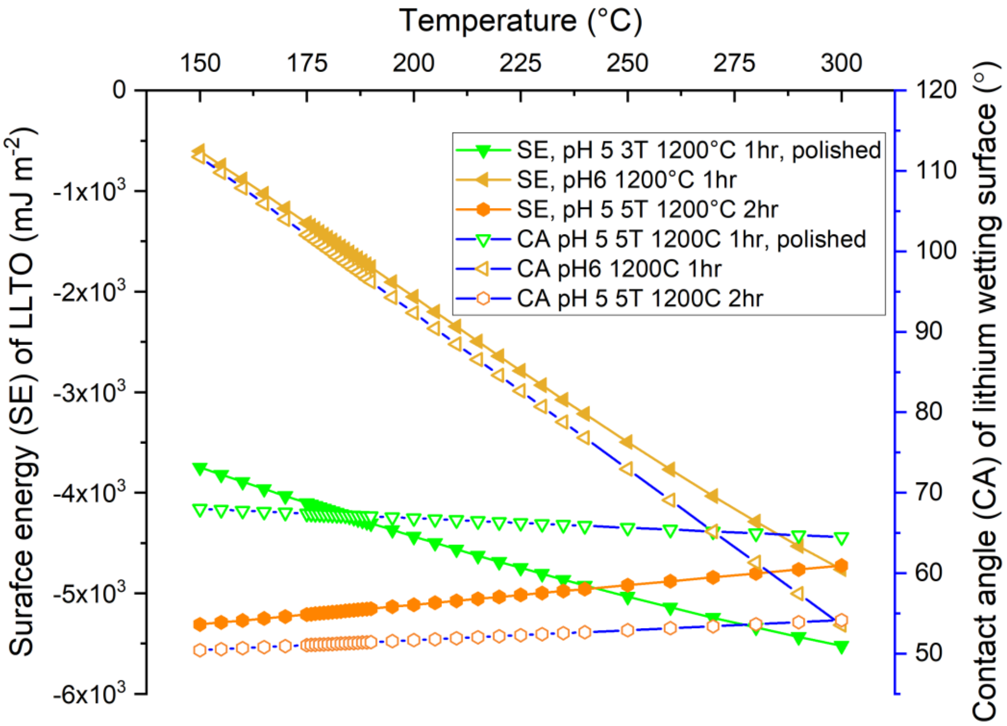

Figure 4-21: The largest, median, and lowest surface energy (SE) of the collected LLTO samples with their respective contact angles (CA) of lithium wetting the surfaces. The highest energy is LLTO pH 6 1200°C 1hr; the median is LLTO pH 5, 5T, 1200°C 1hr polished, and the lowest is LLTO pH 5, 5T, 1200°C 2 hr.

As with the LLZO material, the interface energy of lithium melting the surface of the perovskite material LLTO follows the surface energy values very closely (Figure 4-22). For simplicity, the solid-state synthesised material; is excluded from the interface graph. It indicates that poor wetting regions provide interface energy with higher absorbance of lithium on the surface. As previously noted by the LLZO section, the melt bulk's contributions distort the lithium's contact angle and provide poor interface tension due to its thermodynamic preference to be a sphere rather than spread out over the surface. The wetting parameter of all the synthesis conditions is negative (Figure 4-23). Most of the synthesised LLTO materials spreading parameters are between -440 and -450 (b) in Figure 4-23) with two synthesis conditions resulting in small spreading parameters, 1000°C sintered for 1hr with a precursor of pH 10 and LLTO sintered at 950°C for 1hr with a precursor solution of pH8 (a) in Figure 4-23).

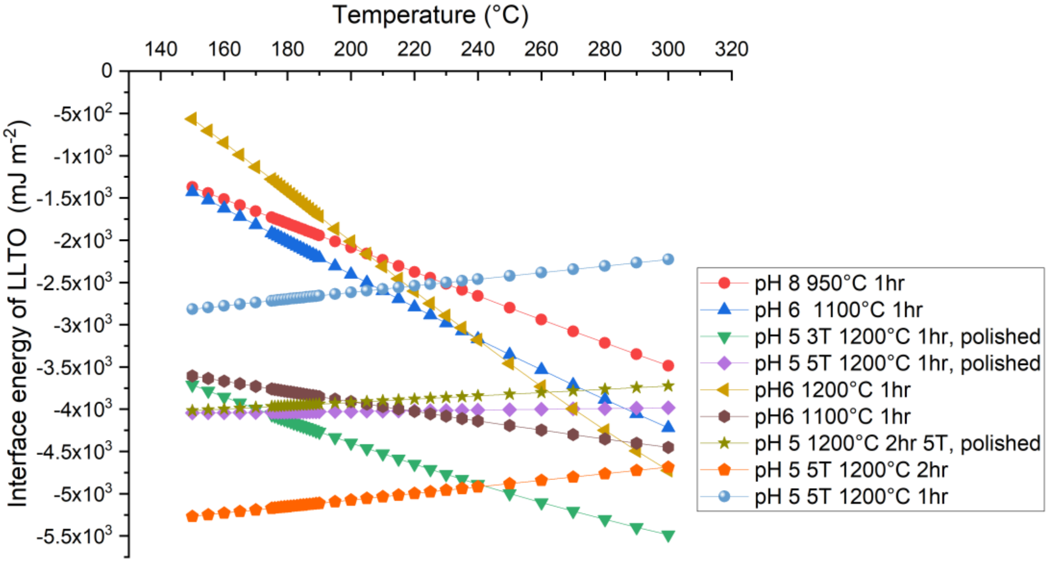

Figure 4-22: The interface energy, in J m^{-2}, of $Li_{3x}La_{2/3}TiO_3$ (LLTO), with their processing conditions and with lithium melt (not taking the absolute value of the surface energy).

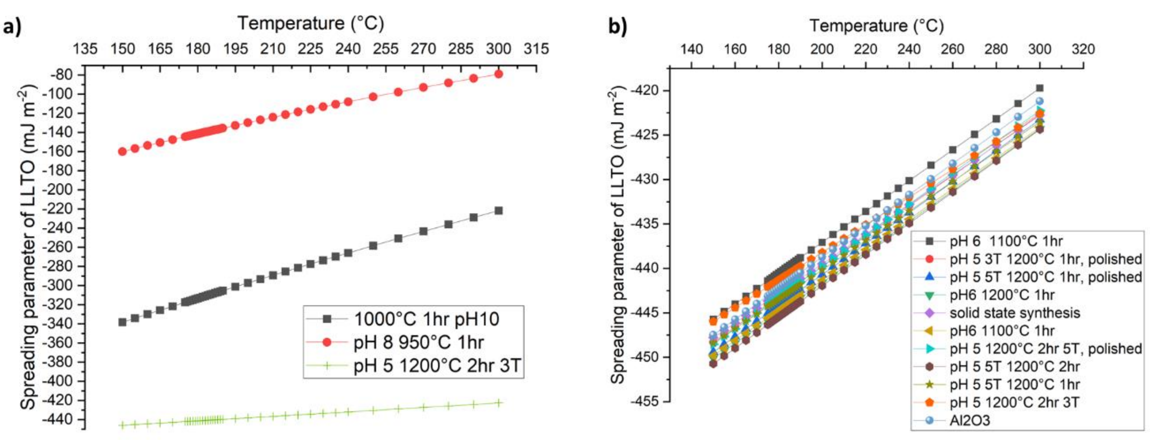

Figure 4-23: The spreading parameter of different synthesis conditions of the perovskite material LLTO. From a wider spread of the possible spreading parameters a) to the synthesis conditions that are similar in energy around -450 mJ m^{-2} b).

Utilising the same equation (Equation 2.23) to provide the reaction Gibbs energy similarly to the LLZO materials (Figure 4-24) and for the perovskite material. The different LLTO surfaces used as the initial reaction Gibbs free energy before the surface treatment process is applied and the surface used for the reaction Gibbs free energy for that surface process treatment are summarised in *Table 4.6*.

Table 4.6: The surface process treatment performed on the LLTO pellets. With the sample used for the initial contact angles listed in the middle column. The sample used for the contact angle changed as a result of the surface process treatment is listed in the right column.

Surface process treatment	**Sample that provides initial reaction free Gibbs energy before surface process.**	**Sample that provides reaction free Gibbs energy because of the surface process.**
Increase sintering temperature from 1100°C to 1200°C *(Sintering 1)*	pH 6, 1100°C, 1 hr, (blue triangle of Figure 4-20)	pH 6, 1200°C, 1hr (yellow triangle, Figure 4-20)
Increase sintering temperature from 1100°C to 1200°C *(Sintering 2)*	pH 6, 1100°C, 1 hr, (brown heptagon of Figure 4-20)	pH 6, 1200°C, 1hr (yellow triangle, Figure 4-20)
Increase sintering time from 1 hr to 2 hr (no polish)	unpolished pH 5 5T 1200°C 1hr (blue spheres of Figure 4-20)	unpolished pH 5 5T 1200°C 2hr (orange hexagon of Figure 4-20)
Increase sintering time from 1 hr to 2 hr (polish)	pH 5 5T 1200°C 1 hr polished (red circle in Figure 4-20)	pH 5 5T 1200°C 2 hr polished (blue triangle in Figure 4-20)
Polishing pellets after sintering for 1 hour	pH 5, 5T, 1200°C 1hr unpolished (blue sphere in Figure 4-20)	pH 5, 5T, 1200°C 1hr polished (pink square in Figure 4-20))
Polishing pellets after sintering for 2 hours	pH 5, 5T, 1200°C 2hr unpolished (orange heptagon in Figure 4-20)	pH 5, 5T, 1200°C 2hr polished (gold star in Figure 4-20)
Increasing the pressure exerted on the pellet	pH 5, 3T, 1200°C 1hr (green triangle in Figure 4-20)	pH5, 5T, 1200°C 1hr (pink square in Figure 4-20)

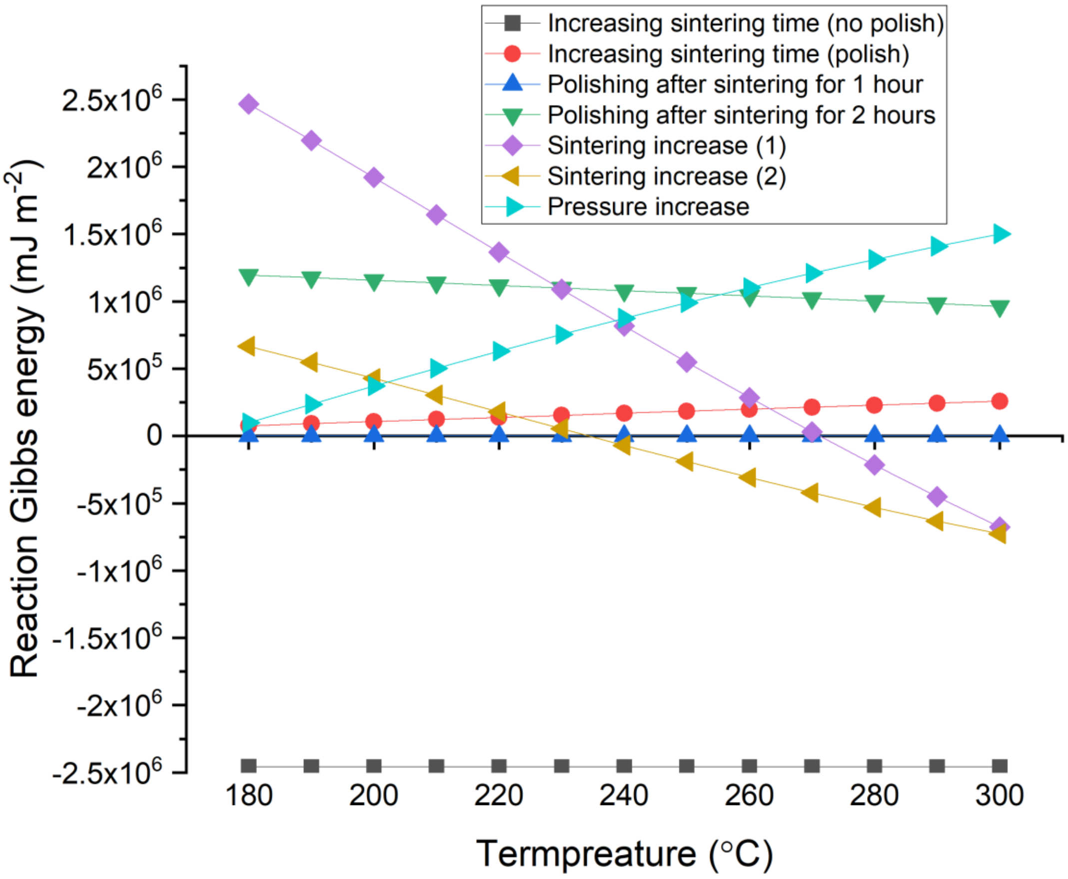

Figure 4-24: Gibbs of reaction of melting lithium on LLTO pellets due to different synthesis conditions to the solid electrolyte.

Increasing the sintering time without polishing presents a reaction Gibbs energy that is always negative, indicating that the extra time allowing densification and coursing of the grains allows for a better wetting interaction of lithium to the solid surface. The spreading parameter shows that the lithium prefers to remain as a bubble; the perovskite material wets lithium better if there are fewer pores. Polishing, as discussed previously, has an inverse effect on the spreading and wetting of lithium with the surface. The increase in Gibbs energy is observed with both the increased sintering time with polishing and the polishing after sintering for one to two hours increasing approximately 1×10^3 J.

Increasing the sintering temperature from 1100°C to 1200°C initially starts with a positive reaction Gibbs value, indicating an unspontaneous process. However, a negative gradient is observed for both the reaction Gibbs energies for increasing temperature, and at 300°C, they converge at the same energy value. Indicating that the increase in temperature allows for a gradual improvement in the reaction Gibbs as lithium liquid tension decreases. In addition to the lithium's interactions with itself, this increase in temperature means that any multiphase is potentially shifting from the tetragonal phase to a more cubic phase; an alternative explanation would be that the grains size increase is more favourable to lithium interaction.

Finally, pressure increase seems to harm the change in reaction Gibbs energy of lithium melting as potentially more cracks formed and allow for lithium wetting of the material. M. Brada and D. Clarke[220] noted that an increase in free energy lowering results from grain boundary wetting rather than surface wetting as grain boundary wetting and free surface energy wetting compete. This wetting of the grain boundary results in a de-wetting of the lithium melt as lithium propagates into the grain boundary material. They also noted that there are more thermodynamically favourable conditions for grain boundary wetting than surface wetting.

Observations of an alloying reaction when lithium melted on the pH 5, 5T, 1200°C for 2hr, polished as a result of a reduction of the titanium in form Ti^{4+} to Ti^{3+} as reported by Y. Wang *et al.* [75,79] (Figure 4-25). Between each of the degree there was a 5-minute interval as the temperature was set to 0.2°C per minute therefore any alloying effects could occur in between and create the new shape in the image. Thus, non-wetting contact angles are a poor wetting condition as the distinction between the lithium melt and the solid surface is blurred.

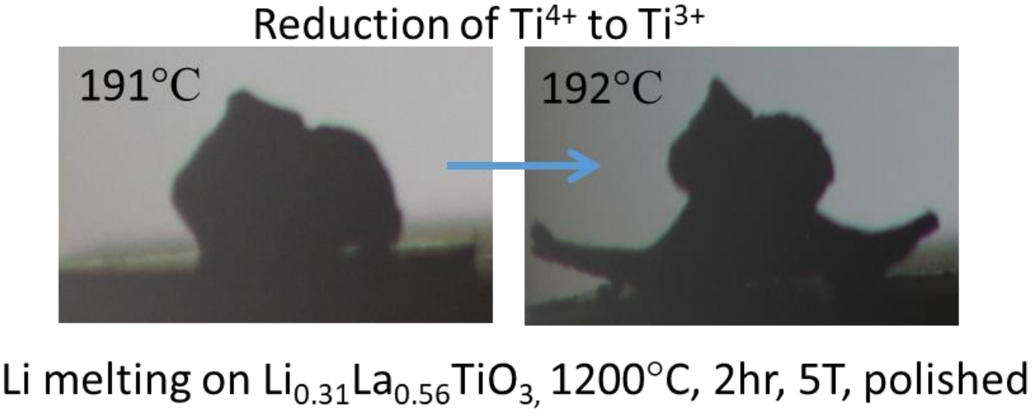

Figure 4-25: The alloying effect of lithium melt at 192°C with $Li_{0.3}La_{0.56}TiO_3$ sintered at 1200°C for 2hr at 5T in the air of Ti reduction.

Moreover, looking at the wetting states that occur for perovskite pellets and Al_2O_3 plate in Table 4.7, it can be noted that only two of the materials show a Cassie-Baxter and that most of the materials show capillary filling (Cassie-Baxter impregnation state). With the alumina plate, lithium was able to alloy as already noted[170] and implemented via ADL[114], indicating that although lithium is intrinsically not inclined to wet and spread over the perovskite surface, there is a possibility that LLTO can be used to help alloy and aid the impregnating wetting of lithium in to reduce the interface resistance by improving contact.

Table 4.7: The wetting parameters describing the wetting state that the different $Li_{0.5}La_{0.5}TiO_3$ *materials are experiencing when lithium melts the surface.*

Sintering condition	**Wetting parameter**	**Wetting state experienced**
pH 5 3T 1200°C 2hr	0.007	Cassie-Baxter
pH 5 5T 1200°C 2hr	0.117	Cassie-Baxter
pH 5 5T 1200°C 1hr	0.353	Wenzel
pH 5 5T 1200°C 2hr, polished	0.366	Wenzel
pH 5 5T 1200°C 1hr, polished	0.395	Wenzel
pH6 1200°C 1hr	0.453	Wenzel
pH6 1100°C 1hr	0.740	Capillary filling
Al_2O_3	0.880	Capillary filling
solid state synthesis	0.924	Capillary filling
pH 5 3T 1200°C 1hr, polished	0.976	Capillary filling
pH 6 1100°C 1hr	0.992	Capillary filling
pH 8 950°C 1hr	0.996	Capillary filling
1000°C Air PH10	0.997	Capillary filling

4.3.5 The effect of surface smoothness on the contact angle.

One of the Young-Dupre equation assumptions is that the surface on which the melt wets need to have a 'smooth' surface. There is no variation in the height, density, and slope. This is impossible and may help explain deviations from the observed contact angle compared to the calculated contact angle. Raising the possibility of improving the contact angle by smoothing the solid-electrolyte surface interface.

Observing the relative smoothness of a surface can be performed on a small scale using the AFM. A colleague, Cao Due Tan, operated the microscope and captured the images using two different medians to allow for different scans of a height variation map (seen in a) and c) of Figure 4-26) and adhesions mapping (b) and d) of (Figure 4-26). Using the perovskite as an example, two pellets of $Li_{0.3}La_{0.567}TiO_3$ (LLTO) synthesised at 1200°C for 2 hours had three different metals wetting the surface of the material. The variation in the surface treatment was the distinguishing factor. The natural thermodynamically formed surface, unaltered by any surface process, was called "rough" LLTO. The other LLTO pellet was polished and smoothed using a diamond polish of 5 microns paste. In the absence of a proper pellet arm holder, allowing a constant force and maximum coverage of the surface to the polishing agent, manual rotation was applied with multiple rotations of the pellet to the paste. This surface-processed sample was assumed and called "smooth" LLTO.

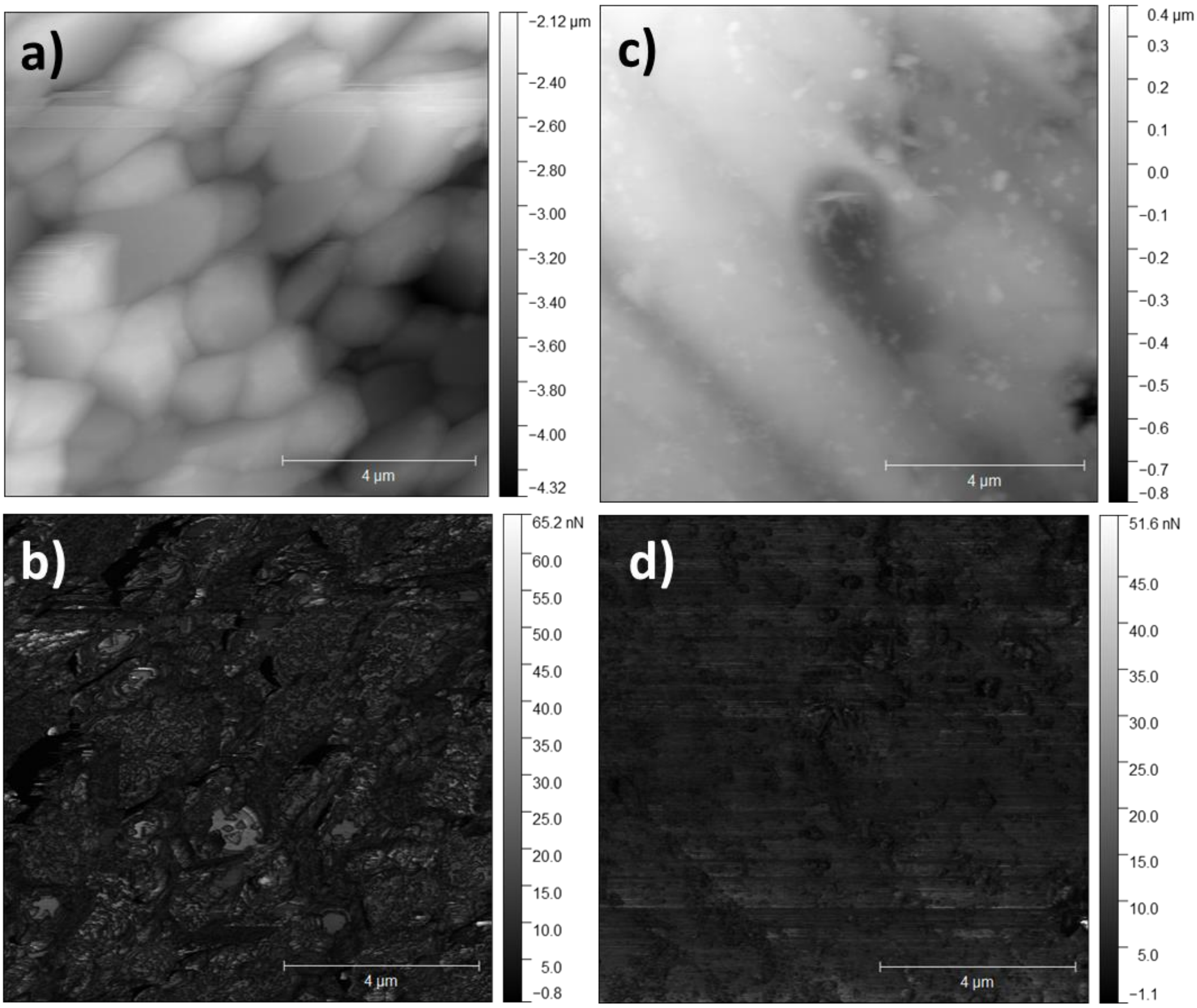

Figure 4-26: Height variation maps with the topography from a 10 µm AFM scan for rough LLTO (a) and smooth LLTO (c). Adhesion maps from a 10 µm AFM scan of the surface of rough LLTO (b) and the smooth LLTO (d).

Using the Gwydion[240] (version 2.57) microscopy software, statistical calculations measure the mean roughness for the rough LLTO to be 662 nm, with a root mean square (RMS) roughness to be 802 nm. While the smooth LLTO mean roughness was only 155 nm and an RMS roughness of 190 nm. However, this is a small 100 µm2 area of the pellets used in the wetting experiments. Observing the whole pellets in SEM, the surface looks like a similar topography throughout most surfaces except for a few pores formed in the sintering interactions. The average adhesion value for the rough LLTO is 7.74 nN, with the mean roughness value having an adhesion of 3.13 nN and the RMS roughness having a value of 4.43 nN. The smooth LLTO surface average value is 6.18 nN, with the mean roughness value having 1.5 nN and the RMS roughness having 2.082 nN.

The contact angles of lithium, gallium and tin wetting both the smooth and rough surfaces (Table 4.8, for the smooth surface and Table 4.9, for the rough surface) were measured to identify if smoothing the surface of the pellets would improve the contact of a metal to the solid electrolyte surface. It was found that rough surfaces produce better wetting conditions as there contact angels are lower. Therefore, when using solid electrolytes in full batteries there is no requirement to polish the surface to minimise the interface resistance.

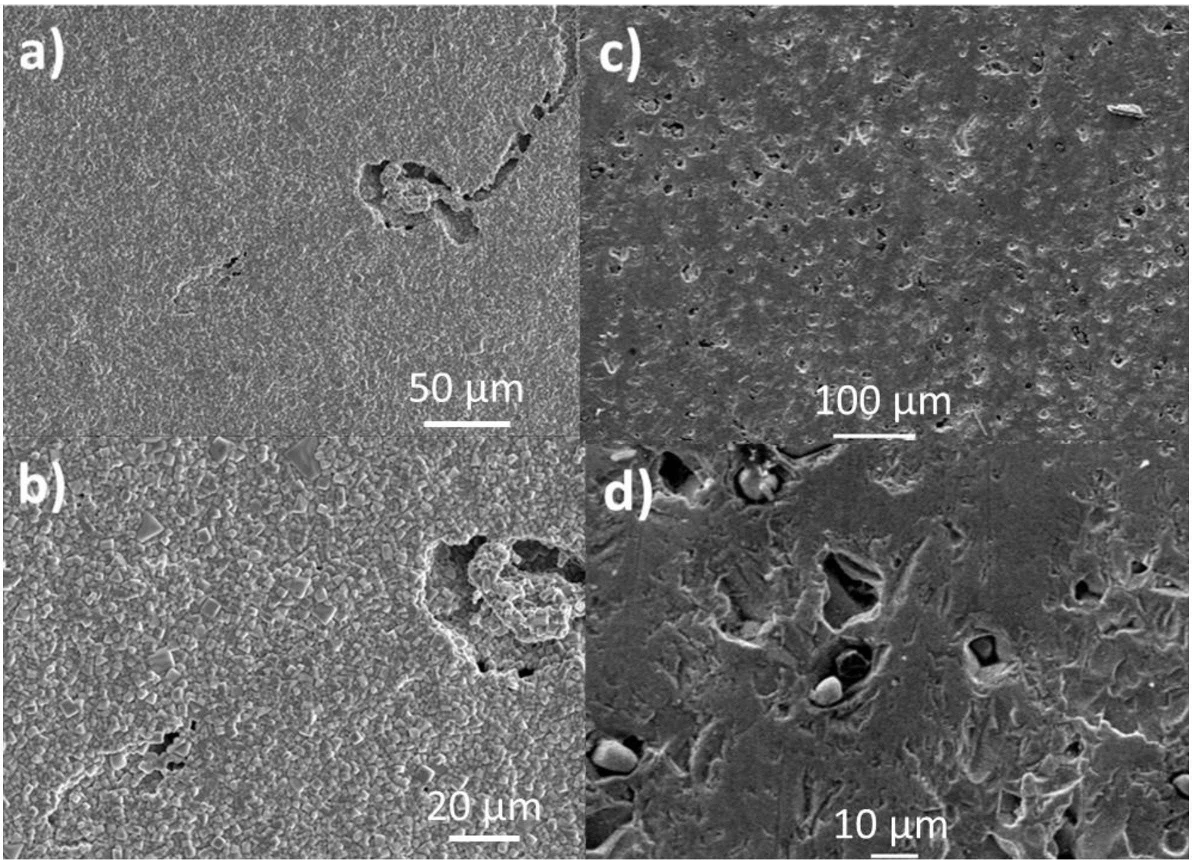

Figure 4-27:SEM images of different lower magnitudes for the "rough" LLTO a) and the "smooth" LLTO b) surfaces. Higher magnitude of the surface for the "rough" LLTO b) and the "smooth" surface d).

Table 4.8: The reported melt temperature, contact angle, and area of melt contact with the "smooth" LLTO. These observations calculate the surface energy, interface energy and work of adhesion for these melts.

Element	Temperature melted (°C)	Contact angle (°)	Area of contact (m^{-2})	Surface energy (Jm^{-2})	Interface energy (Jm^{-2})	Work of adhesion (Jm^{-2})
Lithium	194	146	0.004	-2.18	-2.17	-1.98
Gallium	36	84	0.002	-5.21	-5.65	-4.39
Tin	245	24	0.002	-6.11	-6.82	-29.8

Table 4.9: The reported melt temperature, contact angle, and area of melt contact with the "rough" LLTO. These observations calculate the surface energy, interface energy and work of adhesion for these melts.

Element	Temperature melted (°C)	Contact angle (°)	Area of contact (m^{-2})	Surface energy (Jm^{-2})	Interface energy (Jm^{-2})	Work of adhesion (Jm^{-2})
Lithium	194	91	0.002	1.54	1.95	-1.92
Gallium	36	53	0.002	-3.012	-3.081	-2.132
Tin	245	21	0.004	-6.01	-6.70	-21.3

These energy values indicate that with the roughness value, as indicated by the Cassie-Baxter theory, that having a smooth surface is closer to the main assumptions to the Young-Dupre equation and, in turn, highlights the melts prefer rougher surfaces as the physical alterations increase the surface area and increased surface area for adhesion of the melts to the solid surface. Therefore, for optimising interface surfaces, there is no need to smooth out the surface of a solid electrolyte to improve the contact and hence the interface resistance of the solid electrolyte with lithium.

Tin is a better melt for the perovskite material with excellent wetting but with the drawback of melting at a higher temperature. It has been reported[100] that alloying lithium and tin together improves wettability. When the tin ratio exceeds 10 wt.%, wetting takes place, and the interfacial resistance of the lithium-tin alloy with a LLZO material ($Li_{6.75}La_{2.75}Ca_{0.25}Zr_{1.75}Nb_{0.25}O_{12}$) does fall to 7 Ωcm^2 because of a low contact angle[100], estimating to be below 10°. This reduction in the contact angle highlights that good contact of any metal electrode to a solid electrolyte is paramount to lowering the interface resistance of a solid-state battery. Obtaining good contact will likely optimise barrier coverage at the interface.

Gallium contact angles show a non-wetting phase like lithium, and observation of the contact angles of gallium over different surfaces (a) is presented in Figure 4-28). All four synthetic conditions demonstrate poor wetting or non-wetting at a gallium melting temperature of 30°C. Liquid tension decrease with temperature and there is a gradual decrease in the contact angles with the TiO_2 and LLTO synthesised at 950°C, demonstrating lower contact angles. One possible explanation for this wetting behaviour is gallium infiltrating pores or grain boundaries. Using Equation 2.29, the gallium spreading parameter is not spontaneous for all materials until around 250°C (c) in Figure 4-28. Above 250°C temperature, all, except LLTO pH6 1100°C 1hr, demonstrate that gallium actively spreads spontaneously and prefers the interface tension over its melt's liquid tension. The lowest contact angle material of TiO_2 and LLTO synthesised at 950°C shows a positive interface tension at the gallium melting point that could suggest that there was energy put into synthesising new surfaces of the interface itself, otherwise known as reaction wetting. Suggesting that reaction wetting is heavily dependent on the interfacial tensions[221] and that there may not be a decrease in the contact angle if most of the mass transport of the liquid moves into grain boundaries or the surface to create an alloying surface, explaining the capillary filling and Cassie-Baxter wetting impregnation states of gallium (Table 4.10) for all materials.

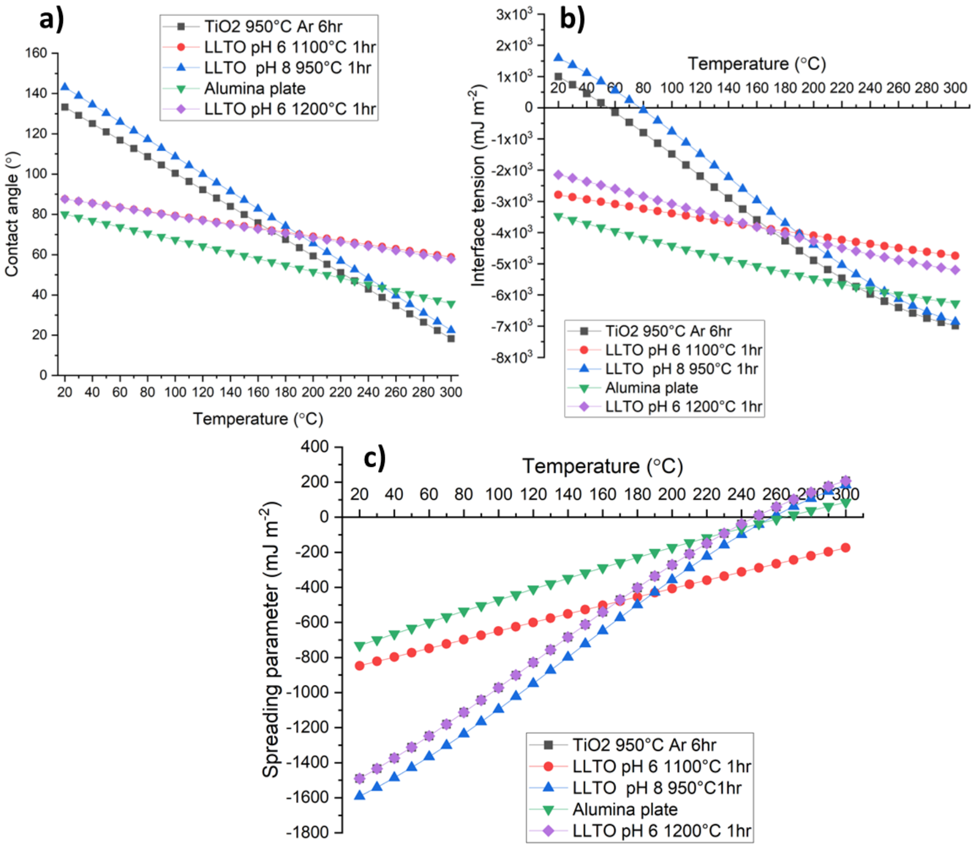

Figure 4-28: a) the contact angle of gallium melt wetting the surfaces of various materials over a temperature range. b) the interface energy of the gallium melt wetting the materials over a temperature range using the contact angles trendlines. c) The spreading parameter of gallium melt on different materials.

Table 4.10: The wetting states of gallium wetting different surfaces and the wetting parameter used to determine the state.

Sintering condition	Wetting parameter	Wetting state
TiO2 950°C Ar 6hr	0.5	Capillary filling
LLTO pH 6 1100°C 1hr	0.5	Capillary filling
LLTO pH 8 950°C 1hr	0.5	Capillary filling
Alumina plate	0.5	Capillary filling
LLTO pH 6 1200°C 1hr	0.5	Capillary filling

4.4 Conclusions

Lithium melting on the most promising solid oxide electrolytes $Li_{3x}La_{2/3}TiO_3$ (LLTO) and $Li_7La_3Zr_2O_{12}$ (LLZO) presents an intrinsic non-wetting situation. All materials require very little adhesion to remove the lithium unless it has been alloyed and reacted with the materials. Lithium's thermodynamic preference is to form a droplet on the surface regardless of whether gas prevents the partial filling of lithium into the pores. Applying a smaller layer of an alloying material has been demonstrated to be the best method of improving not only the wettability of lithium on the surface of a solid oxide electrolyte material but also the filling of lithium into the pores of electrodes. Pore infiltration, in turn, increases the contact area of lithium to the electrolyte to improve electron transfer rates and minimise any impending creep reactions.

Obtaining good contact will likely result from an optimisation of the application of a lithium alloy, as shown by others working with tin or gallium. Sacrificial layers can spread evenly throughout the surface of the interface or with engineering properties of the electrodes and electrolytes, such as with the tape-casted electrolyte.

$Li_7La_3Zr_2O_{12}$ materials, despite their stability with lithium, are thermodynamically unwilling to form Cassi-Baxter wetting impregnation states, with it being more energetically favourable for lithium to have its liquid tension exposed to the air and have larger surface areas exposed. It is unlikely that there will be any unfavourable wetting interactions unless it is the tape-casted format in which the electrolyte surface is more porous, around 70% density.

Gallium is a more favourable wetting and impregnating melt for LLTO and LLZO materials. $Li_{3x}La_{2/3}TiO_3$ perovskite material has significant potential to be used as a sacrificial layer to aid the contact angle of lithium on another solid electrolyte, such as LLZO.

Wetting calculations and experiments are difficult to replicate due to the human error required to analyse the contact angle and ensure the lithium's purity, and surfaces wetted by the lithium are helpful in comparative studies. It was found, amongst the materials used, that if the interface energy is decreasing in energy with an increase in temperature, this can lead to a more favourable capillary filling state in which mass movement of lithium will thermodynamically move to the interface and bond more strongly.

Chapter 5 Applying a thin film of LLTO on LLZO to improve the interface.

5.1 Introduction

In chapter 4 it was observed that lithium is intrinsically unspontaneous in forming good contact with the most promising solid oxide electrolyte material. The other reasons for the high intrinsic resistance with metallic lithium electrodes can be shown during discharging step of a full solid-state battery. As void formation occurs at the interface between the lithium-positive electrode and the solid electrolyte leading to an uneven distribution of lithium at this interface during charging[116,222]. Not only that but Lithium creeps occur between grain boundaries, hence why a density of 90% is required; otherwise, propagation of lithium occurs in the boundaries as well.

Despite lithium having a lower elastic modulus of 5 GPa[223] compared to the 150GPa to 200 GPa[223] elastic modulus of solid oxide electrolyte material, there is still metal infiltration around the grain boundaries of the solid electrolytes around a critical current density of 0.1 to 1 mA cm^{-2}. Therefore to limit this dendrite growth, the density of the solid electrolyte materials plays an important part, Wolfenstine *et al* reported that the elecolyte must be 98% dense with very few void defects on the surface of the solid electrolyte[223]. Park, *et.* al also points out that the overall electrical overpotential of the battery will allow for a flux of the metallic ions to creep into the solid electrolyte material leading to fracture of the solid electrolyte, which in turn also increases the interfacial resistance[224].

LLZO material has a stability advantage over lithium if the current density is below the critical current density and it has a suitable voltage range (0 V – 9 V) [3,4]. The LLZO surface is lithophobic, so having a non-wetting state reduces the charge transfer across the interface. Good lithium contact means that on charge and discharge, there will be an even spread of lithium through the samples at the interface at least and not forming shorter pathways that can lead to a small build-up of lithium dendrites.

Current strategies include the use of compositional tuning of the anodes or electrolytes. A coating or buffer layer is typically added by atomic layer deposition[38,114,209]. There is also the utilisation of a semi-solid state electrolyte using polymer interlayers. Finally, there is evidence that alloying of gallium, tin or other metals to lithium metal improves the wettability and contact of lithium to the electrolyte.

In this chapter the aim is to use the alloying effect of $Li_{3x}La_{2/3-3x}TiO_3$, which allows for good contact of lithium as a coating layer on LLZO. With the hypothesis that LLTO would act as a protective coating between the LLZO electrolyte and the atmosphere effects due to LLTO seemingly stability in air. The LLTO coat wetting effect that we had seen as a type of alloying could also be used to help improve the contact of lithium metal to LLZO. That ability to coat LLZO and protect it from CO_2 and H_2O will help create a scalable process for creating LLZO electrolytes outside an argon-filled glove box, unlike other methods, which in an industrial setting should reduce the cost.

Therefore, the question of whether the coating layer will improve the lithium material's contact angle will be investigated in this thesis. With some of the LLZO materials, a tape-casted material with a "scaffold" surface containing a porosity of 70%, and thus metallic infiltration is required. Three main infiltration methods are possible for LLTO to coat the inner surface of the scaffold material: (1) metal salt with an additive, (2) nanoparticles in a suspension, and (3) molten salt. As the sol contains precursors of nitrates in the one sol-gel synthesis, the hypothesis is that the first infiltration method may coat the porous material's inner surface. The metal-salt has an additive, typically a surfactant, to reduce the surface tension of the parent material, and the wetting behaviour will affect the uniformity of the dispersion of the particles on the surface[225].

The surface energy of the solution used will affect the penetration into the porous substrate material and how it deposits on its surface. The wetting and surface interactions will continue to influence the stability and durability of the electrode even after the thermal treatment. Thus, using XPS or Raman during impregnation can observe the altering surface interactions. Surface interactions are determined by their wetting effect[225]. There is an (l)-(s) interface when the impregnating liquid passes through the scaffolding material, and the surface energies will affect the depth the liquid will pass through. There is also an (s)-(s) interface occurring during the thermal treatment, affecting the morphology and size. Most of the final interaction has been investigated using computational techniques[225].

Another potentially positive aspect of using this protective LLTO coating is to be investigated by establishing if there is good stability on the positive electrode side. One of the most promising cathode materials is the olivine structure of $LiFePO_4$[112]. In this chapter

LLTO will be attempted to be coated on synthesised $LiFePO_4$. Li_xFePO_4 adopts an olivine structure[108], has a rechargeable voltage at 3.4 V, and can achieve Li cycling between $0.1<x<1$ providing a capacity[108] of 152.9 mA h g^{-1}. Li_xFePO_4 is desirable for its reduced cost, reduced human rights violations, and safety. Chemically it is helpful as the polyanion drops, by inductive effects, the fermi energy of Fe^{3+}/Fe^{2+}, reducing the columbic interactions of the Fe with the PO_4 tetrahedra, helping with the 20% energy reduction [2]. $Li_{1-y}FePO_4$ allows 25 cycle stability, 3.4 V plateau with a capacity of 130 $mAhg^{-1}$ at y=0.8 at 2.1 mA g^{-1} current rate. This decrease in capacity occurs because of the movement of Li^+ at the interface of $LiFePO_4$ and $FePO_4$, and this is not an irreversible loss.

The aim of this chapter is to use the previously discussed $Li_{0.5}La_{0.5}TiO_3$ sol precursors of chapter 2, used in the synthesis for LLTO, they are sessile dropped onto LLZO and $LiFePO_4$ materials to observe if the interface stability improves and if lithium forms a better contact with LLZO.

5.2 Experimental methods and conditions

The sols in chapter 2 used to synthesis the $Li_{0.5}La_{0.5}TiO_3$ material were sued to form the protective LLTO coating. The sols were coated in the surface using a sessile dropping technique was used to coat the surface of a solid-state material of about 45 µl, equating to about 25mg of mass. The concentration of these sols was 0.4 M in water.

The samples were dried at 80°C for two minutes, and the drops were reapplied multiple times with solid oxide electrolyte materials, the precursor solutions of various LLTO and LLZO pellet materials, to try and achieve an even coating. Eventually, 1.5 wt.% Polyvinyl alcohol (PVA) was added as a binder material to help aid the spreading of material throughout the surface. Measure out the stoichiometric mass using 10 ml of water and then apply it to heat until the PVA can dissolve in the solution.

Sintering of the material then occurred at 1000°C for 1 hour in the air or at 1100°C for 1hr in argon. Initially the heating rate tried was 5°C min^{-1} but was then reduced to 1°C min^{-1}.

Spray coating was simulated by heating one LLTO pellet to 205°C on a hot plate, and then the sol coating was dropped on the pellet surface as it is a beneficial method to cover and aid infiltration of precusors[226].

Synthesis of $LiFePO_4$ followed the work done by colleagues in China Da Li and Zhiyong by a combustion method. In a 1:1:1 mole ratio, the nitrate precursors for lithium ($LiNO_3$) and iron ($Fe(NO_3)_3.9H_2O$) were added to the phosphate source of $(NH_3)H_2PO_4$ once all the nitrates were dissolved in deionised water. The citric acid solution that was 1.5-mole ratio compared to the other precursors and all the precursors were stirred and mixed for more than 2 hrs. After the dissolving, add NH_3H_2O solution until the pH becomes 3, shifting colour from a golden yellow to a light green emulsion solution. The solutions were heated on a hot plate at 80°C under stirring to allow the self-combustion reaction to occur. The gel is then heated to 300°C. The powder is then milled before calcining at 700°C for 8 hours in hydrogen (5% H_2 in Argon).

Different LLZO material was provided from Morgan materials which was synthesised by Dr. Mihkel Vestli and Dr. Ioanna Pateli from the University of St Andrews. The materials include $Li_{6.4}La_3Zr_2O_{12}$ (LLZO), $Li_{6.4}La_3Zr_{1.4}Ta_{0.6}O_{12}$ (LLZTO) and $Li_{6.5}La_3Zr_{1.5}Nb_{0.5}O_{12}$ (NbLLZO). LLZTO was used as it had the most promising ionic conduction due to the stability of the cubic phase with the added Ta. The NbLLZO material was being used to check the stability of LLZO material in atmosphere.

5.3 Results and discussion

5.3.1 Stability of LLTO in air

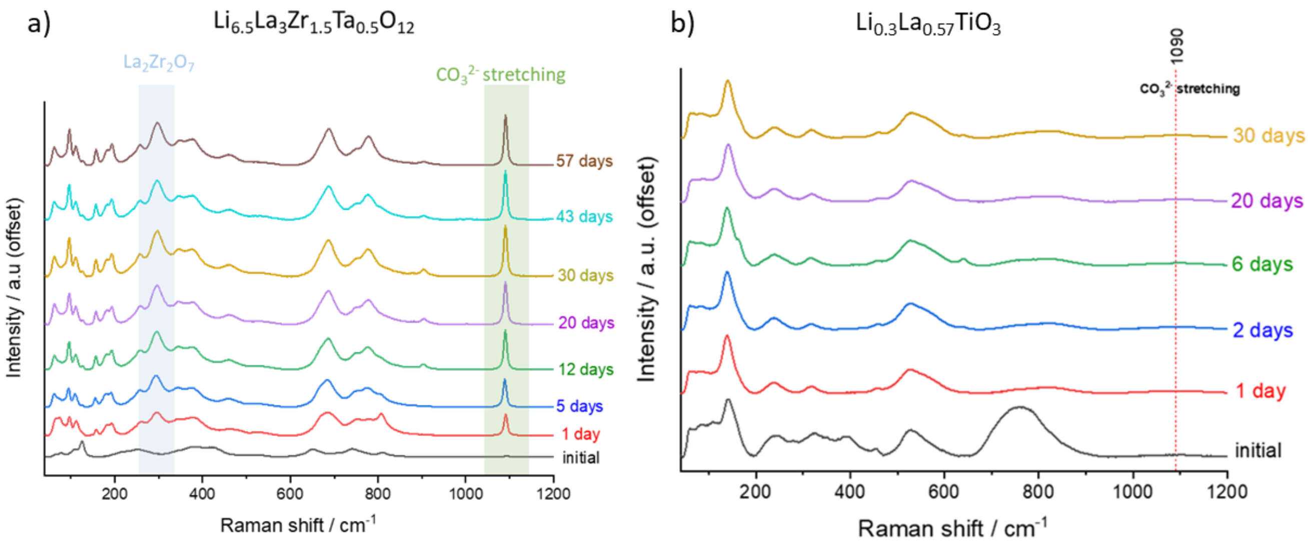

Figure 5-1: Raman spectra of analysing the stability of a) $Li_{6.5}La_3Zr_{1.5}Ta_{0.5}O_{12}$ in 80°C in contact with air after 57 days and b) $Li_{0.45}La_{0.55}TiO_3$ exposed to air for 30 days at 80°C.

Raman spectra can observe the moisture stability of the $Li_{0.35}La_{0.55}TiO_3$ synthesised in a sol of pH 4 at 1200°C for 2 hours in comparison to the Ta-doped $Li_{6.5}La_3Zr_{1.5}Ta_{0.5}O_{12}$ (LLZTO) material stability when exposed to the atmosphere. Ta-doped known to help stabilise the cubic phase of LLZO and by comparing the Raman with a cubic LLTO sample the stability of these promising solid oxide electrolytes can be compared when in atmosphere. When the LLZTO experiences CO_2 absorbance resulting in the CO_3^{2-} There is also the growth of the peak[227] at $La_2Zr_2O_7$ around 300 cm^{-1} as a result of this absorbance of CO_2 hindering the wetting and ionic properties of the LLZO material. With it growing over a month exposed to air. If the $Li_{0.3}La_{0.56}TiO_3$ was a purely cubic material, then no peaks due to the symmetry rules, and so because LLTO primarily exists as this pseudo-cubic double perovskite, we can observe four peaks; although the fluorescence present, it can be hard to identify[228]. There is the presence of a the impurity of as surface $La_2Ti_2O_7$ seen at the broad peak around 800 cm^{-1} as a result , which accounts for the Ti-O interactions of the impurity[229,230]. However, as the days exposed to air continue, there is a decrease at 400 cm^{-1}, leaving the TiO_6 octahedra peaks around 500 cm^{-1} apparent and stable throughout the 30 days exposed to air[228]. And the with no CO_3^{2-} appearing in the LLTO surface, no CO_2 in the air reacts with the surface, implying that LLTO is a more stable solid oxide electrolyte when exposed to the atmosphere.

The stability of LLTO material in the air is present compared to the desirable electrochemical performance of LLZTO, as noted by Raman. As there is no CO_3^{2-} peak on the LLTO over 30 days, will the peak on the LLZTO grows, it can be concluded that LLTO would make for a desirable protective coating for LLZTO.

5.3.2 Coating LLTO on solid oxide electrolytes

Initial application of the sol precursors of $Li_{0.5}La_{0.5}TiO_3$ on LLZO pellet revealed that the evaporation of water at 80°C does leave a cover of a thin gel but has cracks in that cover leading to an incomplete covering (a and b in Figure 5-2). Following tape casting examples, when it comes to drying, we see examples of centre cracking and crow's feet cracking[231].

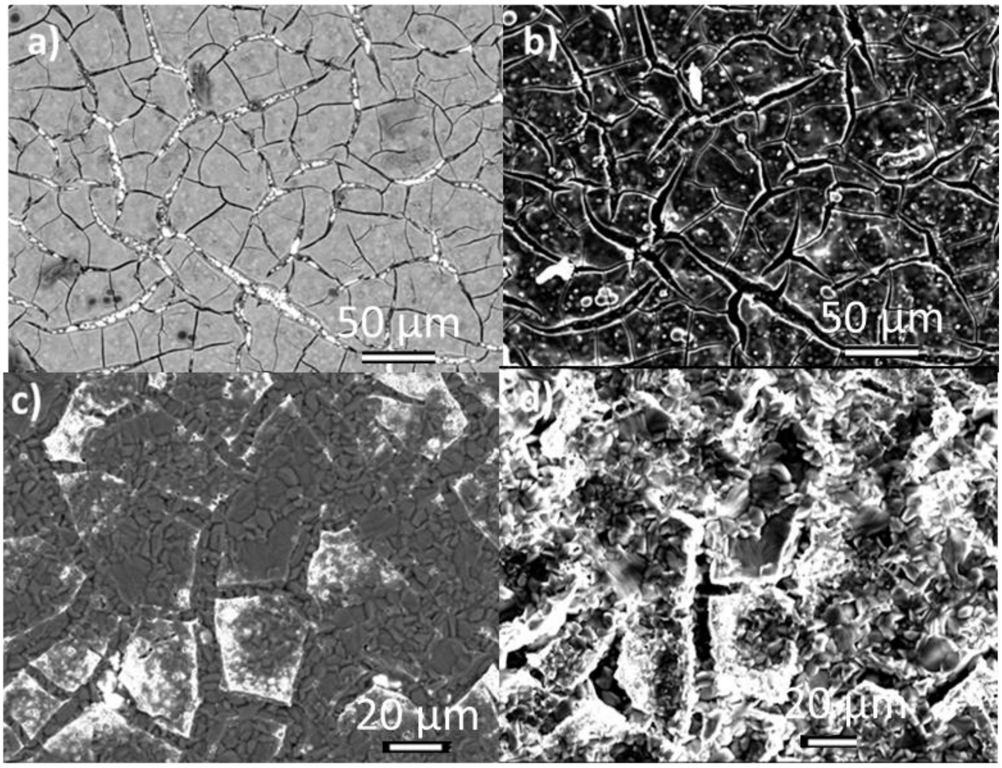

Figure 5-2: SEMs of $Li_{0.5}La_{0.5}TiO_3$ sol sessile dropped on an LLZO pellet after the drying phase at 80°C for 5 minutes (a) is a backscattering analysis, and b) is the secondary electron scan). Then after the sample was heated to 700°C for 1hr in the air, (a) is backscattering analysis and b) is the secondary electron scan)

Centre cracking in the thin film originates from coverage inconsistencies and progresses along furrows. It happens when particle adhesion is weaker than water. As water evaporates, the tape cracks to allow for lateral shrinkage. To minimize centre cracking, one can add binders (holding the matrix body together[144]), plasticisers(aid flexibility of the film to move without cracking[144])to enhance precursor homogeneity. Slowing the drying rate prevents rapid evaporation and subsequent disturbances[144]. "Crow's feet" defects appear in early drying stages[144]. Filtering the sol precursor can remove agglomerates, improving spread on the surface. Additionally, having excess binder reduces the formation of cracks.

Further heating of the sol-precursor at a heating rate of 5°Cmin^{-1} created further cracking and only led to islands of LLTO material (Figure 5-3 c and d). Performing EDS analysis (Figure 5-3) of the surface of a Ta-doped LLZO material with LLTO dried and then heated to 1000C in argon to reduce CO_2 contamination on the LLZO surface showed that Ti peaks occurring from the LLTO coating but broken up into "islands". However, carbon is located throughout the sample, with lower concentrations of carbon observed on the LLTO islands compared to the exposed LLZO material. Indicating that LLZO material CO_2 capture mechanism is more significant than LLTO, so the covering of LLTO can be used as a CO_2 protective coating. There is the possibility that there are leftover carbonates from the LLTO coating but observation of the LLZO pellets after being removed from the tub furnaces showed the yellow powder on the higher 5°Cmin^{-1} rate of the annealed LLTO powder indicates that most of the carbonates had been removed leaving behind LLTO. The EDS spectra (Figure 5-4) linked to the maps (Figure 5-3) show the heightened lanthanum concentration compared to the other elements, and the maps show darker blue, which matches what was expected with increased lanthanum in the LLTO islands. The expected phases of the LLTO at this temperature range is to be the $Li_{0.3}La_{0.57}TiO_3$ tetragonal phase but will be incomplete due to the low time at the sintering.

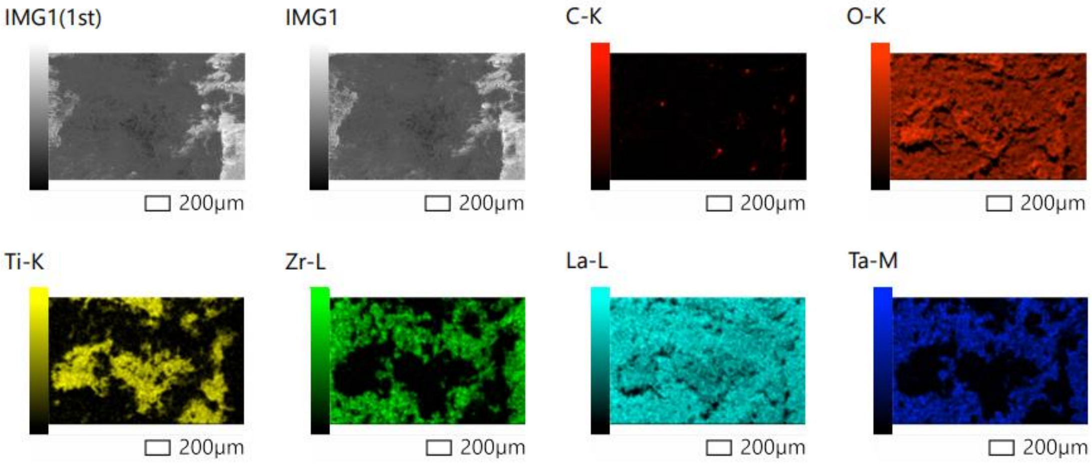

Figure 5-3: EDS maps of LLTO sol precursor dropped on a Ta doped LLZO pellet after being treated at 1000°C in zero grade argon for 1hr.

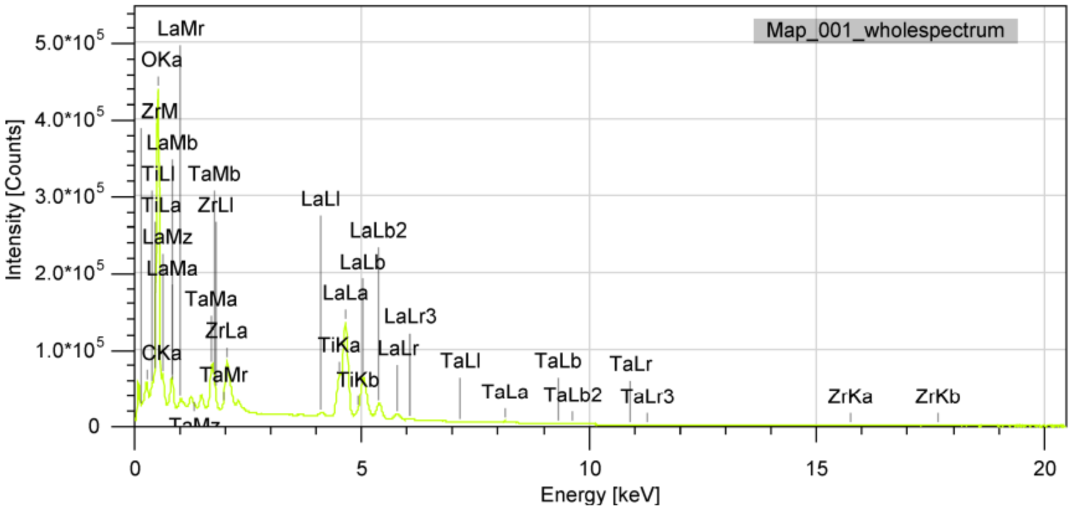

Figure 5-4: EDS spectrum of LLTO sol precursor dropped on a Ta doped LLZO pellet after being treated at 1000°C in zero grade argon for 1 hr.

On a homogeneity issue with the drops, there is incomplete coverage of the complete pellet, not just with the centre and crow's feet cracks but with what appears to be delaminating at the edges of the pellets (Figure 5-5). The sol congregates at the edges of the pellet, where there is variation in the concentration of LLTO. Discolouring is observed in the backscattering in Figure 5-5, possible different impurities or phases of LLTO material synthesising at 1000°C. Too much sol is applied to the pellet when attempting a complete coverage; upon drying, a higher deposition of LLTO is located at the edges than at the middle of the pellet. Therefore, binders are to be incorporated to try and improve the homogeneous coverage of LLTO. After trying different binder materials such as polyethylene glycol, CTAB, Triton Q5-44, and polyvinyl alcohol (PVA), it was observed that PVA at a concentration of 1.5wt% provided the clear transparent film of LLTO without binding the material too much making it too viscous to spread over the surface.

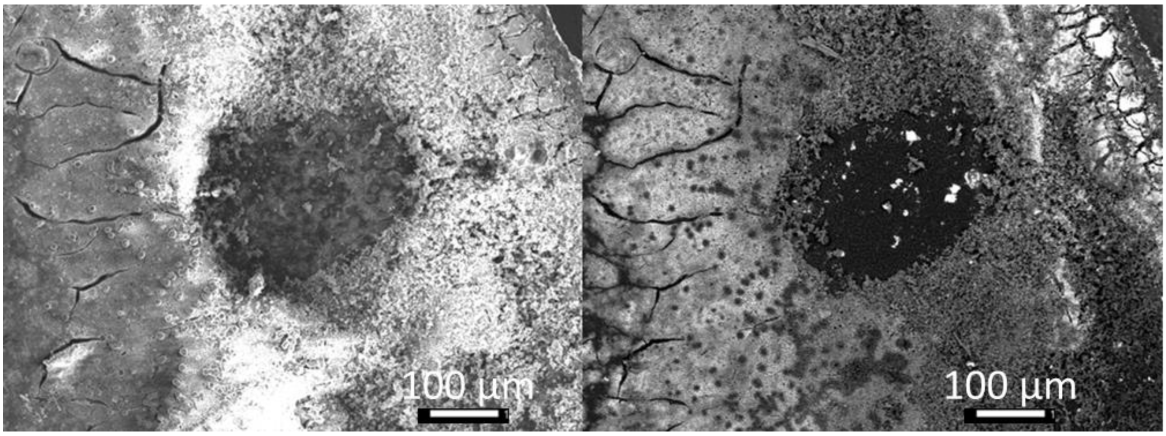

Figure 5-5: The incomplete coverage of LLTO sol precursor seen at the edge of the LLZO pellet.

Using SEM and the backscattering setting, we can see that there is currently a partial covering of sacrificial LLTO on LLZO (*Figure 5-6*).In *Figure 5-6* c) and d), there is a higher depositing of the LLTO sol material in pouches of the LLZO material. Deposit of LLTO in these pores help to wet the scaffold porous LLZO electrolyte with this protective layer. A void exists between the LLTO and the LLZO material; this could be due to a lack of sol material covering the whole surface or a side reaction that burns off the sol material. Alternatively, the temperature profile is incorrect or unwanted phase reactions are altering in different synthesis phases.

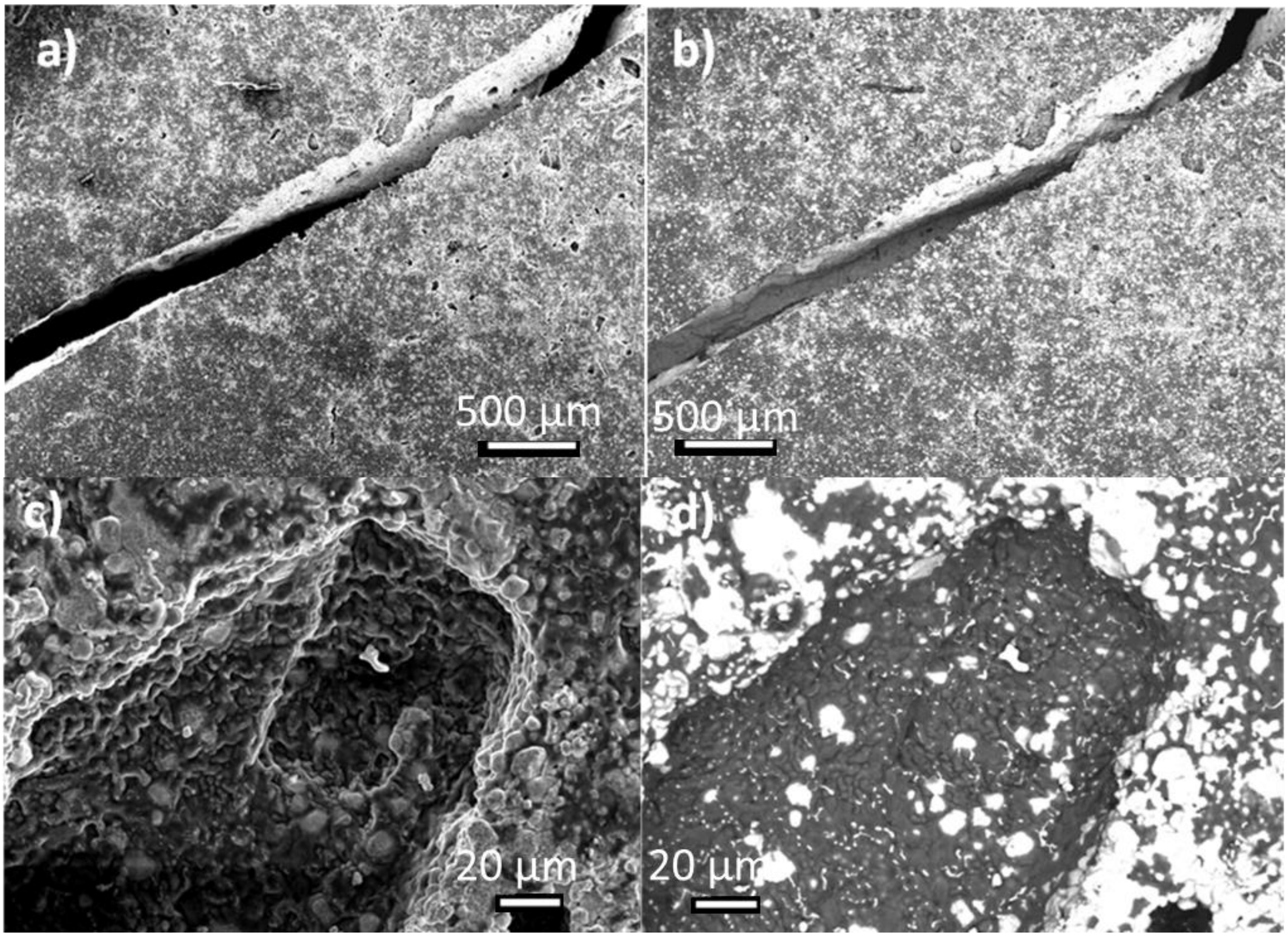

Figure 5-6: SEMs pH 6 LLTO with 10 wt.% PVA deposited on $Li_{6.4}La_3Zr_{1.4}Ta_{0.6}O_{12}$ pellet at a crack (a is secondary, electron diffraction and b is backscattering diffraction) and in a surface pore (c) is secondary electron diffraction and d) is backscattering diffraction).

Through a FIB-SEM imaging, close contact between the 1-micron LLTO layer and the underlying LLZO garnet is observed (Figure 5-6). An EDS would help determine if gaps are due to incomplete coverage or a reaction between LLZO and LLTO altering the composition or the phase. Nonetheless, the observed contact between the materials is ideal.

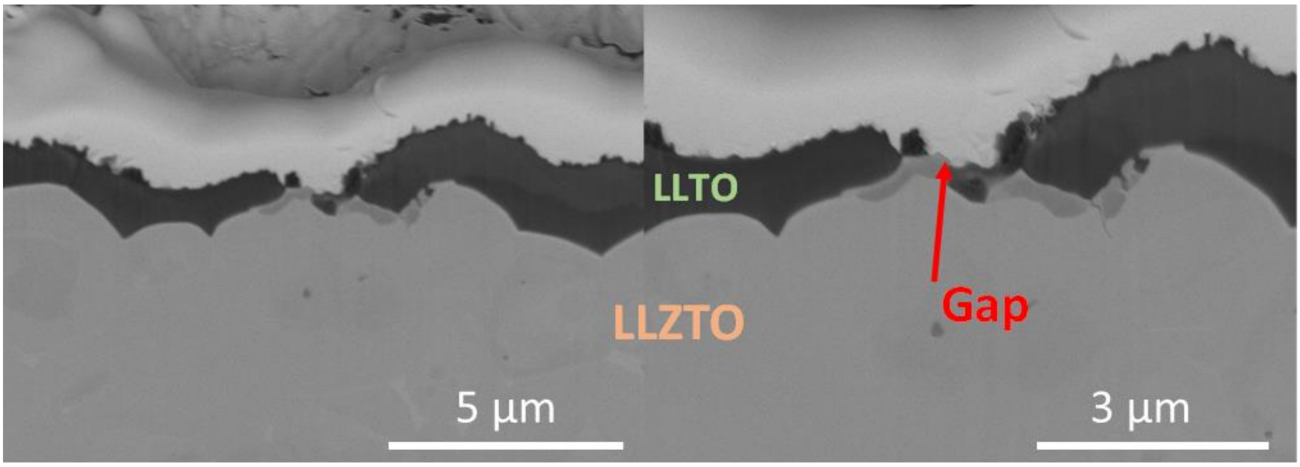

Figure 5-7: SEM FIB images of the interaction between the deposited pH 6 10 wt.% PVA $Li_{0.35}La_{0.65}TiO_3$ (LLTO) mixed-phase sol and the $Li_{6.4}La_3Zr_{1.4}Ta_{0.6}O_{12}$(LLZTO) pellet underneath. The central gap shows either a lack of material or an unwanted side reaction.

Raman analysis of this mixing compared to $Li_{6.5}La_3Zr_{1.5}Nb_{0.5}O_{12}$ (NbLLZO) material indicated that there is also a protective layer from the carbon dioxide in the atmosphere. As indicated by Figure 1-7, there is very little of the non-conductive and poor wetting phase of $La_2Zr_2O_7$ in mixing these materials, as we see no prominent peak around 300 cm^{-1} in the combination of LLTO with LLZO[227]. It is assumed that there will continue to be no $La_2Zr_2O_7$ formation if there is low to no concentration of $La_2Zr_2O_7$ in the bulk of the LLZO. Another set of peaks to be mindful of is rutile, expected around 400 and 520 cm$^{-1,}$ a prerequisite to forming any Li_xTiO_3 material[197].

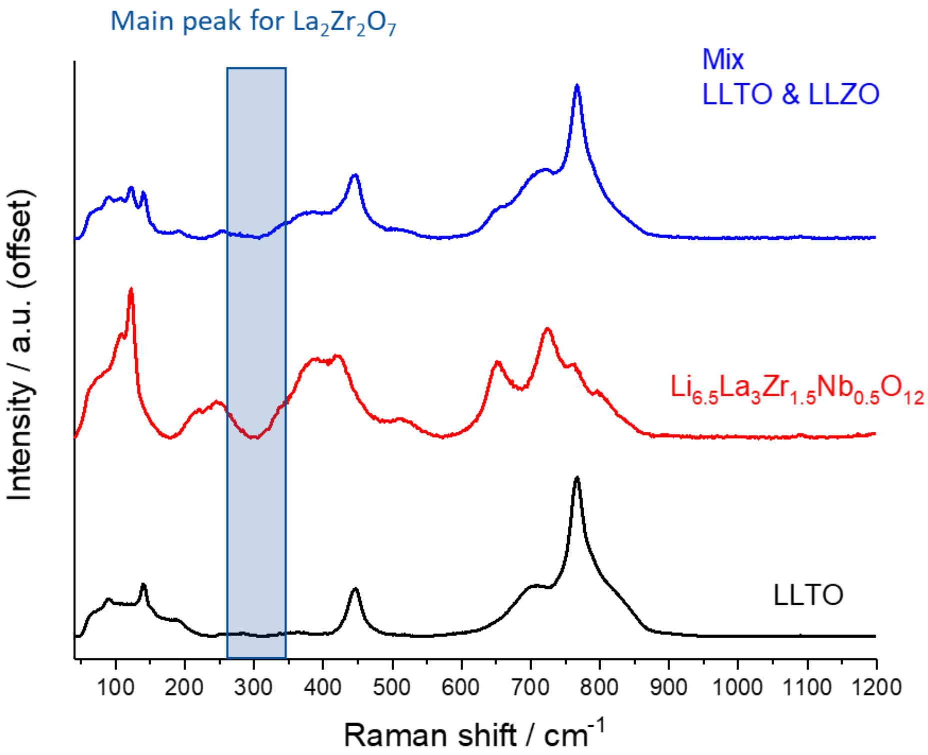

Figure 5-8: Raman stability of $Li_{0.3}La_{0.56}TiO_3$ (LLTO) deposited on $Li_{6.5}La_3Zr_{1.5}Nb_{0.5}O_{12}$ (LLZO) with no peaks of $La_2Zr_2O_7$ showing in depositing on the tape cast.

5.3.3 Influence of thin film on the wetting properties of lithium to solid electrolytes

Coating LLTO onto LLZO is achievable, and the use of FIB-SEM reveals some improvement in the lithium contact with tape-casted LLZO (Figure 5-8). However, inadequate adhesion of lithium to these surfaces leads to dewetting areas visible in the SEM (Figure 5-8a). To assess any differences in the interface contact angles between the micron-scale layer and the millimetre-scale bulk wetting, adhesion calculations based on contact angles during melting can be employed.

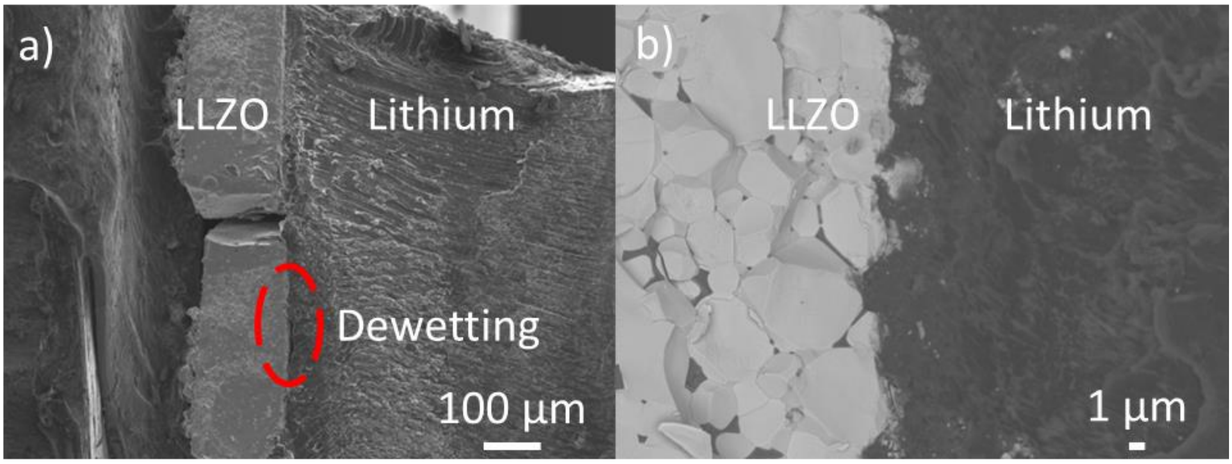

Figure 5-9: Improvement in the wetting of lithium metal on the surface of a tape casted LLZO material because of the addition of an LLTO sol.

At the bulk level, the contact angle variation of molten lithium wetting due to coating LLTO onto LLZO was minimal (as seen in a) Figure 5-10). The non-wetting contact angles of LLZO garnet pellets are observed on the LLTO-coated LLZO pellets. The contact angle trendline of the sol-covered LLZO slopes below the contact angle trend of a non-covered LLZO, so the LLTO-coated LLZO will reach the lowest contact angle at 74° at 300°C in comparison to non-coated LLZO, which can only reach 79°. There is a reduction in the surface energy at room temperature because of the coating. However, as lithium melts on the surface, we see a decrease in the surface energy and the work of adhesion of the coated LLTO pellet compared to the uncoated sample. The work of adhesion also gradually increases with temperature, unlike the uncoated LLZO. The interfacial tension of lithium to the coating of the LLTO decreases with increasing temperature, like that of the surface energy, and has a higher gradient in that generated trendline than the uncoated LLTO interface. The lowest energy of the interface occurs at lower melting temperatures implying that heating the lithium beyond the cross-over point may not help the bonding of lithium to the LLTO coating.

A significant mass of molten lithium was used for these calculations (about 0.015 g of lithium). A smaller mass of lithium would help reduce the size of the bulk of lithium that is exposed. Using a smaller mass of lithium in these wetting experiments would also reflect the micro thickness present in the electrode cells. However, a small mass of lithium would increase the error of the contact angle observed using image J, as the three-phase boundary would be more challenging to spot.

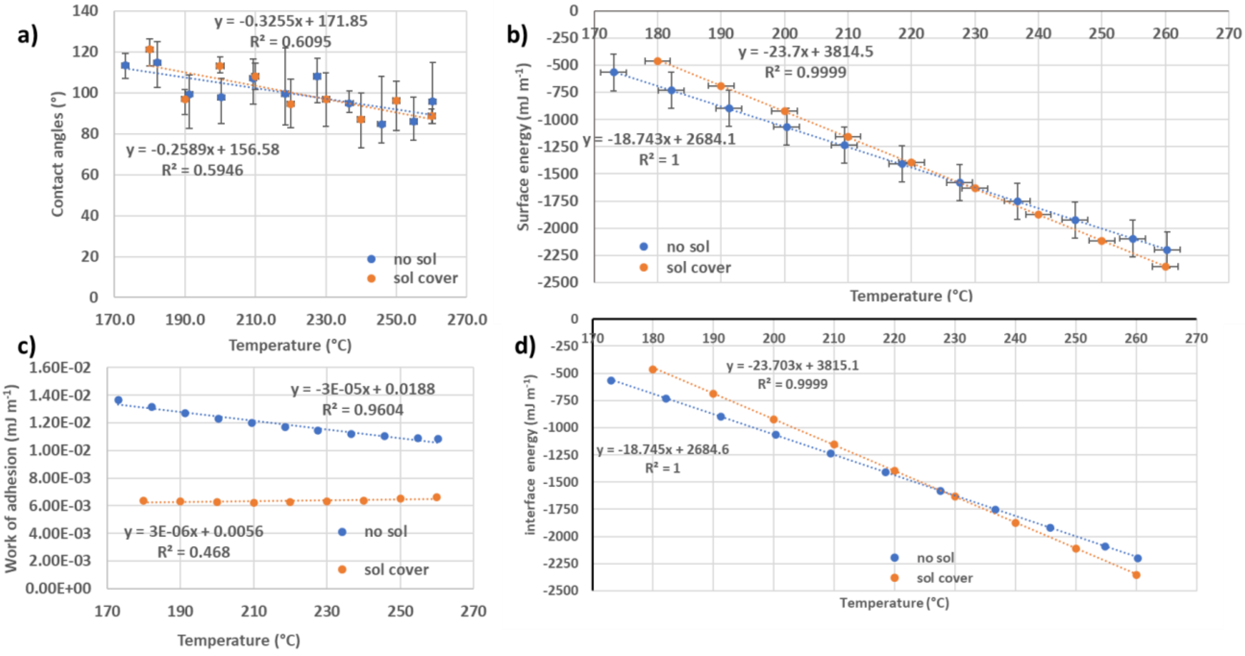

Figure 5-10: The effect of the sol covering of pH 6 10 wt.% PVA $Li_{0.35}La_{0.65}TiO_3$ (LLTO) on a $Li_{6.4}La_3Zr_{1.4}Ta_{0.6}O_{12}$ (LLZO) pellet on the contact angle of lithium melting on the garnet's surface a), the surface energy b), the work of adhesion c) and the interface tension of lithium against the sol involved d).

Moreover, even though contact angles are an excellent way to see contact, it might not be necessary to show if impregnation or chemical bonding is spontaneous. As we can see by the spreading parameters (Figure 5-11)and wetting states (Figure 5-12) of lithium melting the sol covering and the plot underneath that, there is no spontaneous spreading as a result of lithium melting the surface and a Wenzel non-wetting states lithium is occurring with both the pellet and the sol covering on top.

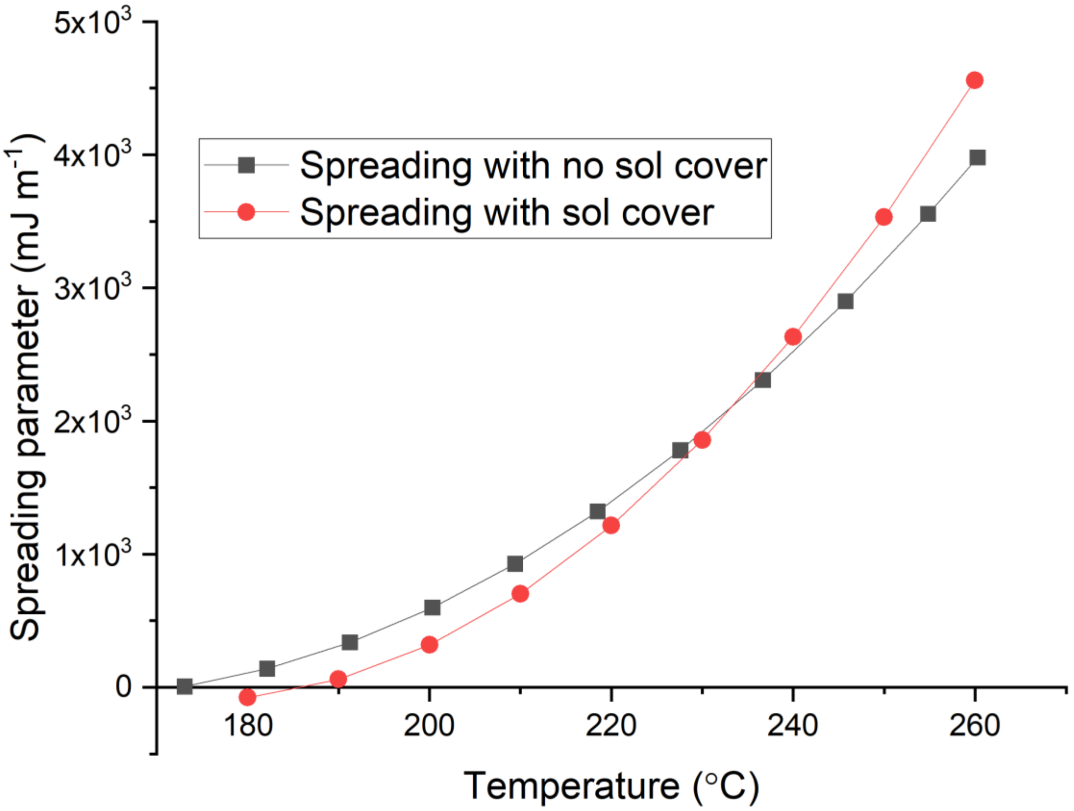

Figure 5-11: Variation on the spreading parameter of lithium as a result of covering the surface with a pH 6 10 wt.% PVA $Li_{0.35}La_{0.65}TiO_3$ *(LLTO) mixed-phase sol on the* $Li_{6.4}La_3Zr_{1.4}Ta_{0.6}O_{12}$ *(LLZO) pellet.*

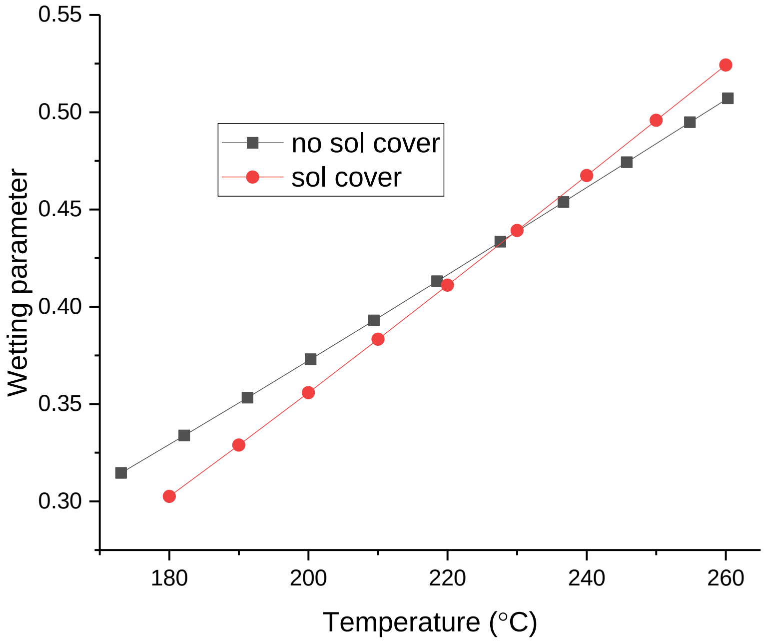

Figure 5-12: Wetting parameters resulting from pH 6 10 wt.% PVA $Li_{0.35}La_{0.65}TiO_3$ (LLTO) mixed-phase sol covering the $Li_{6.4}La_3Zr_{1.4}Ta_{0.6}O_{12}$ (LLZO) pellet the coverage of an LLTO.

Despite the LLTO coating, lithium couldn't penetrate the porous structure of the LLZO tape cast, possibly due to the curved nature of the pore sides[232,233]. This necessitated a switch to use an alloy of lithium like Li-Ga or Li-In. The interaction between lithium and LLTO suggests that lithium might naturally spread at lower temperatures without needing to be melted seen as seen when LLTO is reduced by lithium in Figure 4-25. While melting may not be essential, applying pressure can help lithium contact solid oxide electrolytes, a pressure that's inherent in battery cell stacking[123,210].

Looking at the Cassie-Baxter and Wenzel wetting state theory, the observed contact angle in the experiments will be greater than the theoretical contact angle[177,178], so it is necessary to investigate the pore size of the pellet or scaffold underneath or by applying pressure will influence the infiltration. This can be done by making alterations to the Cassie-Baxter and Wenzel equations. Infiltration with a wetting fluid requires a finite pressure to allow the substances to pass through the material. Looking at Alier Ledgers *et al.*[226] remarks about infiltration wetting is that the work of immersion, work required to exchange the surface energy (γ_{sv}) to the solid-liquid interface (γ_{lv}) [226], is not proportional to the pressure required to aid complete infiltration. Towards the end of a total infiltration, the interface with lithium will be far greater than the liquid tension of lithium on the surface[226]. Although through their findings, there is a threshold pressure that will allow for and aid the infiltration of a melt into the pores, especially in poor wetting situations like the Wenzel state.

However, with Wenzel states, a vacuum in the pores beneath the liquid metal might draw it into pores since the capillary pressure from trapped gas in the pores are the cause for holding the melt at the surface. As shown in Cassie-Baxter states. Applying pressure on solid oxide electrolytes with a lithium melt is feasible, but using different alloys at the interface is the preferable choice. By calculating the work of immersion and considering the surface area and volume fraction of sol-coverage, the reversible work of infiltration for lithium in these materials can be determined. Like other surface and interface energies, these values are qualitative rather than providing a precise measure of the energy needed for lithium infiltration.

Instead of using contact angles, an AFM can produce adhesion maps with Gwydion (version 2.57) microscopy software (Figure 5-13). Such mapping was done on an LLTZO pellet with LLTO coating. There are adhesion spikes linked to the LLZO material's pores, though these values are much smaller than the total interface interaction, as seen in Figure 5-10. Adhesion wells on the pores coincide with the SEM images showing a thicker LLTO coating. The adhesion values in the map, recorded with water, are notably less forceful than in wetting experiments, highest reported adhesion value is in the nN range, which translates to x10^{-6} mJ m^{-1}. Adhesion variations within the pores vary by a factor of ten, ranging from 317 x10^{-6} mJ m^{-1} to 53 x10^{-6} mJ m^{-1}.

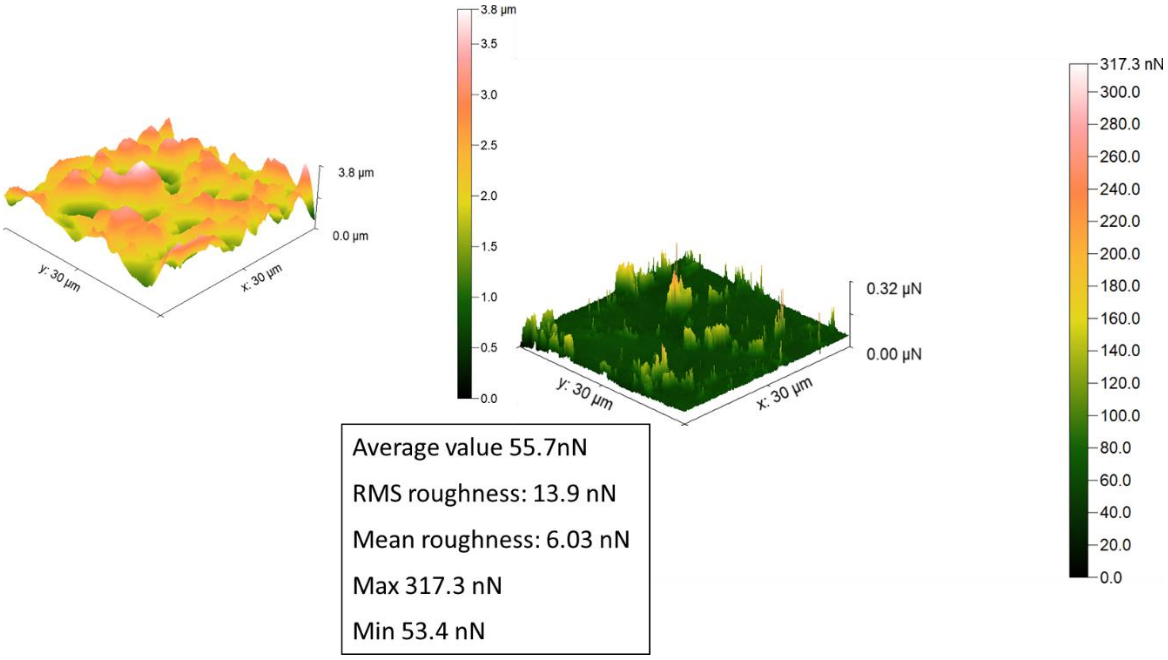

Average value 55.7nN

RMS roughness: 13.9 nN

Mean roughness: 6.03 nN

Max 317.3 nN

Min 53.4 nN

Figure 5-13: Adhesion map of pH 6 10 wt.% PVA $Li_{0.35}La_{0.65}TiO_3$ *(LLTO) mixed-phase sol and on the* $Li_{6.4}La_3Zr_{1.4}Ta_{0.6}O_{12}$ *(LLZO) pellet by a tiny area using AFM.*

With the highest adhesion values occurring, infiltration of a liquid metal usually occurs when high pressure allows the liquid to overcome the capillary pressure in the pores of the ceramic[234]. The main form of capillary pressure is called the threshold pressure (P_c), the critical pressure in which the melt will begin to infiltrate into a pore[235]. Threshold pressure is linked to an equation that Alier ledgers *et al.*[226] used to determine the pressure ranges in their wetting experiments and looks at the contact angle of melt against the side of the wall of the pore (θ), the surface tension of the melt γ_{lv} and the effective pore radius (r_{eff}) (Equation 5.1)[233,234]. In the tape casting system, a pore radius of 10 µm is typical due to burning off the pore-formers. With this equation, the contact angle of the material in the pores will need to be either 90° or 60°, and then pore infiltration is possible[234]. In the lower angle systems, then, it appears there are irreversible energy losses that occur[233]. Although we cannot observe the contact angles in the pores from our experimental set-up, the coverage is better, so it is assumed that the LLTO coverage present on the surface will act like in the pores considering no smoothing to the surface has occurred.

$$P_c = -(\frac{2\gamma_{lv}}{r_{eff}}) \cos\theta$$

Equation 5.1

Achieving a contact angle below 90° does not guarantee perfect wetting infiltration due to the roughness and non-parallel nature of pore walls, which hinder movement[234]. By considering the contact angle of the sol covering and the lithium melt's surface tension, the ratio of threshold pressure to the effective radius of the pores in the pellet can be determined. Modifying Equation 5.1 to incorporate the reciprocal of the surface tension of the metals as the variable in a new figure (x-axis) and the measurable as the cosine of the contact angle (y-axis), the negative gradient can be the ratio, provided the variable is also multiplied by two (Equation 5.2).

$$\cos\theta = -\frac{1}{2\gamma_{lv}}\frac{P_c}{r_{eff}}$$

Equation 5.2

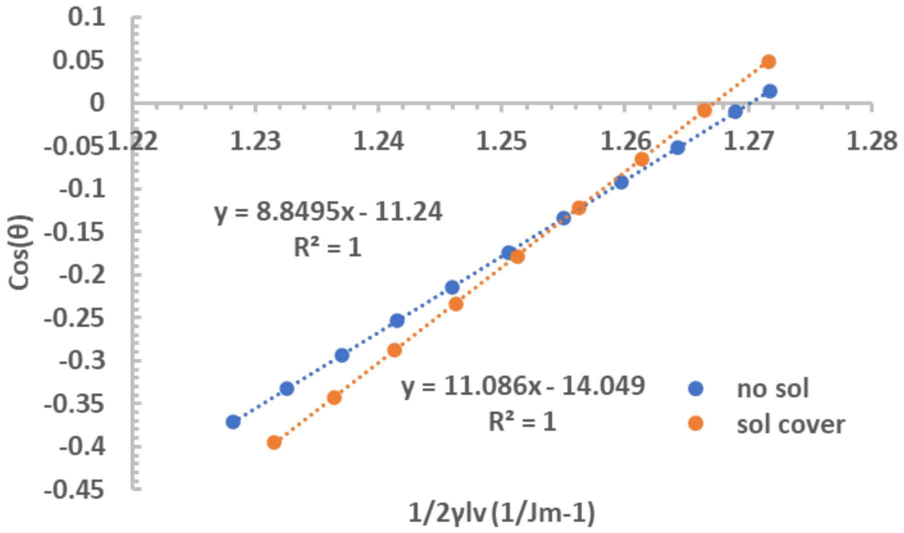

Figure 5-14: Comparison of the threshold pressure to the effective radius of the pores as lithium melts and wets the surface of a $Li_{6.4}La_3Zr_{1.4}Ta_{0.6}O_{12}$ (LLZO) pellet coated by pH 6 10 wt.% PVA $Li_{0.35}La_{0.65}TiO_3$ (LLTO) mixed-phase sol.

By analysing the negative gradients, the ratio of threshold pressure to pore's effective radius shows values of -8.85 for the uncovered $Li_{6.4}La_3Zr_{1.4}Ta_{0.6}O_{12}$ pellet and -11.09 with a $Li_{0.35}La_{0.65}TiO_3$ coating. These negative values suggest a specific vacuum pressure is essential for melt infiltration into the pores. Additionally, the sol coating demands a stronger vacuum due to added Van der Waals forces the lithium must overcome for infiltration. The cosine function has maximum and minimum values that can exist are 1 and -1, implying that this equation ideally does not represent this system effectively, further proving Alier ledgers *et al.*[226] points that pressure of infiltration is not proportional to the work of infiltration of the system. A comparative study shows that work of infiltration of a sol-covered system would require more pressure than a pellet without the process not requiring a vacuum if the surface tension of the melt is higher enough.

In Figure 5-14, a positive value of Cos(θ) indicates lower surface tension. Modifying the lithium's surface tension can enhance its infiltration into a solid-oxide electrolyte, improving contact. Achieving complete infiltration might require using a suitable adhesion alloy to adjust the melt's surface tension and applying a specific pressure. However, when alloying lithium, one must consider the reduced fermi level, which can result in capacity loss and potentially limit SEI formation[236].

5.3.4 Ionic conduction properties of the LLTO thin film on the LLZO pellet

It has been shown that a coating of LLTO protects the surface of LLZO material (Figure 5-8). It is therefore necessary to see if there are any detrimental effects of these LLTO coatings. Unfortunately, the LLTO coating of LLZO was used in the patent work for Dr. Mihkel Vestli work so to show the effects of LLTO coatings ionic conduction effects LLTO was coat onto LLTO pellets.

An EIS was taken of the same 'rough' LLTO pellet used previously in chapter 4.3.5 (Figure 4-27) with this LLTO sol deposit on top using gold-blocking electrodes in a symmetrical arrangement (Figure 5-15 and Table 5.1). There appears to be a shift in either the grain boundary resistance or the bulk resistance. Even using equivalence circuits, it would be hard to determine which ionic processes have increased impedance. XRD data and SEM could show that the bulk grains have increased in size, thus a higher impedance or that the film has created a layer distance for Li-ion transport. The ionic conduction shows a slight decrease in ionic conduction but a slight lowering of the activation energy (Figure 5-16). This decrease could be due to an increase in the bulk, meaning more La channels for lithium transportation.

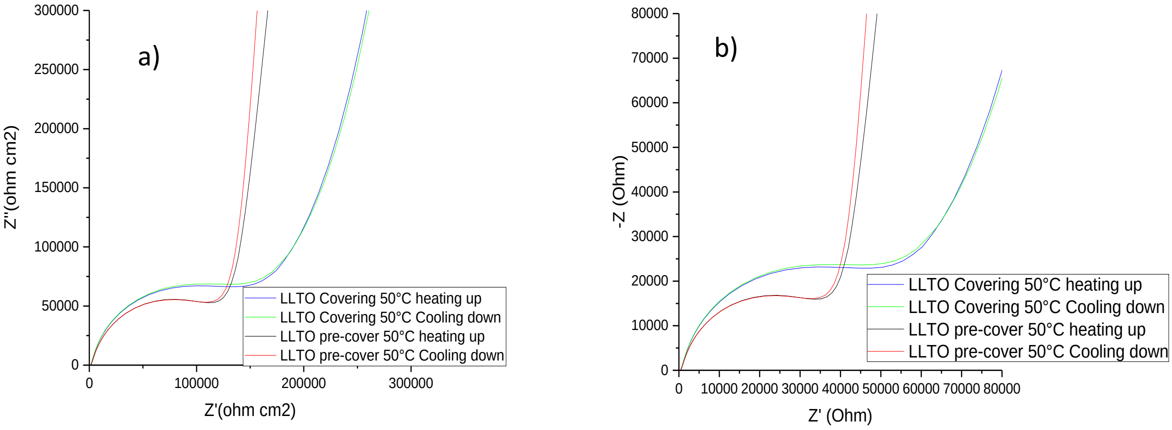

Figure 5-15: EIS of LLTO' rough' pellet synthesised at 1200°C for 2 hours at pH five before and after sol LLTO depositing. Graph a) considers the size of the pellet, and graph b) is the arcs from the direct current response.

Table 5.1: The average values of the arcs from EIS spectra a) at increasing and decreasing 50°C. Recording the average max frequency, resistance, and capacitance of the $Li_{0.5}La_{0.5}TiO_3$ *with and without the sol precursor covering.*

State of coating	**Average max frequency (Hz)**	**Average resistance (Ω)**	**Average capacitance (F cm^{-1})**
Covering	2657.25	65934	5.43x10^{-9}
Pre-cover	3882	47900	5.10 x10^{-9}

The activation energies between the LLTO pellet are 0.416 eV without any sol coverage, and then with sol coverage, it reads as 0.414 eV with only 0.002 eV that can be affected by errors from the instruments, it is safe to consider that the sol coverage has migrated to the bulk, providing more significant arcs. The activation energies are still within the range of expected LLTO materials, though, between 0.3 and 0.4 eV[31]. There is no sol coverage below the gold electrode, and the 1-micron layer has a beneficial effect on the ionic movement of lithium through the electrolyte. One possibility is that lithium is drawn across the interface to the electrolyte due to an increased concentration gradient. Therefore, resulting in a new phase is formed at the interface. The symmetrical gold coating EIS tests were done again, knowing the cubic structures of $Li_{0.5}La_{0.5}TiO_3$ synthesised at 1350°C for 6 hours using a lower temperature range (Figure 5-17). The LLTO pellet without coating had a thickness of 0.06 cm and an area coverage of gold of 0.199 cm^{2,} and the LLTO with a sol coverage had a thickness of 0.04 cm and a gold area of 0.20 cm^2.

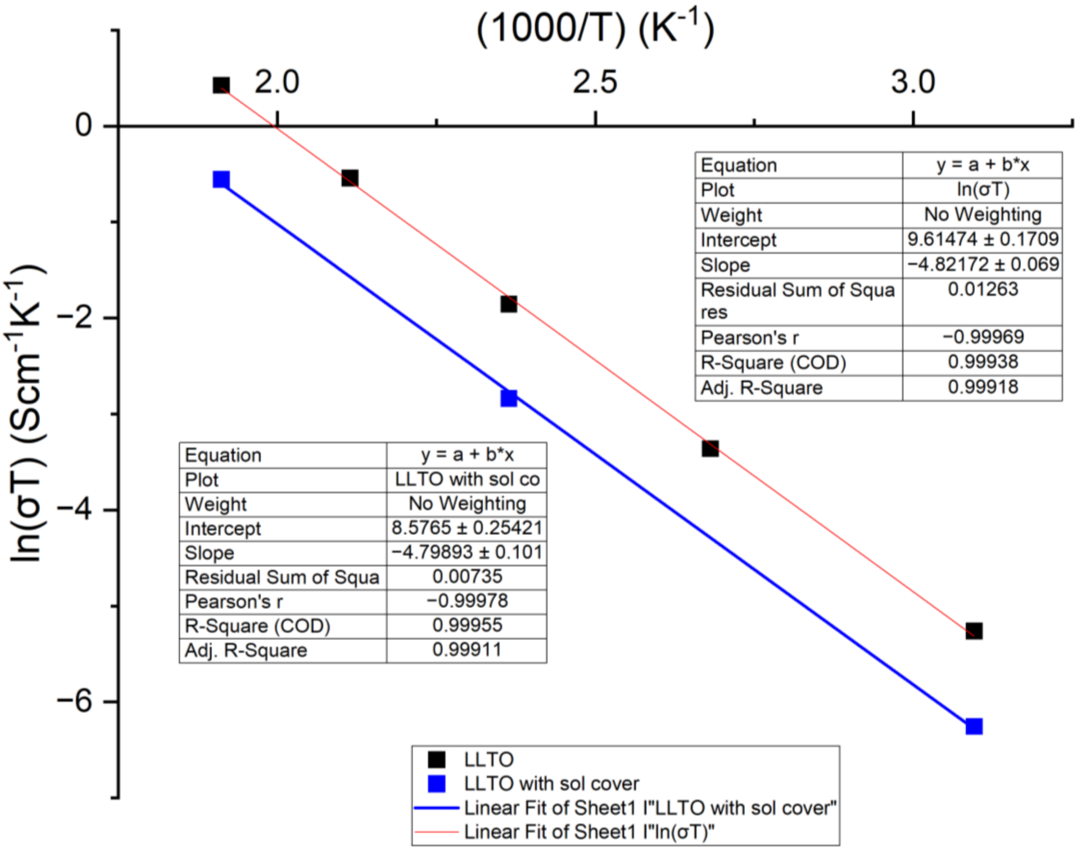

Figure 5-16: Arrhenius response of the rough' LLTO pellet with and without the LLTO sol coating. The activation energy is the gradient of the trendlines.

Using the LLTO pellet, the total resistance was observed to decreases as temperature rises, consistent with the ion hopping model based on the Arrhenius equation[20,203]. The characteristic capacitance of both pellets is not shifting from 10^{-10} F cm^{-1} characteristic of electrolyte grain boundary characteristics[151]. The sol coating appears to decrease the resistance of the grain boundaries indicating that there is a better movement of lithium as a response to the coating. This improvement is different to the previous arcs in Figure 5-15, and an explanation would be the phase stability of LLTO synthesised at 1350°C for 6 hours rather than the LLTO material synthesised at 1200°C for 2 hours. Furthermore, it implies that the LLTO coated on this surface acts as a protective barrier rather than a lithium source for the phase growths of LLTO.

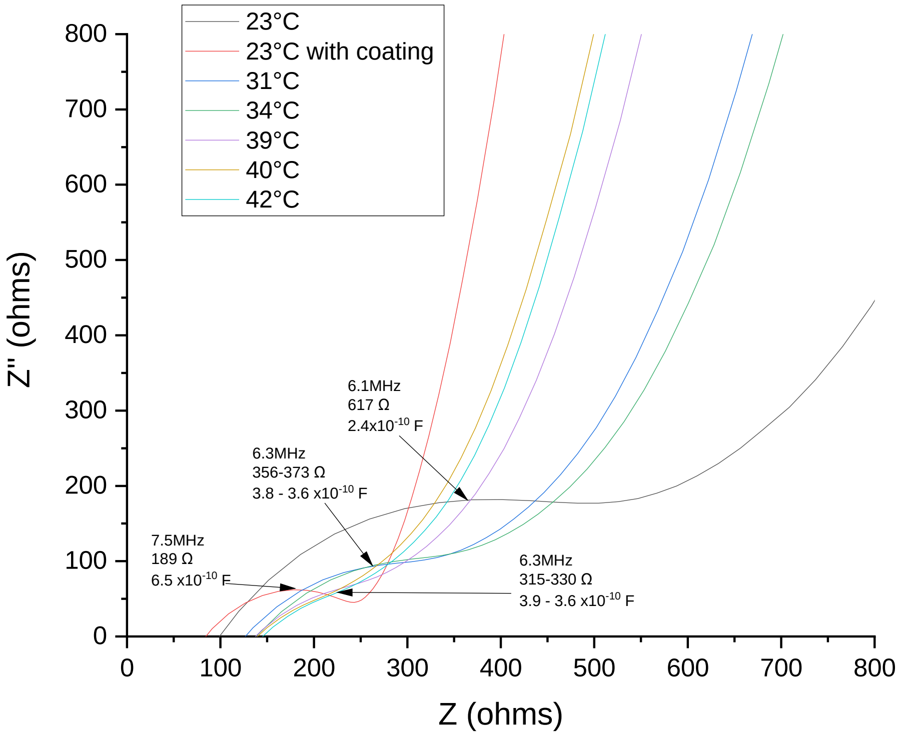

Figure 5-17: EIS of cubic $Li_{0.5}La_{0.5}TiO_3$ pellet sintered at 1350°C for 6 hours and from the same LLTO batch a with a $Li_{0.5}La_{0.5}TiO_3$ sol percussor material dropped off on the surface of the material.

Although it was possible to see the complete arcs of the uncoated $Li_{0.5}La_{0.5}TiO_3$ pellet upon switching to the coated pellet with the LLTO coating on top, there was a snap of the gold wire connecting the pellet to the equipment, only allowing in one arc of the coated sample as no other data beyond that temperature was collected. One of the promising factors was that the sol coating allowed for a decrease in the resistance despite previous thoughts that the LLTO would add to the bulk. With concern, it was due to the distance and area variation between the two pellets that the Nyquist plot can be represented to include cm^2 considering the mean accessible pathway the lithium would travel. The resistance with the coating is still lower but is a straight line rather than an arc (Figure 5-18).

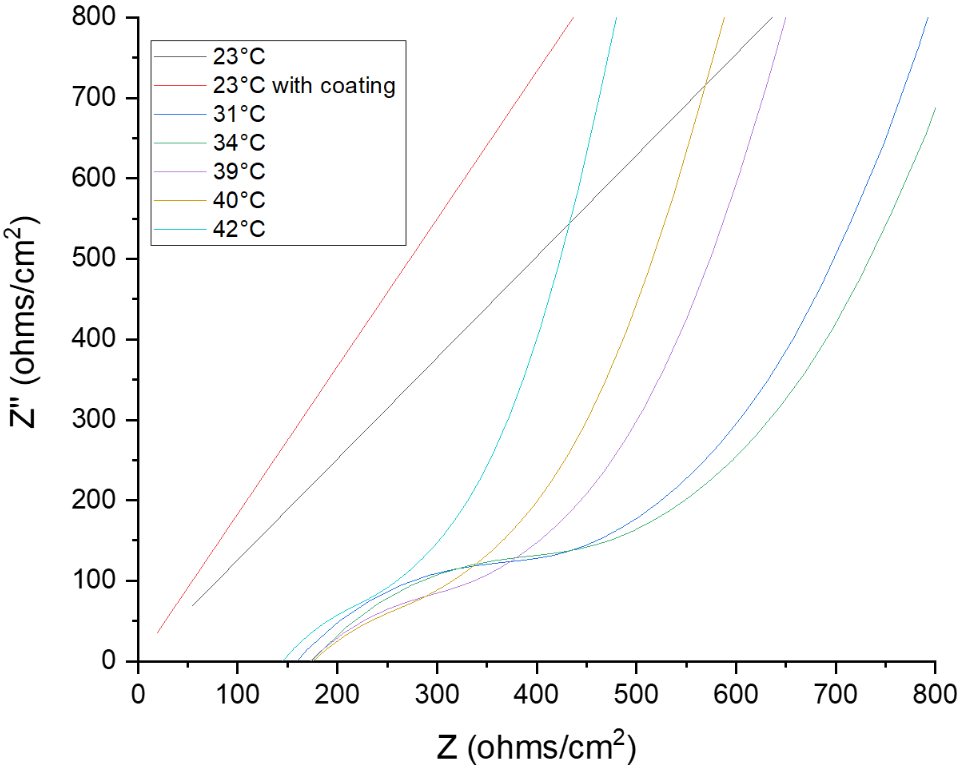

Figure 5-18: EIS of mostly cubic $Li_{0.5}La_{0.5}TiO_3$ pellet sintered at 1350°C for 6 hours and from the same LLTO batch a with a $Li_{0.5}La_{0.5}TiO_3$ sol percussor material dropped off on the surface of the material. The area of the gold coverage is considered and provides the units.

Taking the Arrhenius behaviour of the LLTO pellet and the single point of the LLTO coating on the LLTO pellet of the same material, we find that the activation energies of the uncoated pellet are while it is not possible to say what the activation energy of the coating of the LLTO pellet is 0.48 eV (Figure 5-19). What can be said that at 23°C the uncoated pellet had an ionic conduction of $4.9x10^{-3}$ Scm^{-1} while the coated sample produces an ionic conduction of $1.09x10^{-2}$ Scm^{-1}.

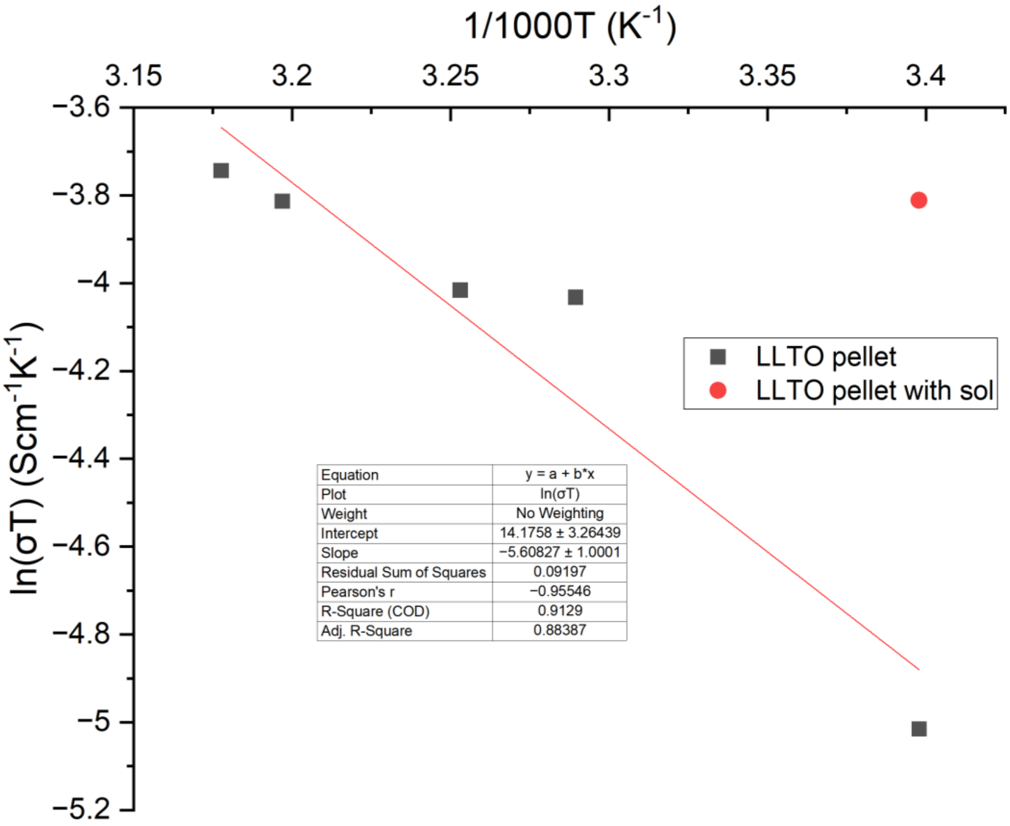

Equation	y = a + b*x
Plot	ln(σT)
Weight	No Weighting
Intercept	14.1758 ± 3.26439
Slope	−5.60827 ± 1.0001
Residual Sum of Squares	0.09197
Pearson's r	−0.95546
R-Square (COD)	0.9129
Adj. R-Square	0.88387

Figure 5-19: Ionic conduction values of mostly cubic $Li_{0.5}La_{0.5}TiO_3$ *pellet sintered at 1350°C for 6 hours and from the same LLTO batch a with a* $Li_{0.5}La_{0.5}TiO_3$ *sol percussor material dropped off on the surface of the material.*

A repeated experiment with improved electrode contact is ideal. However, the coating can enhance lithium ionic conduction at the electrode-electrolyte interface, given complete coverage by the electrolyte and no lithium loss to side phases.

5.3.5 Spray coating LLTO and water content in the sol-precursors

To fine-tune LLTO coating parameters on LLZO pellets, including mass application, solvent evaporation temperature, and heating duration, experimentation with LLTO coatings on LLTO pellets was essential to avoid wasting LLZO material provided by Dr. Mihkel Vestli. As part of these optimizations, the feasibility of spray-coating LLTO sol precursors onto an LLZO pellet was tested, using an LLTO pellet to conserve materials.

When LLTO is coated onto a LLTO pellet, it is unclear if the sol coating is surface-spread or has diffused into the bulk. Using LLTO sol on an LLTO pellet sintered at 1100°C for 2 hrs in pure argon showed no distinct covering like with LLZO. However, the EDS (Figure 5-20) indicated otherwise.

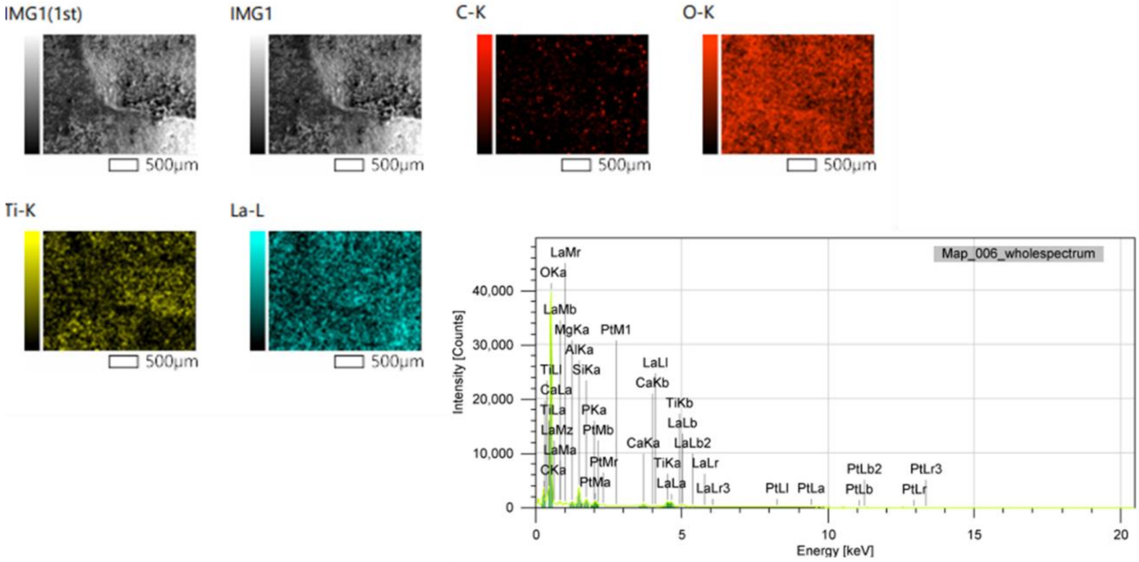

Figure 5-20: LLTO sol depositions after spray coating on LLTO, sintered at 1100°C for 2hrs, after heating the pellet to 205°C on the hot plate and then sintering at 1100°C for 2 hours in zero grade argon.

TGA of the sol-precursors of $Li_{0.5}La_{0.5}TiO_3$ (Figure 5-21) follows the same heating profile of the sol deposition on any of the solid oxide electrolyte surfaces. To investigate any adhesion issues with some of the deposited LLTO not chemically binding to the surface of the LLZO substrates. When the sol used to synthesise the LLTO pellets was statically dropped on solid electrolyte surfaces, it needed to dehydrate first. The solid electrolyte dried off in the oven to dehydrate the sample and then heated to 750°C in a tube furnace in a dry room. Then switched to zero argon and heated to 1000°C.

The evaporation of water starting at 35°C mass starts at 97.77 % going down to 11.73% at 105°C indicates that most of the sol covering is water. Which is to be expected with sol precursors at a concentration of 0.4 M. Therefore, multiple drops of LLTO will be needed for a complete covering. Alternatively, the volume of water used in the sol precursors must significantly reduce LLTO over the LLZO surface. Instead of fixing the volume of water to create a required concentration of precursors, this can be achieved by adding the solvent to dissolve the precursors.

The mass drops from the DTA exothermic bump at 475°C (-0.105 mW/mg) to 495.175°C (0.1683 mW/mg) due to the nitrates burn-off. This exothermic peak explains that a slower heating rate is needed up to 500°C to allow the nitrates to decompose slower. With a heating rate of 5°Cmin$^{-1,}$ particles appear at the surface of the pellets as the precursors expand quickly before the burn-off step leaving particles that are not in contact with the pellet surface. Therefore, the precursor materials form as a powder when exposed to the air and do not chemically bond to the pellet's surface.

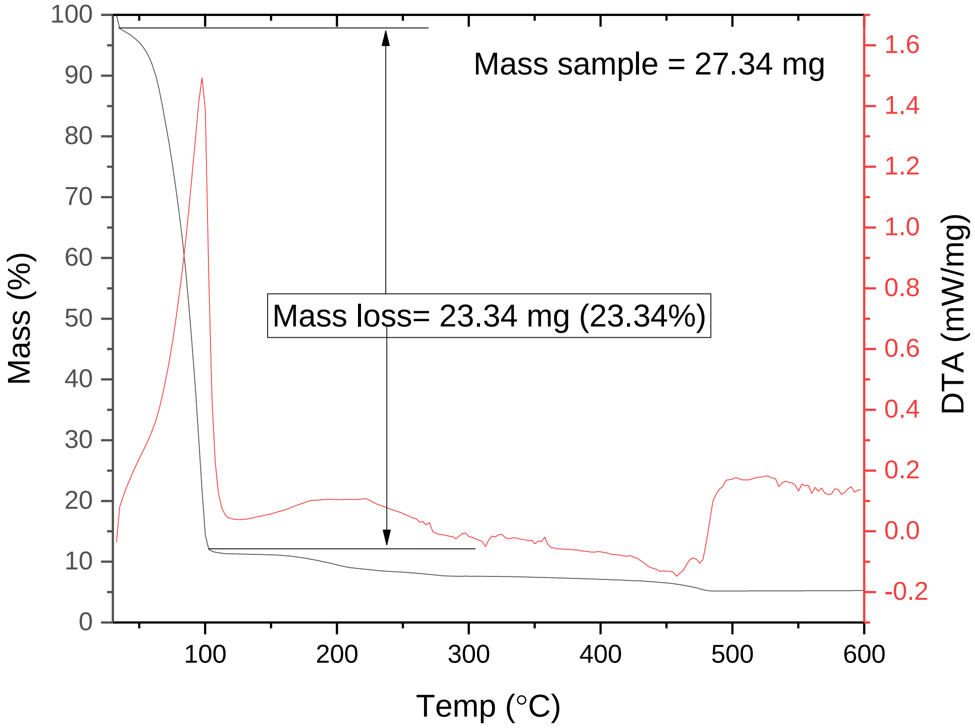

Figure 5-21: TGA and DTA of a drop of the LLTO sol to create a sacrificial LLTO layer.

5.3.6 Addition with $LiFePO_4$

While working to spread the LLTO coating over the LLZO results, it was considered to see the stability of LLTO on the positive electrode. Since LLZO can use an alloy of lithium to improve the surface tension, there is a desire to test with a full cell, and one of the positive electrodes (called cathode conventionally) is suitable in current geopolitical climates is $LiFePO_4$(LFP). A colleague in China (China Da Li and Zhiyong) are currently working on the sol-gel synthesis of the popular cathode material of $LiFePO_4$. Replicating their synthesis route was able to be followed, and a LFP with minimum impurities (Figure 5-22 and Figure 5-24) was formed with a homogenous spread of elements (Figure 5-22). The reference is $LiFePO_4$ XRD pattern provided by ICSD reference from Oshinari, T. *et al* paper[237] (Figure 5-22 and Figure 5-24).

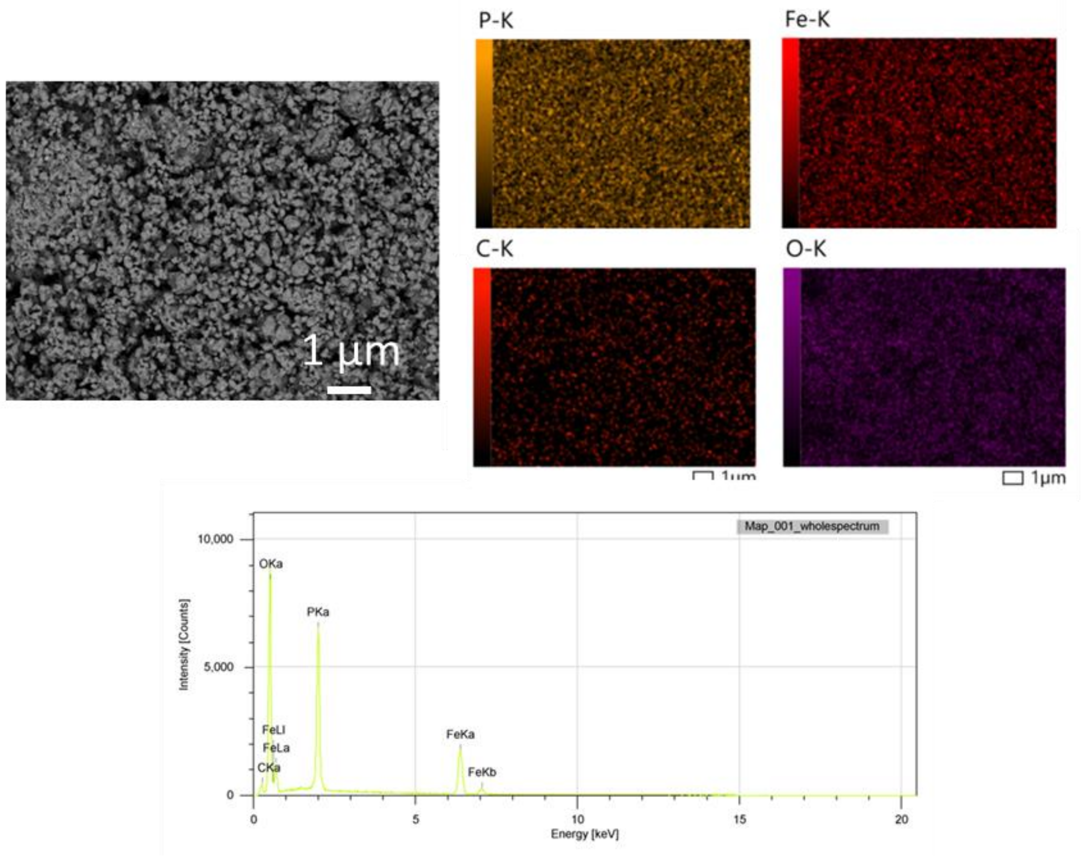

Figure 5-22:EDX mapping of $LiFePO_4$.

Using EDX, it is possible to take points for compositional analysis to help present an idea of the composition and to check the atomic and weight percentages (Table 5.2). This will be used to help make comparisons later and although the lithium cannot be measured with EDX this ratio of elements is to be expected.

Table 5.2: A EDX average over ten points to check the composition of the sol-gel synthesis $LiFePO_4$

Element	Mass (%)	Atomic (%)
C	5.21 ± 1.3	10.13 ± 2.5
O	41.46 ± 2.5	60.6 ± 3
P	20.32 ± 0.7	15.36 ± 0.8
Fe	32.85 ± 1.6	13.77 ± 0.9
Total	100	100

Looking at the material compared to the know olivine, orthorhombic structure with known unit cell parameters of a = 10.348 (24) Å b = 6.0181 (7) Å and c = 4.6997 (12) Å (LFP reference material in Figure 5-24, generated from a ICSD reference)[237], the Braggs positions match with the synthesised material. There is fluorescence noise in the background of the LFP sample because of Fe being very close in elemental size to the Cu this ionising X-rays will lead to the ionising of iron instead of diffraction.

When looking at the stability of LFP with LLTO (Figure 5-25), different synthesis conditions were applied as a $Li_{0.3}La_{0.63}TiO_3$ pellet powder (LLTO in Figure 5-25) was mixed into the LFP powder in a 1:1 ratio. Sintering the mixture in a reducing environment like in the pure synthesis route provided (5% H_2 in Figure 5-23) presented Bragg's positions of the peaks of the underlying LFP and LLTO precursors, implying that no reaction occurred. A discolouring of the mixture to a grey colour indicated a reaction between the LFP and the LLTO powder. Either as a reduction of the iron or removal of lithium from the LLTO. The LLTO material was also compared to Nb-LLZO as there were multiple of those casts available and provided by Dr. Mihkel Vestli. Nb-LLZO was noted to not be stable with LFP as the PO_4^{-3} stretching peak disappears.

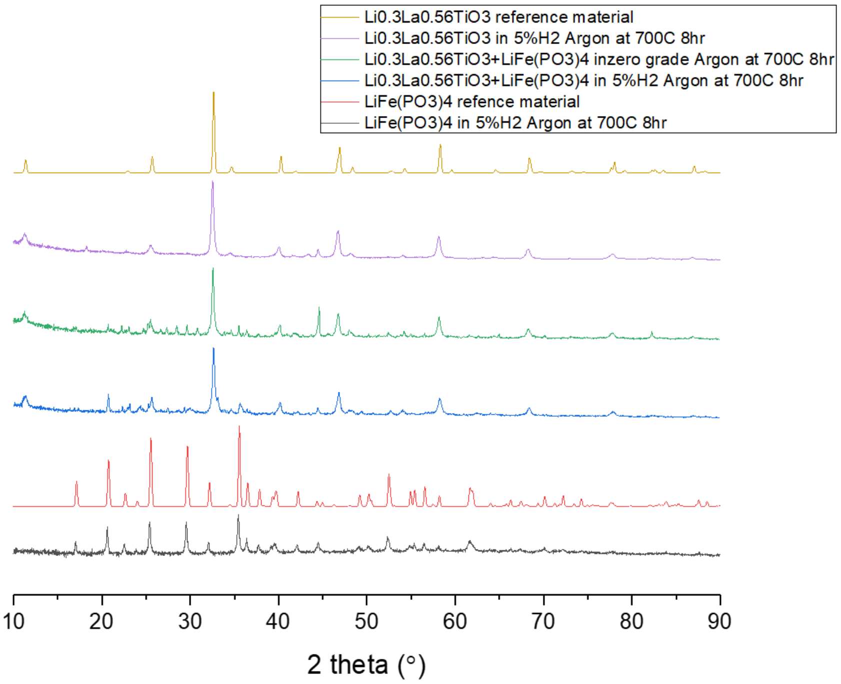

Figure 5-23: The XRD patterns of LiFePO$_4$ (LFP) and the Li$_{0.3}$La$_{0.63}$TiO$_3$ (LLTO) precursor materials before being mixed and at a 1:1 ratio, then sintered in H$_2$ atmosphere and Argon atmosphere at 700°C for 4 hours.

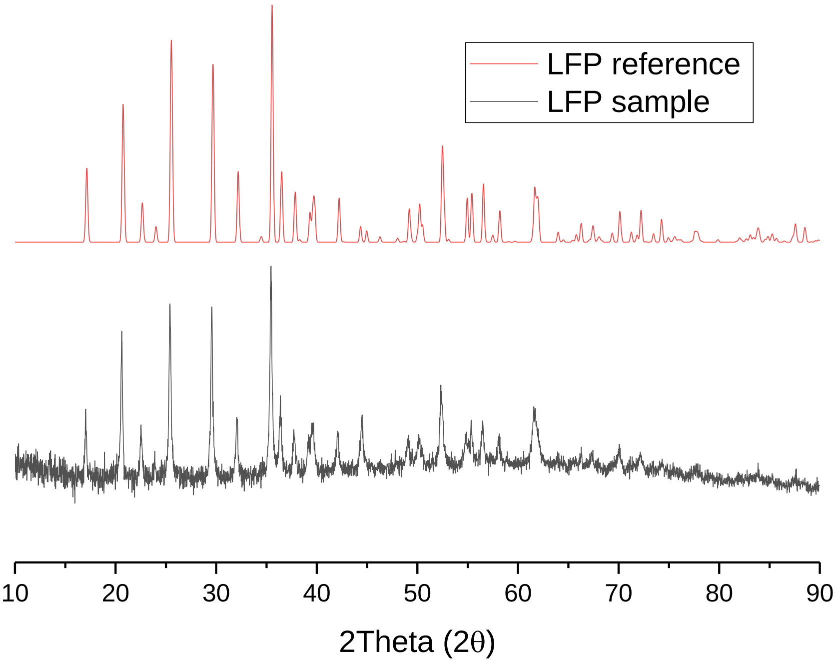

Figure 5-24: Synthesised LiFePO$_4$ (LFP, sample LFP) PXRD pattern compared to the reference PXRD of LFP orthorhombic structure presented by Takahiro Yoshinari (LFP reference)

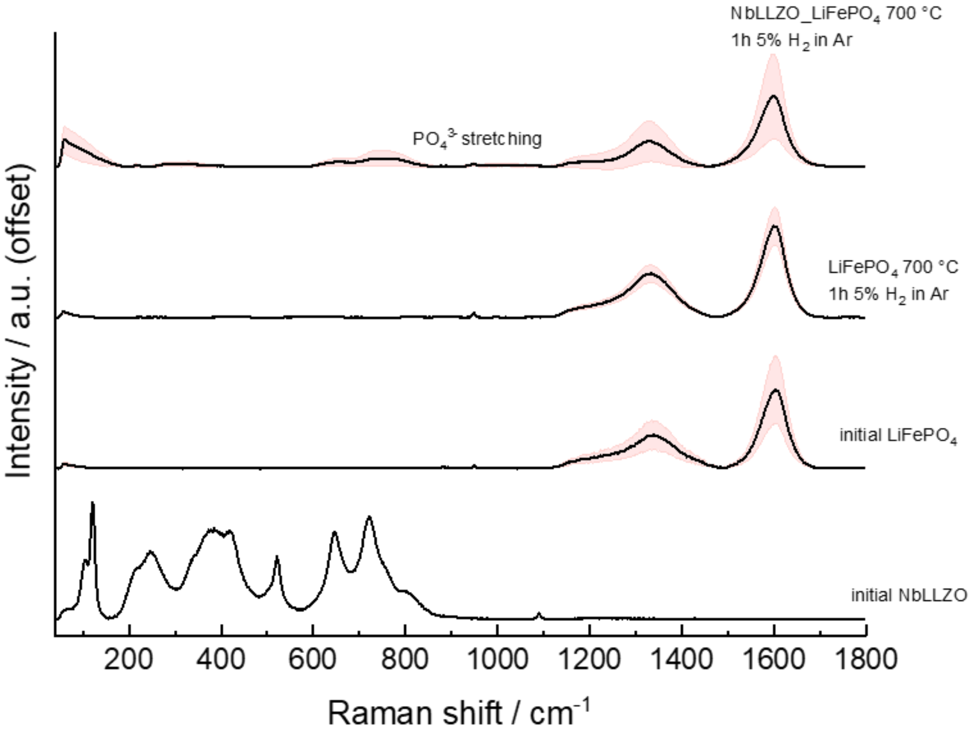

Figure 5-25: Raman spectra of $LiFePO_4$ mixing with $Li_{6.5}La_3Zr_{1.5}Nb_{0.5}O_{12}$ (NbLLZO) tape-casting.

As the LLZO tape cast, the system looked to have the best capabilities for providing good contact with lithium. The hope was to apply LFP as the positive electrode. However, after heating at 700°C for 4 hr in 5% H_2 in Argon (Figure 5-25), reactions formed Iron oxides and Li_3PO_4, and at the higher temperatures, the iron is reduced to Fe^0, leaving iron pieces (b in Figure 5-26).

With LLTO, it is a different story as when a 1:1 mix of LLTO to LFP material is milled together; there is a clear separation of both the LLTO and LFP, implying that there are no secondary phases forming upon contact of LFP at 700°C, 5% H_2 in Argon, temperatures (A in Figure 5-26). A possible application of LLTO coating besides being used on the negative electrode would be applying it to the positive electrode side to act as a protective barrier between the LLZO and LFP by coating the surface with LLTO. At 700°C, 5% H_2 in Argon, we see no secondary phases due to mixing with LFP, just a combination of the LLTO and LFP (Figure 5-27). With the addition of the carbon needed to improve the sample's ionic and electronic conductivity, we see the D and G bands at 1300 cm^{-1} and 1600 cm^{-1}, respectively, Figure 5-27. At 800°C, we see the formation of Iron oxides while the peaks of the cubic phases of LLTAO disappear, implying that lithium is reacting with the PO_4 and forming Li_3PO_4 which does not help maintain the contact as there is now a new surface that will need to undergo sintering although it is a practical ionic conductor for consideration in the future[238].

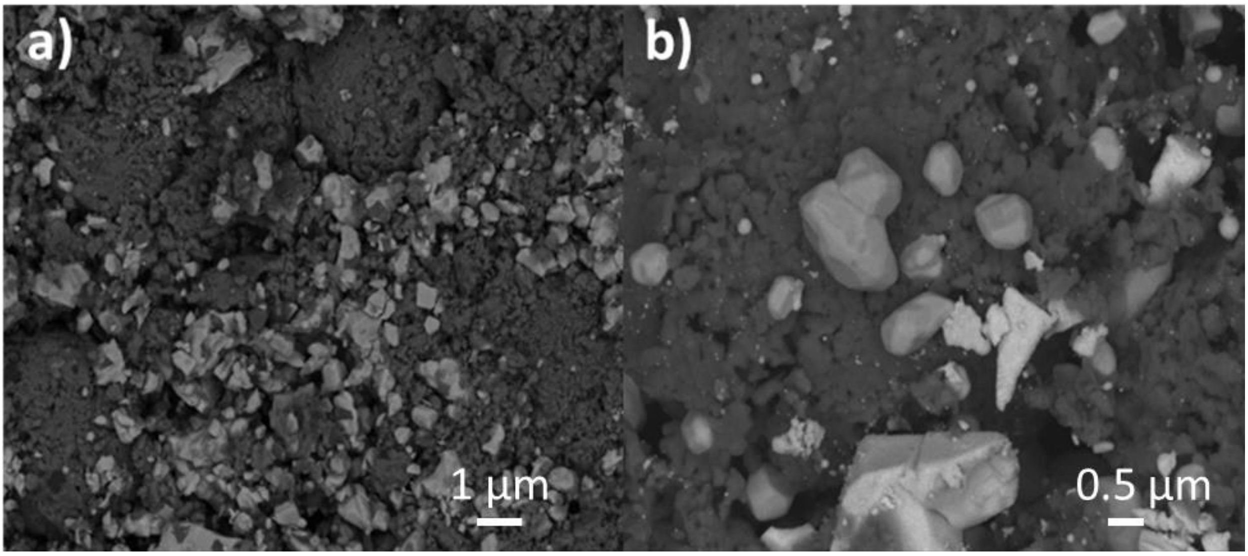

Figure 5-26: SEM images of a) $Li_{0.45}La_{0.55}Ti_{0.9}Al_{0.1}O_3$ mixed with $LiFePO_4$ and b) $Li_{0.65}La_3Zr_{1.5}Nb_{0.5}O_{12}$ mixed with $LiFePO_4$.

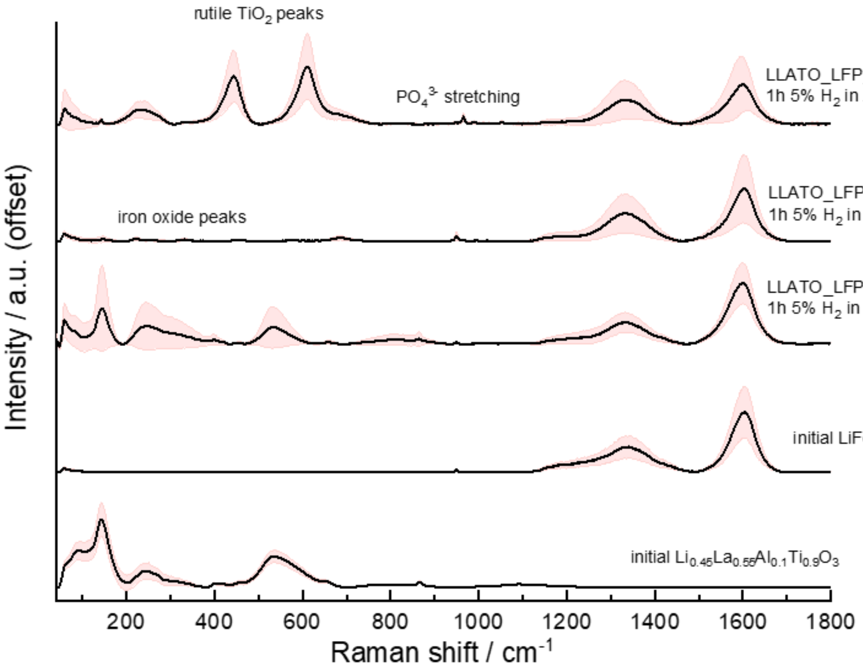

Figure 5-27:Raman spectra of mixing $Li_{0.45}La_{0.55}Ti_{0.9}Al_{0.1}O_3$ (LLATO) with $LiFePO_4$ (LFP) at different synthesis temperatures in a reducing atmosphere (H_2 in Argon)

At 900°C for 1 hour in the reducing atmosphere, the LLTO sample shows rutile peaks (around 400 and 520 cm^{-1}), a prerequisite to forming any of the Li_xTiO_3[197]

impurities (Figure 5-27). Small PO_4^{3-} peaks are observed linking to the formation of Li_3PO_4, which highlights more rich phosphorous areas using EDX seen as compositional box a) in Figure 5-28. There are slight peaks of pure iron oxide at 800°C mixture, confirmed in the EDX in box c) in Figure 5-28. Lithium in the LLTO may have reacted with the PO_4^{3-} resulting in a La-rich material which would be the parent material[239] of $La_{2/3}TiO_3$ (b) in Figure 5-28).

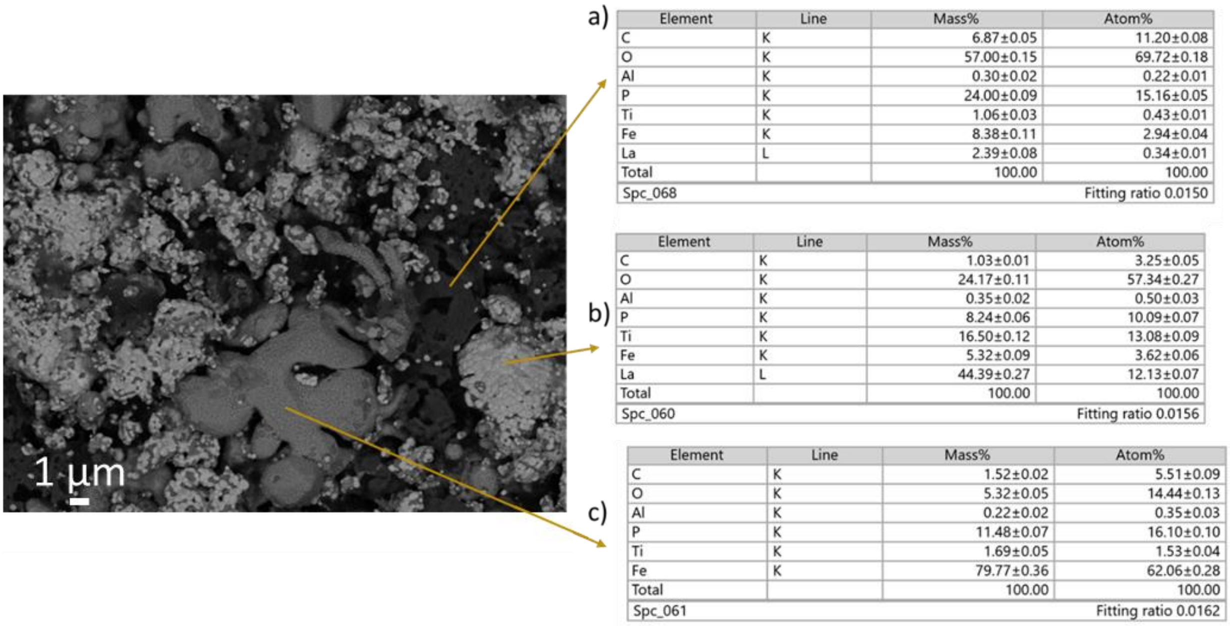

a)

Element	Line	Mass%	Atom%
C	K	6.87±0.05	11.20±0.08
O	K	57.00±0.15	69.72±0.18
Al	K	0.30±0.02	0.22±0.01
P	K	24.00±0.09	15.16±0.05
Ti	K	1.06±0.03	0.43±0.01
Fe	K	8.38±0.11	2.94±0.04
La	L	2.39±0.08	0.34±0.01
Total		100.00	100.00
Spc_068			Fitting ratio 0.0150

b)

Element	Line	Mass%	Atom%
C	K	1.03±0.01	3.25±0.05
O	K	24.17±0.11	57.34±0.27
Al	K	0.35±0.02	0.50±0.03
P	K	8.24±0.06	10.09±0.07
Ti	K	16.50±0.12	13.08±0.09
Fe	K	5.32±0.09	3.62±0.06
La	L	44.39±0.27	12.13±0.07
Total		100.00	100.00
Spc_060			Fitting ratio 0.0156

c)

Element	Line	Mass%	Atom%
C	K	1.52±0.02	5.51±0.09
O	K	5.32±0.05	14.44±0.13
Al	K	0.22±0.02	0.35±0.03
P	K	11.48±0.07	16.10±0.10
Ti	K	1.69±0.05	1.53±0.04
Fe	K	79.77±0.36	62.06±0.28
Total		100.00	100.00
Spc_061			Fitting ratio 0.0162

Figure 5-28: Mixing of $Li_{0.5}La_{0.5}Ti_{0.9}Al_{0.1}O_3$ with $LiFePO_4$ heating the material to 900°C for 1hr in 5% H_2 in argon Showing different phases purity with a) containing higher P and O, b) the LLTO material with some Fe implanted and c) with big drops of Fe on the surface.

A mixture of LLTO as a protective layer for LFP will need to be performed at the synthesis temperature and conditions to prevent any reduction and removal of iron to make iron particles with the lithium in the LFP.

5.4 Conclusions

Although imperfect, there is the possibility for $Li_{0.5}La_{0.5}TiO_3$ coating on the surface of the LLZO material. For LLTO surfaces, the LLTO coating integrates with the surface contributing to the bulk and aids the pellet's continued synthesis.

LLTO materials can allow for a good coating of a LLZO pellet, although incomplete coverage and voids are still present in the final product. Pores contained higher LLTO material, producing an adhesion well that would help the adhesion of lithium within a potential scaffold electrolyte. However, a Wenzel state occurs in these systems due to the capillary pressure of the pores underneath with increasing surface tension of the melt, allowing improved infiltration at a temperature higher than the melting point.

To optimize the solid-state electrolyte interface, alloying lithium is essential ensuring lithium's full integration into a porous solid oxide electrolyte.

Although there are still the same covering issues as with the LLTO sol precursor solution, the hope is that a lower temperature will speed up the coating process and further be a protective coating to the formation of $La_2Zr_2O_7$ impurities on any located LLZO materials.

The stability of LLTO when mixed with LFP at 700°C in a reducing atmosphere compared to LLZO is another future application worth continuing. In using LLTO as a covering for the cathode material, the covering issues would remain the same and is only stable at the synthesising temperature of LFP, but this means that LLTAO can be used to allow for a solid-state battery of LFP, improving the cycle life and costs of any possible, solid-state batteries.

Chapter 6 Conclusions

In this work, an aqueous sol-gel synthesis formed the Pseudo-cubic superstructure of $Li_{0.5}La_{0.5}TiO_3$ (LLTO) and an aluminum doped of $Li_{0.5}La_{0.5}Ti_{0.9}Al_{0.1}O_3$. It achieved a Pm-3m cubic symmetry with the unit cell parameter of approximately a= 3.86 (3) Å. Conduction measurements of the mixed phased $Li_{0.3}La_{0.56}TiO_3$ demonstrated conductions around x10^{-5} Scm$^{-1,}$ which were on the low side of the ionic conduction but to be expected with the more considerable activation energy than other reported LLTO electrolytes. It was found that its reduction of the Ti^{4+} as it alloys to lithium is worthy of further investigation to improve the contact of lithium to the electrolyte. This electrolyte's stability to LFP and in the air compared to the garnet material of LLZO, is a promising characteristic and worthwhile pursuing in the realms of industrial applications.

A theoretical set of wetting experiments were performed to understand metallic lithium's intrinsic wetting properties with the desired solid oxide electrolytes, LLTO and LLZO, for full solid states batteries. It was found that wetting calculations using the contact angle of lithium are a challenge, due to the errors that can occur in ensuring the correct angle, as an influence of the bulk of lithium melting by the degree of freedom and the Gibbs energy of reaction can be investigated. All materials require very little adhesion to remove the lithium unless it has been alloyed and reacted with the materials. Lithium's thermodynamic preference is to form a droplet on the surface regardless of whether gas prevents the partial filling of lithium into the pores. Applying a smaller layer of an alloying material was demonstrated to be the best method of improving not only the wettability of lithium on the surface of a solid oxide electrolyte material but also the filling of lithium into the pores of electrodes. Pore infiltration, in turn, increases the contact area of lithium to the electrolyte to improve electron transfer rates and minimise any impending creep reactions.

It was then clarified, by using coatings of the barriers of $Li_{0.3}La_{0.5}TiO_3$ that the contact of lithium improves on a micro-scale level, but there are still adhesion issues. The wetting experiments with a LLTO sol covering on LLZO demonstrated improved conduction values at x10^{-2} Scm^{-1} for lithium-ion transport. Furthermore, the capillary pressure investigation to the Wenzel states showed that higher temperatures (250°C) would need a positive pressure applied to help lithium impregnation, and at lower temperatures (around 180°C), stronger vacuums are needed for the infiltration.

The wetting experiments highlight that the optimisation of the interface of a solid oxide electrolyte for solid-state batteries is in the surface tension alteration of lithium itself. There will be a slight reduction in the overall voltage window and capacity, but the adhesion improvements and reduction of the interface resistance will be a starting point for commercialising solid-state batteries.

6.1 Future work

1. Confirm the ionic conduction values of $Li_{0.3}La_{0-63}Ti_{0.3}O_3$ and investigate the ionic conduction of $Li_{0.5}La_{0.5}Ti_{0.9}Al_{0.1}O_3$.

2. Experiment with dip coating a $Li_{0.5}La_{0.5}Ti_{0.9}Al_{0.1}O_3$ precursor on an LLZO garnet electrolyte. Observe coverage conditions and any improvement of coverage at the microscale level.

3. Make a complete cell test using LFP as the negative electrode and a lithium indium alloy as the positive electrode. The electrolyte would be a tape casted LLZO with LLTAO coating on the negative electrode and positive electrode side to prevent the capture of CO_2 on the surface and to prevent LFP reacting with LLZO.

Chapter 7 References

1. International Energy Agency. Global Energy Review 2021. in *Global Energy Review 2020* 1–36 (2021).
2. BloombergNEF. Long-Term Electric Vehicle Outlook 2022 | Full Report. *Bloomberg New Energy Finance* (2022). Available at: https://about.bnef.com/electric-vehicle-outlook/.
3. AMTE Power. *Ultra energy cells*. (2022).
4. AMTE Power. *Ultra High power cells*. (2022).
5. Nitta, N., Wu, F., Lee, J. T. & Yushin, G. Li-ion battery materials: Present and future. *Mater. Today* **18**, 252–264 (2015).
6. Chen, R., Qu, W., Guo, X., Li, L. & Wu, F. The pursuit of solid-state electrolytes for lithium batteries: From comprehensive insight to emerging horizons. *Mater. Horiz.* **3**, 487–516 (2016).
7. Kim, K. J., Balaish, M., Wadaguchi, M., Kong, L. & Rupp, J. L. M. Solid-State Li–Metal Batteries: Challenges and Horizons of Oxide and Sulfide Solid Electrolytes and Their Interfaces. *Adv. Energy Mater.* **11**, 2002689 (2021).
8. Zhang, Z. *et al.* New horizons for inorganic solid state ion conductors. *Energy Environ. Sci.* **11**, 1945–1976 (2018).
9. Zheng, F., Kotobuki, M., Song, S., Lai, M. O. & Lu, L. Review on solid electrolytes for all-solid-state lithium-ion batteries. *J. Power Sources* **389**, 198–213 (2018).
10. Choi, J. W. & Aurbach, D. Promise and reality of post-lithium-ion batteries with high energy densities. *Nat. Rev. Mater.* **1**, 16013 (2016).
11. Banza Lubaba Nkulu, C. *et al.* Sustainability of artisanal mining of cobalt in DR Congo. *Nat. Sustain.* **1**, 495–504 (2018).
12. Wang, A., Yiu, N. & Alter, E. Summer News Roundup. *Intercalation* (2022).
13. Oakes, M. J. A Brief History of Batteries and Stored Energy. *NETA World* 6 (2006).
14. Littlewood, P. A brief history of Batteries. 2–3 (2018).

15. Christensen, P. Introduction to electrochemistry. 1–43 (2018).

16. Pletcher, D. *A First Course in electrode processes*. (RSC, 2009).

17. Electrochemistry, S. Instrumental methods in electrochemistry 2019. 1–23 (2019).

18. Goodenough, J. B. Rechargeable batteries: Challenges old and new. *J. Solid State Electrochem.* **16**, 2019–2029 (2012).

19. Christensen, P. 6A Introduction to batteries. 1–20 (2018).

20. Irvine, J. T. S. CH5715-Energy conversion and storage. lecture 2, slide 12 (2018).

21. Bruce, P. G. *Solid State Electrochemistry*. (Cambridge University press, 1997).

22. Knauth, P. & Tuller, H. L. Solid-state ionics: Roots, status, and future prospects. in *J. Am Ceram Soc* **85**, 1654–1680 (Blackwell Publishing Inc., 2002).

23. Schipper, F. *et al.* Review—Recent Advances and Remaining Challenges for Lithium Ion Battery Cathodes. *J. Electrochem. Soc.* **164**, A6220–A6228 (2017).

24. Takada, K. Progress and prospective of solid-state lithium batteries. *Acta Mater.* **61**, 759–770 (2013).

25. Xie, J. & Lu, Y. C. A retrospective on lithium-ion batteries. *Nat. Commun.* **11**, (2020).

26. Takada, K. Progress in solid electrolytes toward realizing solid-state lithium batteries. *J. Power Sources* **394**, 74–85 (2018).

27. Sun, C., Liu, J., Gong, Y., Wilkinson, D. P. & Zhang, J. Recent advances in all-solid-state rechargeable lithium batteries. *Nano Energy* **33**, 363–386 (2017).

28. Brissot, C., Rosso, M., Chazalviel, J. N. & Lascaud, S. Dendritic growth mechanisms in lithium/polymer cells. *J. Power Sources* **81**–**82**, 925–929 (1999).

29. Li, S. *et al.* A multifunctional artificial protective layer for producing an ultra-stable lithium metal anode in a commercial carbonate electrolyte. *J. Mater. Chem. A* (2021).

30. Porz, L. *et al.* Mechanism of Lithium Metal Penetration through Inorganic Solid Electrolytes. *Adv. Energy Mater.* **7**, (2017).

31. Knauth, P. Inorganic solid Li ion conductors: An overview. *Solid State Ionics* **180**, 911–916 (2009).

32. Lahiri, A. K. Transport phenomena and metals properties. in *Fundamentals of Metallurgy* 178–236 (Elsevier, 2005). doi:10.1533/9781845690946.1.178

33. Janek, J. & Zeier, W. G. A solid future for battery development. *Nat. Energy* **1**, (2016).

34. Baker, R. T. CH3513 Semiconductor science. (2016).

35. Randau, S. *et al.* Benchmarking the performance of all-solid-state lithium batteries. *Nat. Energy* **5**, 259–270 (2020).

36. The Faraday Institution. *Solid-State Batteries for Commercial Applications*. (2020).

37. Lin, D., Liu, Y. & Cui, Y. Reviving the lithium metal anode for high-energy batteries. *Nat. Nanotechnol.* **12**, 194–206 (2017).

38. He, M., Cui, Z., Chen, C., Li, Y. & Guo, X. Formation of self-limited, stable and conductive interfaces between garnet electrolytes and lithium anodes for reversible lithium cycling in solid-state batteries. *J. Mater. Chem. A* **6**, 11463–11470 (2018).

39. Harry, K. J., Hallinan, D. T., Parkinson, D. Y., MacDowell, A. A. & Balsara, N. P. Detection of subsurface structures underneath dendrites formed on cycled lithium metal electrodes. *Nat. Mater.* **13**, 69–73 (2014).

40. Li, L. *et al.* design enables dendrite-free lithium metal. *J. Mater. Chem. A* (2022).

41. Luo, W. *et al.* Reducing Interfacial Resistance between Garnet-Structured Solid-State Electrolyte and Li-Metal Anode by a Germanium Layer. *Adv. Mater.* **29**, (2017).

42. Wenzel, S., Sedlmaier, S. J., Dietrich, C., Zeier, W. G. & Janek, J. Interfacial reactivity and interphase growth of argyrodite solid electrolytes at lithium metal electrodes. *Solid State Ionics* **318**, 102–112 (2018).

43. Wu, J. *et al.* In-situ formed shields enabling Li2CO3-free solid electrolytes: A new route to uncover the intrinsic lithiophilicity of garnet electrolytes for dendrite-free Li-metal batteries. *ACS Appl. Mater. Interfaces* acsami.8b18356 (2018).

44. Wang, M. & Sakamoto, J. Correlating the interface resistance and surface adhesion of the Li metal-solid electrolyte interface. *J. Power Sources* **377**, 7–11 (2018).

45. Han, F. *et al.* High electronic conductivity as the origin of lithium dendrite formation within solid electrolytes. *Nat. Energy* **4**, 187–196 (2019).

46. Monroe, C. & Newman, J. The Impact of Elastic Deformation on Deposition Kinetics at Lithium/Polymer Interfaces. *J. Electrochem. Soc.* **152**, A396 (2005).

47. Luntz, A. C., Voss, J. & Reuter, K. Interfacial Challenges in Solid-State Li Ion Batteries. *J. Phys. Chem. Lett.* **6**, 4599–4604 (2015).

48. Faraday, M. XX. Experimental researches in electricity.— fourth series. *Philos. Trans. R. Soc. London* **123**, 507–522 (1833).

49. Gao, J., Zhao, Y. S., Shi, S. Q. & Li, H. Lithium-ion transport in inorganic solid state electrolyte. *Chinese Phys. B* **25**, (2015).

50. Nernst, W. MATERIAL FOR ELECTRIC-LAMP GLOWERS. (1901).

51. Tubandt, C. & Lorenz, E. Molekularzustand und elektrisches Leitvermögen kristallisierter Salze. *Zeitschrift für Phys. Chemie* **87U**, 513–542 (1914).

52. Hagman, L.-O., Kierkegaard, P., Karvonen, P., Virtanen, A. I. & Paasivirta, J. The Crystal Structure of NaM2IV(PO4)3; MeIV = Ge, Ti, Zr. *Acta Chem. Scand.* **22**, 1822–1832 (1968).

53. Bruce, P. G. & West, A. R. The A-C Conductivity of Polycrystalline LISICON, Li2 + 2x Zn1 − x GeO4, and a Model for Intergranular Constriction Resistances. *J. Electrochem. Soc.* **130**, 662–669 (1983).

54. Robertson, A. D., West, A. R. & Ritchie, A. G. Review of crystalline lithium-ion conductors suitable for high temperature battery applications. *Solid State Ionics* **104**, 1–11 (1997).

55. Ohta, N. *et al.* Enhancement of the high-rate capability of solid-state lithium batteries by nanoscale interfacial modification. *Adv. Mater.* **18**, 2226–2229 (2006).

56. Kanno, R., Hata, T., Kawamoto, Y. & Irie, M. Synthesis of a new lithium ionic conductor, thio-LISICON-lithium germanium sulfide system. *Solid State Ionics* **130**, 97–104 (2000).

57. Sudworth, J. L. & Tilley, A. R. *The Sodium Sulfur Battery*. (Chapman & Hall, 1985).

58. Wang, J. C., Gaffari, M. & Choi, S. Il. On the ionic conduction in β-alumina: Potential energy curves and conduction mechanism. *J. Chem. Phys.* **63**, 772–778 (1975).

59. Lu, X., Xia, G., Lemmon, J. P. & Yang, Z. Advanced materials for sodium-beta alumina

batteries: Status, challenges and perspectives. *J. Power Sources* **195**, 2431–2442 (2010).

60. Bettman, M. & Peters, C. R. The crystal structure of Na2O·MgO·5Al2O3 with reference to Na2O·5Al2O3 and other isotypal compounds. *J. Phys. Chem.* **73**, 1774–1780 (1969).

61. YOUNGBLOOD, G. E., MILLER, G. R. & GORDON, R. S. Relative Effects of Phase Conversion and Grain Size on Sodium Ion Conduction in Polycrystalline, Lithia-Stabilized beta-Alumina. *J. Am. Ceram. Soc.* **61**, 86–87 (1978).

62. Meyer, W. H. Polymer electrolytes for lithium-ion batteries. *Adv. Mater.* **10**, 439–448 (1998).

63. Fenton, D. E., Parker, J. M. & Wright, P. V. Complexes of alkali metal ions with poly(ethylene oxide). *Polymer (Guildf).* **14**, 589 (1973).

64. Xu, K. Nonaqueous liquid electrolytes for lithium-based rechargeable batteries. *Chem. Rev.* **104**, 4303–4417 (2004).

65. Oh, D. Y. *et al.* Single-step wet-chemical fabrication of sheet-type electrodes from solid-electrolyte precursors for all-solid-state lithium-ion batteries. *J. Mater. Chem. A* **5**, 20771–20779 (2017).

66. Gao, J., Shi, S., Xiao, R. & Li, H. Synthesis and ionic transport mechanisms of α-LiAlO2. *Solid State Ionics* **286**, 122–134 (2016).

67. Aono, H., Sugimoto, E., Sadaoka, Y., Imanaka, N. & Adachi, G. Ionic Conductivity of the Lithium Titanium Phosphate Systems. *J. Electrochem. Soc* **136**, 590–591 (1989).

68. Zhang, Z. *et al.* New horizons for inorganic solid state ion conductors. *Energy and Environmental Science* **11**, 1945–1976 (2018).

69. Ulusoy, S., Gulen, S., Aygun, G., Ozyuzer, L. & Ozdemir, M. Characterization of thin film Li0.5La0.5Ti1−xAlxO3 electrolyte for all-solid-state Li-ion batteries. *Solid State Ionics* **324**, 226–232 (2018).

70. Teng, S., Tan, J. & Tiwari, A. Recent developments in garnet based solid state electrolytes for thin film batteries. *Curr. Opin. Solid State Mater. Sci.* **18**, 29–38 (2014).

71. JONES, S., AKRIDGE, J. & SHOKOOHI, F. Thin film rechargeable Li batteries. *Solid State*

Ionics **69**, 357–368 (1994).

72. Tong, Z., Wang, S.-B., Liao, Y.-K., Hu, S.-F. & Liu, R.-S. Interface Between Solid-State Electrolytes and Li-Metal Anodes: Issues, Materials, and Processing Routes. *Cite This ACS Appl. Mater. Interfaces* **12**, 47181–47196 (2020).

73. Suzuki, N., Inaba, T. & Shiga, T. Electrochemical properties of LiPON films made from a mixed powder target of Li 3PO 4 and Li 2O. *Thin Solid Films* **520**, 1821–1825 (2012).

74. Chen, C. H. & Amine, K. Ionic conductivity, lithium insertion and extraction of lanthanum lithium titanate. *Solid State Ionics* **144**, 51–57 (2001).

75. Zheng, Z., Fang, H., Liu, Z. & Wang, Y. A Fundamental Stability Study for Amorphous LiLaTiO 3 Solid Electrolyte. *J. Electrochem. Soc.* **162**, A244–A248 (2015).

76. Furusawa, S. I., Tabuchi, H., Sugiyama, T., Tao, S. & Irvine, J. T. S. Ionic conductivity of amorphous lithium lanthanum titanate thin film. *Solid State Ionics* **176**, 553–558 (2005).

77. Zhu, Y. *et al.* Lithium-film ceramics for solid-state lithionic devices. *Nat. Rev. Mater.* (2020).

78. Kirk, C. A. & West, A. R. Crystal structure of the perovskite-related phase of approximate composition LaLi1/3Ti2/3O3. *Solid State Sci.* **4**, 1163–1166 (2002).

79. Stramare, S., Thangadurai, V. & Weppner, W. Lithium Lanthanum Titanates: A Review. *Chem. Mater.* **15**, 3974–3990 (2003).

80. Varez, A., Fernández-Ďaz, M. T., Alonso, J. A. & Sanz, J. Structure of fast ion conductors Li3xla2/3-xTiO 3 deduced from powder neutron diffraction experiments. *Chem. Mater.* **17**, 2404–2412 (2005).

81. Moriwake, H. *et al.* Lithium Atom and A-Site Vacancy Distributions in Lanthanum Lithium Titanate. *Chem. Mater.* **25**, 1607–1614 (2013).

82. Inaguma, Y. *et al.* High ionic conductivity in lithium lanthanum titanate. *Solid State Commun.* **86**, 689–693 (1993).

83. Chen, C. H. & Du, J. Lithium ion diffusion mechanism in lithium lanthanum titanate solid-state electrolytes from atomistic simulations. *J. Am. Ceram. Soc.* **98**, 534–542

(2014).

84. Fourquet, J. L., Duroy, H. & Crosnier-Lopez, M. P. Structural and microstructural studies of the series La2/3-xLi3x□1/3-2xTiO3. *J. Solid State Chem.* **127**, 283–294 (1996).

85. Ruiz, A. Electrical properties of La1.33âˆ’xLi3xTi2O6 (0.1<x<0.3). *Solid State Ionics* **112**, 291–297 (1998).

86. Kwon, W. J. *et al.* Enhanced Li+ conduction in perovskite Li3XLa2/3-x□1/3-2xTiO3 solid-electrolytes via microstructural engineering. *J. Mater. Chem. A* **5**, 6257–6262 (2017).

87. Catti, M., Sommariva, M. & Ibberson, R. M. Tetragonal superstructure and thermal history of Li0.3La 0.567TiO3 (LLTO) solid electrolyte by neutron diffraction. *J. Mater. Chem.* **17**, 1300–1307 (2007).

88. Takada, K. Progress in solid electrolytes toward realizing solid-state lithium batteries. *J. Power Sources* **394**, 74–85 (2018).

89. West, A. R. *Solid state chemsitry and its applications*. (Wily, 2014).

90. Wu, J. F. *et al.* Supporting information for In-situ Formed Shields Enabling Li2CO3-Free Solid Electrolytes: A New Route to Uncover the Intrinsic Lithiophilicity of Garnet Electrolytes for Dendrite-Free Li-Metal Batteries, *ACS Appl. Mater. Interfaces*, **11**, (2018).

91. Wu, J. F. *et al.* In Situ Formed Shields Enabling Li 2 CO 3 -Free Solid Electrolytes: A New Route to Uncover the Intrinsic Lithiophilicity of Garnet Electrolytes for Dendrite-Free Li-Metal Batteries. *ACS Appl. Mater. Interfaces* **11**, 898–905 (2019).

92. Sudo, R. *et al.* Interface behavior between garnet-type lithium-conducting solid electrolyte and lithium metal. *Solid State Ionics* **262**, 151–154 (2014).

93. Sharafi, A. *et al.* Surface Chemistry Mechanism of Ultra-Low Interfacial Resistance in the Solid-State Electrolyte Li7La3Zr2O12. *Chem. Mater.* **29**, 7961–7968 (2017).

94. Yang, C. *et al.* Garnet/polymer hybrid ion-conducting protective layer for stable lithium metal anode. *Nano Res.* **10**, 4256–4265 (2017).

95. Ferraresi, G. *et al.* Electrochemical Performance of All-Solid-State Li-Ion Batteries Based on Garnet Electrolyte Using Silicon as a Model Electrode. *ACS Energy Lett.* **3**, 1006–1012 (2018).

96. Jin, Y. & McGinn, P. J. Al-doped Li7La3Zr2O12 synthesized by a polymerized complex method. *J. Power Sources* **196**, 8683–8687 (2011).

97. Rangasamy, E., Wolfenstine, J. & Sakamoto, J. The role of Al and Li concentration on the formation of cubic garnet solid electrolyte of nominal composition Li 7La 3Zr 2O 12. *Solid State Ionics* **206**, 28–32 (2012).

98. Cheng, L. *et al.* Effect of microstructure and surface impurity segregation on the electrical and electrochemical properties of dense Al-substituted Li7La 3Zr2O12. *J. Mater. Chem. A* **2**, 172–181 (2014).

99. Kingery, W., Bowen, H. & Uhlmann, D. *Introduction to Ceramics*. (Wiley, 2006).

100. Wang, C. *et al.* Universal Soldering of Lithium and Sodium Alloys on Various Substrates for Batteries. *Adv. Energy Mater.* **8**, 1–8 (2018).

101. Rehnlund, D. *et al.* Lithium trapping in alloy forming electrodes and current collectors for lithium based batteries. *Energy Environ. Sci.* **10**, 1350–1357 (2017).

102. Wang, X. *et al.* Glassy Li Metal Anode for High-Performance Rechargeable Li Batteries. *Nat. Mater.* (2019).

103. Zhao, B., Ran, R., Liu, M. & Shao, Z. A comprehensive review of Li4Ti5O12-based electrodes for lithium-ion batteries: The latest advancements and future perspectives. *Mater. Sci. Eng. R Reports* **98**, 1–71 (2015).

104. Ohzuku, T., Ueda, A. & Yamamoto, N. Zero-Strain Insertion Material of Li [Li1 / 3Ti5 / 3] O 4 for Rechargeable Lithium Cells. *J. Electrochem. Soc.* **142**, 1431 (1995).

105. Abraham, D. P., Heaton, J. R., Kang, S.-H., Dees, D. W. & Jansen, A. N. Investigating the Low-Temperature Impedance Increase of Lithium-Ion Cells. *J. Electrochem. Soc.* **155**, A41 (2007).

106. Ganapathy, S. & Wagemaker, M. Fast interfaces. *Nat. Energy* **5**, 424–425 (2020).

107. Zhang, S. Z. *et al.* Facile interfacial modification via in-situ ultraviolet solidified gel

polymer electrolyte for high-performance solid-state lithium ion batteries. *J. Power Sources* **409**, 31–37 (2019).

108. Oudenhoven, J. F. M., Baggetto, L. & Notten, P. H. L. All-solid-state lithium-ion microbatteries: A review of various three-dimensional concepts. *Adv. Energy Mater.* **1**, 10–33 (2011).

109. Manthiram, A. A reflection on lithium-ion battery cathode chemistry. *Nat. Commun.* **11**, 1550 (2020).

110. Xu, C. *et al.* Bulk fatigue induced by surface reconstruction in layered Ni-rich cathodes for Li-ion batteries. *Nat. Mater.* **20**, 84–92 (2021).

111. Kim, J. *et al.* Prospect and Reality of Ni-Rich Cathode for Commercialization. *Adv. Energy Mater.* **8**, 1–25 (2018).

112. Goodenough, J. B. & Padhi, A. K. Phospho-olivines as Positive-Electrode Materials for Rechargeable Lithium Batteries. **144**, 2–8 (1997).

113. Larcher, D. & Tarascon, J. M. Towards greener and more sustainable batteries for electrical energy storage. *Nat. Chem.* **7**, 19–29 (2015).

114. Han, X. *et al.* Negating interfacial impedance in garnet-based solid-state Li metal batteries. *Nat. Mater.* **16**, 572–579 (2017).

115. Sakuda, A., Hayashi, A. & Tatsumisago, Interfacial Observation between LiCoO 2 Electrode and Li 2 S - P 2 S 5 Solid Electrolytes of All-Solid-State Lithium Secondary Batteries Using Transmission Electron Microscopy†. *Chem. Mater.* **22**, 949–956 (2010).

116. Kasemchainan, J. *et al.* Critical stripping current leads to dendrite formation on plating in lithium anode solid electrolyte cells. *Nat. Mater.* **18**, 1105–1111 (2019).

117. Wang, M., Wolfenstine, J. B. & Sakamoto, J. Temperature dependent flux balance of the Li/Li7La3Zr2O12 interface. *Electrochim. Acta* **296**, 842–847 (2019).

118. Lin, L. *et al.* Synergistic effect of interface layer and mechanical pressure for advanced Li metal anodes. *Energy Storage Mater.* **26**, 112–118 (2020).

119. Abhilash, K. P., Selvin, P. C., Nalini, B., Nithyadharseni, P. & Pillai, B. C. Investigations

on pure and Ag doped lithium lanthanum titanate (LLTO) nanocrystalline ceramic electrolytes for rechargeable lithium-ion batteries. *Ceram. Int.* **39**, 947–952 (2013).

120. Fu, K. (Kelvin) *et al.* Toward garnet electrolyte–based Li metal batteries: An ultrathin, highly effective, artificial solid-state electrolyte/metallic Li interface. *Sci. Adv.* **3**, (2017).

121. Richards, W. D., Miara, L. J., Wang, Y., Kim, J. C. & Ceder, G. Interface Stability in Solid-State Batteries. *Chem. Mater.* **28**, 266–273 (2016).

122. Heligman, B. T. & Manthiram, A. Elemental Foil Anodes for Lithium-Ion Batteries. *ACS Energy Lett.* 2666–2672 (2021).

123. Krauskopf, T., Mogwitz, B., Rosenbach, C., Zeier, W. G. & Janek, J. Diffusion Limitation of Lithium Metal and Li–Mg Alloy Anodes on LLZO Type Solid Electrolytes as a Function of Temperature and Pressure. *Adv. Energy Mater.* 1902568 (2019).

124. Lopez, J. *et al.* Effects of Polymer Coatings on Electrodeposited Lithium Metal. *J. Am. Chem. Soc.* **140**, 11735–11744 (2018).

125. Takada, K., Ohta, N. & Tateyama, Y. Recent Progress in Interfacial Nanoarchitectonics in Solid-State Batteries. *J. Inorg. Organomet. Polym. Mater.* **25**, 205–213 (2015).

126. Bi, J. *et al.* Materials Chemistry A Materials for energy and sustainability Materials Chemistry A Materials for energy and sustainability Accepted Manuscript A hybrid solid electrolyte of Li 0.33 La 0.557 TiO 3 /poly(acylonitrile) membrane infiltrated with succinonitri. *J. Mater. Chem. A Accept. Manuscr.* **6**, 4883–5230 (2019).

127. Huang, Y., Shao, B. & Han, F. Li alloy anodes for high-rate and high-areal-capacity solid-state batteries. *J. Mater. Chem. A* **10**, 12350–12358 (2022).

128. Santhosha, A. L., Medenbach, L., Buchheim, J. R. & Adelhelm, P. The Indium−Lithium Electrode in Solid-State Lithium-Ion Batteries: Phase Formation, Redox Potentials, and Interface Stability. *Batter. Supercaps* **2**, 524–529 (2019).

129. Zhou, Y. *et al.* A novel dual-protection interface based on gallium-lithium alloy enables dendrite-free lithium metal anodes. *Energy Storage Mater.* **39**, 403–411 (2021).

130. Yang, W. *et al.* Gallium-based anodes for alkali metal ion batteries. *J. Energy Chem.* **55**, 557–571 (2021).

131. Kravchyk, K. V., Karabay, D. T. & Kovalenko, M. V. On the feasibility of all-solid-state batteries with LLZO as a single electrolyte. *Sci. Rep.* **12**, 1–10 (2022).

132. Ren, Y., Liu, T., Shen, Y., Lin, Y. & Nan, C. W. Chemical compatibility between garnet-like solid state electrolyte Li6.75La3Zr1.75Ta0.25O12and major commercial lithium battery cathode materials. *J. Mater.* **2**, 256–264 (2016).

133. Barai, P. *et al.* Investigation of Delamination-Induced Performance Decay at the Cathode/LLZO Interface. *Chem. Mater.* **33**, 5527–5541 (2021).

134. Kim, K. J. & Rupp, J. L. M. All ceramic cathode composite design and manufacturing towards low interfacial resistance for garnet-based solid-state lithium batteries. *Energy Environ. Sci.* **13**, 4930–4945 (2020).

135. Masaki Yoshio, H. N. *Lithium-Ion Batteries, Chapter 2*. *Lithium-Ion Batteries* (2009).

136. Kravchyk, K. V., Zhang, H., Okur, F. & Kovalenko, M. V. Li-Garnet Solid-State Batteries with LLZO Scaffolds. *Accounts Mater. Res.* **3**, 411–415 (2022).

137. Hitz, G. T. *et al.* High-rate lithium cycling in a scalable trilayer Li-garnet-electrolyte architecture. *Mater. Today* **22**, 50–57 (2019).

138. Schnell, J. *et al.* All-solid-state lithium-ion and lithium metal batteries – paving the way to large-scale production. *J. Power Sources* **382**, 160–175 (2018).

139. Schnell, J. *et al.* All-solid-state lithium-ion and lithium metal batteries – paving the way to large-scale production. *J. Power Sources* **382**, 160–175 (2018).

140. Chen, A., Qu, C., Shi, Y. & Shi, F. Manufacturing Strategies for Solid Electrolyte in Batteries. *Front. Energy Res.* **8**, 1–18 (2020).

141. Bouchard, P., Guerin, P.-E., St-Amant, G. & Laroche, G. 5528920 Process for laminating a thin film of lihium by controlled detachment. *J. Power Sources* **67**, 342 (1997).

142. Liang, Z. *et al.* Composite lithium metal anode by melt infusion of lithium into a 3D conducting scaffold with lithiophilic coating. *Proc. Natl. Acad. Sci. U. S. A.* **113**, 2862–2867 (2016).

143. Neudecker, B. J., Dudney, N. J. & Bates, J. B. “Lithium-Free” Thin-Film Battery with In Situ Plated Li Anode. *J. Electrochem. Soc.* **147**, 517 (2000).

144. Savaniu, C. CH5716 -processing materials. lecture 11 (2018).

145. Wright, J. D. & Sommerdijk, N. A. J. M. *Sol-Gel Materials*. *CRC Press* **6**, (CRC Press, 2001).

146. West, A. R. *Solid state and its applications*. (Wiley, 2014).

147. Jadhav, L. D., Patil, S. P., Jamale, A. P. & Chavan, A. U. Solution combustion synthesis: Role of oxidant to fuel ratio on powder properties. *Mater. Sci. Forum* **757**, 85–98 (2013).

148. Sands, D. *Introduction to Crystallography*. (Dover publications, 2012).

149. Southworth, H. N. *Scanning Electron Microscopy and Microanalysis*. *Physicochemical Methods of Mineral Analysis* (1975).

150. Zhou, W. CH5717 Nanostructure materials. 2.2 (2017).

151. Irvine, J. T. S., Sinclair, D. C. & West, A. R. Electroceramics: Characterization by Impedance Spectroscopy. *Adv. Mater.* **2**, 132–138 (1990).

152. Lazanas, A. C. & Prodromidis, M. I. Electrochemical Impedance Spectroscopy–A Tutorial. *ACS Meas. Sci. Au* (2022).

153. Kendig, M. Electrochemical Impedance Analysis and Interpretation. *ASTM Spec. Tech. Publ.* (1993). doi:10.1520/stp1188-eb

154. Lee, C., Dutta, P. K., Ramamoorthy, R. & Akbar, S. A. Mixed Ionic and Electronic Conduction in Li[sub 3]PO[sub 4] Electrolyte for a CO[sub 2] Gas Sensor. *J. Electrochem. Soc.* **153**, H4 (2006).

155. García, R. & Pérez, R. Dynamic atomic force microscopy methods. *Surf. Sci. Rep.* **47**, 197–301 (2002).

156. Seo, Y. & Jhe, W. Atomic force microscopy and spectroscopy. *Reports Prog. Phys.* **71**, (2008).

157. Kittel, C. *Introduction to Solid State Physics*. (Wiley, 1986).

158. Banerjee, D. Experimental Techniques in Thermal Analysis Thermogravimetry (TG) & Differential Scanning Calorimetry (DSC). *Anal. Proc.* 469–508 (1993).

159. Karger-Kocsis, J. Thermal Analysis of Polymers: Fundamentals and Applications. *Macromol. Chem. Phys.* **210**, 1661–1661 (2009).

160. Sperazza, M., Moore, J. N. & Hendrix, M. S. *HIGH-RESOLUTION PARTICLE SIZE ANALYSIS OF NATURALLY OCCURRING VERY FINE-GRAINED SEDIMENT THROUGH LASER DIFFRACTOMETRY*. *JOURNAL OF SEDIMENTARY RESEARCH* **74**, (SEPM (Society for Sedimentary Geology, 2004).

161. Malvern Instruments. Mastersizer 2000 laser diffractometer. (2000).

162. Theory, I., Yguerabide, J. & Yguerabide, E. E. *Light-Scattering Submicroscopic Particles as Highly Fluorescent Analogs and Their Use as Tracer Labels in Clinical and Biological Applications*. (1998).

163. KERKER, M. *The Scattering of Light and Other Electromagnetic Radiation*. (Elsevier, 1969).

164. Edwards, H. G. M. *Modern Raman spectroscopy—a practical approach. J. Raman Spectrosc.* **36**, (John Wiley, 2005).

165. Munters. No moisture . No Ice. Munters cold storage dehumidification solutions. *Brochure* (2021).

166. Ab, M. E. Users manual Desiccant dehumidifier. (2014).

167. Wallace, J. M. & Hobbs, P. V. Atmospheric Thermodynamics. in *Atmospheric Science* 63–111 (Elsevier, 2006).

168. Attension, technical note. Surface free energy - theory and calculations. *Lect. Contact Angl.* **3**, 457–460 (2013).

169. Kwok, D. Y. & Neumann, A. W. Contact angle measurement and contact angle interpretation. *Adv. Colloid Interface Sci.* **81**, 167–249 (1999).

170. Wang, J. *et al.* Fundamental study on the wetting property of liquid lithium. *Energy Storage Mater.* **14**, 345–350 (2018).

171. Aksay, I. A., Hoge, C. E. & Pask, J. A. Wetting under Chemical Equilibrium. *J. Phys. Chem.* **i**, 1178–1183 (1973).

172. Aqra, F. & Ayyad, A. Surface energies of metals in both liquid and solid states. *Appl.*

Surf. Sci. **257**, 6372–6379 (2011).

173. Kaptay, G. A unified model for the cohesive enthalpy, critical temperature, surface tension and volume thermal expansion coefficient of liquid metals of bcc, fcc and hcp crystals. *Mater. Sci. Eng. A* **495**, 19–26 (2008).

174. Triantafyllou, G., Angelopoulos, G. N. & Nikolopoulos, P. Surface and grain-boundary energies as well as surface mass transport in polycrystalline yttrium oxide. *J. Mater. Sci.* **45**, 2015–2022 (2010).

175. Schrader, M. E. Young-Dupre Revisited. *Langmuir* **11**, 3585–3589 (1995).

176. Gambaryan-Roisman, T. Liquids on porous layers: Wetting, imbibition and transport processes. *Curr. Opin. Colloid Interface Sci.* **19**, 320–335 (2014).

177. Pierre-Louis, O. Solid-state wetting at the nanoscale. *Prog. Cryst. Growth Charact. Mater.* **62**, 177–202 (2016).

178. Hou, W., Ding, G., Liu, W., Deng, Y. & Ran, C. Wetting on Nanoporous Alumina Surface: Transition between Wenzel and Cassie States Controlled by Surface Structure. *Langmuir* **24**, 9952–9955 (2008).

179. McHale, G., Orme, B. V., Wells, G. G. & Ledesma-Aguilar, R. Apparent Contact Angles on Lubricant-Impregnated Surfaces/SLIPS: From Superhydrophobicity to Electrowetting. *Langmuir* **35**, 4197–4204 (2019).

180. Vladsinger. Contact angle microstates. (2014). Available at: https://commons.wikimedia.org/wiki/File:Contact_angle_microstates.svg. (Accessed: 19th May 2020)

181. Zheng, Z., Zhang, Y., Song, S. & Wang, Y. Sol-gel-processed amorphous inorganic lithium ion electrolyte thin films sol chemistry. *RSC Adv.* **7**, 30160–30165 (2017).

182. Bohnke, C., Regrag, B., Le Berre, F., Fourquet, J. L. & Randrianantoandro, N. Comparison of pH sensitivity of lithium lanthanum titanate obtained by sol-gel synthesis and solid state chemistry. *Solid State Ionics* **176**, 73–80 (2005).

183. Bugrov, A. N. *et al.* Soft chemistry synthesis and dielectric properties of A-site deficient perovskite-type compound La2/3TiO3-δ. *Ceram. Int.* **42**, 1698–1704 (2016).

184. Jimenez, R., Rivera, A., Varez, A. & Sanz, J. Li mobility in Li0.5-xNaxLa0.5TiO 3 perovskites (0≥x≥0.5) Influence of structural and compositional parameters. *Solid State Ionics* **180**, 1362–1371 (2009).

185. Sotomayor, M. E., Levenfeld, B., Varez, A. & Sanz, J. Study of the La1/2+1/2xLi1/2-1/2xTi1-xAlxO3 (0 ≤ x ≤ 1) solid solution. A new example of percolative system in fast ion conductors. *J. Alloys Compd.* **720**, 460–465 (2017).

186. Ibarra, J. *et al.* Influence of composition on the structure and conductivity of the fast ionic conductors La2/3-xLi3xTiO3 (0.03≤x≤0.167). *Solid State Ionics* **134**, 219–228 (2000).

187. Várez, A., García-Alvarado, F., Morán, E. & Alario-Franco, M. A. Microstructural study of La0.5Li0.5TiO3. *J. Solid State Chem.* **118**, 78–83 (1995).

188. Zinkevich, T. *et al.* Effect of sintering temperature on Li diffusivity in Li0.29La0.57TiO3: Local hopping and long-range transport. *Solid State Ionics* **357**, 115486 (2020).

189. Borisevich, A. Y. & Davies, P. K. La(Li1/3Ti2/3)O3: A new 1:2 ordered perovskite. *J. Solid State Chem.* **170**, 198–201 (2003).

190. Ishizawa, N., Marumo, F., Iwai, S., Kimura, M. & Kawamura, T. Compounds with perovskite-type slabs. V. A high-temperature modification of La2Ti2O7. *Acta Crystallogr. Sect. B Struct. Crystallogr. Cryst. Chem.* **38**, 368–372 (1982).

191. Lee, H. J., Park, H. M., Cho, Y. K. & Nahm, S. Microstructure Characterization of the (1−x)La2/3TiO3-xLaAlO3 System. *J. Am. Ceram. Soc.* **86**, 1395–1400 (2003).

192. Brous, J., Fankuchen, I. & Banks, E. Rare earth titanates with a perovskite structure. *Acta Crystallogr.* **6**, 67–70 (1953).

193. Liu, Z., Zhang, N. & Sun, K. A novel grain restraint strategy to synthesize highly crystallized Li 4Ti 5O 12 (∼20 nm) for lithium ion batteries with superior high-rate performance. *J. Mater. Chem.* **22**, 11688–11693 (2012).

194. Kim, J. G., Kim, H. G. & Chung, H. T. Microstructure-ionic conductivity relationships in perovskite lithium lanthanum titanate. *J. Mater. Sci. Lett.* **18**, 493–496 (1999).

195. Sotomayor, M. E., Levenfeld, B., Varez, A. & Sanz, J. Study of the La1/2+1/2xLi1/2-1/2xTi1-xAlxO3 (0 ≤ x ≤ 1) solid solution. A new example of percolative system in fast

ion conductors. *J. Alloys Compd.* **720**, 460–465 (2017).

196. Nolze, G. PowderCell : a mixture between crystal structure visualizer, simulation and refinement tool. *Powder Diffr. Int. Sch.* (2002).

197. Baddour-Hadjean, R., Bach, S., Smirnov, M. & Pereira-Ramos, J. P. Raman investigation of the structural changes in anatase Li xTiO2 upon electrochemical lithium insertion. *J. Raman Spectrosc.* **35**, 577–585 (2004).

198. Lakshmi, D., Nalini, B., Jayapandi, S. & Christopher Selvin, P. Augmented conductivity in Li3xLa2/3−xTiO3 nanoparticles: all-solid-state Li-ion battery applications. *J. Mater. Sci. Mater. Electron.* **31**, 1343–1354 (2020).

199. Yang, K. Y., Wang, J. W. & Fung, K. Z. Roles of lithium ions and La/Li-site vacancies in sinterability and total ionic conduction properties of polycrystalline Li3xLa2/3-xTiO3 solid electrolytes (0.21 ≤ 3x ≤ 0.50). *J. Alloys Compd.* **458**, 415–424 (2008).

200. Fernandez, N. *et al.* Crystal Structure and Electrical Properties of La 0.45 Ce 0.1 Li 0.27 TiO 3 Synthesized by Sol-Gel Technique. *New J. Glas. Ceram.* **2**, 59–64 (2012).

201. Wang, M. J., Wolfenstine, J. B. & Sakamoto, J. Mixed Electronic and Ionic Conduction Properties of Lithium Lanthanum Titanate. *Adv. Funct. Mater.* **30**, 1–9 (2020).

202. Moriwake, H. *et al.* Domain boundaries and their influence on Li migration in solid-state electrolyte (La,Li)TiO3. *J. Power Sources* **276**, 203–207 (2015).

203. Fergus, J. W. Ceramic and polymeric solid electrolytes for lithium-ion batteries. *J. Power Sources* **195**, 4554–4569 (2010).

204. Thangadurai, V. & Weppner, W. Effect of B-site substitution of (Li,La)TiO3 perovskites by Di-, tri-, tetra- and hexavalent metal ions on the lithium ion conductivity. *Ionics (Kiel).* **6**, 70–77 (2000).

205. Duan, J. *et al.* Is graphite lithiophobic or lithiophilic? *Natl. Sci. Rev.* **7**, 1208–1217 (2021).

206. Lu, Y. *et al.* An: In situ element permeation constructed high endurance Li-LLZO interface at high current densities. *J. Mater. Chem. A* **6**, 18853–18858 (2018).

207. Morgan, B. J., Carrasco, J. & Teobaldi, G. Variation in surface energy and reduction

drive of a metal oxide lithium-ion anode with stoichiometry: A DFT study of lithium titanate spinel surfaces. *J. Mater. Chem. A* **4**, 17180–17192 (2016).

208. Eustathopoulos, N. & Voytovych, R. The role of reactivity in wetting by liquid metals: a review. *J. Mater. Sci.* **51**, 425–437 (2016).

209. Wang, C. *et al.* Conformal, Nanoscale ZnO Surface Modification of Garnet-Based Solid-State Electrolyte for Lithium Metal Anodes. *Nano Lett.* **17**, 565–571 (2017).

210. Krauskopf, T., Hartmann, H., Zeier, W. G. & Janek, J. Toward a Fundamental Understanding of the Lithium Metal Anode in Solid-State Batteries - An Electrochemo-Mechanical Study on the Garnet-Type Solid Electrolyte Li 6.25 Al 0.25 La 3 Zr 2 O 12. *ACS Appl. Mater. Interfaces* **11**, 14463–14477 (2019).

211. Mathur, A. *et al.* Negative surface energy - Clearing up confusion (multiple letters). *Nat. Mater.* **4**, 186 (2005).

212. Rulison, C. *et al.* Effect of temperature on the surface energy of solids. *KRUSS Application Note AN250e* 39–40 (2005).

213. Meade, R. D. & Vanderbilt, D. Origins of Stress on Elemental and Chemisorbed Semiconductor Surfaces. **63**, 1404–1407 (1989).

214. Gumbsch, P. & Daw, M. S. Interface stresses and their effects on the elastic moduli of metallic multilayers. *Phys. Rev. B* **44**, 3934–3938 (1991).

215. Lancaster, J. F. *Metallurgy of Welding: 3- The use of adhesives for making structural joints*. *Metallurgy of Welding* (Woodhead Publishing, 1999).

216. Fang, X., Fan, T. & Zhang, D. Work of adhesion in Al/SiC composites with alloying element addition. *Metall. Mater. Trans. A Phys. Metall. Mater. Sci.* **44**, 5192–5201 (2013).

217. Kinloch, A. J., Hall & Chapman. *Adhesion & Adhesives - Science & Technology*. (1987).

218. Xin, J., Wang, N., Chen, M. & Gan, L. Surface tension calculation of molten slag in SiO2–Al2O3–CaO–MgO systems based on a statistical modelling approach. *ISIJ Int.* **59**, 759–767 (2019).

219. Hejda, F., Solaˇ, P. & Kousal, J. Surface Free Energy Determination by Contact Angle

Measurements – A Comparison of Various Approaches. in *WDS'10 Proceedings of Contributed Papers* 25–30 (2010).

220. Brada, M. P. & Clarke, D. R. A thermodynamic approach to the wetting and dewetting of grain boundaries. *Acta Mater.* **45**, 2501–2508 (1997).

221. Ren, Y., Zhou, R., Zhu, D. & Zhang, T. The reactive wetting kinetics of interfacial tension: a reaction-limited model. *RSC Adv.* **7**, 13003–13009 (2017).

222. Yan, H. *et al.* How Does the Creep Stress Regulate Void Formation at the Lithium-Solid Electrolyte Interface during Stripping? *Adv. Energy Mater.* **12**, 1–11 (2022).

223. Wolfenstine, J. *et al.* A preliminary investigation of fracture toughness of Li7La 3Zr2O12 and its comparison to other solid Li-ionconductors. *Mater. Lett.* **96**, 117–120 (2013).

224. Park, R. J. Y. *et al.* Semi-solid alkali metal electrodes enabling high critical current densities in solid electrolyte batteries. *Nat. Energy* (2021).

225. Connor, P. A. *et al.* Tailoring SOFC Electrode Microstructures for Improved Performance. *Adv. Energy Mater.* **8**, 1–20 (2018).

226. Kim, D. H. *et al.* Infiltration of Solution-Processable Solid Electrolytes into Conventional Li-Ion-Battery Electrodes for All-Solid-State Li-Ion Batteries. *Nano Lett.* **17**, 3013–3020 (2017).

227. Zhang, S. X. *et al.* Vibrational modes in La2Zr2O7 pyrochlore irradiated with disparate electrical energy losses. *Chinese Phys. B* **28**, (2019).

228. Sanjuán, M. L., Laguna, M. A., Belous, A. G. & V'Yunov, O. I. On the local structure and lithium dynamics of la0.5(Li,Na) 0.5TiO3 ionic conductors. A Raman study. *Chem. Mater.* **17**, 5862–5866 (2005).

229. Romero, M., Faccio, R., Vázquez, S., Davyt, S. & Mombrú, Á. W. E. and theoretical R. study on the structure and microstructure of L. 30La0. 57TiO. electrolyte prepared by the sol-gel method in acetic medium. Experimental and theoretical Raman study on the structure and microstructure of Li0.30La0.57TiO3 electrolyte prepared by the sol-gel method in acetic medium. *Ceram. Int.* **42**, 15414–15422 (2016).

230. Asadov, A. G. *et al.* A structural phase transition in La2Ti2O7 at high pressure. *Phys. B*

Condens. Matter **655**, 414753 (2023).

231. Richard, M. E. & Twiname, E. R. *Tape Casting Theory and practice*. (Wiley, 2000).

232. Zhang, C., Oliaee, S. N., Hwang, S. Y., Kong, X. & Peng, Z. A Generic Wet Impregnation Method for Preparing Substrate-Supported Platinum Group Metal and Alloy Nanoparticles with Controlled Particle Morphology. *Nano Lett.* **16**, 164–169 (2016).

233. Léger, A., Weber, L. & Mortensen, A. Influence of the wetting angle on capillary forces in pressure infiltration. *Acta Mater.* **91**, 57–69 (2015).

234. Eustathopoulos, N. Wetting by Liquid Metals—Application in Materials Processing: The Contribution of the Grenoble Group. *Metals (Basel).* **5**, 350–370 (2015).

235. Guan, J. T., Qi, L. H., Liu, J., Zhou, J. M. & Wei, X. L. Threshold pressure and infiltration behavior of liquid metal into fibrous preform. *Trans. Nonferrous Met. Soc. China (English Ed.* **23**, 3173–3179 (2013).

236. Gao, J., Shi, S. Q. & Li, H. Brief overview of electrochemical potential in lithium ion batteries. *Chinese Phys. B* **25**, (2015).

237. Yoshinari, T. *et al.* Quantitative Elucidation of the Non-Equilibrium Phase Transition in LiFePO4 via the Intermediate Phase. *Chem. Mater.* **31**, 7160–7166 (2019).

238. Sun, Y., Zan, L. & Zhang, Y. Effects of Li3PO4 additive on the electrochemical properties of Li2FeSiO4 as cathode material for lithium-ion batteries. *J. Mater. Sci. Mater. Electron.* **30**, 15582–15591 (2019).

239. Ruiz, A. I., Lopez, M. L., Pico, C. & Veiga, M. L. New La2/3TiO3 derivatives: Structure and impedance spectroscopy. *J. Solid State Chem.* **163**, 472–478 (2002).

240. Gwyddion, version 2.57, microscopy software, available at: http://gwyddion.net/